University of Southampton

Faculty of Social Sciences
School of Mathematical Sciences

Modelling Black Hole Binaries in the Intermediate-Mass-Ratio Regime

by

Mekhi Dhesi
ORCiD: 0000-0003-0017-4302

A thesis for the degree of
Doctor of Philosophy

February 2023

University of Southampton

Abstract

Faculty of Social Sciences
School of Mathematical Sciences

Doctor of Philosophy

Modelling Black Hole Binaries in the Intermediate-Mass-Ratio Regime

by Mekhi Dhesi

This work presents a new method for creating gravitational waveform templates for black hole binaries with an intermediate mass-ratio. Intermediate-mass-ratio inspirals (IMRIs) are currently an open problem in gravitational-wave source modelling. While black hole perturbation theory can accurately model extreme-mass-ratio inspirals, and numerical relativity has seen much success modelling comparable-mass inspirals, neither approach currently works well on its own for IMRIs. It is not clear how adequate a purely perturbative treatment can be at intermediate mass-ratios of 1:100-1:1000, and at such mass ratios the length-scale disparity remains large enough to pose a serious challenge for numerical relativity.

Here we work to provide accurate modelling of such binaries through a synergistic combination of black-hole perturbation and numerical relativity techniques. Our approach matches an approximate analytical solution near the smaller black hole (formed from the tidally perturbed black hole metric) to a fully nonlinear numerical solution in the bulk of the spacetime. This has the effect of relieving some of the scale disparity.

This thesis presents the details of this worldtube excision model and goes on to develop and test the architecture using a simple toy model of a scalar charge in orbit around a Schwarzschild black hole. We then present results from numerical implementations of such a test setup in 1+1D, as well as in 3+1D. Finally, we detail the model's infrastructure in the full binary black hole case. The theoretical foundations of the model are erected, which includes the derivation of a suitable approximate analytical solution.

Contents

List of Figures **ix**

List of Tables **xi**

Declaration of Authorship **xiii**

Acknowledgements **xv**

List of Acronyms **xvii**

1 Introduction **1**
1.1 Gravitational Wave Astronomy . . . 1
1.1.1 Binary Systems and Future Detections . . . 4
1.2 Intermediate-Mass-Ratio Inspirals . . . 6
1.2.1 Formation Mechansisms . . . 6
1.2.2 Detection Prospects . . . 7
1.2.3 Relevant LIGO Detections . . . 7
1.3 Binary Black Hole Modelling Techniques . . . 9
1.3.1 Overview . . . 9
1.3.2 Numerical Relativity . . . 11
1.3.2.1 Progress towards IMRIs . . . 12
1.3.3 Black Hole Perturbation Theory . . . 14
1.3.3.1 Gravitational Self-Force Theory . . . 14
1.3.3.2 Progress towards IMRIs . . . 15
1.4 Thesis Outline . . . 16
1.5 Research Collaboration Details . . . 18

2 Method Overview **21**
2.1 Worldtube Excision . . . 21
2.2 Comparisons to Existing Methods . . . 22
2.3 Estimated Runtime Saving . . . 25

3 Scalar-Field Model in 1+1D **27**
3.1 Multipole Decomposition . . . 27
3.2 Static-Mode Solution . . . 29
3.3 Local Approximate Solution . . . 30
3.4 Matching Overview . . . 32

4 1+1D Scalar-Field Model: Scheme I **35**
4.1 Setup . . . 35
4.1.1 Characteristic Grid . . . 35
4.1.2 Numerical Method . . . 36
4.2 Test Setups . . . 39
4.2.1 Evolution with a Point Particle Source . . . 39
4.2.2 Evolution with the Exact Analytical Solution inside a Worldtube . 42
4.3 Evolution with a Worldtube . . . 45
4.3.1 Matching Method . . . 45
4.3.1.1 Ethos . . . 45
4.3.1.2 Implementation . . . 48
4.3.2 Results . . . 51
4.3.2.1 Static Modes . . . 51
4.3.2.2 Radiative Modes . . . 51
4.3.2.3 Convergence . . . 52
4.3.2.4 Convergence with Resolution . . . 53
4.3.2.5 Convergence with Worldtube Size . . . 55

5 1+1D Scalar-Field Model: Scheme II **63**
5.1 Setup . . . 63
5.1.1 Numerical Method . . . 64
5.1.1.1 Foundations of Spectral Methods . . . 64
5.1.1.2 Our Spectral Method . . . 65
5.2 Evolution with a Worldtube . . . 65
5.2.1 Matching Method . . . 65
5.2.1.1 Implementation . . . 66
5.2.1.2 Boundary Treatment . . . 68
5.2.2 Results . . . 70
5.2.2.1 Static Modes . . . 70
5.2.2.2 Radiative Modes . . . 71
5.2.2.3 Convergence . . . 72
5.2.2.4 Convergence with Resolution . . . 72
5.2.2.5 Convergence with Worldtube Size . . . 74

6 3+1D Scalar-Field Model **79**
6.1 Setup . . . 79
6.2 Numerical Evolution . . . 81
6.2.1 SpECTRE . . . 81
6.2.2 Kerr-Schild Coordinates . . . 81
6.2.3 Numerical Details . . . 82
6.3 Local Approximate Solution and Matching Method . . . 85
6.3.1 First Principles Derivation . . . 85
6.3.2 Matching Ethos . . . 89
6.3.3 High-Order Covariant Expressions . . . 90
6.3.4 Transformation to Kerr-Schild Coordinates . . . 92
6.4 Matching Method in Kerr-Schild Coordinates . . . 94
6.4.1 Zeroth-Order Implementation . . . 95

6.4.2 First-Order Implementation . . . 95
6.4.3 Second-Order Implementation . . . 95
6.5 Results . . . 98
6.5.1 Convergence with Resolution . . . 98
6.5.2 Convergence with Worldtube Size . . . 99

7 Gravity Model 105
7.1 Setup . . . 105
7.2 Generalised Harmonic Gauge . . . 106
7.3 Coordinate Systems in our Worldtube Scheme . . . 108
7.4 Matching Method . . . 110

8 Tidally Perturbed Black Hole Metric 113
8.1 Manifolds, Coordinates, Metrics . . . 114
8.2 Spherical-Harmonic Decomposition . . . 114
8.3 Regge-Wheeler Gauge . . . 116
8.4 The Field Equations in the Regge-Wheeler Gauge . . . 117
8.5 Solution for a Tidally Perturbed Black Hole . . . 119

9 Transformation to Harmonic Coordinates 123
9.1 Forward Transformation . . . 123
9.1.1 Set Up . . . 123
9.1.2 Solution at $\mathcal{O}(\epsilon^0)$ . . . 126
9.1.3 Solution at $\mathcal{O}(\epsilon^1)$ . . . 127
9.1.4 Solution at $\mathcal{O}(\epsilon^2)$ . . . 128
9.1.5 Final Results . . . 132
9.2 Inverse Transformation . . . 133
9.2.1 Setup . . . 133
9.2.2 Inversion at $\mathcal{O}(\epsilon^0)$ . . . 135
9.2.3 Inversion at $\mathcal{O}(\epsilon^1)$ . . . 136
9.2.4 Inversion at $\mathcal{O}(\epsilon^2)$ . . . 137
9.2.5 Final Results . . . 141
9.3 Transformed Metric . . . 144
9.3.1 Preliminaries . . . 144
9.3.2 Tidally Perturbed Black Hole Metric in Harmonic Coordinates . . . 148

10 Summary and Concluding Remarks 153
10.1 Future Work . . . 154
10.2 Perspective . . . 155

Appendix A Singular Part of the Scalar Field in Kerr-Schild Coordinates 157

Appendix B Derivatives of Spherical Harmonics 161

References 163

List of Figures

1.1 A Michelson interferometer . . . 2
1.2 GW150914 observed by the LIGO detector . . . 3
1.3 Compact binaries observed by LIGO-Virgo-KAGRA to date . . . 4
1.4 Artistic impression of the LISA mission . . . 5
1.5 Predicted multiband detectability of various binary populations . . . 8
1.6 Analysis of O3 observations . . . 9
1.7 Analysis of O3b observations . . . 10
1.8 Modelling methods for black hole binaries . . . 11
1.9 NR waveform for a 1:128 mass-ratio binary . . . 13
1.10 NR simulations up to 1:1024 mass-ratios . . . 13
1.11 2SF waveform for a mass-ratio 1:10 nonspinning binary . . . 15
1.12 2SF waveform for a mass-ratio 1:1 nonspinning binary . . . 16
1.13 Modelling methods for black hole binaries, a quantitative adaptation . . . 17

2.1 The worldtube excision method . . . 22
2.2 The puncture scheme used in GSF theory . . . 24
2.3 The moving puncture method in NR . . . 24
2.4 The excision method in NR . . . 25

4.1 Characteristic grid without a source . . . 36
4.2 Depiction of a characteristic grid cell . . . 37
4.3 Evolution of a Gaussian wave packet in a characteristic grid . . . 38
4.4 Convergence test with respect to h for a non-sourced evolution . . . 39
4.5 Characteristic grid with a point particle source . . . 39
4.6 Field values for a point particle evolution, at a slice of late time . . . 42
4.7 Convergence test with respect to h for a point particle evolution . . . 43
4.8 Characteristic grid with a worldtube . . . 43
4.9 Field values for a worldtube evolution with the exact analytical solution in the interior, at a slice of late time . . . 44
4.10 Convergence test with respect to h for a worldtube evolution using the exact analytical solution within the interior . . . 44
4.11 Characteristic grid with a worldtube and illustration of data points . . . 45
4.12 Spacetime diagram illustrating regions involved in the 1+1D matching method . . . 46
4.13 Data points used to fit for the unknown parameters $\psi^{\mathcal{R}}_{ij}$ . . . 49
4.14 Field values for a worldtube evolution, at a slice of late time and for a static mode . . . 52
4.15 Point selection for convergence tests with respect to h . . . 53

4.16 Convergence of the worldtube method with respect to grid resolution h . 54
4.17 The relative error for the Ψ_{20} mode 56
4.18 The relative error for the Ψ_{22} mode 57
4.19 Convergence of the numerical solution with respect to worldtube radius R 59
4.20 The relative L^1 error norm as a function of worldtube radius R 60
4.21 Convergence of the L^1 error norm as a function of worldtube radius R . . 61

5.1 The relative error for the Ψ_{20} mode. 71
5.2 The relative error for the Ψ_{44} mode. 72
5.3 Exponential convergence with resolution at fixed worldtube radius R. . . 73
5.4 The error of the Ψ_{20} mode as a function of resolution. 73
5.5 The relative L^1 error norm and its convergence, as a function of the worldtube radius R for the Ψ_{20} mode, with $n_{\mathcal{R}} = 5$ 75
5.6 The relative L^1 error norm and its convergence, as a function of the worldtube radius R for the Ψ_{20} mode, with $n_{\mathcal{R}} = 3$ 76
5.7 The relative L^1 error norm and its convergence, as a function of the worldtube radius R for the Ψ_{44} mode, with $n_{\mathcal{R}} = 5$ 77
5.8 The relative L^1 error norm and its convergence, as a function of the worldtube radius R for the Ψ_{44} mode, with $n_{\mathcal{R}} = 3$ 78

6.1 SpECTRE domain for the 3+1D scalar toy model 80
6.2 3+1 decomposition of spacetime 83
6.3 Illustration of field points used in the calculation of the singular field . . . 91
6.4 Scalar waves emanating from a charge e on orbit around a Schwarzschild black hole M, using the worldtube excision method 99
6.5 Exponential convergence with resolution at fixed worldtube radius R . . . 100
6.6 The relative error of the scalar field Φ^N along the z-axis 102
6.7 The relative L^1 error norm along the z-axis and its convergence, as a function of worldtube radius 103
6.8 The relative error of the scalar field Φ^N along the x-axis 104
6.9 The relative L^1 error norm along the x-axis and its convergence, as a function of worldtube radius 104

7.1 Sketch of the various coordinate systems involved in the BBH worldtube excision model. 110

List of Tables

9.1 $f^0_{\epsilon\ell}$-type functions featuring in Eqs. (9.56)-(9.57) 133
9.2 $f^i_{\epsilon\ell}$-type functions featuring in Eqs. (9.56)-(9.57) 133
9.3 e_0, e_1-type functions featuring in Eqs. (9.112)-(9.114) 142
9.4 e_2-type functions featuring in Eqs. (9.112)-(9.114) 143
9.5 e^A_2-type functions featuring in Eqs. (9.112)-(9.114) 144
9.6 g^{TT} metric components in harmonic coordinates 149
9.7 g^{Ta} metric components in harmonic coordinates 150
9.8 g^{ab} metric components in harmonic coordinates 151

Declaration of Authorship

I declare that this thesis and the work presented in it is my own and has been generated by me as the result of my own original research.

I confirm that:

1. This work was done wholly or mainly while in candidature for a research degree at this University;
2. Where any part of this thesis has previously been submitted for a degree or any other qualification at this University or any other institution, this has been clearly stated;
3. Where I have consulted the published work of others, this is always clearly attributed;
4. Where I have quoted from the work of others, the source is always given. With the exception of such quotations, this thesis is entirely my own work;
5. I have acknowledged all main sources of help;
6. Where the thesis is based on work done by myself jointly with others, I have made clear exactly what was done by others and what I have contributed myself;
7. Parts of this work have been published as:
   Mekhi Dhesi, Hannes R. Rüter, Adam Pound, Leor Barack and Harald P. Pfeiffer. Worldtube excision method for intermediate-mass-ratio inspirals: Scalar-field toy model. *Phys. Rev. D*, 104(124002), Dec 2021.

Signed:..... Date:.....

Acknowledgements

First and foremost, I would like to thank my two supervisors, Leor Barack and Adam Pound. I could not have asked for better supervisors, academically or personally, and I am extremely lucky to have had the opportunity to work with them both. Their patience, intelligence, and mastery of explaining the complex is what made this thesis possible. Even when the mathematics became particularly gritty, we would always find something to laugh about during meetings. The physics was theoretical but the fun was real. Without them, I certainly could not have realised this dream of mine.

Secondly, I would like to thank our collaborators at the Albert Einstein Institute. Harald Pfeiffer was like a third supervisor to me, and I thank him for all his help and guidance over the years. I am grateful to Hannes Rüter for the hours spent writing C++ code with me and to Nikolas Wittek for all the discussions and beautiful plots. I feel very fortunate to have been a part of this exciting research collaboration. A further acknowledgement to the self-force group at The University of Southampton for being so welcoming and helpful, especially Patrick Bourg, Oliver Long, Andrew Spiers and Sam Upton.

I would like to thank Pam and Gurjeet for being the best parents. They have always been there for me and supported me throughout my entire education. Dad, you laid down the physics PhD path to follow. More importantly, you consistently made wonderful meals when I was grouchy and revising for exams. Mum, you continually motivated me and restored my mood with our outings. I would like to thank Lee for encouraging me to pursue theoretical physics and for being there through the entire mathematical journey. All the guidance, textbooks, and discussions over the years were invaluable.

I would like to thank Katie for her friendship, and all those much needed coffee breaks walking along the Southampton pier. Throughout my research she was always there to celebrate my wins and drink wine with me after my losses!

Finally, I would like to thank Joe. The insanity he has witnessed and the fact he is still with me is something I find hard to understand but am very grateful for! His support was constant, from the very start of my MSc to the end of this PhD, including the Coronavirus lockdowns where I was in the depth of my calculations and at the height of my stresses. Joe, I definitely could not have done any of this without you.

Now that I am moving further away from black holes, time will begin to tick faster again. I will look back on those slow seconds immersed in the maths with fond memories.

List of Acronyms

BBH	binary black hole
BNS	binary neutron star
BHNS	black hole-neutron star
CMRI	comparable-mass-ratio inspiral
EMRI	extreme-mass-ratio inspiral
GR	general relativity
GSF	gravitational self-force
GW	gravitational wave
IMBH	intermediate-mass black hole
IMRI	intermediate-mass-ratio inspiral
LISA	Laser Interferometer Space Antenna
NR	numerical relativity
PN	post-Newtonian
SMBH	supermassive black hole
SNR	signal-to-noise ratio
TPBH	tidally perturbed black hole

Chapter 1

Introduction

1.1 Gravitational Wave Astronomy

Einstein's theory of general relativity (GR) resulted in a paradigm shift for our perception of nature [61]. The theory's construction of spacetime, the interwoven fabric of the universe that bends and warps in response to matter, led to the prediction of many rich phenomena. One of the most exciting of these was gravitational waves (GWs), ripples in spacetime itself. Produced in scenarios of accelerating matter, only the most violent astrophysical events have the potential to emit waves with amplitudes detectable by our GW detectors. Such spectacular celestial events include the inspiral of compact object binaries, black hole mergers, and exploding supernovae.

A unique beauty of GWs is their ability to travel almost unimpeded through the universe. Unlike electromagnetic radiation, GWs are not strongly affected by intermediary matter and so can carry information from distant cosmic events, allowing us to probe gravity in some of its strongest regimes. The first indirect detection of gravitational waves came in 1974, with the binary pulsar PSR B1913+16 discovery by Hulse and Taylor [127]. Through electromagnetic observations, the orbital decay of the binary system was able to be calculated. The magnitude of this decay was then found to be consistent with the energy loss due to GW emission, as predicted by the theory of GR [143, 54]. This indirect discovery then spurred on the community's desire to directly detect GWs.

The next breakthrough came with the design of the GW interferometer, building on the architecture of the Michelson interferometer. When a gravitational wave propagates, it stretches and compresses the space-time through which it travels. This effect can be measured via the relative separation of two test particles. The basic design of the laser interferometer consists of perpendicular arms with mirrors (suspended as test masses) at each end, see Fig. 1.1. Laser beams are then sent back and forth along the perpendicular arms. Any relative change in the length of the arms, i.e. due to a transient gravitational

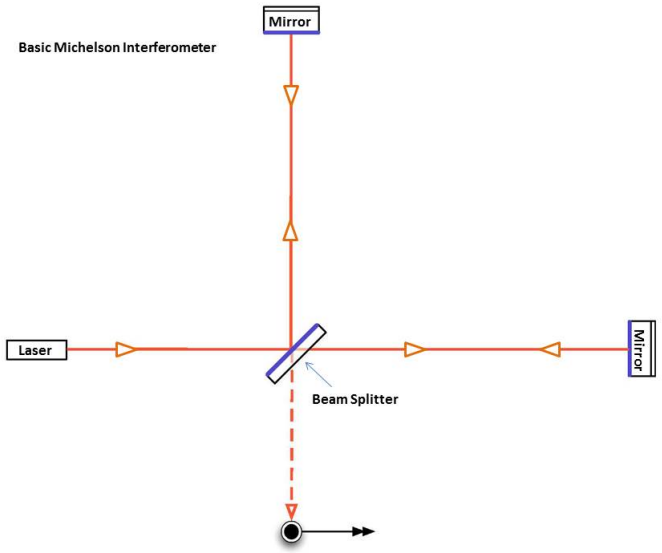

FIGURE 1.1: Layout of a basic Michelson interferometer. Laser beams are sent back and forth along the instrument's two perpendicular arms. Analysis of the light's interference upon recombination of the beams is undertaken. The LIGO gravitational wave detector is an advancement of this basic design. Image credit: Caltech/MIT/LIGO.

wave, can be measured by the analysis of the light's interference upon recombination of the beams.

Gravitational waves originate in violent astrophysical events, the brightest of which are expected to produce a relative change in distance of approximately one part in 10^{21}. For a 4km long interferometric detector, this is equivalent to the change in its arm length a thousand times smaller than the diameter of a single proton. This astonishing observational precision was not reached by ground-based gravitational wave detectors until the 2005 enhanced Laser Interferometer Gravitational Wave Observatory (LIGO) [38, 2]. Despite this, many quiet years still followed without detection. However, the gravitational wave community did not give up hope. Major advances to LIGO were steadily made and other ground-based detectors (VIRGO [6], GEO600 [1]) were built to add weight to the search.

Finally, on the 15th September 2015, the newly advanced LIGO detector resounded at both its Livingston and Hanford sites. The first gravitational wave signal [8], GW150914, was recorded; see Fig. 1.2. The event took place in a distant galaxy, more than one billion light years away. The peak GW power radiated during the final merger was more than ten times greater than the combined light power from all the stars in the observable universe. This was, by far, the most powerful astrophysical observation by mankind to the date.

The signal had a peak gravitational-wave strain of 10^{-21}, it was observed with a matched-filter signal-to-noise (SNR) ratio of 24 and had a significance greater than 5.1σ. The components of the event were black holes of masses $36^{+5}_{-4}\ M_\odot$ and $29^{+4}_{-4}\ M_\odot$, merging

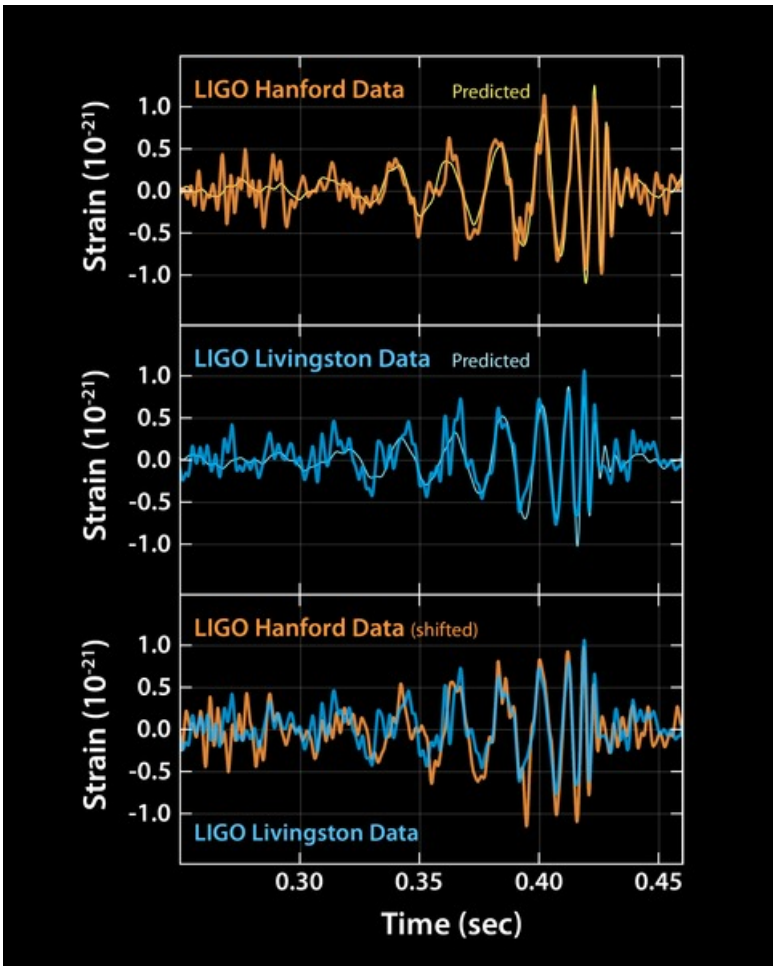

FIGURE 1.2: Plot from [9] showing the GW150914 gravitational wave signal detected by the LIGO observatories. The plots show the data received at LIGO Livingston and LIGO Hanford, alongside the prediction for the waveform using the theory of General Relativity. Time is plotted on the x-axis and strain is plotted on the y-axis. The match across detection sites confirms the detection, and the data is seen to closely match what is expected from theory. Image credit: LIGO.

to form a final $62^{+4}_{-4}\ M_\odot$ black hole, with $3.0^{+0.5}_{-0.5}\ M_\odot$ radiated outward in gravitational waves. This discovery marked three fundamental achievements in the community: the first direct detection of GWs, the first direct detection of black holes themselves [9] and the first direction detection of a binary black hole (BBH) system. A new era of GW astronomy had just begun. The universe was now observable through a novel lens.

After GW150914 the flood gates opened. It was a matter of months later, on 26th December 2015, that a second gravitational wave event GW151226 was recorded [7]. Two years after this, on the 17th August 2017, GW170817 then provided the first observation of a binary neutron star collision [10]. This GW signal came with an accompanying electromagnetic counterpart, triumphantly demonstrating the newly possible complementarity between astronomical observations. To date there have been over 90 observed gravitational wave events from compact binaries (see Fig. 1.3), whose constituents span

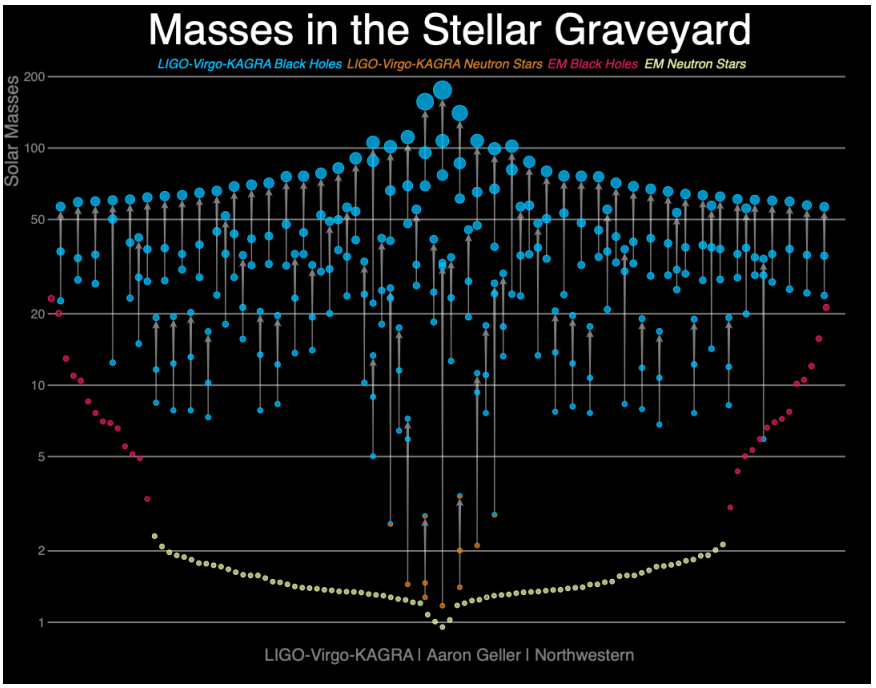

FIGURE 1.3: The plot shows the masses of all compact binaries detected by LIGO-Virgo-KAGRA GW and EM observations, to date. Image credit: LIGO-Virgo-KAGRA.

an exciting parameter range. Detections are now abundant, each providing a wealth of information on the nature of gravity and a new test for Einstein's theory.

1.1.1 Binary Systems and Future Detections

The strongest and most abundantly detectable sources of GWs are binary systems, either binary black holes (BBHs), binary neutron stars (BNSs) or black hole-neutron star (BHNS) pairs. The binary systems that will be the focus of this thesis are BBHs (though the extension of our model to cover BNSs is discussed in Sec. 10.1). GWs from BBHs will allow us to test models of black hole formation, growth and evolution, as well as probe the environments in which they reside [67, 135]. More fundamentally still, GWs from certain BBHs will test the theory of GR itself, probing the strongest gravity regimes within the cosmos [14].

For the clear detection of GW signals from BBH systems, models of the predicted waveforms are required to filter the data, facilitating the extraction of signals from background and instrumental noise. These theoretically predicted waveforms are referred to in the community as waveform templates. The accuracy of our templates will need to increase in line with the sensitivity of the latest detectors, or else modelling error will act as the limiting factor for scientific progress.

Given the advancement in GW instrumentation, there is a pressing need to improve existing BBH waveform templates in their accuracy and parameter-space reach, as well

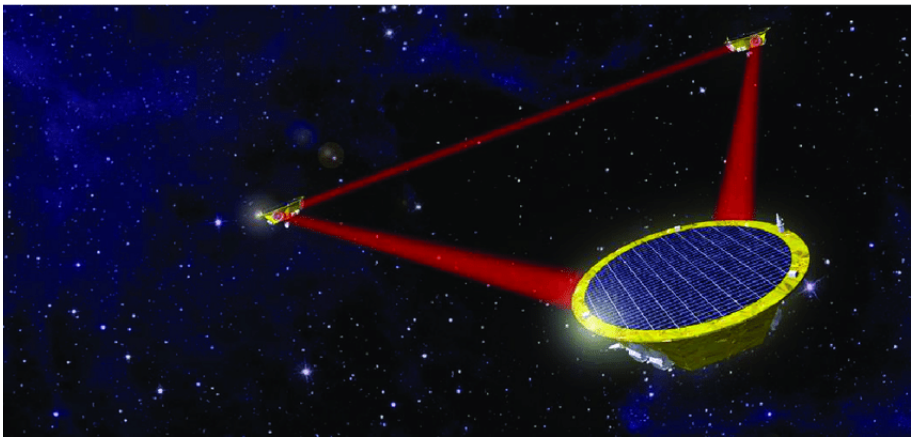

FIGURE 1.4: Artist's impression of the LISA space mission. Three satellites form a Michelson interferometer with an arm-length of 2.5 million kilometers. Image credit: Astrium GmbH.

as their overall computational efficiency [31]. These templates must be constructed to cover all stages of the binary's lifetime—inspiral, merger and ringdown. The overarching aim is to have a bank of waveform templates that covers the entire parameter range of detectable sources.

The next landmark in GW astronomy will be the launch of the Laser Interferometer Space Antenna (LISA), expected in 2034 [3, 19]; see Fig. 1.4 for an artist's impression. The advent of LISA will bring about a new, low-frequency observational range for GWs (0.1 mHz to 1 Hz). This range will allow the detection and study of signals from a plethora of sources, ranging from stellar-mass BBHs within our own galaxy, to mergers between supermassive black holes out at high redshifts ($z \approx 10$-15). TianQin is a further proposed space-borne GW observatory, with a projected launch date in the 2030s [94].

As the frequency of the emitted GWs scales inversely with the total mass of the system at merger, the lower frequency range of LISA will allow the detection of BBHs with heavier total masses that include intermediate and supermassive black holes in their components. This will allow the observation of BBH mergers with larger mass-ratios [82].

A further landmark will be the third generation of ground-based GW detectors. Those currently proposed include the Einstein Telescope, Cosmic Explorer and Voyager [74]. It is assumed that this next generation of detectors will be operational during LISA's lifetime. The synergy between ground-based and space-based detectors, and between that of GW and traditional EM signals, should propel our understanding of astrophysics across a breadth of areas.

1.2 Intermediate-Mass-Ratio Inspirals

1.2.1 Formation Mechansisms

Black holes are grouped into three categories depending on their mass. Stellar-mass black holes range from ~ 3 to several tens of solar masses ($M_\odot$), intermediate-mass black holes (IMBHs) range between $\sim 10^2$–10^4 $M_\odot$, and supermassive black holes (SMBHs) range between $\sim 10^5$–10^9 $M_\odot$. BBHs in turn fall into three categories depending on the mass-ratio between the constituents. Comparable-mass-ratio inspirals (CMRIs) are systems in which the bodies have a mass-ratio $\sim$ 1:1–1:10s, intermediate-mass-ratio inspirals (IMRIs) are systems with a mass-ratio 1:100–1:1000s, and extreme-mass-ratio inspirals (EMRIs) are systems with a mass-ratio $1{:}10^4$ and upwards. An outstanding theoretical and computational challenge is to accurately model binaries in the intermediate-mass-ratio regime [31, 139]. Such IMRI waveform templates must be ready in advance of third-generation ground detectors and of LISA's launch, in order to obtain maximum scientific return. It is the production of such IMRI waveform templates that is the focus of this work.

IMRIs can be formed in two ways [20, 96]. The first is when a stellar-mass compact object, such as a neutron star or a stellar-mass black hole inspirals into an IMBH. These 'category I' IMRIs should emit GWs with frequencies that could make them, in principle, detectable with LIGO [95, 96]. The analysis of these IMRI waveforms would provide us insight into the dynamics of globular clusters, as this is their likely birthplace [96, 66]. The second is when IMBHs collide with SMBHs, forming heavier IMRI systems. Given the supermassive component in these systems, these 'category II' IMRIs will be exciting sources for LISA. Their emitted GWs would allow us to explore the dynamics of galactic nuclei [96], thus providing fundamental insight into black hole formation. Both sources will undergo longer inspirals than we have been accustomed to with comparable-mass-ratio observations, further probing the strong gravity regime and providing richer information about the space-time geometry of black holes.

For category II IMRIs, the inspiral, merger and ringdown are all within the LISA frequency band. However, for some category I IMRIs the merger and ringdown may also be accessible to ground-based detectors [18, 52]. A detection of a single source with both space and ground detectors is referred to as a multiband detection. Multiband detections will be particularly useful for IMRIs, as their GWs contain larger contributions from sub-dominant multipolar modes ($\ell > 2$) during the merger and ringdown stages, compared to CMRIs [13, 152]. Having acquired information from LISA regarding various source parameters of the BBH, the measurement of the lower-amplitude modes in ground-based detectors should then become possible. This multiband era of GW astronomy will bring about improved constraints on the parameters of binary constituents, as well as greater statistical confidence associated to a detection.

The potential for multiband reach with future detectors across the GW band is illustrated in Fig. 1.5.

1.2.2 Detection Prospects

Ref. [97] predicts category I and category II IMRIs to be detected by Advanced LIGO and LISA respectively, at rates of a few per year. However, detection rates remain highly uncertain due to a number of debated assumptions over IMBH formation mechanisms, along with our limited knowledge about the dynamics of globular clusters and galactic nuclei [20, 48, 82].

Although detection *rates* are uncertain, detectability *ranges* can be calculated to a higher degree of certainty. For IMBH binaries, [82] showed that multiband observations involving LIGO and LISA should detect their inspiral, merger and ringdown out to redshift $z \approx 2$. Assuming the third generation of ground detectors are online at this time, [82] predicts the multiband detection capability should then extend this out to redshift $z \approx 5$.

Ref. [82] goes on to examine the detection ranges of binaries with mass ratios between 1:10 and 1:100 (which can inform our expectations for the 1:100–1:1000 intermediate-mass-ratios). For the coalescence of an 80 $M_\odot$ black hole with a 1200 $M_\odot$ black hole (a medium IMBH), we should expect that LISA plus the Einstein Telescope will be able to detect this with a signal-to-noise ratio (SNR) of ≥ 100 within 0.4 Gpc, or SNR ≥ 8 when within 12.8 Gpc. These measurements will allow high resolution black hole spectroscopy and tests of the no-hair theorem [82, 26, 129]. If instead using LISA plus Voyager, we should expect a SNR of ~ 5 within 1 Gpc. Alternatively, for the coalescence of a 20 $M_\odot$ black hole with a 600 $M_\odot$ black hole (a small IMBH), we expect that LISA in combination with either ET or Voyager will be able to detect the signal out to 1.4 Gpc. These types of multiband observations would provide strong constraints on the growth and formation of IMBHs in dense stellar environments, potentially validating the hierarchical merger growth theory [42, 112]. This, in turn, would then allow us to better constrain their detection rates.

1.2.3 Relevant LIGO Detections

2020 saw two groundbreaking observations from the LIGO-Virgo Collaboration (LVC) with respect to IMRIs. The GW signals detected in the first two observing runs (O1 and O2) of the LVC all originated from binaries with mass-ratios close to unity. However, the June 2020 announcement of GW190814 [13] presented the first system with mass ratio close to 1:10. The system comprised of a 22.2–24.3 $M_\odot$ black hole and a compact object of 2.50–2.67 $M_\odot$, either a low-mass black hole or a heavy neutron star [13]. The

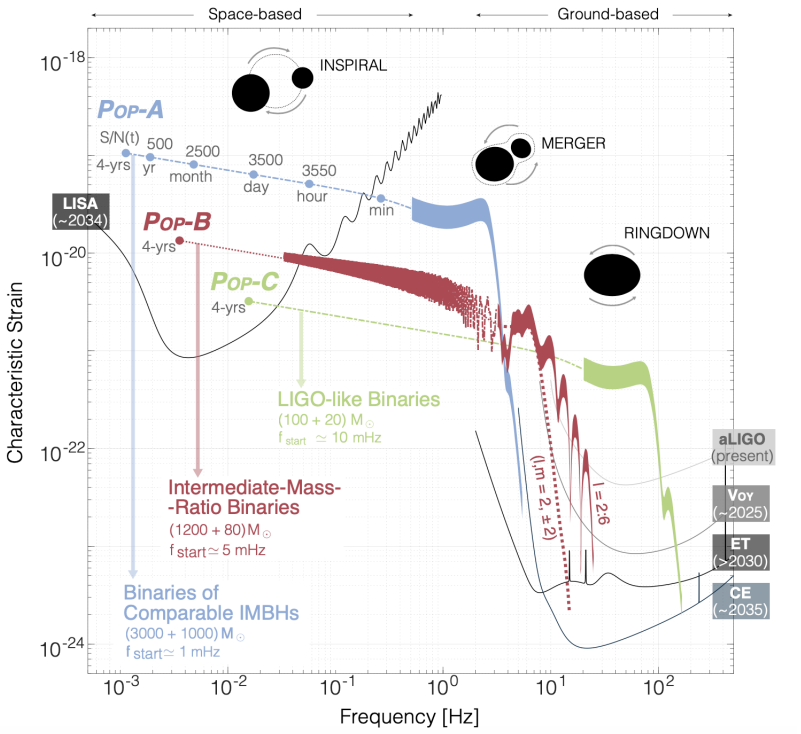

FIGURE 1.5: Plot from [82] showing the predicted multiband detectability of binaries with varying masses, over the course of their merger, with a variety of future GW detectors. Category I IMRIs (red curve) start off in the LISA band and merge in the LIGO band. See [82] for further details on BBH populations.

LVC now estimates a merger rate density of 1–23 $\mathrm{Gpc}^{-3}\ \mathrm{yr}^{-1}$ for the new class of binary sources that GW190814 represents.

GW190814, along with others, helped to push the Gravitational Wave Transient Catalogue (the collection of observed GW events from each observing run) to contain events with smaller mass ratios in O3. Ref. [15] and [16] present analysis of the observed binaries with LIGO-Virgo through to the end of O3. In Fig. 1.6 from [16], black contours represent the expected distributions from analysis of O2 data, while blue regions represent new O3 observations. The left-most panel plots the small-mass-ratio $q := \frac{m_2}{m_1}$, against the primary mass m_1. Here we can see O3 data reaching down into the smaller q domain, substantially past our O2 expectations. Fig. 1.7 from [15] shows the marginal posterior distributions for q, for all observed events in the second part of O3, O3b. Here, we see q now extending down to a value of 0.02.

Upgrades and future generations of ground-based detectors [11, 74], and especially the planned space-based detector LISA [19], will open up a new window of observation in the low-frequency band of the gravitational-wave spectrum, enabling the detection of signals from ever heavier binary systems, containing intermediate-mass and supermassive black holes. In consequence, it is expected that the detection of high mass-ratio events will become routine, and that the catalogue of detected binary sources will extend to

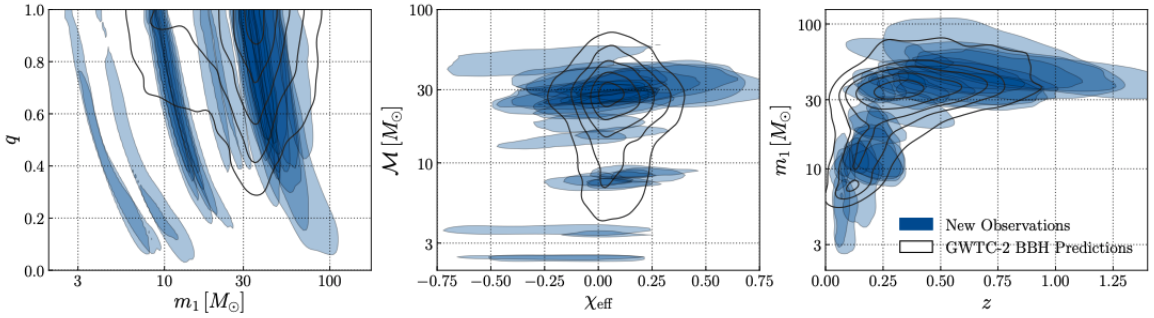

FIGURE 1.6: Plot from [16], showing the new observations from the third LIGO-Virgo observing run (O3). Black contours represent the expected distributions from analysis of O2 data, while blue regions represent new O3 observations. The left-most panel plots the small-mass-ratio q, against the primary mass m_1. The O3 data show a reach down into the smaller q domain.

include a broad range of mass ratios—potentially up to $\sim 1{:}10^6$ with LISA [82, 132]. In anticipation of this remarkable expansion in observational reach, it is important to develop accurate theoretical waveform templates that reliably cover the entire relevant range of mass ratios.

The second groundbreaking discovery of 2020 was GW190521, with its merger product weighing 142 $M_\odot$, providing the first clear detection of an IMBH [12]. Prior to this observation, IMBHs had only been hinted at by electromagnetic observations, kinematical measurements of massive star clusters and scaling relations between the central SMBH and its host galaxy [12, 42]. As IMBHs are a core constituent in either channel of IMRI formation, this conclusive evidence for their existence strongly corroborated the need for accurate IMRI waveform templates. Only with accurate waveform templates will we be able to confirm detections and perform accurate parameter estimation from our data.

1.3 Binary Black Hole Modelling Techniques

1.3.1 Overview

Four primary techniques currently exist for modelling gravitational waves from binary systems: the post-Newtonian (PN) approach, the effective one-body (EOB) formalism, numerical relativity (NR) and perturbation theory/gravitational self-force (GSF) theory. Chapters in the Springer publication "Mass and Motion in General Relativity" [45] provide detailed introductions to each technique. The fundamental factors that dictate which technique can be used when modelling a BBH are the orbital separation and mass-ratio between the two bodies; see Fig. 1.8.

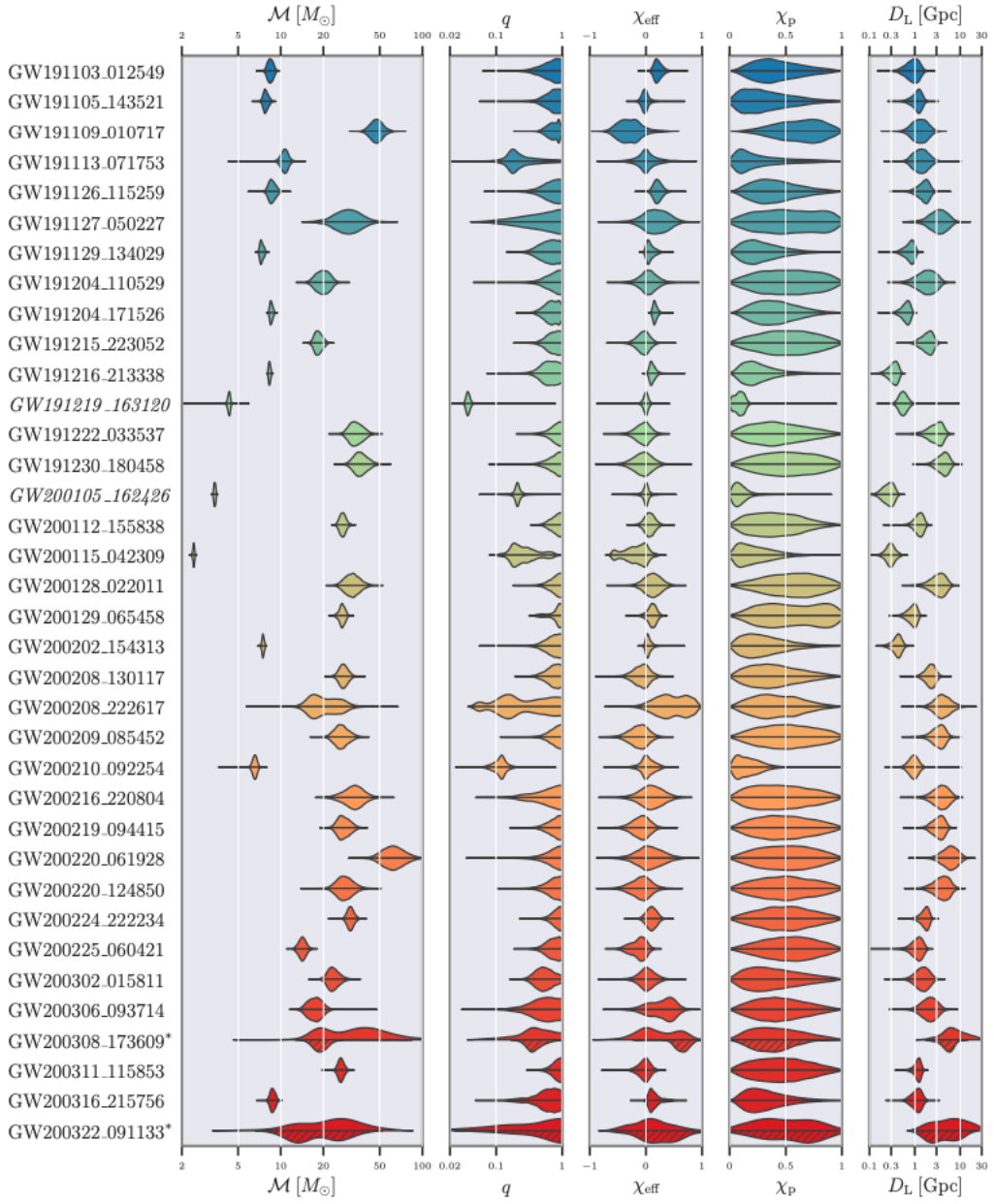

FIGURE 1.7: Plot from [15]. The marginal posterior distributions for the source chirp mass $\mathcal{M}$, small-mass-ratio q, effective inspiral spin χ_{eff}, effective precession spin χ_P and luminosity distance D_L for O3b candidates. We note q now extends down to a value of 0.02.

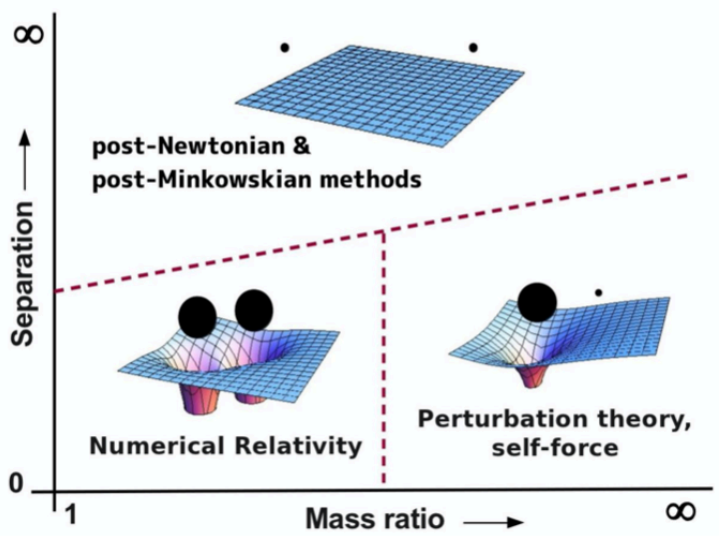

FIGURE 1.8: Plot from Barack and Pound [35] illustrating the modelling methods used for binary systems, depending on their orbital separation and mass ratio.

The PN approach expands the spacetime metric in powers of the parameter $\frac{v}{c}$, where v is the orbital velocity of the system and c is the speed of light. This method works well for weak-field regimes where the two bodies are orbiting at relatively slow velocities, but breaks down near the inner-most stable orbit (ISCO) regime of a binary, regardless of the mass-ratio. This approach shall not be expanded upon further in this thesis as its techniques are not incorporated into our modelling method.

The EOB formalism interpolates solutions obtained using NR and the analytic approximations (PN and GSF), and so relies on solutions from these methods for its tests and calibration. As a result, EOB can describe all phases of the binaries lifetime—inspiral, merger and ringdown, and work across the mass-ratio parameter space. Rather than being considered distinct from the other modelling techniques, EOB should be thought of as a way to resum information from them. We will now provide further detail on the two modelling techniques used in our model, NR and perturbation theory.

1.3.2 Numerical Relativity

NR numerically evolves the fully nonlinear Einstein field equations governing the spacetime of a binary system. NR techniques have been in development for decades [138]. Despite progress on BBHs in head-on collisions [22, 17, 140, 24, 21, 27, 99, 23, 165, 163], it was not until the 2005-2006 breakthroughs on BBH evolutions of quasi-circular coalescence [124, 50, 28] that the field saw rapid growth. This advancement is detailed in several reviews of the field [88, 51, 60]. It is now routine for numerical simulations to

evolve two-body systems through inspiral, merger and ringdown, at least for comparable mass-ratios.

Solving the Einstein field equations in the strong-field regime with NR is a two step process. The first is to produce valid initial data that corresponds to the physical situation in question. The second is to evolve that initial data in time. Two main approaches for the evolution schemes in the context of binary evolutions have developed: the generalized-harmonic formulation [125, 89], and the Baumgarte-Shapiro-Shibata-Nakamura (BSSN) formulation [39] coupled to the Gamma driver gauge conditions (also known as the moving puncture method) [50, 29]. A detailed summary of these two approaches can be found in [79].

The limitation on the extension of NR to more disparate mass-ratios is the computational runtime. The runtime scales proportionally to the square of the large mass-ratio of the system, q^{-2} [150, 31]. One factor of $1/q$ comes from the number of orbits the binary spends in the strong-field regime, there being $1/q$ of these over the course of the inspiral. The second factor of $1/q$ comes from the Courant-Friedrichs-Lewy (CFL) limit [53] on the timestep of the simulation, which requires the number of timesteps per orbit to increase as $\propto 1/q$. As the size of the small body decreases, the numerical resolution required to resolve the field surrounding it increases. The need to preserve phase accuracy over the increasingly long inspiral only increases this computational cost further. When there is a significant disparity in the binary's constituent masses, as in the case of IMRIs, this method becomes computationally intractable.

1.3.2.1 Progress towards IMRIs

Recently, there has been significant progress on modelling mass-ratios up to $\sim$ 1:100 using adaptive mesh refinement techniques. The Dendro-GR code of the Brigham Young University group [102, 63] has seen successful simulations of a number of orbits for mass-ratios up to 1:100, as a proof of principle. The group at the Rochester Institute of Technology (RIT) published results in June 2020 where a 1:128 mass-ratio binary was evolved through a record 13 orbits before merger [91]. The plot in Fig. 1.9 shows the obtained waveforms from successively higher mass ratios from 1:15 up to 1:128. New results from the RIT group have now applied adapted gauge choices to improve their numerical results, including numerical convergence results for mass-ratios 1:7, 1:15 and 1:32 [130]. These results required around one year of runtime.

A more recent 2022 paper by the RIT group [92] pushed numerical simulations up to 1:1024 mass-ratios. The plot in Fig. 1.10 shows the radiated energy spectrum from ever more extreme-mass-ratios compared to a calculation in linear black hole perturbation theory. Reaching the required numerical resolution to sufficiently resolve a 1:1024 binary is a ground-breaking result, however it is one that was only achieved with a substantial

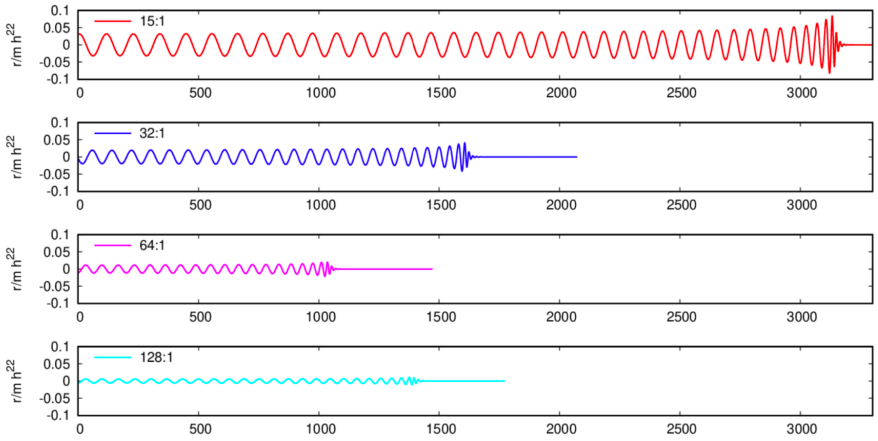

FIGURE 1.9: Results from [91] using NR. The strain waveform for the real part of a Y_{22} mode is plotted vs. time (t/m), for 1:15, 1:32, 1:64, 1:128 mass-ratio binaries. The 1:128 mass-ratio binary undergoes 13 orbits before merger.

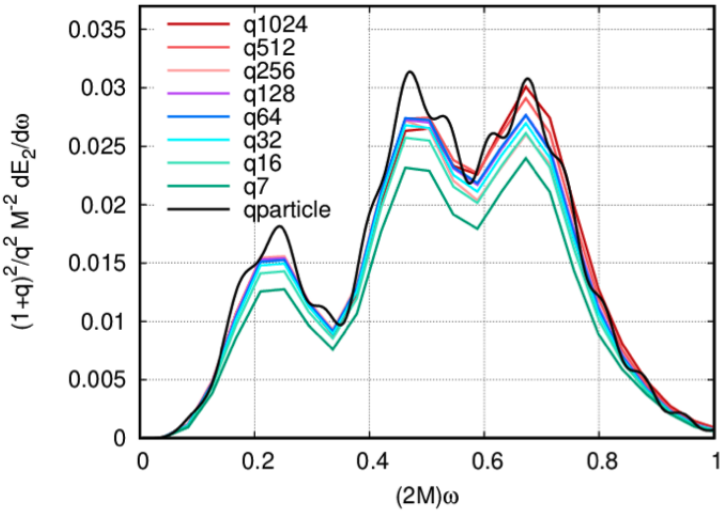

FIGURE 1.10: NR results from [92] showing the radiated energy spectrum from ever more extreme-mass-ratios. The comparative scaled spectra for mass ratios from 1:7 up to 1:1028 are shown, against the particle limit case in black.

trade-off in evolution time. The numerical simulations of Fig. 1.10 are taken with the smaller body starting at rest from a proper distance $D \approx 13M$ from the larger body. The smaller body is then allowed to collide head-on with the larger black hole, resulting in a simulation that takes a factor $1/q$ less times than a full inspiral.

Complete waveform templates for IMRIs will of course require the modelling of many hundreds of orbits. Therefore, there is still much work to be done in the field of NR, if relied upon alone, to fill the intermediate-mass-ratio parameter space.

1.3.3 Black Hole Perturbation Theory

The technique of perturbing a known solution of a simple system in order to form an approximate solution of a more complicated system, is a well-established approach in mathematical physics. In black hole modelling, the known solution is the Kerr (or Schwarzschild) metric of the primary black hole, to which a perturbation is added in order to represent the gravitational effect of an external environment. In the case of EMRI BBH systems, the external environment is a secondary black hole of much smaller mass $m_2 \ll m_1$. In this case, the perturbative parameter is naturally taken to be $q = \frac{m_2}{m_1} \ll 1$. The Einstein field equations are then solved order by order in q, producing an approximate analytical solution for the spacetime. This is the standard GSF approach; we give more details on its status in Sec. 1.3.3.1.

The external environment can be kept more generic by instead choosing a perturbative parameter $\frac{r}{\mathcal{R}} \ll 1$, where r is a measure of distance from the black hole and $\mathcal{R}$ is the local radius of curvature, assumed to be much larger than the mass of the black hole. This approach is taken in the literature by Poisson and collaborators in a series of papers deriving tidally perturbed Schwarzschild metrics [107, 144, 109, 111]. An extension of this work to the Kerr metric begins in [108], though the state of the expressions are much behind that of Schwarzschild. An extensive body of work also exists in the neutron star community for metrics of a more general class of tidally perturbed compact bodies [43, 55, 86, 128, 80].

Ref. [107] derives the tidally perturbed Schwarzschild metric in a particular light-cone gauge. The metric has unknown tidal terms that can only be determined by matching to a specified external environment. Ref. [144, 109] provide examples of this matching, by placing the black hole in a post-Newtonian external spacetime. Ref. [109] provides the tidally perturbed Schwarzschild metric to the highest order in the literature, $(\frac{r}{\mathcal{R}})^4$, now in the Regge-Wheeler gauge. We shall make use of these expressions in [109] for our Schwarzschild BBH model, described in Sec. 2.1.

1.3.3.1 Gravitational Self-Force Theory

As aforementioned, traditional gravitational self-force theory uses a perturbative approach to expand the spacetime metric in powers of the small mass-ratio q. This therefore requires $m_2 \ll m_1$, and so it is applicable to EMRI systems. The effects of the smaller body and its dynamics create an effective force term, known as the gravitational self-force. For accurate EMRI templates, the inclusion of self-force effects up to second-order in q is necessary, as it is at this order we achieve sub-radian precision in the waveform over the full inspiral [158].

Numerical computations of the full first-order self-force have advanced greatly and their formulation is now firmly entrenched. They have evolved from Lorenz-gauge calculations

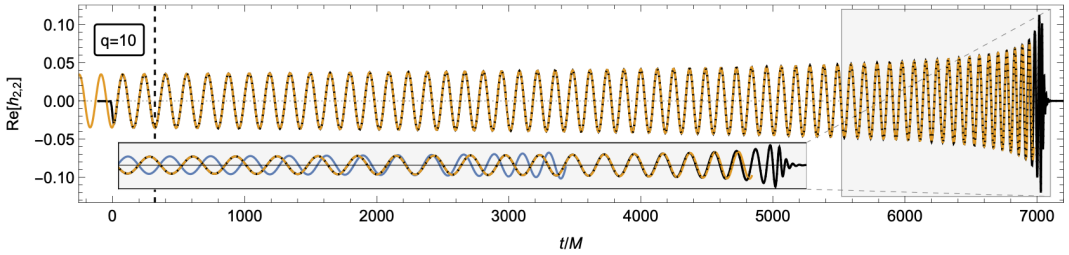

FIGURE 1.11: Results from [158]. A 1PA waveform for a mass-ratio 1:10 nonspinning binary is given in orange. The NR simulation for the same binary is shown in black. The inset shows the corresponding 0PA waveform, in blue. The 1PA and NR waveforms show remarkable agreement up until late time and merger. Ref. [158] defines q as the *large* mass-ratio m_1/m_2.

[33, 36, 37, 59] to more efficient methods relying on radiation gauges [121, 151, 147, 148]. First-order self-force results are now available for generic bound geodesics in Kerr spacetime [149].

The formalism at second-order is now also well-established [131, 57, 117, 68, 113, 118, 120, 146] and there has been strong progress with regards to practical implementation methods in the last decade [115, 157, 160, 114, 100, 101, 122]. The first complete calculations of physical second-order quantities (fluxes) were reported in [123, 156], for the restricted case of quasicircular orbits around a Schwarzschild black hole.

1.3.3.2 Progress towards IMRIs

In December 2021 [158] brought about the highly anticipated first waveform results using second-order self-force theory. Figure. 1.11 shows a waveform at "first post-adiabatic" (1PA) order, which requires the perturbation of the metric to second-order. The results are for a mass-ratio 1:10 nonspinning binary, in a circular orbit. 1PA results are plotted in orange, whilst NR results are plotted for comparison in black. The inset shows the corresponding adiabatic (0PA) waveform in blue. With self-force results designed to work best when the mass-ratio is extreme, the agreement of results at $q = 1/10$ is remarkable. There is a strong agreement with NR up until late time in the merger, with the inset evidencing the leap in accuracy from 0PA to 1PA. Remarkably, an impressive agreement is obtained even for a 1:1 mass-ratio, far outside the perturbative regime; see Fig. 1.12.

The main caveat to note is that these 1PA/2SF waveform results were obtained for nonspinning binaries, on circular orbits only. The extension to Kerr and generic orbits remains a *major* theoretical endeavour, one for which the timeframe is still highly uncertain.

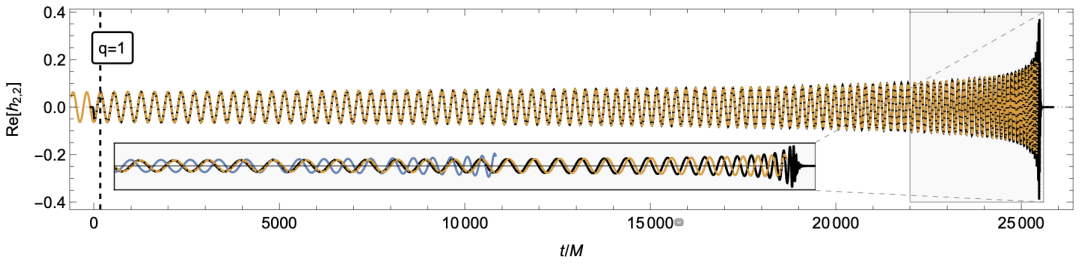

FIGURE 1.12: Results from [158]. A 1PA waveform for a mass-ratio 1:1 nonspinning binary is given in orange. The NR simulation for the same binary is shown in black. The inset shows the corresponding 0PA waveform, in blue. Impressive agreement is still seen in this mass-ratio regime. Ref. [158] defines q as the *large* mass-ratio m_1/m_2.

Prior to the results of [158], Van de Meent and Pfeiffer [150] performed an assessment of the potential accuracy of future self-force models at smaller mass-ratios by comparing NR and GSF results. Ref. [150] concluded that a perturbative approach accurate to 1PA order could possibly bridge the mass-ratio gap from binaries with extreme ratios down to the comparable ratios covered by NR. Their findings are shown in Fig. 1.13, which is in effect a quantitative adaptation of Fig. 1.8. The analysis of [150] is for the restricted case of black hole binaries without spin or orbital eccentricity.

The challenges still facing both the NR and GSF approaches motivate a new model for bridging the mass-ratio gap, in order to complement current efforts. Our proposed method attempts to tackle the problem of modelling IMRIs using a hybrid of NR and perturbation theory. The idea is to leverage existing successful NR infrastructure, while excising a region surrounding the smaller black hole from the numerics. Within this excision region we use an approximate analytical solution for the spacetime, formed from a tidally perturbed black hole metric. We match this analytical solution to the NR solution at each time step of the evolution. It is our hope that this method will dramatically increase the numerical efficiency of binary simulations with small mass ratios and extend our reach into the intermediate-mass-ratio regime.

1.4 Thesis Outline

Chapter 2 overviews our proposed worldtube excision method for modelling IMRIs. Section 2.2 provides context with respect to other methods for modelling BBHs and we highlight the inspiration our method has drawn from existing techniques. An initial estimate of runtime saving using our method, compared to NR alone, is presented in Sec. 2.3.

Chapter 3 introduces the physical set up of our scalar toy model, a scalar charge e orbiting a black hole M. The equation governing this system, the scalar wave equation in Schwarzschild spacetime with a delta point source, is presented and then decomposed

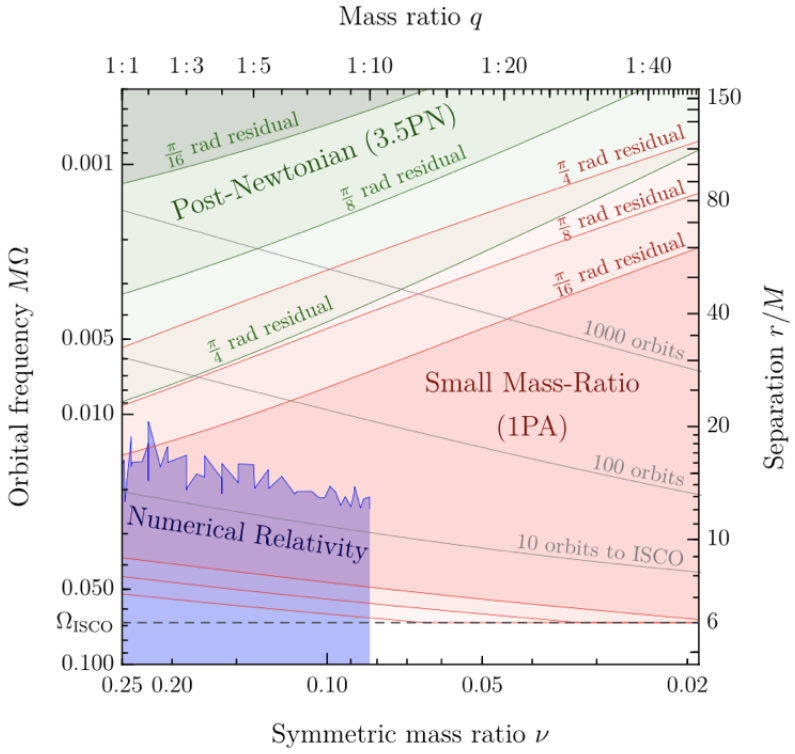

FIGURE 1.13: Results from [150] illustrating the regions of applicability of different modelling techniques for a non-spinning quasi-circular BBH inspiral. The shaded regions are ranges within which the cumulative orbital-phase error is less than $\pi/4, \pi/8$ and $\pi/16$ radians, respectively. The plot illustrates the ability of the first order post-adiabatic (1PA) expansion to bridge the mass-ratio modelling gap, extending down to $\nu = 0.25$ and the blue region of NR.

into spherical harmonic modes in order to reduce the system to a 1+1 dimensional (1+1D) problem. In Sec. 3.2, we derive the exact analytical solution for static modes of this system. This solution provides a baseline against which we can compare results from static modes of our worldtube excision model. Section 3.3 derives the local approximate analytical solution valid for all multipole modes, which we then use to populate the worldtube in our 1+1D models. Section 3.4 outlines the core constituents of our two 1+1D implementations, referred to as Schemes I and II.

Chapter 4 presents the setup and results from Scheme I, the first implementation of our 1+1D scalar-field model. Chapter 5 presents the set up and results from Scheme II, the second implementation. Scheme I uses finite difference evolution methods, a numerical grid with characteristic slicing, and numerical data in open regions surrounding the worldtube to perform the matching. Scheme II uses spectral evolution methods, a numerical grid with Cauchy slicing, and data only on the worldtube surface to perform the matching. We therefore have two independent test setups for the worldtube excision model in 1+1D. Results assess the behaviour of static and non-static modes of the field, as well as the convergence with respect to numerical resolution, worldtube size and the

order of accuracy of the analytical solution. The results from these two schemes appear in [58].

Chapter 6 presents a 3+1 dimensional (3+1D) scalar-field model. The scalar charge e is now evolved on a circular orbit around the black hole M, in 3-dimensional space. For the numerical evolution we now use the SpECTRE code developed by the SXS collaboration. The local approximate analytical solution for this 3+1D model is then presented. This is first done schematically, then high-order covariant expressions from the literature are given. This is followed by a transformation into our preferred coordinate system. The matching method is then presented in practice. We again assess the convergence with respect to numerical resolution, worldtube size and the order of accuracy of the analytical solution.

Chapter 7 describes the setup for the full gravity model, two black holes with masses m_1 and m_2 and an intermediate mass-ratio. The numerical implementation will again use the SpECTRE code and we give more detail on the numerical set up in the BBH case. We then explain the overall infrastructure of the BBH model and discuss the principles of the matching method.

Chapter 8 presents the derivation of the tidally perturbed Schwarzschild metric, in light-cone coordinates and the Regge-Wheeler gauge. These existing metrics shall be the starting point for the formation of our local approximate analytical solution in the BBH model. Chapter 9 then derives the transformation of this metric from light-cone coordinates to harmonic coordinates, as a function of generalised harmonic time. This transformation facilitates our matching method across the worldtube boundary, and it is completed up to second-order in the perturbation. Final results for the transformed metric are presented, grouped by their multipolar structure.

Chapter 10 summarises the main results presented in this thesis and outlines the future research milestones necessary to take the worldtube excision method to its full BBH implementation. We also provide a reminder of how this research effort fits into the work currently being done by the broader waveform modelling community.

1.5 Research Collaboration Details

This research is work done as part of a collaboration with colleagues at the Albert Einstein Institute (AEI): Harald Pfeiffer, Hannes Rüter, and Nikolas Wittek. Materials in Chapters 2 - 5 of this thesis have been published under this joint authorship in [58].

Since parts of the research reported here were collaborative in nature, it is appropriate to identify and highlight my own contribution to the collaborative elements: (i) the design and numerical implementation of Scheme II (Chapter 5). Here my contribution was to provide the appropriate form of the local approximate analytical solution. (ii)

The numerical implementation of the scalar-field model in 3+1D (Chapter 6). Here my contribution was again to to derive and provide the appropriate form of the local approximate analytical solution. The design of this scheme, including the matching method, was decided in joint conversations. The design of the BBH scheme, presented in Chapter 7, was also decided in joint conversations.

Chapter 2

Method Overview

2.1 Worldtube Excision

Our approach is a hybrid method that seeks to model IMRIs using direct synthesis of black-hole perturbation and NR techniques. The central idea is simple, and illustrated in Fig. 2.1 as applied to a compact-object binary with masses $m_1 \gg m_2$. An excision region is introduced around the small object, of radial extent R chosen such that $m_2 \ll R \ll \mathcal{R}$, where $\mathcal{R}$ is the characteristic lengthscale associated with the tidal field of m_1 at the location of m_2 (such that $\mathcal{R} \sim m_1$ near the end of the inspiral).

Inside this region—a "worldtube" in spacetime—an approximate analytical solution is prescribed for the spacetime metric, arising from the perturbation theory of compact objects in a tidal environment. An NR simulation is set up for the binary, in which the worldtube's interior is excised from the numerical domain, and replaced with the analytical solution. At each time step of the numerical evolution, the numerical solution (outside the tube) and analytical solution (inside the tube) are matched across the tube's boundary, in a process that fixes *a priori* unknown tidal coefficients in the analytical solution, as well as gauge degrees of freedom. The intended effect of this construction is to partially alleviate the scale disparity that thwarts the efficiency of the numerical evolution at small q. An outline of such a strategy was first (to our knowledge) put forward by B. Schutz in a conference talk a few years ago [134].

To begin thinking about how such a strategy may work in practice, we restrict attention to the simplest scenario, where the smaller object is a black hole. The appropriate analytical solution inside the worldtube is then that of a tidally perturbed Kerr black hole, where the tidal perturbation arises from the presence of the larger body. Such geometries are examples of a broader class of spacetimes studied extensively in recent literature [107, 111, 144, 109, 87, 55, 128, 164, 80], where the tidal response of a compact object to an external perturbative tidal field is derived analytically order by order in

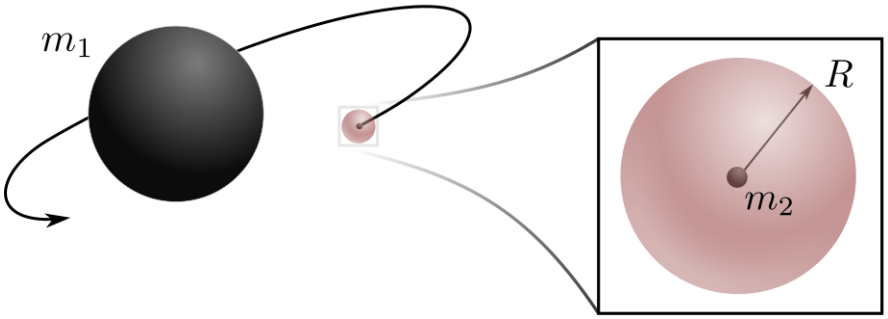

FIGURE 2.1: A cartoon of our excision method. We excise a region of size R from the computational domain. In the interior of the excised region, we use an analytical approximation.

$s/\mathcal{R}$—the ratio of distance s from the smaller object and the characteristic lengthscale $\mathcal{R}$ of the tidal field—under the assumption $s \ll \mathcal{R}$. For a nonrotating black hole, the perturbed metric has so far been constructed through order $(s/\mathcal{R})^4$ [109]. For our excision method we would need the perturbed metric near the worldtube's boundary, where it takes the form of an expansion in $R/\mathcal{R} \ll 1$.

Since the analytically prescribed metric on the worldtube's boundary is only an approximation, the spacetime constructed in the numerical simulation is also approximate, even if numerical error could be reduced to zero. If our analytical solution is correct only up to $\mathcal{O}\left((R/\mathcal{R})^n\right)$—what we later call an "$n$th-order model"—we would naively expect an error of $\mathcal{O}\left((R/\mathcal{R})^{n+1}\right)$ at the boundary. However, as we lay out in Sec. 4.3.2.5, we achieve an error of $\mathcal{O}\left((R/\mathcal{R})^n\right)$. This error is then fed from the tube's boundary to the numerical solution, and propagates to the bulk of the numerical domain. One could then only hope to construct the binary's spacetime up to an error of $\mathcal{O}\left((R/\mathcal{R})^n\right)$, even in the continuum limit. This worldtube error can be reduced either by increasing the order n of the analytical model, or by decreasing the tube's radius R. Of course, decreasing R restores the original scale disparity and thus diminishes the gain from the introduction of a tube. There is hence a fundamental trade-off in our method between precision and computational cost, with R serving as a control parameter.

The NR evolution of our BBH worldtube excision model will be carried out using SpECTRE [83], an open-source code for multi-scale, multi-physics problems in astrophysics and gravitational physics. SpECTRE is a successor to the Spectral Einstein Code (SpEC) [84] and is currently in development by the Simulating eXtreme Spacetimes (SXS) collaboration. We provide more details in Subsec. 6.2.1.

2.2 Comparisons to Existing Methods

Our worldtube excision method draws inspiration from GSF and NR methods, and existing techniques used in the modelling of various aspects of EMRIs and CMRIs. A

direct similarity between GSF when modelling EMRIs and our method, is that they both match an external solution to a local approximate solution around the smaller object in the binary. In GSF, both the external and local solution use perturbation theory. The external solution is a perturbed form of the larger black hole's metric, whilst the local approximate solution is a perturbed form of the smaller black hole's metric. In our method the local solution is the same, but the external solution is fully nonlinear.

When modelling EMRIs using GSF theory, the metric perturbation is divergent at the location of the smaller body [110]. This singularity creates a technical difficulty when numerically evolving the field, which must be dealt with in some way. A formalism known as the puncture method has been developed, which is now a standard approach in self-force calculations to deal with this feature. The puncture method was first implemented for a scalar field in [155, 32] and later extended to a gravitational field in [59]. The method involves the implementation of a worldtube in a region surrounding the smaller body, thus splitting the numerical domain into two regions. Inside this region a suitable analytically derived, puncture function is subtracted from the full field, removing the part responsible for the singular nature. The remaining field, referred to as the regular field, is then independently numerically evolved inside the worldtube. Outside the worldtube, the full, original field is numerically solved for. The evolution variable is suitably adjusted for across the boundary of the worldtube. An illustration of this is given by Fig. 2.2. In the context of pure self-force calculations, the regular field is all that is required for the calculation to proceed.

Our method draws obvious inspiration from the standard puncture method. We too insert a worldtube around the smaller body, dividing the spacetime domain into two regions. We then also construct a suitable puncture field, but instead subtract it from the full numerical field outside the worldtube. This then allows us to match the regular field across the boundary and fit for the unknown coefficients in the approximate regular field solution. Our method performs a numerical evolution of the field outside the worldtube, but excises the interior region from the computation grid. Inside the region we populate the spacetime by evaluating the expression for the fitted approximate analytical solution.

When modelling CMRIs using NR, the singularities inside black holes must be dealt with in some way. There are now two mainstream methods that address this. The first is the *moving puncture* method associated with the ADM formulation of the Einstein equations [25] and a BSSN formalism of NR [39, 136]. The moving puncture method relies in its exploitation on the topology around a black hole. A coordinate transformation, first discovered by Einstein and Rosen [62], is used that creates a wormhole-type structure at the black hole singularity. In doing so, the physical singularity at $r = 0$ on the spatial hypersurface is effectively removed from the computational grid, being sent to spatial infinity of the introduced duplicate hypersurface; see Fig. 2.3. As our method does not make use of the moving puncture technique in NR we shall not elaborate upon it further.

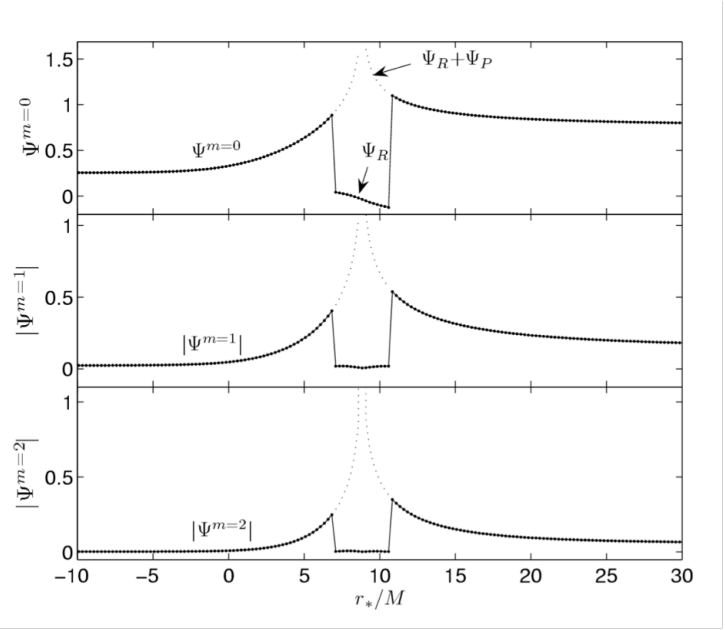

FIGURE 2.2: Results from [32]. The field Ψ is displayed for three m modes along a spatial slice. The full field Ψ^m is displayed outside the worldtube, and the residual field $\Psi^m_R := \Psi^m - \Psi^m_P$ inside it, where Ψ^m_P is a particular puncture function. The dotted line indicates the full divergent field, obtained through $\Psi^m := \Psi^m_R + \Psi^m_P$.

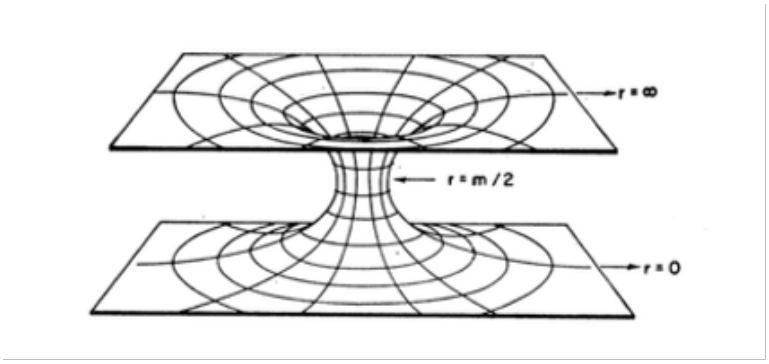

FIGURE 2.3: A visualisation of the moving puncture technique used in NR for dealing with black hole singularities, taken from [47]. A wormhole structure is introduced via a coordinate transformation. The singularity at $r = 0$ is sent to spatial infinity of the duplicate hypersurface.

The second mainstream method to deal with black hole singularities is the *excision method*, associated with the generalised harmonic formalism of NR [125]. The idea here is to entirely remove the region contained within the black hole event horizon from the grid; see Fig. 2.4. Fundamentally, this works due to the fact that information cannot propagate outwards from a black hole horizon. However, the event horizon is difficult to numerically track in practice, and instead the apparent horizon is used as the excision boundary due to the clear geometric features associated with it [76]. Excision methods are generally implemented in NR codes that use spectral methods [142]. The main code responsible for many of the successful NR simulations of this kind is the Spectral Einstein Code (SpEC) [4].

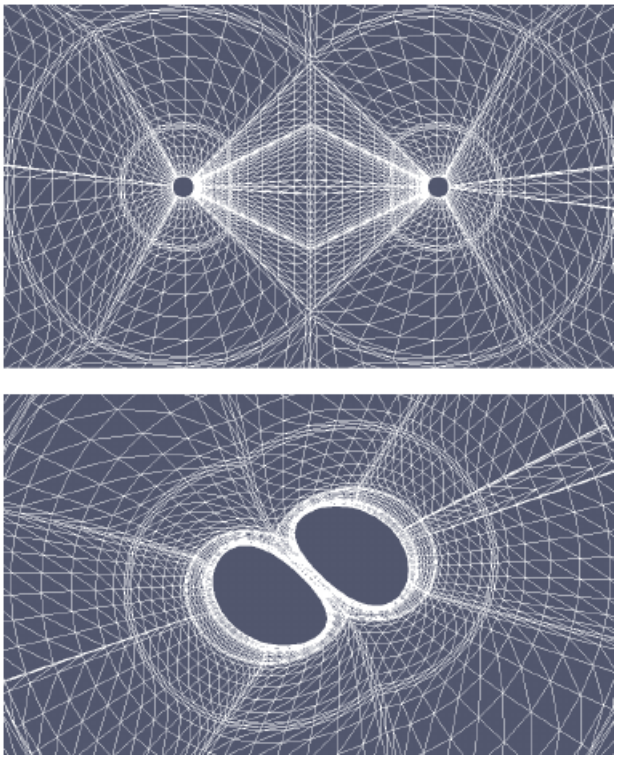

FIGURE 2.4: Illustration of the computational domain with excision regions taken from [76]. In the top panel the black holes are initially at rest. In the bottom panel the black holes are near merger and the excision boundaries have distorted to track the apparent horizons of the bodies.

Our method draws inspiration from this second method in NR, as it too excises a region from the computational grid. The crucial difference is that our excision region not only contains the spacetime within the black hole's horizon, but rather the black hole plus a portion of the spacetime surrounding it. Spacetime within the excision region is therefore in causal contact with the numerical domain and information must propagate outwards from within. This is achieved with our matching methods described in Sec. 4.3.1 and Sec. 5.2.1.

2.3 Estimated Runtime Saving

Our method seeks to speed up the numerical evolution by effectively excising the smaller scale from the IMRI problem. Before describing the details of the implementation, we can develop a quantitative estimate of what the potential runtime savings might be.

The approximation error of the perturbative solution on the worldtube boundary is expected to be

$$\varepsilon_{\mathrm{WT}} \sim \left(\frac{R}{\mathcal{R}}\right)^{n}, \tag{2.1}$$

where n is the order of the analytic solution, R is the radius of the worldtube, and $\mathcal{R}$ is the characteristic length scale associated with the tidal field of m_1 at m_2. Optimally, the approximation error $\varepsilon_{\rm WT}$ should be comparable to the error $\varepsilon_{\rm NR}$ of the NR simulation, i.e. $\varepsilon_{\rm WT} \sim \varepsilon_{\rm NR}$. This gives an "optimal" worldtube radius of

$$R \sim \varepsilon_{\rm NR}^{1/(n)}\, \mathcal{R}. \tag{2.2}$$

For $n = 4$ (as presently available for a tidally perturbed Schwarzschild black hole [111]) the dependence on $\varepsilon_{\rm NR}$ is quite weak. As an example, $\varepsilon_{\rm NR} = 10^{-4}$ and $n = 4$ yield $R \sim 0.1\mathcal{R}$. As a measure of $\mathcal{R}$ we may use the Kretschmann scalar $K = R_{\alpha\beta\gamma\delta}R^{\alpha\beta\gamma\delta}$ associated with the Schwarzschild field of m_1, with Riemann tensor $R_{\alpha\beta\gamma\delta}$. This gives $\mathcal{R} \sim K^{-1/4} \sim 0.4(D^3/m_1)^{1/2}$, where D is the separation between the two black holes. For example, near the end of the inspiral ($D \sim 6m_1$) we have $\mathcal{R} \sim 6m_1$, and an optimal choice of $R \sim 0.6m_1$.

The efficiency gain of the worldtube method arises from the weakened CFL condition [53]. The smallest scale on the numerical grid with a worldtube is $\sim R$ (as long as the worldtube is smaller than the more massive BH), while the smallest scale for the traditional simulation is $\sim m_2$. Therefore, the CFL condition allows a time-step larger by a factor $\sim R/m_2$. Assuming a comparable computational cost per time-step between worldtube and traditional methods, the speed-up will be

$$\text{speed-up} \sim \frac{R}{m_2} \sim \varepsilon_{\rm NR}^{1/(n)}\, \frac{\mathcal{R}}{m_2} = \varepsilon_{\rm NR}^{1/(n)}\, \frac{\mathcal{R}}{m_1}\, q^{-1}. \tag{2.3}$$

Equation (2.3) suggests a potential speed-up proportional to $q^{-1} \gg 1$, with the constant of proportionality depending on the target error $\varepsilon_{\rm NR}$, the order of the analytical approximation n and the length scale $\mathcal{R}$, itself depending on the orbital radius D. For D in the relevant strong-field range between $\sim 6m_1$ and $\sim 10m_1$, and with our sample values $n = 4$ and $\varepsilon_{\rm NR} = 10^{-4}$, the constant of proportionality is around unity. Therefore, for example, a speed-up by a factor 100 seems feasible for mass-ratio $1 : 100$. To phrase this differently, the computational cost of evolving for one orbit with the worldtube approach could be similar to evolving one orbit of a comparable-mass BBH with traditional NR methods at the same numerical error $\varepsilon_{\rm NR}$.

We caution that our estimate here is extremely crude. Moreover, Eq. (2.3) assumes that time-stepping error is always subdominant, which may only hold for high-order time-stepping schemes like those employed by the SpEC code [46]. Even if the substantial speed-up of Eq. (2.3) can be realized, high-mass-ratio simulations will remain more challenging than comparable mass simulations, because the duration of the inspiral increases with more extreme mass-ratios. A tighter $\varepsilon_{\rm NR}$ might also be required at more extreme mass-ratios, to resolve the smaller amplitude of the gravitational waves and to preserve phase accuracy over the longer inspiral.

Chapter 3

Scalar-Field Model in 1+1D

We wish to start with a toy model with which to develop and test a matching methodology for the field across the worldtube's boundary. For that purpose we employ a linear scalar-field model, in which the small black hole is replaced with a pointlike scalar charge, and the large object is a Schwarzschild black hole. This setup has been examined frequently in the literature, for different purposes, see e.g. [72, 49, 162]. Instead of tackling the full Einstein's equations, we thus solve the massless linear Klein-Gordon equation for a scalar field on a fixed Schwarzschild background.

Furthermore, we decompose the field equation into multipole modes on the Schwarzschild geometry, and solve for each mode of the field individually as an evolution problem in 1+1 dimensions (radius+time). Our worldtube is then a 2-dimensional "strip" confined between two parallel timelike curves. As a final simplification, we set the scalar charge to move on a fixed circular geodesic orbit around the large black hole (ignoring radiation reaction), meaning we can fix our worldtube in advance of the evolution, and it has a simple geometry. All of these simplifications take us very far, of course, from the actual physical problem in question. However, our toy problem retains enough relevant features to make it useful as a development platform for worldtube matching procedures.

3.1 Multipole Decomposition

The orbiting charge sources a linear scalar field Φ, which satisfies the Klein-Gordon equation

$$g^{\alpha\beta}\nabla_\alpha\nabla_\beta\Phi(x) = -4\pi\rho(x)\,. \tag{3.1}$$

Here ∇_α is the covariant derivative compatible with the background Schwarzschild metric $g_{\alpha\beta}$, and $\rho(x)$ is the scalar charge density, represented by the distribution

$$\rho(x) = e\int_{-\infty}^{\infty}\frac{\delta^4[x^\mu - x_p^\mu(\tau)]}{\sqrt{-g}}d\tau\,, \tag{3.2}$$

in which e is the scalar charge, x_p^μ denotes the coordinates of the particle's worldline, parametrised with proper time τ, and g is the determinant of $g_{\alpha\beta}$. In a Schwarzschild coordinate system attached to the background Schwarzschild geometry we have, for our circular orbit, $r_p := x_p^r = const$, and, without loss of generality, we set $\theta_p := x_p^\theta \equiv \pi/2$. The particle's geodesic orbit then has a tangent four-velocity given (in Schwarzschild coordinates t, r, θ, ϕ) by

$$u^\alpha := dx_p^\alpha/d\tau = \gamma\,(1,\, 0,\, 0,\, \Omega)\ , \tag{3.3}$$

where $\Omega := (d\phi_p/d\tau)/(dt_p/d\tau) = (M/r_p^3)^{1/2}$ is the orbital angular velocity with respect to time t, $\gamma := (1-3M/r_p)^{-1/2}$ is a gravitational redshift factor, and M is the mass parameter of the Schwarzschild background. In terms of time t, the particle's Schwarzschild coordinates are

$$x_p^\alpha = \left(t, r_p, \frac{\pi}{2}, \Omega t\right)\ , \tag{3.4}$$

where, again without loss of generality, we have set $\phi_p = 0$ at $t = 0$.

Our toy model makes a further simplification: rather than tackling the field equation (3.1) in the 3+1D spacetime, we separate it into spherical-harmonic multipole modes (taking advantage of the background's spherical symmetry), and solve for each multipole of the field in 1+1D (time+radius). To achieve this, we write

$$\Phi = \frac{e}{r}\sum_{\ell=0}^{\infty}\sum_{m=-\ell}^{\ell}\Psi_{\ell m}(r,t)Y_{\ell m}(\theta,\phi)\,, \tag{3.5}$$

where $Y_{\ell m}(\theta,\phi)$ are standard spherical harmonics, defined on 2-spheres $r = const$ around the large black hole, and the factor $\frac{1}{r}$ is introduced for later convenience. We insert the expansion (3.5) into Eq. (3.1), and on the right-hand side of the latter we substitute the completeness relation $\delta(\theta-\theta_p)\delta(\phi-\phi_p)/\sin\theta = \sum_{\ell m} Y_{\ell m}(\theta,\phi)\bar{Y}_{\ell m}(\theta_p,\phi_p)$, where an overbar denotes complex conjugation. By virtue of the orthogonality of the $Y_{\ell m}$ functions, one immediately obtains a separate equation for each of the time-radial functions $\Psi_{\ell m}(r,t)$. The equation reads

$$\frac{\partial^2\Psi_{\ell m}}{\partial t^2} - \frac{\partial^2\Psi_{\ell m}}{\partial r^{*2}} + V_\ell(r)\Psi_{\ell m} = S_{\ell m}(t)\delta(r^*-r_p^*)\,, \tag{3.6}$$

where

$$V_\ell(r) = \left(1-\frac{2M}{r}\right)\left(\frac{\ell(\ell+1)}{r^2}+\frac{2M}{r^3}\right), \tag{3.7}$$

and

$$S_{\ell m}(t) = \frac{4\pi}{\gamma r_p}\,\bar{Y}_{\ell m}\left(\frac{\pi}{2},\Omega t\right)\ . \tag{3.8}$$

Here we have introduced the tortoise radial coordinate $r^* = r + 2M\ln[r/(2M)-1]$, with $r_p^* := r^*(r_p)$.

Equation (3.6) is the basic field equation of our 1+1D toy model, and we apply our excision method to it in order to develop our strategy and test its performance. We aim

to construct a solution of Eq. (3.6) subject to "physical" boundary conditions, namely that there is no radiation coming in from past null infinity or out of the past event horizon; we refer to that solution as the "physical" one. For benchmarking, it is useful to have at hand the actual physical solution of Eq. (3.6) (without a worldtube), and for that purpose we have developed a simple time-domain numerical code capable of accurately computing $\Phi_{\ell m}(r) := \Psi_{\ell m}(r)/r$ for given mode numbers ℓ, m and orbital radius r_p. The algorithm of our code, to be described in Sec. 4.2.1, is based on characteristic evolution with a second-order-convergent finite-difference formula, with the δ-function source term incorporated by way of imposing suitable jump conditions along the particle's worldline.

3.2 Static-Mode Solution

For $m = 0$ (axially symmetric) modes of the scalar-field perturbation, the source $S_{\ell m}$ becomes time-independent, and the physical solution is static. The field equation (3.6) then reduces to an ordinary differential equation, and admits simple *analytical* solutions. Such solutions are particularly useful for benchmarking purposes, and they will serve us well in that capacity later in our analysis.

For a "physical" $m = 0$ field we look for a static solution of Eq. (3.6) for which the modal Klein-Gordon field $\Phi_{\ell 0}(r) := \Psi_{\ell 0}(r)/r$ is bounded on the event horizon and falls off at infinity. These conditions define a unique solution for each ℓ.

After a coordinate transformation, the field equation takes the form of Legendre's equation and we can obtain a solution in terms of Legendre functions

$$\Psi_{\ell 0}(r) = AP_\ell(z) + BQ_\ell(z), \tag{3.9}$$

where A and B are constants and P_ℓ and Q_ℓ are Legendre functions of the first and second kind, respectively, with the arguments $z := r/M - 1$:

$$P_\ell(z) = \frac{1}{2^l l!}\frac{d^l}{dz^\ell}(z^2-1)^\ell, \tag{3.10}$$

$$Q_\ell(z) = \frac{1}{2}P_\ell(z)\ln\frac{1+z}{1-z}. \tag{3.11}$$

At the horizon $z = 1$ and here Q_ℓ is singular. Toward spatial infinity $z \to \infty$ and here P_ℓ diverges. For the solution to satisfy the desired regularity, we chose the following ansatz,

$$\Psi(r) = AP_\ell(z)\Theta(r_p - r) + BQ_\ell(z)\Theta(r - r_p), \tag{3.12}$$

where Θ is the Heaviside step function. The coefficients A and B are obtained by substituting Eq. (3.12) into Eq. (3.6) and then equating the coefficients of δ and δ'. This

procedure yields the inhomogeneous solution

$$\Psi_{\ell 0}(r) = \frac{r r_p}{M} S_{\ell 0}\Big(Q_\ell(z_p)P_\ell(z)\Theta(r_p - r) + Q_\ell(z)P_\ell(z_p)\Theta(r - r_p)\Big)\,, \tag{3.13}$$

where $z_p := r_p/M - 1$. An example of such a static solution, with $\ell = 2$, is shown in Fig. 4.14. All modes are continuous at the location of particle, but display a finite jump discontinuity in the first radial derivative there.

3.3 Local Approximate Solution

The field satisfying Eq. (3.1) can be split into a singular and regular piece

$$\Psi(x) = \Psi^S(x) + \Psi^R(x). \tag{3.14}$$

The Ψ^S singular piece i) is a solution to Eq. (3.1), ii) displays a singular structure near the particle's worldline, iii) does not exert a force on the particle. The Ψ^R regular piece i) satisfies the homogeneous version of Eq. (3.1), ii) is smooth on the particle's wordline, iii) determines the self-force acting on the particle [73].

In our 1+1D toy model we replace the actual solution in a worldtube surrounding the particle's worldline with an analytical approximation $\Psi^A_{\ell m}$ that consists of two terms: a "puncture" field $\Psi^{\mathcal{P}}_{\ell m}$, and a "regular" field $\Psi^{\mathcal{R}}_{\ell m}$. In this 1+1D model, $\Psi^{\mathcal{P}}_{\ell m}$ is *not* a mode decomposition of Ψ^S. Instead, it is formed using an ansatz such that it does capture the local irregularity in (i.e. discontinuous derivatives of) the field at the particle, as seen in the singular field. The "regular" field $\Psi^{\mathcal{R}}_{\ell m}$, accounts for the remaining, smooth part of the local field.

Both these terms are expressed as a power series in the distance to the worldline, truncated at a certain order (to be referred to as "the order" of the analytical model). The expansion coefficients of $\Psi^{\mathcal{P}}_{\ell m}$ can be determined analytically from the field equation (3.6) using a local asymptotic analysis, as we explain below, and are fixed in advance in our model. The expansion coefficients of $\Psi^{\mathcal{R}}_{\ell m}$, on the other hand, can only be determined by matching to the external field outside the worldtube; these coefficients remain *a priori* unknown, and they are to be determined dynamically during the numerical evolution as described in later sections. In the rest of this section we describe the construction of a suitable local analytical model $\Psi^A_{\ell m}$ for the scalar field.

We begin with the construction of a suitable puncture field $\Psi^{\mathcal{P}}_{\ell m}$. Recalling our observation that the physical solution is continuous but has a finite jump discontinuity in its first radial derivative at the particle, we introduce the ansatz

$$\Psi^{\mathcal{P}}_{\ell m}(r,t) = |\Delta r| \sum_{j=1}^{n} a_{j\ell m} (\Delta r)^{j-1} S_{\ell m}(t)\,, \tag{3.15}$$

where $\Delta r := r - r_p$. Our choice of time dependence here makes sense, because the source function $S_{\ell m}(t)$ depends on t harmonically, via the factor $e^{-im\Omega t}$ implicit in $\bar{Y}_{\ell m}\left(\frac{\pi}{2}, \Omega t\right)$ in Eq. (3.8), and the retarded solution inherits this harmonic time dependence. We terminate the expansion at order $(\Delta r)^n$ for some $n \geq 1$, referring to the resulting field as an "nth-order puncture", denoted $\Psi^{\mathcal{P}(n)}_{\ell m}$.

The constant coefficients $a_{j\ell m}$ in Eq. (3.15) are determined by substituting (3.15) in the field equation (3.6), re-expanding in powers of Δr, and then demanding that the resulting equation is satisfied at the particle as a distributional equality. This produces a hierarchy of algebraic equations for $a_{j\ell m}$, which we can solve recursively order by order in Δr. More specifically, once Eq. (3.15) is substituted in Eq. (3.6), the requirement that the delta-function terms balance in the equation immediately determines $a_{1\ell m}$. Then, the requirement that the remaining discontinuity vanishes at $\mathcal{O}(\Delta r^0)$ determines $a_{2\ell m}$ in terms of $a_{1\ell m}$, the requirement that it vanishes at $\mathcal{O}(\Delta r^1)$ determines $a_{3\ell m}$ in terms of $a_{1\ell m}$ and $a_{2\ell m}$, and so on. For the first five coefficients one obtains, in this fashion,

$$a_{1\ell m} = -\frac{1}{2f_p}\,, \tag{3.16a}$$

$$a_{2\ell m} = \frac{M}{2f_p^2 r_p^2}\,, \tag{3.16b}$$

$$a_{3\ell m} = \frac{r_p^4 m^2\Omega^2 - \lambda r_p^2 f_p - 2M(3r_p - 2M)}{12 f_p^3 r_p^4}\,, \tag{3.16c}$$

$$a_{4\ell m} = \frac{\lambda r_p^3 f_p - 3M r_p^4 m^2\Omega^2 + 2M(3r_p^2 - 4Mr_p + 2M^2)}{12 f_p^4 r_p^6}, \tag{3.16d}$$

$$\begin{aligned} a_{5\ell m} = \frac{1}{240 f_p^5 r_p^8}\Big[&2r_p^4 m^2\Omega^2\left(\lambda r_p^2 f_p + 2M(11r_p + 13M)\right) - r_p^8 m^4\Omega^4 - 2\lambda r_p^2 f_p \\ &(9r_p^2 + 2Mr_p - 4M^2) - 24M(5r_p^3 - 10Mr_p^2 + 10M^2 r_p - 4M^3) - \lambda^2 r_p^4 f_p^2\Big]\,, \end{aligned} \tag{3.16e}$$

where $f_p := f(r_p) = 1 - 2M/r_p$ and $\lambda := \ell(\ell+1)$. With this, we have all that we need to construct puncture fields through fifth order.

Next, consider the remaining piece of the local field, $\Psi^{\mathcal{R}(n)}_{\ell m}$, which we now *define* as the difference between the full physical field and the nth-order puncture field $(\Psi_{\ell m} - \Psi^{\mathcal{P}(n)}_{\ell m})$, expanded in Δr, with the expansion truncated at $\mathcal{O}(\Delta r^n)$. Since, by construction, $\Psi^{\mathcal{P}(n)}_{\ell m}$ has the same singular structure as $\Psi_{\ell m}$ through $\mathcal{O}(\Delta r^n)$, the so-defined field $\Psi^{\mathcal{R}(n)}_{\ell m}$ is smooth through $\mathcal{O}(\Delta r^n)$, and takes the form of a polynomial:

$$\Psi^{\mathcal{R}(n)}_{\ell m}(t, r) = \sum_{j=0}^{n} \psi^{\mathcal{R}}_j(t)(\Delta r)^j\,. \tag{3.17}$$

The $n+1$ coefficients $\psi^{\mathcal{R}}_k(t)$ (their ℓ, m indices suppressed for brevity) are *a priori* unknown; they are to be determined by matching to the numerical field outside the

worldtube at each time step in the numerical evolution, as we describe in the next section.

Our full nth-order analytical approximate field inside the worldtube is given by

$$\Psi^{A(n)}_{\ell m}(t,r;\psi^{\mathcal{R}}_k) = \Psi^{\mathcal{P}(n)}_{\ell m}(t,r) + \Psi^{\mathcal{R}(n)}_{\ell m}(t,r;\psi^{\mathcal{R}}_k)\,, \tag{3.18}$$

where our notation acts as a reminder that $\Psi^{A(n)}_{\ell m}$ inherits from $\Psi^{\mathcal{R}(n)}_{\ell m}$ a parametric dependence on the $n+1$ time-dependent coefficients $\psi^{\mathcal{R}}_k := \{\psi^{\mathcal{R}}_0(t),\ldots,\psi^{\mathcal{R}}_n(t)\}$. We use the field $\Psi^{A(n)}_{\ell m}$ to populate the interior of the excision worldtube in our numerical simulations, with $\psi^{\mathcal{R}}_k$ determined by matching at each time step. The "approximate" nature of $\Psi^{A(n)}_{\ell m}$ comes from the finite truncation of the expansion in Δr at order n. Note that, due to the finite truncation, our definition of $\Psi^{A(n)}_{\ell m}$ is attached to our particular choice of a distance expansion parameter: using e.g. Δr^* instead of Δr would yield a slightly different (but equally valid) analytic approximation. Note also that $\Psi^{A(n)}_{\ell m}$ cannot be "made exact" (even in principle) with a fine-tuned choice of the parameters $\psi^{\mathcal{R}}_k$, since these parameters control only the smooth piece of the field and cannot correct the error in the non-smooth piece caused by the finite truncation of $\Psi^{\mathcal{P}(n)}_{\ell m}$. The error in $\Psi^{A(n)}_{\ell m}$ is inherent, and can only be controlled by varying the model order n (or the worldtube radius).

In Scheme I of our numerical implementation we, in fact, use a characteristic grid, with numerical evolution proceeding along null rays $v = t + r^*$ and $u = t - r^*$. We therefore appropriately transform our analytical solution into these coordinates and the regular field is then given by a double Taylor expansion,

$$\Psi^{\mathcal{R}}(t,u,v) = \sum_{j+k=0}^{n} \Psi^{\mathcal{R}}_{jk}(t)(\Delta u)^j(\Delta v)^k. \tag{3.19}$$

$\Psi^{\mathcal{R}}_{jk}(t)$ are the coefficients to be determined by the matching, and $\Delta u, \Delta v$ are the distances in u, v from the point of field evaluation to the position of the scalar charge.

3.4 Matching Overview

In the next two chapters we formulate two (alternative) matching strategies for the field in and outside of the worldtube. The first is based on matching the analytical and numerical solutions in an open "buffer" region around the tube's boundaries. At each step of the time evolution, the matching determines the set of unknown coefficients in the analytical solution. Once the analytical solution has been fixed inside the tube, the evolution can proceed to the next time step. This approach is close in spirit to the standard method of matched asymptotic expansions, which underlies most of the literature on tidally perturbed black hole spacetimes and GSF theory. However, whereas

in standard matched expansions one matches together two asymptotic expansions, here one matches an asymptotic expansion (the approximate analytical solution in the tube) to an "exact" numerical solution.

The second matching approach we explore is conceptually different, reminiscent more of the standard treatment of interfaces between media in hyperbolic systems using a junction condition. In this approach we regard the worldtube boundary as a strict interface, where boundary conditions are set for the numerical evolution outside the tube. These boundary conditions are obtained (at each time step) from solutions of a certain set of first-order ordinary differential equations (ODEs) along the boundary, formulated in a way that ensures well-posedness of the evolution scheme.

We formulate each of the two matching approaches quite independently of any implementation details; indeed, each approach can in principle be implemented using whichever one's favorite numerical evolution method happens to be (finite difference or spectral, Cauchy or characteristic, etc.). Here, to illustrate the applicability of our two approaches and test their performance, we present two independent numerical implementations, one for each approach. For the first approach (matching in a buffer region), hereafter referred to as 'Scheme I', we present a finite-difference implementation in characteristic coordinates. For the second approach (matching on the boundary), hereafter referred to as 'Scheme II', we present a spectral implementation with Cauchy evolution. For each approach we demonstrate the stability of the numerical evolution, compare with analytical solutions where possible, and explore the convergence of the solutions with respect to numerical resolution, worldtube radius (R) and approximate analytical solution order (n).

Chapter 4

1+1D Scalar-Field Model: Scheme I

This chapter presents our first 1+1D scalar-field toy model, "Scheme I". Here we use a finite-difference method for the numerical evolution and match the approximate analytical solution to the numerical solution using a sample of data points around the worldtube boundaries. We go on to explore the dependence of the worldtube excision model on the key parameters, namely numerical resolution, worldtube radius and approximate analytical solution order.

4.1 Setup

4.1.1 Characteristic Grid

Scheme I uses finite difference methods for the numerical evolution of the scalar wave equation, on a grid with characteristic coordinates $u = t - r^*$, $v = t + r^*$. The resolution is defined as the distance along the side of a grid cell given by h, illustrated in Fig. 4.1. The evolution proceeds along characteristic slices, $u = const, v = const$. Such characteristic grid evolutions are tried and tested numerical schemes, with examples of use given in [93, 90, 36, 37, 72]. Characteristic grid evolutions have benefits, compared to Cauchy grid evolutions, due to their lack of a need for strict boundary conditions. This is a result of the fact that the boundaries of the Schwarzschild exterior are null surfaces and out of causal contact with the evolutionary domain. We construct the grid such that the initial vertex u_0, v_0 is at coordinate values $t = 0$ and $r = 7M, r^* \approx 8.8M$.

The numerical evolution in Scheme I follows the principles laid out in [93, 90, 36, 37, 72]. Initial data must be specified on the lines $u = u_0$ and $v = v_0$. Since we do not know the physical solution, we treat the initial data as freely specifiable; the deviation from

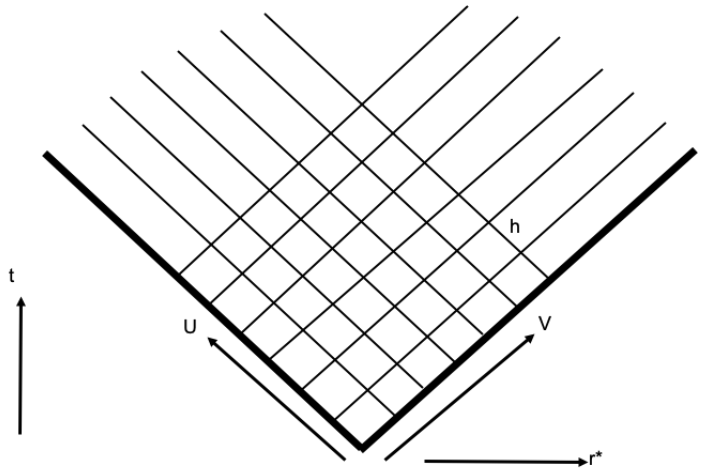

FIGURE 4.1: Illustration of the characteristic grid. Initial data is set along the initial u, v rays which are depicted in bold.

the physical solution is then equivalent to adding an incoming or outgoing wave in the form of a homogeneous solution. This "junk" data will then radiate away, exiting the numerical domain of interest and leaving behind the correct physical behaviour.

Typically we evolve the Scheme I model for $t \approx 500M$, to allow sufficient time for junk data to dissipate. Scalar (or gravitational) perturbations of the Schwarzschild black hole exterior die off at late times with an inverse power law. For a spherical harmonic wave mode of multipole ℓ, this power law is given by $t^{-2\ell+3}$ [126, 30].

When we introduce a scalar charge e, we fix it to be on a circular, equatorial orbit with $r_p = 7M$ i.e. the vertex of our grid, $\theta_p = \frac{\pi}{2}$ and $\phi_p = \Omega t$, where $\Omega = \sqrt{\frac{M}{r_p^3}}$. The orbital period of the particle is given by $P = \frac{2\pi}{\Omega} \approx 116M$. For simplicity in Schemes I and II, we set $M = 1$ and $e = 1$ going forward.

4.1.2 Numerical Method

The finite difference scheme we use to numerically evolve the field over the characteristic grid follows the quadratic-order algorithms laid out in [93, 90].

For simplicity we first consider the homogeneous scalar wave equation. In terms of u, v coordinates, $-\Psi^2_{,t} + \Psi^2_{,r^*} = -4\Psi_{,uv}$ this is

$$-4\Psi_{,uv} - V(r)\Psi = 0. \tag{4.1}$$

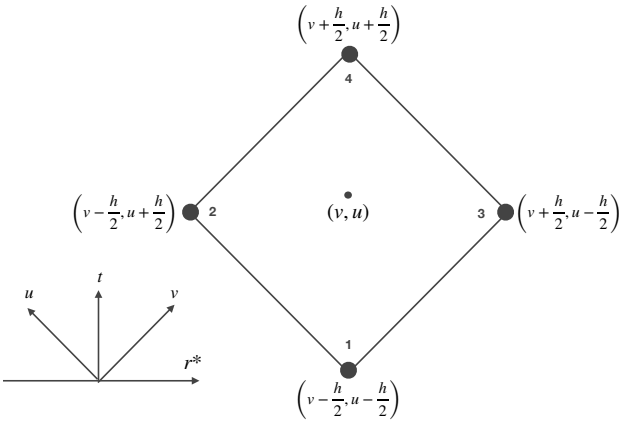

FIGURE 4.2: Depiction of grid cell in null coordinates. The centre of the cell is at (v, u), whilst the values at the vertices show the relative changes in terms of the gridsize h.

By performing an integration over the grid cell whose centre has coordinate values (t_c, r_c^*), we have

$$\begin{aligned}\int\int_{cell} -4\Psi_{,uv} du dv &= -4\big[\Psi(t_c + \frac{h}{2}, r_c^*) + \Psi(t_c - \frac{h}{2}, r_c^*) - \Psi(t_c, r_c^* - \frac{h}{2}) - \Psi(t_c, r_c^* + \frac{h}{2})\big] \\ &= -4[\Psi_4 + \Psi_1 - \Psi_2 - \Psi_3],\end{aligned} \tag{4.2}$$

where $\Psi_1, \Psi_2, \Psi_3, \Psi_4$ denote the field values at the four vertices labelled in Fig. 4.2. This result is exact, containing no finite-difference errors. The integral of the potential term is approximated to $\mathcal{O}(h^4)$ using a trapezoidal rule [90],

$$\int\int_{cell} V(r)\Psi du dv = h^2 V(r_c)\left(\frac{\Psi_2 + \Psi_3}{2}\right) + \mathcal{O}(h^4), \tag{4.3}$$

where $V(r_c)$ is the value of the potential at the centre of the grid cell. Given Eq. (4.2) and (4.3) the integral of Eq. (4.1) can be rearranged to obtain a formula for the field at point 4 in terms of field values at the three prior points

$$\Psi_4 = -\Psi_1 + (\Psi_2 + \Psi_3)\left(1 - \frac{h^2}{2}\frac{V(r_c)}{4}\right) + \mathcal{O}(h^4). \tag{4.4}$$

As a first test of our characteristic evolution, we evolve the field without a source. In this scenario we introduce a Gaussian wave packet along an initial ray, either

$$\Psi(u = u_0, v) = \exp\left(-\frac{(v - v_i)^2}{2\sigma^2}\right), \quad \Psi(u, v = v_0) = 0, \tag{4.5}$$

or

$$\Psi(u, v = v_0) = \exp\left(-\frac{(u - u_i)^2}{2\sigma^2}\right), \quad \Psi(u = u_0, v) = 0, \tag{4.6}$$

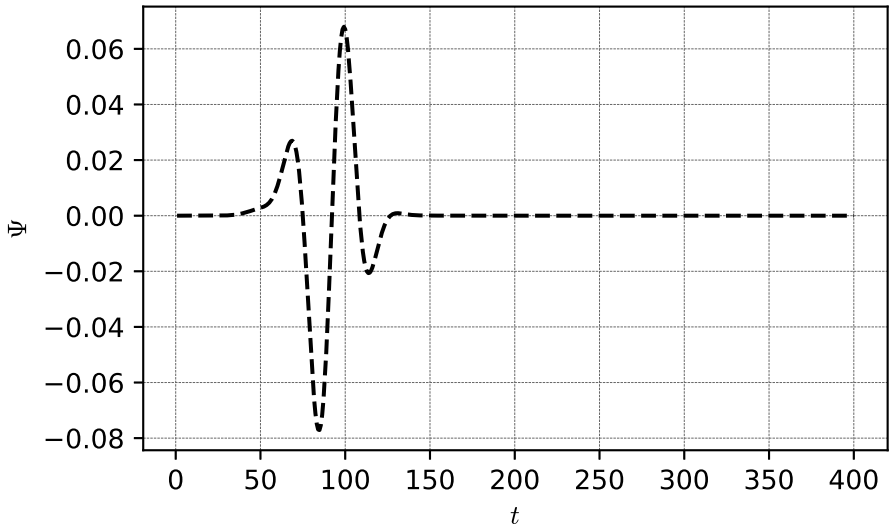

FIGURE 4.3: We seed the evolution with a Gaussian wave packet and allow this to evolve in Schwarzschild spacetime, using the finite difference scheme. Here we plot the value of Ψ at $r = 7M$ against t.

We set $u_i, v_i = 15M$, $\sigma = 10M$ and where $u_0 \approx -8.83258M$, $v_0 \approx 8.83258M$ due to $t = 0$ and $r^* \approx 8.83258M$ at this position. Figure (4.3) shows the field Ψ at $r = 7M$ against t, with this Gaussian initial seed data. We now use this as a scenario to test the convergence of the finite difference scheme with respect to h.

In a complete run of the numerical simulation there is a total number $N \propto \frac{1}{h^2}$ of cells in the grid. This then results in the accumulation of the local $\mathcal{O}(h^4)$ error, to an overall global error of $\mathcal{O}(h^2)$. Our convergence test takes a ratio of Ψ values from three numerical runs with grid sizes that differ by a factor of 2, using the formula

$$\mathcal{I}_h := \frac{\Psi(h) - \Psi(\frac{h}{2})}{\Psi(\frac{h}{2}) - \Psi(\frac{h}{4})}. \tag{4.7}$$

The ratio test compares the field value either along slices of constant time, hence as a function of r^*, or along slices of constant radius, hence as a function of t. The test allows us to assess the convergence index across an entire domain, giving us a local view of the behaviour. A global error of $\mathcal{O}(h^2)$, i.e. a quadratic-order scheme, would produce a convergence index of $\mathcal{I}_h = 4$. In Fig. 4.4 we plot $\mathcal{I}_h$ for an $\ell = 2, m = 0$ Ψ mode at $r = 7M$ against time t, to see the settling of this convergence index with the evolution. The figure shows $\mathcal{I}_h$ settling to 4, corroborating the expected quadratic convergence.

The numerical evolution of our BBH models will be carried out using spectral methods as opposed to finite difference methods. Spectral methods are characterised by their exponential convergence with respect to resolution and so will vastly improve on this $\mathcal{I}_h$. Therefore, for the purposes of the Scheme I toy model where we are focusing our

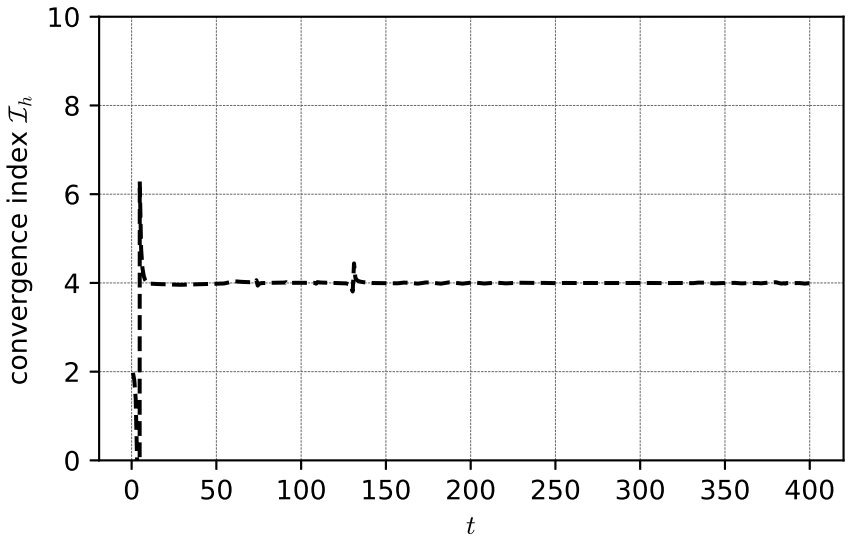

FIGURE 4.4: We plot the convergence index I_h given in Eq. 4.7 as a function of t, for a non-sourced evolution of Ψ seeded by a Gaussian wave packet. We take the value of Ψ at $r = 7$ and use runs of $h = 0.8, 0.4, 0.2$. Due to our second-order finite difference scheme, we obtain quadratic convergence.

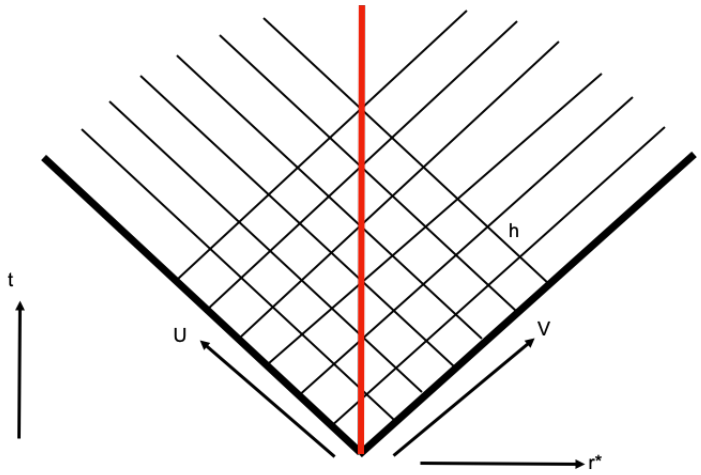

FIGURE 4.5: Illustration of the characteristic grid with a point particle source at a fixed radius. The worldline of the point particle is depicted by the red line.

efforts on the architecture of the worldtube and the matching procedure, a quadratic-order scheme is sufficient.

4.2 Test Setups

4.2.1 Evolution with a Point Particle Source

Instead of moving to excise a region from our numerical evolution straight away, we first introduce a point particle on a circular orbit into our numerics. This will allow

us to adapt our finite difference scheme to the presence of a source. The worldline of the source in the characteristic grid is illustrated in Fig. 4.5. The value of this intermediary construction is twofold. It will act as an initial check on our basic numerical evolution scheme, as we can compare results to the exact analytical solution for static modes computed in Sec. 3.2. Here we should see convergence with increasing resolution (decreasing h). Secondly, for non-static modes, as no closed-form analytical solution exists, the numerical results for the point particle source will act as the baseline to which we can compare results from our worldtube model.

Our scalar wave equation in u, v coordinates becomes

$$\Psi_{,uv} + \frac{V(r)}{4}\Psi = \frac{\pi e}{r_p}\frac{f^2(r_p)}{E}Y^*_{\ell m}(\frac{\pi}{2}, \Omega t)\delta(r - r_p). \tag{4.8}$$

The evaluation of the finite difference scheme on grid vertices will remain the same, except if the vertex is crossed by the particle's trajectory. In this case the formula reads

$$\Psi_4 = -\Psi_1 + (\Psi_2 + \Psi_3)\left(1 - \frac{h^2}{2}\frac{V(r_c)}{4}\right) + Z + \mathcal{O}(h^4), \tag{4.9}$$

where Z is given by the integral of the source over the u, v grid cell. As the source has a delta function in r, it is convenient to use $dudv = 2f^{-1}drdt$:

$$Z_{\ell m} = \iint_{cell} \frac{2\pi e}{r}\frac{f(r)}{E}Y^*_{\ell m}(\frac{\pi}{2}, \Omega t)\delta(r - r_p)drdt, \tag{4.10}$$

where we have reinstated the ℓ, m indices on Z. The conjugate spherical harmonic has the form

$$Y^*_{\ell m}\left(\frac{\pi}{2}, \Omega t\right) = A_{\ell m}e^{-im\Omega t}, \tag{4.11}$$

where $A_{\ell m} = (-1)^{(\ell+m)/2}\left[\frac{(2\ell+1)(\ell+m-1)!!(\ell-m-1)!!}{4\pi(\ell+m)!!(\ell-m)!!}\right]^{1/2}$ if $\ell - m$ is even, or $A_{\ell m} = 0$ if $\ell - m$ is odd [36]. For the $m = 0$ case the explicit integral of the source term is then

$$Z_{\ell 0} = \frac{2\pi e}{r_p}\frac{f(r_p)}{E}A_{\ell 0}\Big[t\Big]^{t_c+\frac{h}{2}}_{t_c-\frac{h}{2}} = \frac{2\pi e}{r_p}\frac{f(r_p)}{E}A_{\ell 0}h. \tag{4.12}$$

For non-zero m modes, the explicit integral is evaluated as follows:

$$\begin{aligned} Z_{\ell m} &= \frac{2\pi e}{r_p}\frac{f(r_p)}{E)}A_{\ell m}\int_{t_c-\frac{h}{2}}^{t_c+\frac{h}{2}} e^{-im\Omega t}dt \\ &= -\frac{2\pi e}{r_p}\frac{f(r_p)}{E}\frac{A_{\ell m}}{im\Omega}e^{-im\Omega(t_c)}\left[e^{-im\Omega\frac{h}{2}} - e^{im\Omega\frac{h}{2}}\right] \\ &= \frac{2\pi e}{r_p}\frac{f(r_p)}{E}\frac{A_{\ell m}}{m\Omega}e^{-im\Omega(t_c)}\left[2\sin\left(m\Omega\frac{h}{2}\right)\right]. \end{aligned} \tag{4.13}$$

Here $t_c - \frac{h}{2}, t_c + \frac{h}{2}$ are the values for t at the entry (t_{in}) and exit (t_{out}) points of the cell on a circular geodesic. Therefore the full finite difference scheme is given by

$$\Psi_4 = -\Psi_1 + (\Psi_2 + \Psi_3)\left(1 - \frac{h^2}{2}\frac{V(r_c)}{4}\right) + \frac{2\pi e}{r_p}\frac{f(r_p)}{E}A_{\ell 0}h + \mathcal{O}(h^4) \tag{4.14}$$

for static modes and

$$\begin{aligned}\Psi_4 = &- \Psi_1 + (\Psi_2 + \Psi_3)\left(1 - \frac{h^2}{2}\frac{V(r_c)}{4}\right) \\ &+ \frac{2\pi e}{r_p}\frac{f(r_p)}{E}\frac{A_{\ell m}}{m\Omega}e^{-im\Omega(t_c)}\left[2\sin\left(m\Omega\frac{h}{2}\right)\right] + \mathcal{O}(h^4)\end{aligned} \tag{4.15}$$

for non-static modes. For the initial data along the initial rays, u_0, v_0, we set the field to be zero.

Non-static modes of the field Ψ are radiative, with oscillations representing scalar-field waves. This can be seen from the form of Eq. (4.15) and in Fig. 4.6. Figure 4.6 shows the absolute, real and imaginary parts of the field generated from the point particle code, for an $\ell = 2, m = 2$ mode on a slice of time $t = 400M$. For all ℓ, m, the field is continuous at the location of the particle but has a finite jump discontinuity in its first radial derivative there. Scalar waves are seen to emanate from the particle out towards infinity ($r^* \to \infty$), as well as down towards the event horizon ($r^* \to -\infty$), with a much smaller amplitude. We can also see the outgoing junk radiation at the edge of the r^* domain.

Two types of convergence test with respect to h can be performed. The first is an internal convergence test where three runs of the point particle code are compared. The formula for the convergence index would be

$$\mathcal{I}_h := \frac{\Psi(h) - \Psi(\frac{h}{2})}{\Psi(\frac{h}{2}) - \Psi(\frac{h}{4})}. \tag{4.16}$$

The second is an external convergence test, where two runs of the point particle code and the exact analytical solution given by Eq. (3.13) are compared. We now denote the exact analytical solution, Ψ_{exact}. These tests confirm convergence of the code to the correct solution. The formula for the convergence index would then be

$$\mathcal{I}_{hE} := \frac{\Psi(h) - \Psi_{\text{exact}}}{\Psi(\frac{h}{2}) - \Psi_{\text{exact}}}. \tag{4.17}$$

The latter is of course only applicable for static mode ($m = 0$) runs of the point particle code. Both tests confirm quadratic-order convergence, i.e. an index $\mathcal{I}_h = \mathcal{I}_{hE} = 4$. Figure (4.7) shows the internal convergence between $h = 0.8, 0.4, 0.2$ runs for an $\ell = 2, m = 2$ mode. When performing an internal convergence test using Eq. (4.16) for a non-static mode, it is preferable to compare the absolute value of Ψ. This is due to

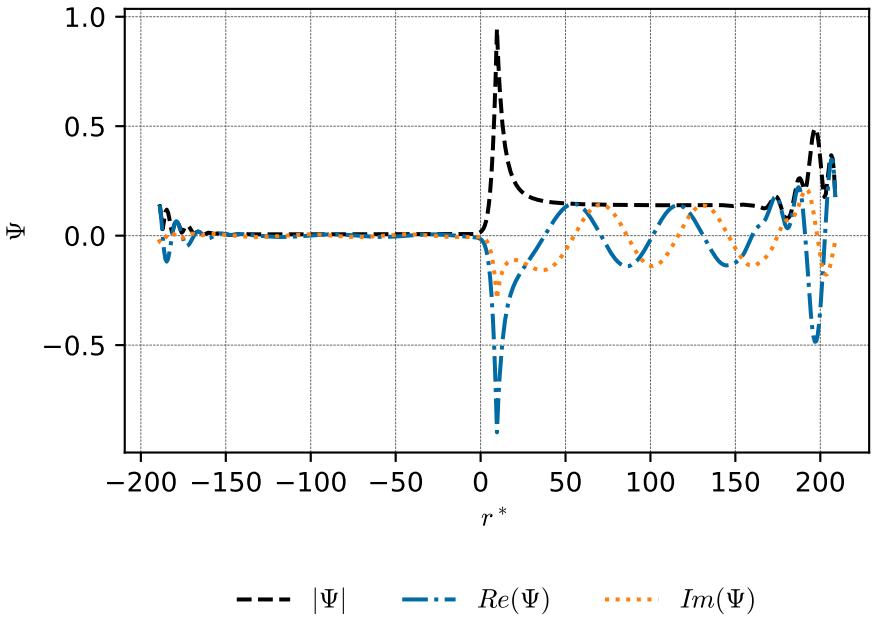

FIGURE 4.6: The field values for an $\ell = 2, m = 2$ mode using the point particle code at a slice of time $t = 400M$. Scalar waves are seen to emanate from the particle out towards infinity ($r^* \to \infty$), as well as down towards the event horizon ($r^* \to -\infty$), with much smaller amplitude. Outgoing junk radiation can also be seen at the edge of the r^* domain.

the fact that the settled index would be obscured by zero crossings, as a result of the oscillatory nature of the propagating sinusoidal waves. An additional test for non-static modes is to compare the phase of Ψ.

4.2.2 Evolution with the Exact Analytical Solution inside a Worldtube

We now introduce a worldtube into our characteristic grid; see Fig. 4.8. The radius of the worldtube is denoted by R. As a final check on our code, before the implementation of a matching procedure, we populate the worldtube with the exact analytical solution for static modes. For initial data we set the field values along the initial rays inside the worldtube to be equal to the analytical solution and outside the worldtube we introduce a Gaussian function to smoothly send the field values to zero. This avoids creating a discontinuity in the initial data, which would result in larger amplitude junk radiation.

In this test setup the finite difference scheme numerically evolves up to the boundaries. The values of the field at vertices on the boundaries are then given by the exact analytical solution, evaluated at the appropriate coordinate distance. Although our boundary data corresponds to a static mode, we are not imposing staticity on the numerical evolution outside it. Figure 4.9 shows a slice of the field Ψ at $t = 400M$, where the worldtube size has been set to $R = 0.8M$, centred on $r = 7M$.

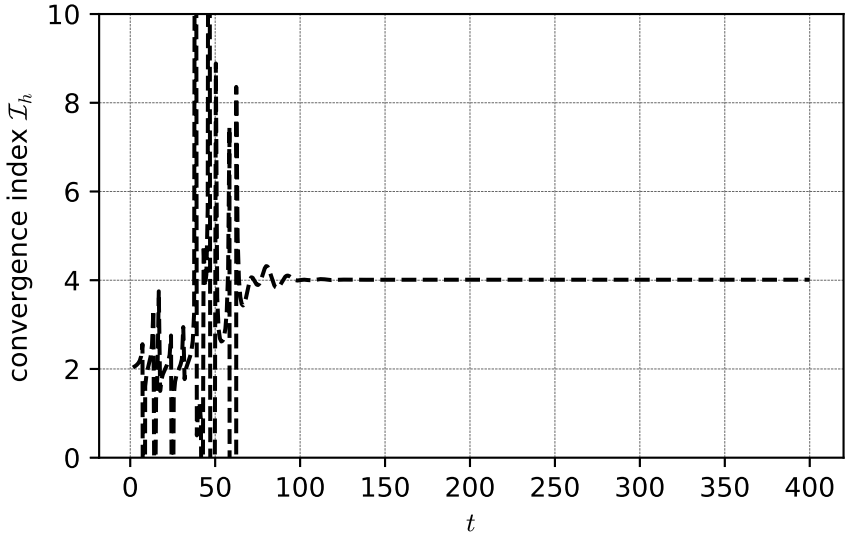

FIGURE 4.7: The convergence index I_h given in Eq. (4.16) as a function of t for the point particle code. We examine the absolute value of Ψ for an $\ell = 2, m = 2$ mode at $r = 7M$, using runs of $h = 0.8, 0.4, 0.2$. Due to our second-order finite difference scheme, we obtain quadratic convergence.

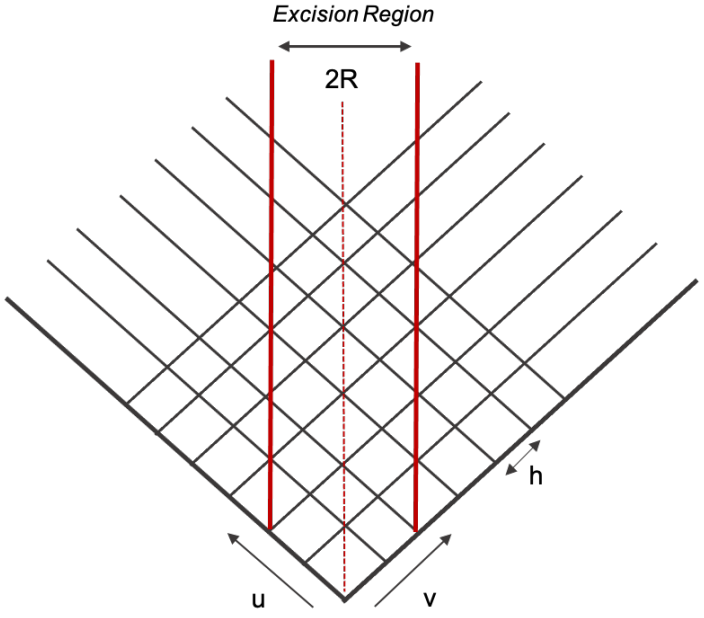

FIGURE 4.8: Illustration of the characteristic grid with a worldtube, whose boundaries are given by vertical red lines. The region within the worldtube is excised from the numerical evolution.

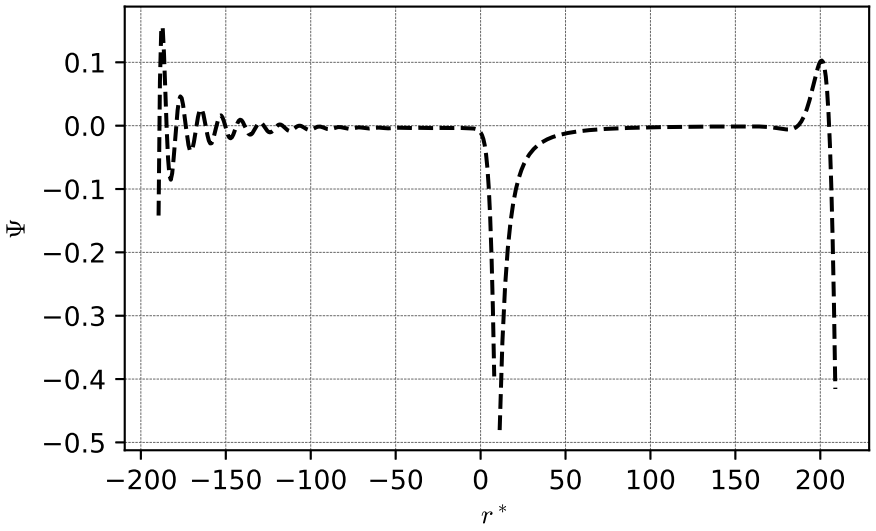

FIGURE 4.9: The field values for an $\ell = 2, m = 2$ mode worldtube evolution, where the worldtube interior has been populated with the exact analytical solution, at a slice of time $t = 400M$. The worldtube size has been set to $R = 0.8M$, centered on $r = 7M$.

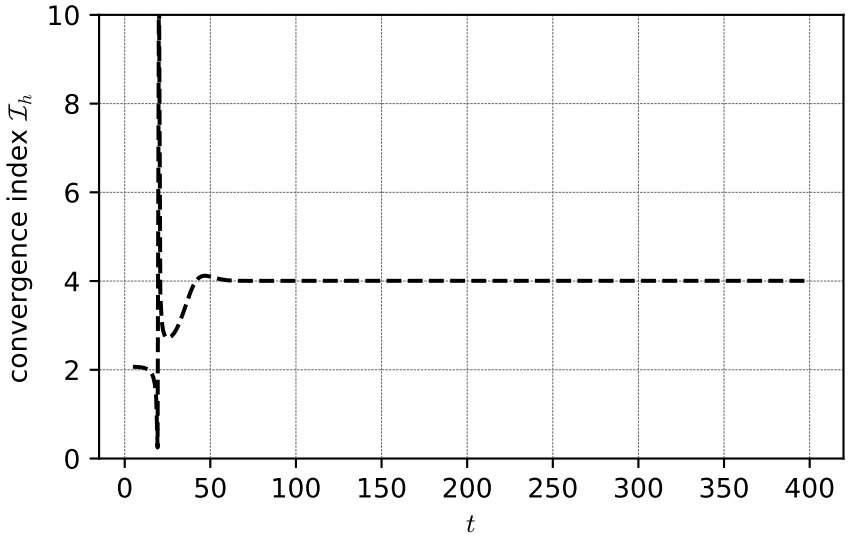

FIGURE 4.10: We plot the convergence index I_h given in Eq. (4.16) as a function of t, for the worldtube evolution using the exact analytical solution within the interior. We examine the absolute value of Ψ for an $\ell = 2, m = 0$ mode at $r = 7M$, using runs of $h = 0.8, 0.4, 0.2$. Due to our second-order finite difference scheme, we obtain quadratic convergence.

Once again we want to check whether the model gives the expected quadratic convergence with respect to h. As done with the point particle evolution, we can perform an internal convergence and an external convergence test, examining convergence to the correct solution. Both tests confirm quadratic-order convergence, i.e. an order $\mathcal{I}_h = \mathcal{I}_{hE} = 4$. Figure (4.10) shows the internal convergence between $h = 0.8, 0.4, 0.2$ runs for an $\ell = 2, m = 0$ mode.

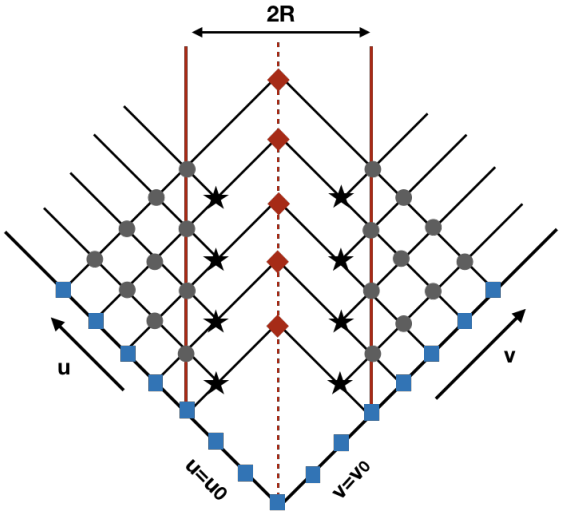

FIGURE 4.11: The 1+1D characteristic mesh used in Scheme I. The particle's circular orbit is represented by the dashed (red) line running vertically down the center. At each time step the particle sits at a red diamond point. The solid (red) vertical lines mark the boundaries of the excision worldtube. Outside the worldtube we evolve the field equation numerically along characteristic rays (as described in the text) using a finite-difference formula. The evolution starts from characteristic initial data set on the two initial rays $v = v_0$ and $u = u_0$ (blue square grid points) and proceeds to determine the data points in the bulk of spacetime outside the tube and on its boundaries (grey circle points). At each time step, a matching procedure, described in Subsec. 4.3.1, is applied to determine the parameters of the approximate analytical solution on the remaining sections of the characteristic rays inside the tube, and in particular on the two "ghost" grid points (black, starred) needed at subsequent steps of the evolution.

4.3 Evolution with a Worldtube

4.3.1 Matching Method

4.3.1.1 Ethos

Our first approach is inspired by the method of matched asymptotic expansions. Let us recall how that method is traditionally applied to the small-mass-ratio limit of the binary problem [110], with reference to Fig. (2.1). The binary is treated as a one-parameter system, using m_1 as an overall length scale and the small mass ratio $q = m_2/m_1$ as a small parameter (in this treatment, the length $\mathcal{R}$ is replaced with m_1 rather than being treated as an independent scale). In the bulk of the binary spacetime, one expands the metric in powers of q. Sufficiently near m_2, at distances $\sim m_2$, such an expansion breaks down because the gravity of m_2 dominates over that of m_1. One then constructs a complementary local approximation using an expansion in powers of q while holding s/m_2 fixed, where s is a suitable measure of spatial distance from the companion's representative worldline. By holding s/m_2 fixed, this expansion zooms in on the region $s \sim m_2 \ll m_1$, such that $s/m_1 \sim q$. In a buffer region $m_2 \ll s \ll m_1$, s/m_1 and m_2/m_1 are both small, and the exterior and interior approximations must agree. This

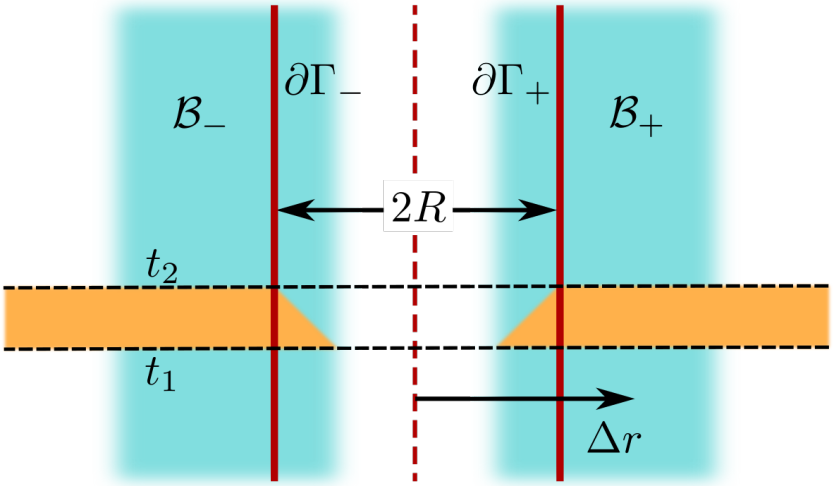

FIGURE 4.12: Spacetime diagram (in t, r coordinates) illustrating the various regions involved in our first matching approach. The vertical dashed line indicates the particle's worldline at constant orbital radius. The disjoint shaded regions $\mathcal{B}_\pm$ make up the buffer region $\mathcal{B} = \mathcal{B}_- \cup \mathcal{B}_+$ where the matching occurs. The excision region Γ has a disjoint boundary $\partial\Gamma = \partial\Gamma_+ \cup \partial\Gamma_-$ that lies within $\mathcal{B}$. We carry out the matching by expanding the numerical field Ψ^N in powers of Δr and equating the coefficients in the expansion to the coefficients in Ψ^A. The orange shaded region shows the domain of dependence of the field outside Γ at time t_2, given data at time t_1.

requirement translates into a precise matching condition: if the local approximation inside the worldtube is re-expanded in powers of q at fixed s (no longer holding s/m_2 fixed), and the external solution is re-expanded in powers of s/m_1, then in both cases one arrives at a double series in q and s/m_1, which should be a good approximation in the buffer region. The matching condition states that because they are expansions of the same metric, the two double expansions must agree term by term.

Now consider the translation of these notions into our toy problem. For simplicity we use t–r coordinates in our description rather than the double-null coordinates we ultimately use in Scheme I. The setup in the t–r plane is illustrated in Fig. 4.12. We define a buffer region $\mathcal{B}$, made up of disjoint regions $\mathcal{B}_\pm$, in which Δr is small compared to M. We then define an excision region $\Gamma = [-R \leq \Delta r \leq R]$ around the particle's orbital radius, with boundaries $\partial\Gamma_\pm$ lying in $\mathcal{B}_\pm$. We loosely imagine that outside of Γ, we solve for Ψ using the homogeneous field equation, Eq. (3.6) with the right-hand side set to zero, and that inside, we use the analytical approximation $\Psi^A_{\ell m}$. For convenience, we label the numerically evolved field outside Γ as $\Psi^N_{\ell m}$. However, following the dictates of matched expansions, we operate under the principle that in $\mathcal{B}$, $\Psi^N_{\ell m}$ and $\Psi^A_{\ell m}$ can be used interchangeably.

As in the method of matched expansions, to match the two fields we expand Ψ^N to put it in the same form as Ψ^A (we hereafter omit the indices ℓm for brevity). In each of the

regions $\mathcal{B}_\pm$, Ψ^N can be approximated by a power series in Δr,

$$\Psi^{N\pm}(t,r) = \sum_{j=0}^{n} \psi_j^\pm(t)(\Delta r)^j + \mathcal{O}(\Delta r^{n+1}), \tag{4.18}$$

where $\Psi^{N\pm}$ denotes the restriction of Ψ^N to $\mathcal{B}_\pm$. The coefficients $\psi_j^\pm$ can be found by projecting Ψ^N onto the basis of functions $\{(\Delta r)^0, \ldots, (\Delta r)^n\}$ using a suitable inner product

$$\langle x, y\rangle = \int_{\mathcal{B}'} x(r)y(r)dr. \tag{4.19}$$

Here $\mathcal{B}'$ is some open interval (with fixed t) in $\mathcal{B}$, or a collection of multiple such intervals; we consider the choice of integration domain below. Our matching condition is then that the coefficients in Eq. (4.18) are identical to the coefficients in Ψ^A:

$$\psi_j^\pm(t) = \psi_j^{\mathcal{R}}(t) + \psi_j^{\mathcal{P}\pm}(t), \tag{4.20}$$

where $\psi^{\mathcal{P}\pm}$ are the puncture coefficients, which can be read off Eq. (3.15): $\psi_j^{\mathcal{P}\pm}(t) = \pm a_{j\ell m} S_{\ell m}(t)$.

To satisfy Eq. (4.20), we must ensure that $\psi_j^\pm$ satisfies the same jump conditions as $\psi_j^{\mathcal{P}\pm}$, meaning $\psi_j^+ - \psi_j^- = \psi_j^{\mathcal{P}+} - \psi_j^{\mathcal{P}-}$. If we were to construct the approximations (4.18) separately in their respective regions $\mathcal{B}^\pm$, with no regard to the relationship between them, then these jump conditions would *not* be precisely satisfied. We enforce the correct jumps by demanding that the difference $\Psi^N - \Psi^{\mathcal{P}}$ is approximated by the smooth field $\Psi^{\mathcal{R}}$,

$$\Psi^N(t,r) - \Psi^{\mathcal{P}}(t,r) = \sum_{j=0}^{n} \psi_j^{\mathcal{R}}(t)(\Delta r)^j + \mathcal{O}(\Delta r^{n+1}). \tag{4.21}$$

This requires choosing the integration domain in Eq. (4.19) to have support in both $\mathcal{B}_+$ and $\mathcal{B}_-$. Taking the inner product of Eq. (4.21) with $(\Delta r)^k$ and discarding higher-order terms, we obtain a linear system for $\psi_j^{\mathcal{R}}$,

$$\sum_{j=0}^{n} A_{jk}\psi_j^{\mathcal{R}}(t) = b_k(t) \qquad \text{for } k = 0, \ldots, n, \tag{4.22}$$

with $A_{jk} = \langle(\Delta r)^j, (\Delta r)^k\rangle$ and $b_k = \langle\Psi^N - \Psi^{\mathcal{P}}, (\Delta r)^k\rangle$. We note that the solution to Eq. (4.22) yields the L^2 best approximation of $\Psi^N - \Psi^{\mathcal{P}}$. Since this equation must hold for all t, it also implies an analogous equation for $\partial_t\psi_j^{\mathcal{R}}$, which is required for a Cauchy evolution.

To enforce the matching condition in a numerical evolution, we can use the following scheme:

1. Suppose that at time t_1, we have data for Ψ^N and $\partial_t\Psi^N$ everywhere outside Γ.

2. Determine the approximate solution $\Psi^A(t_1)$ and $\partial_t\Psi^A(t_1)$ by solving Eq. (4.22) and the analogous equation for $\partial_t\psi_j^{\mathcal{R}}$. We then have Ψ and $\partial_t\Psi$ for all r at time t_1, given by the field values from Step 1 outside Γ and by Ψ^A and $\partial_t\Psi^A$ inside Γ.

3. Use the homogeneous equation, Eq. (3.6) with the right-hand side set to zero, together with the data at t_1 to obtain Ψ^N at a later time t_2 everywhere outside Γ, as illustrated in Fig. 4.12. This requires data from inside Γ at t_1, which is provided by $\Psi^A(t_1, r)$ and $\partial_t\Psi^A(t_1, r)$.

This can then be repeated indefinitely. Note that the time interval from one slice to the next is tied to the length scale of the buffer region. The evolution from t_k to t_{k+1} should only draw upon data for Ψ^A in the buffer region, implying that the time intervals must be of order R or shorter. In principle, this division of spacetime into time intervals need not be associated with one's numerical discretisation, and the spacetime region between t_k and t_{k+1} can be spatially discretised in any convenient way.

Our description here refers to an evolution between slices of constant t, but it extends straightforwardly to any choice of slicing, including particularly the characteristic slicing we work with in Scheme I. In general, the one-dimensional series approximation (4.18) is replaced by a two-dimensional series in powers of coordinate distances (Δt and Δr or Δu and Δv, for example) from a reference point on the worldline. The inner product (4.19) is then replaced by an integral over a two-dimensional region. We can also naturally extend the method to an evolution in $3 + 1$ dimensions by matching to a local approximation in a three- or four-dimensional region around the companion.

One additional aspect of this matching approach that should be noted is that it does not inherently impose any degree of differentiability across $\partial\Gamma_\pm$, except in the limit $n \to \infty$. This contrasts with the matching method we employ in Scheme II.

4.3.1.2 Implementation

In practice, the implementation is a discretised version of the above approach, and the integral in Eq. (4.19) reduces to a summation over discrete data points. With i labelling the discrete data points, Eq. (4.22) becomes

$$\sum_{j=0}^{n} A_{jk}\psi_j^{\mathcal{R}}(t)h = b_k(t)h \qquad \text{for } k = 0, \ldots, n\,, \tag{4.23}$$

with $A_{jk} = \sum_{i=1}^{d} \Delta r_i^j \Delta r_i^k$ and $b_k = \sum_{i=1}^{d} (\Psi_i^N - \Psi_i^{\mathcal{P}})\Delta r_i^k$. The discretisation factor h appears on both sides of Eq. (4.23) and cancels. The number d of data points must be taken to be greater than or equal to the number of unknown coefficients $\psi_j^{\mathcal{R}}$, and the solution to Eq. (4.23) then yields the least-squares polynomial regression of $\Psi_i^N - \Psi_i^{\mathcal{P}}$.

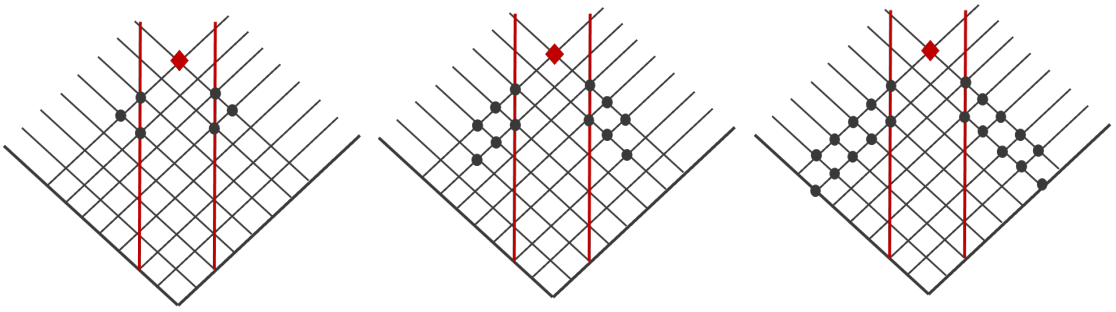

FIGURE 4.13: Data used to fit for the unknown parameters $\psi_{ij}^{\mathcal{R}}$ in the linear, quadratic and cubic-order approximate analytical models ($n = 1, 2$ and 3, left to right respectively). Red vertical lines mark the worldtube's boundaries, and red diamonds mark the location of the particle about which the regular field is expanded in a double Taylor series. Black circles represent the numerically determined field data points used to the fit the parameters $\psi_{ij}^{\mathcal{R}}$ of the analytical model inside the tube, using the procedure described in the text.

The above description assumes (for simplicity) a Cauchy-type evolution, and it needs to be adapted for use in our characteristic evolution setup. In the Cauchy evolution case, the regular field component of the analytical solution is expanded in powers of Δr about the point where the current Cauchy slice intersects the particle's worldline (at the center of the tube; refer again to Fig. 4.12). In our characteristic implementation, we instead choose to expand $\Psi^{\mathcal{R}}(u, v)$ as a double Taylor series in $\Delta u := u - u_p$ and $\Delta v := v - v_p$ about the point of intersection of the two current null slices (u_p, v_p), which in our setup is a point along the particle's worldline at the center of the tube (refer again to the points labelled with red diamonds in Fig. 4.11). The expansion takes the form

$$\Psi^{\mathcal{R}}(u, v) = \sum_{i=0}^{n} \sum_{j=0}^{n-i} \psi_{ij}^{\mathcal{R}} \Delta u^i \Delta v^j, \tag{4.24}$$

where n is the puncture order, and the coefficients $\psi_{ij}^{\mathcal{R}}$ are *a priori* unknown constant coefficients at each time step. There are $N = (n + 1)(n + 2)/2$ such coefficients. The matching conditions in Eq. (4.23) are then replaced with a suitable two-dimensional version, with solutions that are the least-squares 2D polynomial regression model of $\Psi_i^N - \Psi_i^{\mathcal{P}}$ over a 2D array of data points in the u, v plane. For this to work, one must take $d \geq N$, i.e. the number of data points must be greater than or equal to the number of coefficients $\psi_{ij}^{\mathcal{R}}$.

In our particular implementation we choose to take $d = 2N$, i.e. twice as many data points as unknown coefficients. This choice appeared to provide a good balance in the tradeoff between accuracy and runtime. Since, with this choice, the number of data points is always even, it allows us to distribute them evenly and symmetrically on either side of the worldtube. Our choice of data points for the matching, for model orders $n = 1, 2$ and 3, is shown in Fig. 4.13. In all cases, we draw our matching points from the current u, v null rays and from the u, v null rays in the preceding time step (it

is necessary to use data from more than a single time step in order to fit for mixed-derivative coefficients like $\psi^{\mathcal{R}}_{11}$).

With these choices, the matching procedure is as follows. As described already, at each time step we evolve the initial data using successive applications of our finite-difference formula along the corresponding two null rays $u = \text{const}$ and $v = \text{const}$ (such that $v - u = 2r^*_p$) running from the initial null surfaces to the boundaries of the tube. Once this step is completed, we record the d numerical data points Ψ^N_i shown in Fig. 4.13, all of which are known to us from the current or previous steps of the numerical evolution, and then construct the d values $\Psi^N_i - \Psi^{\mathcal{P}}_i$ by subtracting the analytically known puncture values at the corresponding grid points. To these d values we now match the nth-order 2D polynomial given in Eq. (4.24) using a least-square minimisation procedure to obtain the coefficients $\psi^{\mathcal{R}}_{ij}$. This, in turn, determines the regular field $\Psi^{\mathcal{R}}$, and thus also the complete analytical approximation $\Psi^A = \Psi^{\mathcal{R}} + \Psi^{\mathcal{P}}$ inside the worldtube, in the vicinity of the current characteristic rays. We record the values of Ψ^A at the two "ghost" grid points inside the tube adjacent to the boundaries on the current ray (starred points in Fig. 4.11); these two values will be required when calculating the numerical field on the boundary in the next time step. This concludes the computation for the current time step, and we can now step forward in (advance/retarded) time and repeat.

A few comments are in order. First, it may be noticed that in the first few time steps of the evolution there may not be available sufficiently many data points to fit all of the N model parameters. In such cases we simply set to zero the values of the "missing" data points. This does not cause a problem, because the early evolution is in any case dominated by non-physical junk radiation; all this does is modify the profile of the initial junk.

Second, we note that in our procedure we choose not to impose that Ψ^A satisfies the field equation in the tube; if we did, some of the coefficients $\psi^{\mathcal{R}}_{ij}$ would become mutually dependent. For example, in the quadratic model with $n = 2$, imposing the field equation would determine the coefficient $\psi^{\mathcal{R}}_{11}$ in terms $\psi^{\mathcal{R}}_{00}$, $\psi^{\mathcal{R}}_{01}$ and $\psi^{\mathcal{R}}_{10}$. Such an alternative approach is possible, but for simplicity we opt to treat all N coefficients $\psi^{\mathcal{R}}_{ij}$ as independent for the purpose of the matching. By matching Ψ^A to a vacuum solution over an extended region, we guarantee the field equation is satisfied within the tube to the overall order of accuracy of the scheme. We have confirmed numerically that the violation of the field equation appropriately goes to zero with decreasing worldtube size R.

Finally, we comment on the degree of differentiability of our solution on the tube's boundary. As already mentioned, since we are not explicitly imposing continuity of the field or its derivatives at the tube's boundary, there is no reason to expect that the field constructed via our matching procedure should exhibit any level of differentiability there. In practice, for our specific choice of matching data points, we find that the

discrepancy between Ψ^N and Ψ^A, and between their radial derivatives, are numerically small and seem to decrease to zero with h, as expected on theoretical grounds.

4.3.2 Results

4.3.2.1 Static Modes

The scheme is tested with a scalar charge kept fixed at the Schwarzschild coordinate $r = 7M$, using the $\ell = 2, m = 0$ spherical harmonic mode. For initial data we set the field values along the initial rays inside the worldtube to be equal to the puncture field Ψ_P given in Sec. 3.3. Outside the worldtube we again introduce a Gaussian function to smoothly send the field values to zero.

As highlighted, for static modes we can compare our results to the exact analytical solution Ψ_{exact} given in Sec. 3.2. This provides us a baseline against which to compare our worldtube results. One way of doing this is to calculate the absolute and relative error on a late-time slice, as a function of r^*.

The absolute error is calculated by

$$|\Psi - \Psi_{\text{exact}}| \tag{4.25}$$

and the relative error is calculated by

$$\frac{|\Psi - \Psi_{\text{exact}}|}{|\Psi_{\text{exact}}|}. \tag{4.26}$$

4.3.2.2 Radiative Modes

To test the scheme in a radiative mode situation we investigate the $\ell = 2$, $m = 2$ spherical harmonic mode. We use the same type of initial data as in the static mode case. For radiative modes there is no analytical solution against which we can compare the results from our worldtube model. Instead, we remove the worldtube from our characteristic grid and use numerical baseline results obtained from an exposed point particle source of the same ℓ, m mode, as described in Sec. 4.2.1

Agreement between worldtube model results and the point particle solution is again examined by calculating the absolute and relative error on a late time slice. Field values for radiative modes are complex-valued and so we examine the magnitude of the field $|\Psi|$ to avoid zero-crossings.

Figure 4.14 shows the typical profile of the field $\Psi_{\ell m}$ for $\ell = 2$, $m = 0$ and $\ell = 2$, $m = 2$ mode obtained using our excision method, at a slice of constant late time t. We typically evolve the scheme for a coordinate time of $500M$, as we find after this time most of the

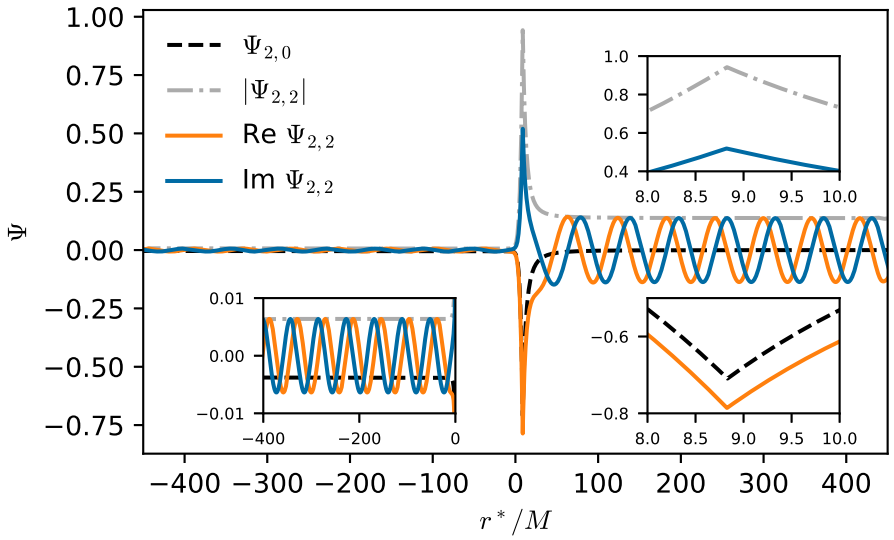

FIGURE 4.14: Solutions to the modal scalar-field Eq (3.6), with a source corresponding to a scalar charge on a circular geodesic orbit of radius $r_p = 7M$ ($r_p^* \approx 8.83M$), obtained using worldtube excision. Shown here are Ψ_{22} and Ψ_{20} as functions of the radial coordinate r^* at $t = 500M$.

junk radiation has sufficiently decayed in all cases. We see that Fig. 4.14 qualitatively recovers all the features of Fig. 4.6 obtained using the point particle code. In Ψ_{22} we see the (i) scalar-field waves (of frequency $m\Omega$) that emanate from the particle and appear in the outer "wave zone", $r^* \gg M$; (ii) scalar-field waves (again of frequency $m\Omega$ but typically of a lower amplitude) going into the black hole, visible at $r^* \ll -M$; and (iii) the cusp in the scalar field at the particle's location, where $\Psi_{\ell m}$ is continuous but has a finite jump in its first radial derivative.

4.3.2.3 Convergence

Our numerical solutions depend on three 'control' parameters: the uniform grid resolution h, the worldtube radius R, and the order n of the analytical model inside the tube. For our numerical convergence tests we use the sequence of values $h = \{0.02, 0.01, 0.005\}M$, fixing the resolution at $h = 0.005M$ for all other tests. The value of R for our various tests is chosen in the interval $[0.0125M, 0.8M]$. In Scheme I we restrict to models with $n = 1, 2, 3$ (while Scheme II extends this to $n = 4, 5$).

Convergence towards our benchmark solution is observed, as expected, when decreasing h, or when decreasing R, or when increasing n (for a sufficiently small R). In what follows we demonstrate, explore and better quantify this behaviour using a range of numerical experiments.

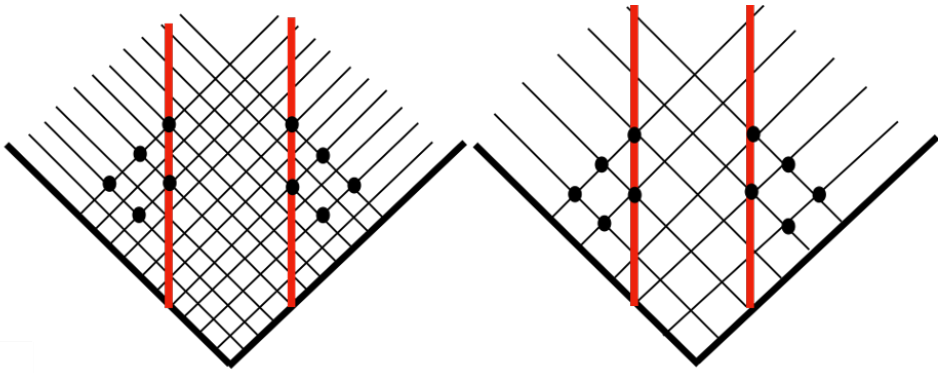

FIGURE 4.15: The numerical data pattern selected to evaluate a model where the approximate analytical solution is taken to quadratic order. The left shows the data points selected for $h = 0.1$, whilst the right shows the data points selected for $h = 0.2$. The number of numerical data points and their physical location is held fixed, independent of the resolution.

4.3.2.4 Convergence with Resolution

We start by examining the convergence of the finite difference scheme with respect to grid resolution h, using a local convergence test. Three runs are performed, with fixed worldtube width R and model order n, and variation of h. Denoting the field computed with resolution h by Ψ_h, we now construct the local convergence index

$$n_h := \log_2 \left| \frac{\Psi_h - \Psi_{\frac{h}{2}}}{\Psi_{\frac{h}{2}} - \Psi_{\frac{h}{4}}} \right| , \tag{4.27}$$

note this is log base 2 of index previously used, to match the convention in Chapter 5. Given our second-order finite difference scheme, this should yield approximately 2 i.e. quadratic-order convergence.

We have a choice in how the array of matching points outside the tube is modified as we vary h. A sensible "like-to-like" comparison is one in which the *physical* position and pattern of the data points around the worldtube is held fixed as h is varied. Figure 4.15 illustrates this choice. Proceeding in this way, our convergence test with a worldtube excision yields $n_h \approx 1$, indicating that the convergence is only linear; see Fig. 4.16. We find this deterioration in convergence rate affects all ℓ, m modes examined (static as well as radiative), and all model orders attempted ($n = 1, 2, 3$). Repeating the test with a sequence of smaller h values does not improve the situation, and the convergence remains linear. However, quadratic convergence is recovered if (for a static mode) we replace the regression model in the tube with the known exact analytical solution. We also recover quadratic convergence if we "freeze" the matched analytical model in the tube as we vary h (i.e. fit the model using one value of h and then apply the same polynomial regression model when running with the other two h values participating in our convergence test).

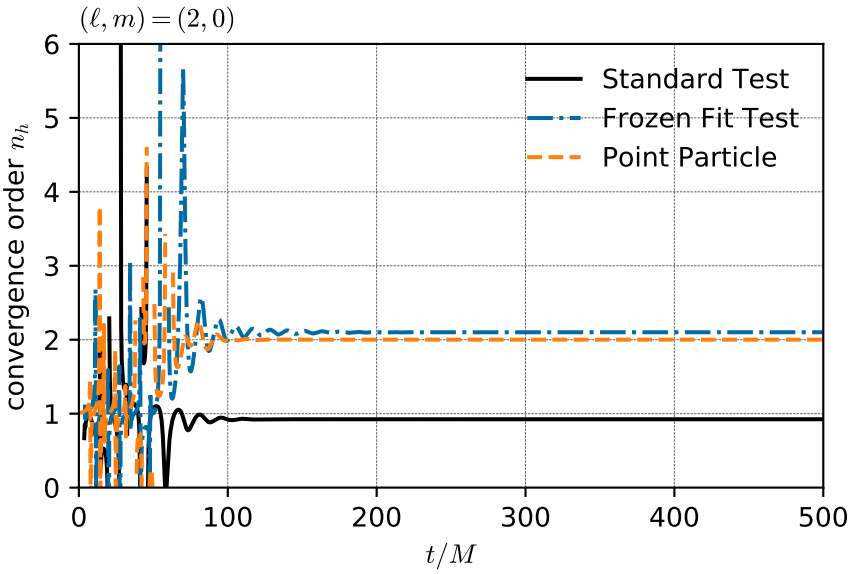

FIGURE 4.16: Convergence of the numerical solution with respect to grid resolution h. Plotted is the convergence index n_h, defined in Eq. (4.27), as a function of t along a slice of constant radius $r^* = 8.93258$ (corresponding to the right boundary of the excision tube). In the "standard" test, the analytical solution in the tube is fitted for afresh for each choice of grid resolution, and the observed steady-state convergence is linear ($n_h \approx 1$). For comparison, when we fix the analytical solution in the tube as we vary h ("frozen fit"), the observed convergence is quadratic ($n_h \approx 2$), as it is for a run with an exposed point particle without a worldtube ("point particle"). The reduction in convergence rate evidently caused by the matching procedure is discussed in the text.

The apparent reduction in convergence rate may be explained as resulting from a coupling between h-related and R-related errors, expected when the approximate analytical model in the tube is allowed to depend on h, as in our convergence test. To understand this, consider that the value of the numerical field at a point x outside the worldtube is a function $\Psi(x; \tilde{h}, \tilde{R}) = \Psi_{\text{exact}}(x) + \delta\Psi(x; \tilde{h}, \tilde{R})$ depending parametrically on both $\tilde{h} := h/m_1$ and $\tilde{R} := R/m_1$ (we ignore here the dependence on n, assumed fixed for the rest of this discussion). For small $\tilde{h}$ and $\tilde{R}$, the error term may be expressed as a double Taylor expansion, $\delta\Psi = \sum_{i,j} a_{ij} \tilde{h}^i \tilde{R}^j$. The terms with $j = 0$ describe the usual discretization error for $R \to 0$ (exposed point particle); we have $a_{00} = 0 = a_{10}$, with the leading term being $a_{20}\tilde{h}^2$ for our quadratically convergent code. The terms with $j \neq 0$ arise from the approximate nature of the analytical solution in the tube. As demonstrated, the leading finite-R error is of $\mathcal{O}(R^n)$, and it is therefore expected to have the form $\delta\Psi \simeq (a_{0n} + a_{1n}\tilde{h} + \cdots)\tilde{R}^n$ in general. When we construct the index n_h in our convergence test, the contribution from the $\propto a_{0n}$ term cancels out, and n_h is dominated by the $\propto a_{1n}$ error term, giving rise to the observed linear convergence in h at fixed R.

The crucial point here is that, in our convergence test, we allow the value of the approximate analytical model on the tube's boundary to depend on h (in a complicated way, via a matching procedure that involves numerical data points that themselves depend on h), and as a result the R-related error also becomes h-dependent. When we freeze

the analytical model (or use the exact analytical solution for it) we decouple between the h-related and R-related errors, and quadratic convergence is recovered.

We note the occurrence of such linear-in-h error terms is not necessarily a weakness of our scheme: in practice, for a particular choice of h and R, the error term $a_{1n}\tilde{h}R^n$ is not necessarily numerically larger than the term $a_{02}\tilde{h}^2$. Rather, the occurrence of a linear term is a somewhat artificial combined feature of the particular matching procedure applied and the particular way the convergence test is designed. The lesson from the above discussion is that one should exercise caution in designing and interpreting convergence tests for a worldtube scheme, being mindful about the potential effect of coupling between finite-difference and worldtube-related sources of error.

4.3.2.5 Convergence with Worldtube Size

It is of greater interest, in the context of this work, to quantify and understand the scaling of our solutions with the tube size R and model error n. Figures 4.17 and 4.18 show how the local finite-R error in our numerical solutions varies as a function of R (at fixed n; top panels) and as a function of n (at fixed R; bottom panels). In Fig. 4.17 we measure the finite-R error by comparing with the exact analytical solution for the static mode $(2, 0)$, and in Fig. 4.18 we measure it by comparing with numerical solutions obtained using our exposed point-particle code. In both cases we display the relative differences as functions of r^* on a late-time $t = \text{const}$ slice.

We see that, as expected, our solutions generally become more accurate as we decrease R or increase n. We note that even with the simplest, linear ($n = 1$) analytical model, and with a tube radius as large as $R = 0.1M$, the worldtube-related error is only around 1% almost uniformly. There is a marked reduction in error at smaller R and larger n, except near the worldtube (at $r^* \approx 9M$ in these figures, too narrow to be resolved), where the error seems to saturate. As we demonstrate further below, the saturation marks the point where finite-difference error becomes dominant over R-related error, so that a further decrease in R (or increase in n) does not lead to a further reduction in overall error. The effect is most pronounced near the worldtube, since the finite-difference error is largest there (where field gradients are largest), while worldtube error (we expect) remains roughly spatially uniform. The effect is exacerbated by the fact that as we decrease R we expose more of the high-gradient region surrounding the particle. To fully demonstrate convergence with R or n near the tube would require a concurrent refinement of resolution there.

Next we examine the convergence rate with respect to R (at fixed n and h). To form our theoretical expectations, consider the error in our method inside the worldtube, Γ, which is introduced through our matching method and independent of any discretisation. In that region we use the approximation Ψ^A, which differs from Ψ by an amount of order

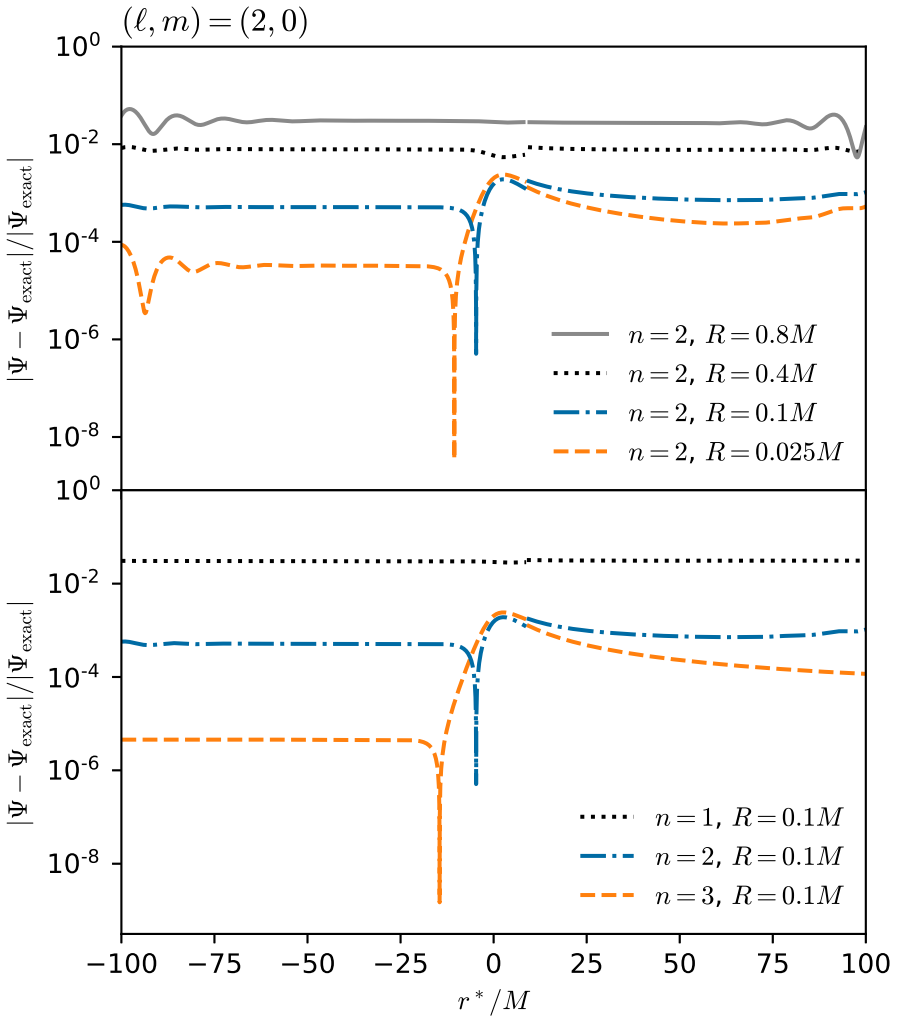

FIGURE 4.17: The relative finite-R error in Ψ_{20} as measured by comparison with the exact analytical solution $\Psi_{\rm exact}$. In the upper panel we vary the tube radius R at fixed model order $n = 2$, and in the lower panel we vary n at fixed $R = 0.1M$. The relative difference is shown on a late-time $t = \text{const}$ slice. The numerical resolution is $h = 0.005M$ in all cases.

$(\Delta r)^{n+1}$ at best. This is a best-case estimate because it assumes that our matching methods enforce the exact values $\frac{1}{j!}\partial_r^j(\Psi - \Psi^{\mathcal{P}})|_{r=r_p}$ for the coefficients $\psi_j^{\mathcal{R}}$ in Eq. (3.17). For simplicity, let us assume this best case.

Now consider the field outside Γ. More concretely, consider a bounded region V with $\partial\Gamma$ as one of its boundaries; in a Cauchy evolution, the other boundaries might be an initial-data surface (outside Γ) and timelike boundaries far away, for example. Inside V, our field Ψ^N satisfies the same homogeneous field equation as Ψ, $\Box\Psi^N = 0$, but it inherits errors that propagate out from Γ. Those errors can be understood by writing Ψ^N in a Kirchhoff integral form [110]. We introduce a retarded Green's function satisfying

$$\Box G(\boldsymbol{x}, \boldsymbol{x}') = \Box' G(\boldsymbol{x}, \boldsymbol{x}') = \delta^2(\boldsymbol{x}, \boldsymbol{x}')\,, \tag{4.28}$$

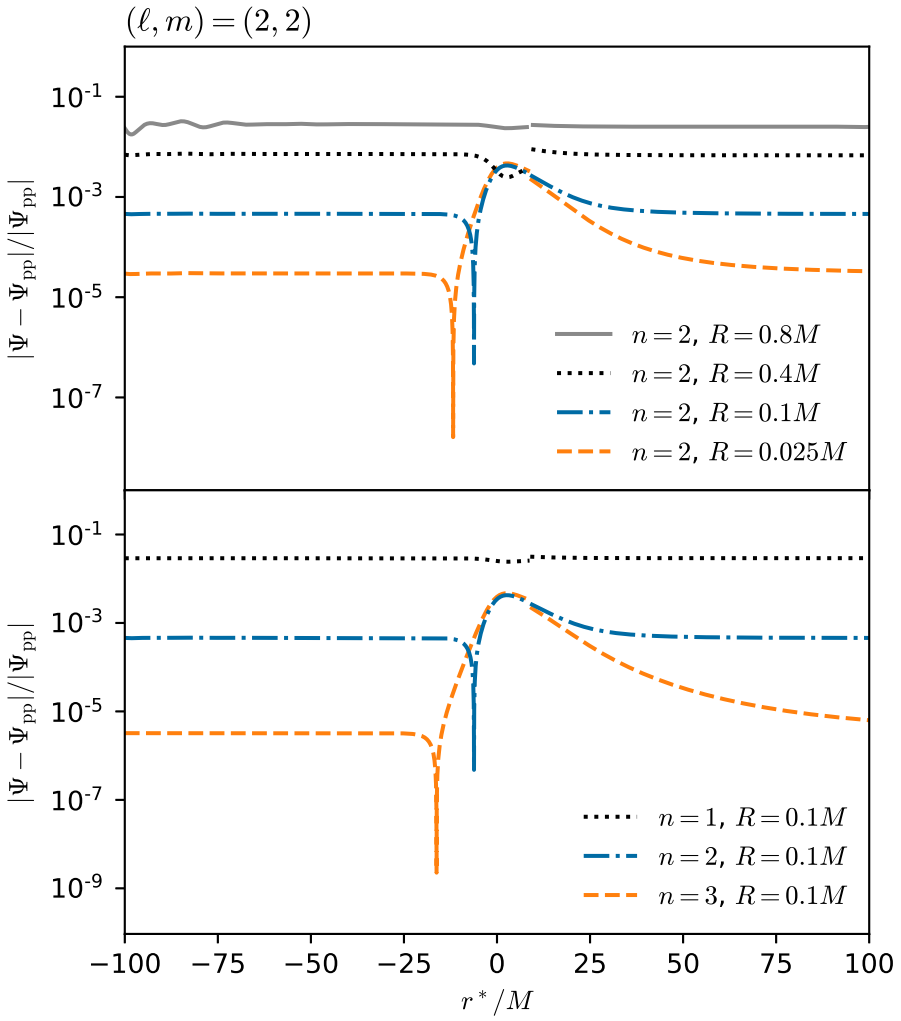

FIGURE 4.18: The relative finite-R error in Ψ_{22} as measured by comparison with the (accurate) numerical solution from our point-particle code, denoted $\Psi_{\rm pp}$. The format of this plot and all other details are as in Fig. 4.17.

where $\boldsymbol{x} = (t, r^*)$, $\Box' := \partial_{t'}^2 - \partial_{r'*}^2 + V(r')$, and $\delta^2(\boldsymbol{x}, \boldsymbol{x}') := \delta(t - t')\delta(r^* - r'^*)$. If we now take any point $\boldsymbol{x} \in V$, then Eq. (4.28) and $\Box\Psi^N = 0$ imply the identity

$$\Psi^N(\boldsymbol{x}')\Box' G(\boldsymbol{x}, \boldsymbol{x}') - G(\boldsymbol{x}, \boldsymbol{x}')\Box'\Psi^N(\boldsymbol{x}') = \Psi^N(\boldsymbol{x}')\delta^2(\boldsymbol{x}, \boldsymbol{x}'). \tag{4.29}$$

Integrating this equation over all $\boldsymbol{x}' \in V$ and then using integration by parts, we obtain the Kirchhoff representation

$$\begin{aligned}\Psi^N(\boldsymbol{x}) &= \int_V \big[\Psi^N(\boldsymbol{x}')\Box' G(\boldsymbol{x}, \boldsymbol{x}') \\ &\qquad - G(\boldsymbol{x}, \boldsymbol{x}')\Box'\Psi^N(\boldsymbol{x}')\big]\, d^2x' \,, \\ &= \int_{\partial V} \big[\Psi^N(\boldsymbol{x}')\partial_{n'} G(\boldsymbol{x}, \boldsymbol{x}') \\ &\qquad - G(\boldsymbol{x}, \boldsymbol{x}')\partial_{n'}\Psi^N(\boldsymbol{x}')\big]\, ds' \,.\end{aligned} \tag{4.30}$$

Here the coordinate area element in V is $d^2x' = dt'dr'^*$. $\partial_{n'}$ is the partial derivative normal to the boundary ∂V, and ds' is the coordinate line element on the boundary. For us the relevant portions of ∂V are the worldtube boundaries $\partial\Gamma_\pm$, where $\partial_{n'} = \mp\partial_{r'^*}$ and $ds' = dt'$.

From the Kirchhoff form, we see that Ψ^N inherits two errors, respectively proportional to the errors in $\Psi^N|_{\partial\Gamma}$ and $\partial_{r^*}\Psi^N|_{\partial\Gamma}$. Suppose that $\Psi^N = \Psi^A + \mathcal{O}(|\Delta r|^{n+1})$ in an open neighbourhood of $\partial\Gamma$, as we seek to enforce in our first matching approach. Then $\Psi^N|_{\partial\Gamma}$ has an error of order R^{n+1}, but $\partial_{r^*}\Psi^N|_{\partial\Gamma}$ has an error of order R^n. The field Ψ^N therefore differs from Ψ by $\mathcal{O}(R^n)$ throughout V. This represents a loss of one order relative to the $\mathcal{O}(R^{n+1})$ scaling that one might naively expect.

Analogous error estimates can be obtained for the 3+1D problem using a covariant Kirchhoff representation of the form Eq. (138) in [116]. A similar estimation might also be possible in fully nonlinear general relativity using Eq. (39) in [116].

To quantity the convergence rate and test the above theory we construct the index

$$n_R = \log_2 \left| \frac{\Psi_R - \Psi_{\frac{R}{2}}}{\Psi_{\frac{R}{2}} - \Psi_{\frac{R}{4}}} \right| , \tag{4.31}$$

where $\Psi_{R'}$ represents the value of the field calculated with a tube radius $R = R'$. This measures the internal convergence of the numerical solution as we decrease R (as opposed to convergence to the exact solution, illustrated in Figs. 4.17 and 4.18). Figure 4.19 shows n_R as a function of t along an $r = \text{const}$ slice. We observe $n_R \approx n$, indicating that the dominant tube-related error is of $\mathcal{O}(R^n)$—precisely as predicted.

So far we have been considering "local" measures of error, ones depending on location and time. It is also informative to examine a global error norm, which we now introduce and adopt for the rest of our analysis here and in Scheme II. We denote by $||\Psi||_{L^1}$ the L^1 norm of a numerical field Ψ evaluated on a $t = \text{const}$ slice. The numerical data points for this norm are sampled uniformly in r^* in the domain $[-100M, r_p^* - R] \cup [r_p^* + R, 100M]$. When comparing norms corresponding to runs with different R values, the largest of the R values is used for all norms.

The top panel in Fig. 4.20 shows the value of the relative error norm

$$\frac{||\Psi - \Psi_{\text{exact}}||_{L^1}}{||\Psi_{\text{exact}}||_{L^1}} \tag{4.32}$$

as a function of R for the static mode $(2, 0)$, with Ψ_{exact} being the exact analytical solution. We see that the error norm decreases with increasing model order n and decreasing tube size R, but for $n = 2, 3$ it seems to saturate at small R. This behavior is consistent with what we saw in Figs. 4.17 and 4.18: when the worldtube error magnitude falls below that of the discretization error, a further reduction in tube size does not

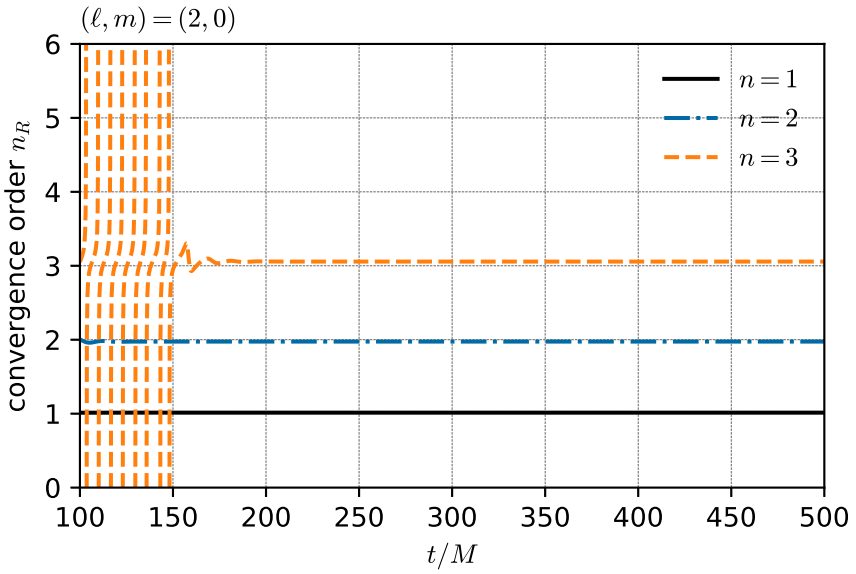

FIGURE 4.19: Convergence of the numerical solution with respect to worldtube radius R, at fixed model order n and resolution $h(= 0.005M)$. We plot the internal convergence index n_R, defined in Eq. (4.31), as a function of t along a fixed radius of $r^* = 8.93258M$. To obtain n_R (for each model order n) we carry out three runs with $R = 0.1M$, $0.05M$ and $0.025M$. After the decay of initial junk, the convergence index appears to be $n_R \approx n$, indicating that the dominant tube-related error is of $\mathcal{O}(R^n)$.

improve the accuracy of the solution. This explanation is further supported by the data shown in the lower panel of Fig. 4.20, where we display the *internal* error norm $||\Psi_R - \Psi_{R/2}||_{L^1}/|\Psi_{R/2}||_{L^1}$. Here we see a monotonic convergence with R at a constant rate even for $n = 2, 3$; the field norm converges to a value that differs slightly from $||\Psi_{\rm exact}||_{L^1}$ due to the dominating h-related error.

To quantify the rate of convergence of the global norm with R, we introduce the convergence index

$$n_R^{(\rm norm)} := \log_2 \frac{||\Psi_R - \Psi_{\frac{R}{2}}||_{L^1}}{||\Psi_{\frac{R}{2}} - \Psi_{\frac{R}{4}}||_{L^1}}\,, \tag{4.33}$$

plotted in Fig. 4.21. Again we observe $n_R^{(\rm norm)} \approx n$; i.e. the tube-related error is $\mathcal{O}(R^n)$ also as measured by the global L^1 norm. Similar results are obtained for other ℓ, m modes.

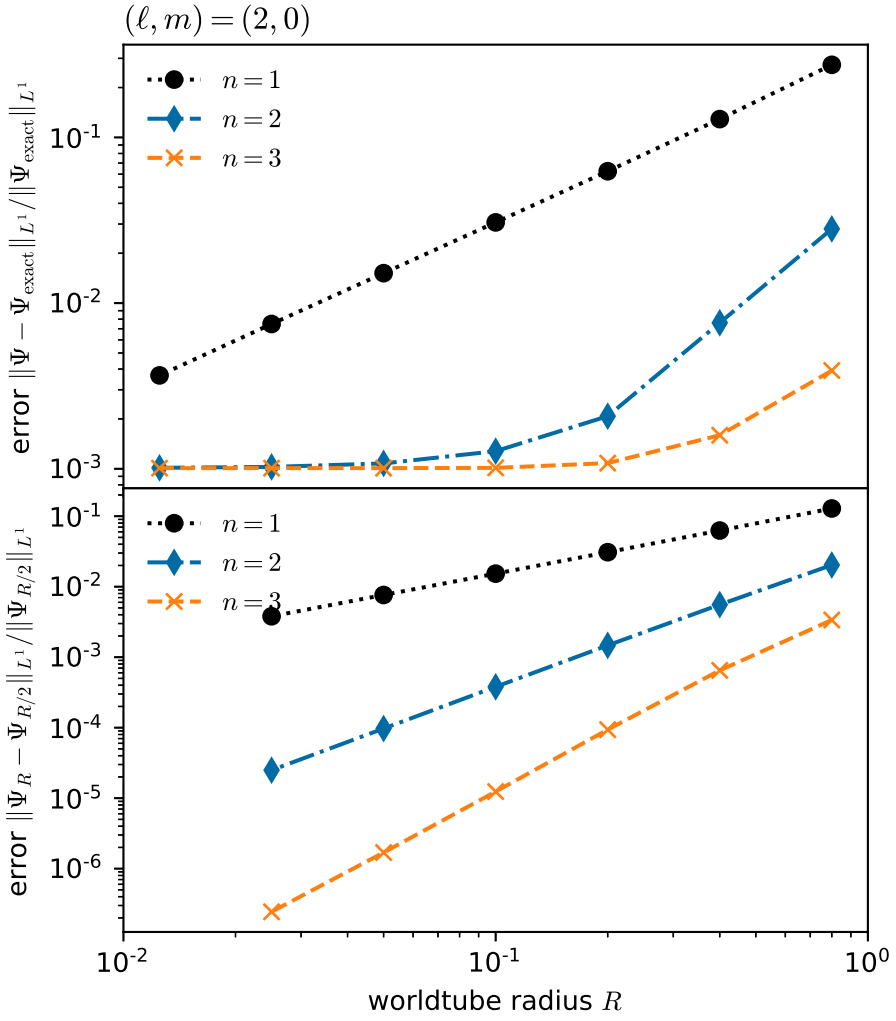

FIGURE 4.20: Top panel: Relative L^1 error norm with respect to the exact analytical solution, as a function of worldtube radius R. Bottom panel: Internal relative error norm calculated by varying R. In both cases the finite-difference resolution is held fixed at $h = 0.005$. The saturation of error in the upper panel is due to the finite-difference error becoming dominant at small R.

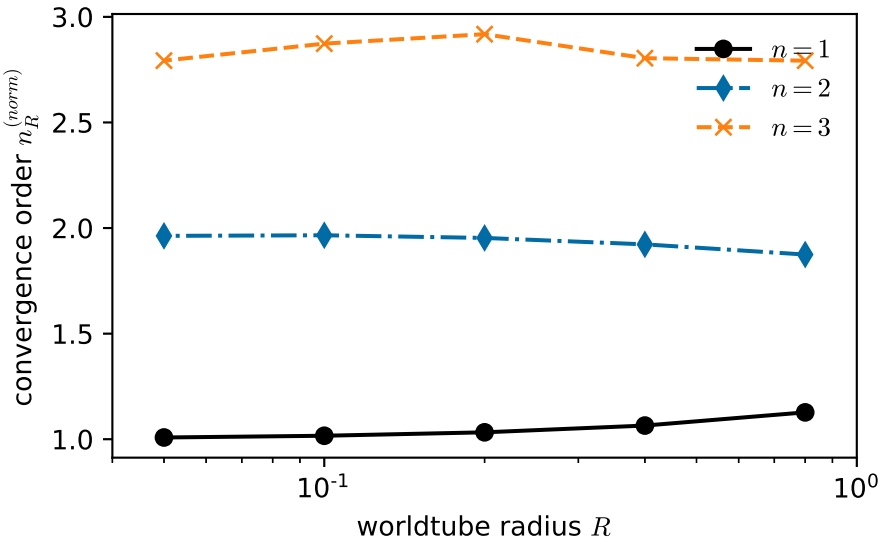

FIGURE 4.21: Convergence of the L^1 error norm with respect to R, at fixed order n and resolution $h(= 0.005M)$. We plot the internal convergence index $n_R^{(\mathrm{norm})}$, defined in Eq. (4.33), and observe $n_R^{(\mathrm{norm})} \approx n$. Thus the worldtube error scales like $\sim R^n$.

Chapter 5

1+1D Scalar-Field Model: Scheme II

This chapter presents a second 1+1D scalar-field toy model, "Scheme II". Here we use spectral methods for the numerical evolution and treat the worldtube boundaries as a strict interfaces, using data on these surfaces only to perform the matching. This implementation provides us another testbed in which to trial our worldtube excision method, whose architecture now more closely resembles the setup that will be used in the BBH model.

5.1 Setup

Scheme II comprises of a spectral numerical method based on a Cauchy evolution in (t, r^*) coordinates. Such Cauchy evolutions are standard in NR and the ADM formulation of the Einstein Field Equations [25], and so we adopt this structure in order to move closer to the setup of the BBH model. Here the boundaries of the Schwarzschild exterior are timelike surfaces and so are in causal contact with the evolution domain and will require well-formulated boundary conditions. The particle is again at $r = 7M, r^* \approx 8.8M$, and the initial time-slice is set with the coordinate value $t = 0$. Initial data for the field must be specified on the $t = 0$ slice, and various choices can be made. These include setting the field entirely to zero, using a Gaussian wave packet as in Scheme I, or using the exact analytical solution (Eq. (3.13)) if working with a static mode. This last choice minimizes the amplitude of the resulting transient junk data that propagates outwards over the course of the numerical evolution.

5.1.1 Numerical Method

5.1.1.1 Foundations of Spectral Methods

Before proceeding to explain the numerical details of the evolution in Scheme II, a very brief overview of spectral methods will be given. The overarching idea of a spectral method is to approximate a function by polynomials. A function u will be approximated by

$$u(x) \approx \hat{u}^N(x) = \sum_{n=0}^{N} \hat{u}_n \Phi_n(x), \tag{5.1}$$

where $\hat{u}(x)$ are coefficients and $\Phi_n(x)$ are the chosen polynomials. In finite difference schemes $\Phi_n(x)$ are often local polynomials of a low degree. In contrast, in spectral methods $\Phi_n(x)$ are global polynomials and contributions from the higher order basis functions $\Phi_n(x)$ decrease quickly with n.

In spectral methods, the chosen polynomials must constitute an orthogonal set on $[-1, 1]$, and common choices are Legendre or Chebyshev polynomials. The chosen polynomials are also referred to as the chosen set of basis functions. A benefit of spectral methods is that the derivatives of the polynomial basis functions $\Phi_n(x)$ are known analytically. The derivatives of $\hat{u}^N(x)$ can then be calculated exactly using

$$\frac{d\hat{u}^N(x)}{dx} = \sum_{n=0}^{N} \hat{u}_n \frac{d\Phi_n(x)}{dx}. \tag{5.2}$$

Spectral methods converge exponentially with N, so long as the function being approximated is $\mathcal{C}^\infty$. Finite difference methods, on the other hand, only converge with some low power of N. Therefore, spectral methods often reach a much higher accuracy with lower computational resources than achieved by finite difference methods.

However, spectral methods are usually more complicated to implement than finite difference methods, and, as they make use of global polynomials (and so information from the entire numerical domain), they are far more affected by the presence of boundaries [69, 70]. Scheme II requires well-formulated boundary conditions at the key interfaces of the domain, namely, the standard spectral element boundaries, the outer domain boundaries and the worldtube boundaries. In Scheme II we choose to treat the worldtube boundary as a strict interface. We can therefore import existing methods of transporting information between spectral elements at this junction. Our chosen boundary conditions are that of the Penalty method [78] and the Bjørhus method [44]. Details of these are given in Sec. 5.2.1.2.

5.1.1.2 Our Spectral Method

We evolve the scalar field in Schwarzschild time t using the classic fourth-order Runge–Kutta method [161] on the spatial domain $[-300M, 300M] \setminus \Gamma$, where the worldtube Γ is centered on the position r_p^* of the particle. The spatial domain is divided into a set of spectral elements. On each element, field values are expanded into a series of basis polynomials and on every element the series is truncated at the same order. For the results presented here, Chebyshev polynomials are used as the spectral basis and the grid is collocated on Chebyshev-Gauss-Lobatto points. Further details on this aspect of the numerical evolution can be found in [85], which we mostly followed for our code.

For the evolution of the system to be stable, the time step has to satisfy a CFL condition, where the relevant length interval is given by the minimal interval $\Delta r^*_{\rm min}$ between collocation (grid) points. Henceforth we choose the time step to be $\Delta t = c_{\rm CFL}\Delta r^*_{\rm min}$. The constant $c_{\rm CFL}$ is set to 0.5 for static setups ($m = 0$ modes), whereas for the evolution of radiative modes we chose $c_{\rm CFL} = 0.25$, which we have checked to be sufficiently small for the results in our setups to converge with respect to Δt.

For radiative modes it is important to treat the phase factor $e^{-im\Omega t}$, which is implicit in $S_{\ell m}(t)$ in Eq. (3.15), with high numerical precision. Because of the high precision of the spectral scheme, we are sensitive to machine round-off in the argument of the phase factor. If we were to use the total time t, the round-off error would grow linearly with t and thus affect the precision of the phase factor as well. Instead we use an approach where after every time step Δt we multiply the phase factor by $e^{-im\Omega\Delta t}$ to update it for the next time step, and normalise the result such that the norm of the phase factor remains exactly 1. Furthermore, we use quadruple precision in evaluating the evolution time. We find this necessary to ensure that our convergence tests are not limited by round-off error in the time at which different configurations are compared.

5.2 Evolution with a Worldtube

5.2.1 Matching Method

Our second approach consists of matching the field and its derivatives on the surface of the worldtube. As in the first approach, the regular part $\Psi^{\mathcal{R}}$ is a truncated Taylor series in Δr^*

$$\Psi^{\mathcal{R}}(t, r^*) = \sum_{j=0}^{2d+1} \psi_j^{\mathcal{R}}(t)(\Delta r^*)^j \tag{5.3}$$

where $2d + 1$ is our chosen order of expansion. The expansion order of $\Psi^{\mathcal{R}}$ jumps by two and is always odd, for reasons which will become clear below.

In order to determine the coefficients we now treat the Taylor series for $\Psi^{\mathcal{R}}$ as a Hermite interpolation of the field $\Psi^N - \Psi^{\mathcal{P}}$. (We now drop the explicit (t, r^*) dependence of the field for brevity.) Concretely, we equate the values of the field and its first d derivatives on both the worldtube boundaries $\partial\Gamma_-$ and $\partial\Gamma_+$ at each timestep (see Fig. 4.12). We then solve the system

$$\partial_{r^*}^k \left(\Psi^N - \Psi^{\mathcal{P}} - \sum_{j=0}^{2d+1} \psi_j^{\mathcal{R}} (\Delta r^*)^j \right) \Bigg|_{\partial\Gamma_\pm} = 0, \qquad \text{for } k = 0, \ldots, d\,, \tag{5.4}$$

which is a system of $(2d + 2)$ linear equations for the $(2d + 2)$ coefficients $\psi_j^{\mathcal{R}}$. It is for this reason that in Scheme II we restrict to odd-$n_{\mathcal{R}}$ models. Unlike in the previous scheme, here we take the expansion order of the puncture field, $n_{\mathcal{P}}$, and that of the regular field, $n_{\mathcal{R}} = 2d + 1$, as independent. The overall convergence of the scheme with respect to R is hence limited by both $n_{\mathcal{P}}$ and $n_{\mathcal{R}}$. This will allow us to explore the effect of independently varying the accuracy of the puncture field and the regular field.

The matched analytical solution ($\Psi^A = \Psi^{\mathcal{P}} + \Psi^{\mathcal{R}}$) is then required to construct the boundary conditions, which are implemented as modifications to the partial differential equations (PDEs) in the numerical domain (henceforth referred to as in "the bulk"). We assume these PDEs are strongly hyperbolic, as is the case for our wave equation toy model. The system remains well-posed if the boundary conditions retain strong hyperbolicity [104]. This means ensuring the principal part (i.e. the second-derivative terms) of the wave equation remains unchanged. As such the coefficients $\psi_j^{\mathcal{R}}$ of the series expansion can only be constructed from non-principal derivatives of Ψ^N.

At first sight this may seem to severely limit the achievable expansion order, because we can use at most up to first derivatives of Ψ^N. This limitation can be overcome by introducing an auxiliary system of ODEs, evolving independent variables that represent the restriction of the field and its derivatives to the worldtube boundary. In practice, the coefficients $\psi_j^{\mathcal{R}}$ are then computed using *these* auxiliary variables, denoted $\tilde{\Psi}^N(t)$, instead of data directly from the bulk PDEs, $\Psi^N(t, r^*)$.

5.2.1.1 Implementation

By introducing the new variables

$$\pi := \partial_t \Psi\,, \tag{5.5}$$

$$\chi := \partial_{r^*} \Psi\,, \tag{5.6}$$

we can reduce the evolution equation (3.6) in the vacuum region outside the worldtube to the first-order system

$$\partial_t \Psi = \pi \,, \tag{5.7a}$$
$$\partial_t \pi = \partial_{r^*} \chi - V \Psi \,, \tag{5.7b}$$
$$\partial_t \chi = \partial_{r^*} \pi + \kappa (\partial_{r^*} \Psi - \chi) \,, \tag{5.7c}$$

where κ is a constraint damping parameter controlling how strongly violations of the constraint in Eq. (5.6) are damped. Ref. [81] provides further details on constraint damping. In practice we chose $\kappa = 1$ for all the results presented for this scheme. In Eqs. (5.6)-(5.7) we have omitted the superscript N on the fields for brevity, but it is to be understood that these are the numerical fields.

The next stage is to introduce the auxiliary variables $\tilde{\Psi}(t)$, $\tilde{\pi}(t)$, $\tilde{\chi}(t)$, mentioned above. In what follows we explain the method as it applies in the case of $n_{\mathcal{P}} = n_{\mathcal{R}} = 1$ for simplicity, though the generalisation to higher order is straightforward.

Let us assume that the values of the auxiliary variables are known at a given timestep, as is the puncture field $\Psi^{\mathcal{P}}$ to order $n_{\mathcal{P}} = 1$ and its analytical derivatives, $\pi^{\mathcal{P}}$ and $\chi^{\mathcal{P}}$. We now wish to calculate the auxiliary variables at the next timestep. To this end we solve for $\Psi^{\mathcal{R}}$ to leading order, evaluating

$$\left(\tilde{\Psi}^N - \Psi^{\mathcal{P}} - \psi_0^{\mathcal{R}} - \psi_1^{\mathcal{R}} \Delta r^* \right) |_{\partial \Gamma_\pm} = 0, \tag{5.8}$$

which is the reduction of Eq. (5.4) to the case of $n_{\mathcal{R}} = 1$. This is repeated analogously for the π and χ variables. At this timestep we can subsequently form the analytical solution for each variable: $\Psi^A = \Psi^{\mathcal{P}} + \Psi^{\mathcal{R}}$, $\pi^A = \pi^{\mathcal{P}} + \pi^{\mathcal{R}}$ and $\chi^A = \chi^{\mathcal{P}} + \chi^{\mathcal{R}}$.

The evolution of these auxiliary fields is then determined by solving a set of ODEs along $\partial\Gamma$, obtained from the restriction of Eqs. (5.7) to the boundary:

$$\partial_t \tilde{\Psi} \stackrel{\triangle}{=} \tilde{\pi} \,, \tag{5.9a}$$
$$\partial_t \tilde{\pi} \stackrel{\triangle}{=} \tilde{\chi}' - V \tilde{\Psi} \,, \tag{5.9b}$$
$$\partial_t \tilde{\chi} \stackrel{\triangle}{=} \tilde{\pi}' + \kappa (\tilde{\Psi}' - \tilde{\chi}) \,, \tag{5.9c}$$

where $\stackrel{\triangle}{=}$ denotes equality on Γ. At this timestep we know the values of $\tilde{\Psi}$, $\tilde{\pi}$, $\tilde{\chi}$, however $\tilde{\Psi}'$, $\tilde{\pi}'$, $\tilde{\chi}'$ remain unknown. To close the set of equations we then replace these variables with derivatives of the analytical solution that has just been computed:

$$\partial_t \tilde{\Psi} \stackrel{\triangle}{=} \tilde{\pi} \,, \tag{5.10a}$$
$$\partial_t \tilde{\pi} \stackrel{\triangle}{=} \partial_{r*} \chi^A - V \partial_{r*} \Psi^A \,, \tag{5.10b}$$
$$\partial_t \tilde{\chi} \stackrel{\triangle}{=} \tilde{\partial}_{r*} \pi^A + \kappa (\tilde{\partial}_{r*} \Psi^A - \tilde{\chi}) \,. \tag{5.10c}$$

This replacement has converted the set of partial differential equations in (5.7) into a set of ordinary differential equations for the auxiliary variables. We can then numerically evolve these using the RK4 stepper to find $\tilde{\Psi}, \tilde{\pi}, \tilde{\chi}$ at the next timestep. The process then repeats from Eq. (5.8).

The auxiliary system can be extended to arbitrary derivatives by taking sufficiently many derivatives of the field equations. Such extensions allow us to fit for a higher order analytical solution. In order to match for $\Psi^{\mathcal{R}}$ up to $n_{\mathcal{R}} = 5$ we require the introduction of the further auxiliary variables $\tilde{\Psi}', \tilde{\Psi}'', \tilde{\pi}', \tilde{\pi}'', \tilde{\chi}', \tilde{\chi}''$. Again we assume all auxiliary variables are known at the given timestep, along with the puncture field $\Psi^{\mathcal{P}}$ to $n_{\mathcal{P}} = 5$. We are then able to solve for $\Psi^{\mathcal{R}}$ up to $j = 5$ using

$$\partial_{r^*}^k \left(\tilde{\Psi}^N - \Psi^{\mathcal{P}} - \sum_{j=0}^{5} \psi_j^{\mathcal{R}} (\Delta r^*)^j \right) \Bigg|_{\partial\Gamma_\pm} = 0, \qquad \text{for } k = 0, 1, 2 \tag{5.11}$$

and analogously for the π and χ variables. Our closed set of ODEs for the auxiliary variables then becomes Eqs. (5.9) along with

$$\partial_t \tilde{\Psi}' \triangleq \tilde{\pi}' \,, \tag{5.12a}$$
$$\partial_t \tilde{\pi}' \triangleq \tilde{\chi}'' - \tilde{\Psi} \partial_{r^*} - V \tilde{\Psi}' \,, \tag{5.12b}$$
$$\partial_t \tilde{\chi}' \triangleq \tilde{\pi}'' + \kappa (\tilde{\Psi}'' - \tilde{\chi}') \,, \tag{5.12c}$$

$$\partial_t \tilde{\Psi}'' \triangleq \tilde{\pi}'' \,, \tag{5.13a}$$
$$\partial_t \tilde{\pi}'' \triangleq \partial_{r^*}^3 \chi^A - \tilde{\Psi} \partial_{r^*}^2 V - 2 \tilde{\Psi}' \partial_{r^*} V - V \tilde{\Psi}'' \,, \tag{5.13b}$$
$$\partial_t \tilde{\chi}'' \triangleq \partial_{r^*}^3 \pi^A + \kappa (\partial_{r^*}^3 \Psi^A - \tilde{\chi}'') \,. \tag{5.13c}$$

Note that we have closed the system by replacing the highest (in this case the third) derivatives with the analytical fields. Just as in the $n_{\mathcal{R}}$ system, we then numerically evolve using the RK4 stepper to find $\tilde{\Psi}, \tilde{\Psi}', \tilde{\Psi}'', \tilde{\pi}, \tilde{\pi}', \tilde{\pi}'', \tilde{\chi}, \tilde{\chi}', \tilde{\chi}''$ at the next timestep and the process repeats.

5.2.1.2 Boundary Treatment

Boundary conditions must be provided in three cases: i) at the interfaces between standard neighbouring elements, ii) on the outer boundaries of the computational domain, and iii) on the excision boundary $\partial\Gamma$. These conditions are implemented by introducing what are known as *characteristic variables*, u^0 and $u^\pm$, which are constructed from linear combinations of Ψ, π and χ. The variable u^0 represents the static mode, while the

variables u^+ and u^- are derivatives of Ψ in the incoming and outgoing null directions, respectively (see Sec.VI.B. of [58] for precise definitions).

Standard Neighbouring Elements

In order to impose boundary conditions at element boundaries, we modify the time derivatives of the incoming characteristic variables at the boundary points. The time derivative of the incoming characteristic field $\hat{u}^+$ are modified in two ways, dependent on the boundary type. At standard spectral element boundaries, we employ the penalty method, in which we replace all time derivatives according to

$$\partial_t \hat{u}^+ \to \partial_t \hat{u}^+ + \lambda(\hat{u}^- - \hat{u}^+). \tag{5.14}$$

We take the λ parameter to be as in [78]. This addition of a penalty term, $\lambda(\hat{u}^- - \hat{u}^+)$, ensures that the evolution converges towards the desired continuous solution, with discontinuities exponentially suppressed in a dynamical fashion.

Outer Domain Boundaries

At outer domain boundaries and on the worldtube boundary we found that a modified penalty method, known as the Bjørhus method works better. In this method we replace all time derivatives according to

$$\partial_t \hat{u}^+ \to \partial_t \hat{u}^+ - \lambda(\partial_{r^*} \hat{u}^+ - g). \tag{5.15}$$

The term g models the expression for $\partial_{r^*}\hat{u}^+$ that one desires to impose at the boundary. The physical purpose of this damping term is the same as in penalty method, namely to ensure convergence towards the desired continuous solution.

At the outer boundaries, for the radiative modes we find that for large r^* the characteristic variables behave like $\hat{u}^+ - \kappa\Psi \sim \exp[im\Omega(r^* - t)]/{r^*}^2$, and so we impose

$$g = \left(-\frac{2}{r} + im\Omega\right)(\pi + \chi) + \kappa\chi\,. \tag{5.16}$$

On the other hand, near the horizon the characteristic variables behave like $\hat{u}^+ - \kappa\Psi \sim \exp(im\Omega(-r^* - t))$, and so we impose

$$g = -im\Omega(\pi + \chi) + \kappa\chi\,. \tag{5.17}$$

We find these choices minimise numerical reflection at the outer boundaries and ensure stability of the evolution.

Worldtube Boundaries

On the excision boundary, our choice for g is

$$g = \partial_{r^*}(\pi^A + \chi^A + \kappa\Psi^A)\,. \tag{5.18}$$

where Ψ^A, π^A, χ^A are the matched analytical fields evaluated at the radial position of the boundary. This allows us to couple the auxiliary ODEs to the bulk PDEs.

One also needs a way of communicating information back from the bulk into the auxiliary system. This is practically implemented by introducing a fiducial element within the worldtube, such that the auxiliary system can be treated on the same footing with the spectral method. In the fiducial element we collocate grid points, again employing a Chebyshev-Gauss-Lobatto [85] collocation scheme. We require a spectral collocation of sufficiently high polynomial order to enable satisfying the boundary conditions for all auxiliary variables.

We can now employ the same technique as before when imposing boundary conditions, i.e. we modify each block of the boundary ODEs with Eq. (5.15), where we choose g to be

$$g = (\partial_{r^*}\pi + \partial_{r^*}\chi + \kappa\chi)\,. \tag{5.19}$$

Here Ψ, π, χ are the numerical fields evaluated at the position of the boundary. The system generalises in an obvious way to higher orders by taking higher and higher derivatives in r^*.

5.2.2 Results

5.2.2.1 Static Modes

We first test the scheme for the static mode $\ell = 2, m = 0$, with the scalar charge on a fixed circular geodesic orbit with $r_p = 7M$. As initial data for the evolution, the static analytical solution (Eq. (3.13)) is used. The transition from the analytical initial data to the numerical static solution causes transient radiation propagating off the numerical domain, with a small partial reflection at the outer domain boundaries. After a coordinate time of $t \sim 5000M$ the transient radiation has decayed, and the numerical data at this time is taken as the representation of the numerical static solution.

Figure 5.1 shows the relative difference between the numerical and analytic solution. The results show errors on the scale of 10^{-10} for a fifth-order model, ($n_{\mathcal{P}} = n_{\mathcal{R}} = 5$), with $R = 0.1$ and 15 collocation points per element. The small differences are amplified at large r^*, because they are normalised by the solution, which approaches zero in this limit. The data shows that the numerical solution does not settle down completely, but that there remains some residual numerical noise propagating on the grid, which can be

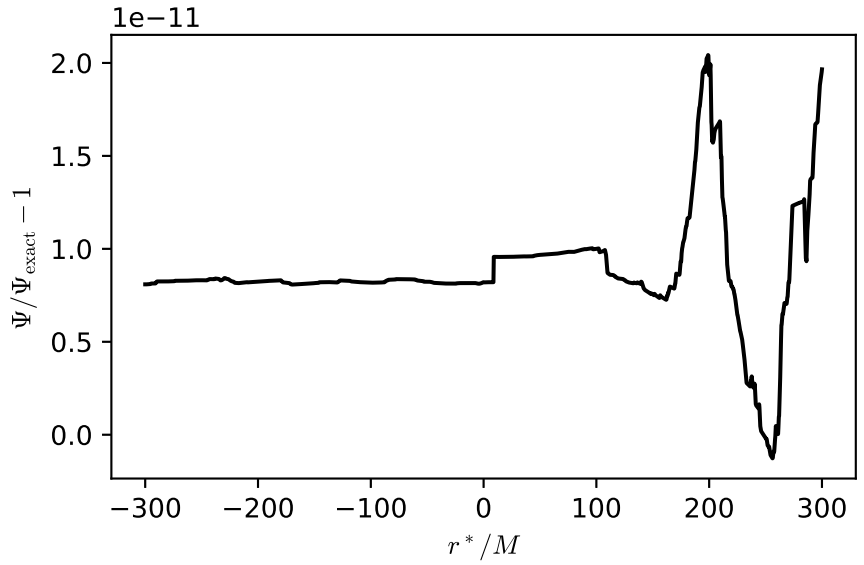

FIGURE 5.1: Relative error of the Ψ_{20} mode for 15 points per element using the 5th order expansions for the puncture and regular field, and a worldtube radius of $R = 0.1$.

attributed to the finite machine precision. The numerical scheme has also been tested with different initial data and found to settle to the same static solution. However, in these cases the transient radiation has a larger amplitude and so takes longer to decay.

5.2.2.2 Radiative Modes

To test the convergence with R in a non-static situation, we investigate the $\ell = 4, m = 4$ mode, with the charge again being fixed at $r_p = 7M$. For these modes there is no known analytical solution, and so we choose to start with zero initial data, i.e. $\Psi = 0, \dot{\Psi} = \pi = 0$. As in the static case, there is some transient radiation that is radiated away until the system settles down to a stationary state. The presence of this junk radiation is partially obscured by the periodic changes in Ψ, but it can be observed when looking at $|\Psi|$.

We calculate the relative errors for radiative modes by comparing two runs that differ in worldtube size by a factor of two, i.e. an internal comparison. Figure 5.2 shows the estimated relative error for the highest resolution used in our results. It can be observed that the error on the left side of the particle is dominated by numerical noise, whereas on the right the difference between the two runs looks smooth and is modulated by the periodic waveform of the signal. The noise on the left side can be attributed to an insufficient resolution, which is amplified by the relatively small modulus $|\Psi|$ in that area; cf. Fig. 4.14.

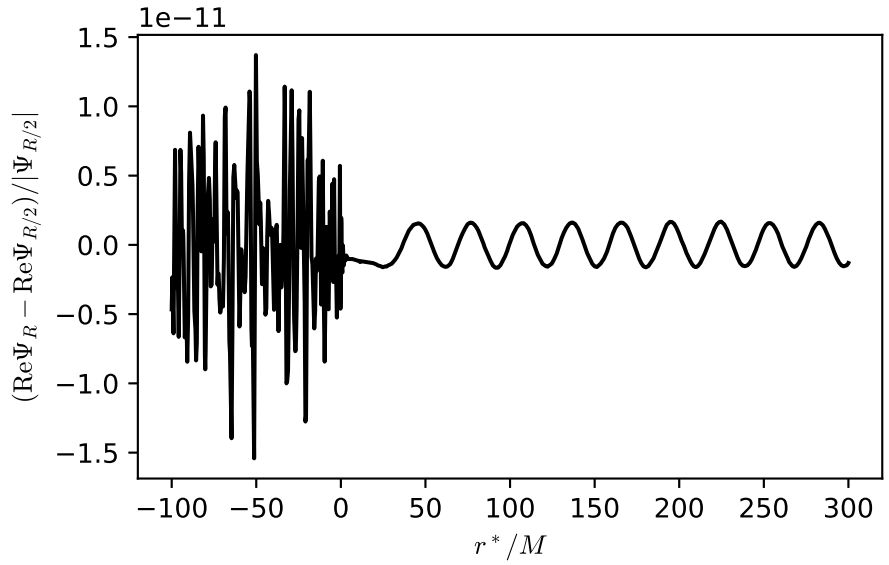

FIGURE 5.2: Relative error of the Ψ_{44} mode for 15 points per element using the 5th order expansions for the puncture and regular field and a worldtube radius of $R = 0.05$. The data is taken for the stationary end state at $t = 11000M$.

5.2.2.3 Convergence

We use a numerical resolution of 15 grid points per spectral element and up to 256 spectral elements covering r^* values in the interval $[-100, 300] \setminus [r_p^* - R, r_p^* + R]$. As the numerical domain changes when the worldtube radius is changed, we always compute norms on the reference r^* interval covering values $[-100, 300] \setminus [r_p^* - 2M, r_p^* + 2M]$ to ensure comparability. For the internal convergence tests we interpolate all solutions on a common reference grid before subtracting the different solutions. This accounts for the change of grid collocation when the resolution or the worldtube radius is changed. With this we can then undertake meaningful internal convergence tests with respect to numerical resolution or worldtube radius, comparing runs using formulas like those in Eq. (4.7) and Eq. (4.31).

5.2.2.4 Convergence with Resolution

As the scheme uses spectral methods, we should see exponential convergence with respect to numerical resolution. We first examine the error of a particular global norm, computing the difference between its value at a particular resolution n and at the highest resolution in our data set, n_{high}. The quantity we choose to examine is the sum of the values of the spectral coefficients c, calculating $|c - c_{high}|$. We then make a semi-log plot of this error versus the number of grid points. Fig. 5.3 shows this for two worldtube radii $R = 0.2M$ and $R = 0.4M$. The exponential convergence is manifest with the approximately straight line.

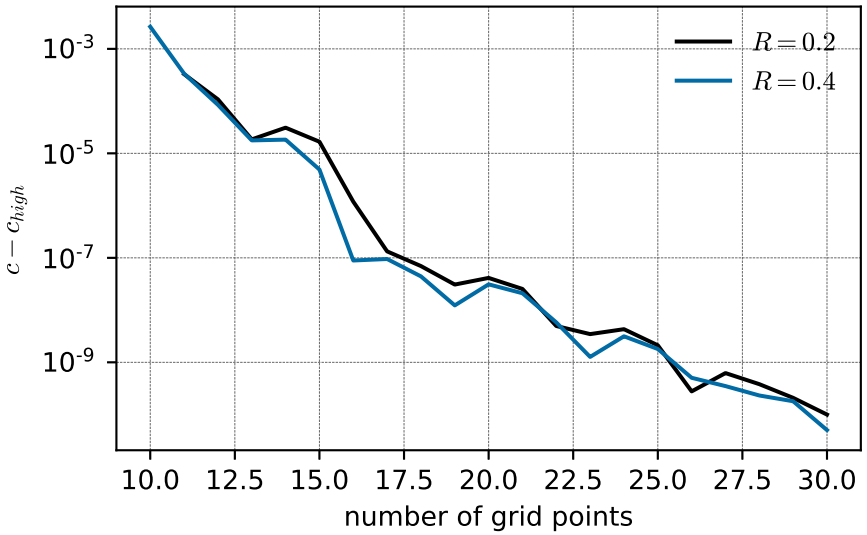

FIGURE 5.3: The difference between the value of the spectral coefficients c obtained with n grid points and their value c_{high} obtained with the highest number of grid points in our data set, n_{high}. Results are displayed for two fixed worldtube radii R. The linear decay on the semi-log scale shows the exponential convergence with respect to resolution, achieved with the spectral method.

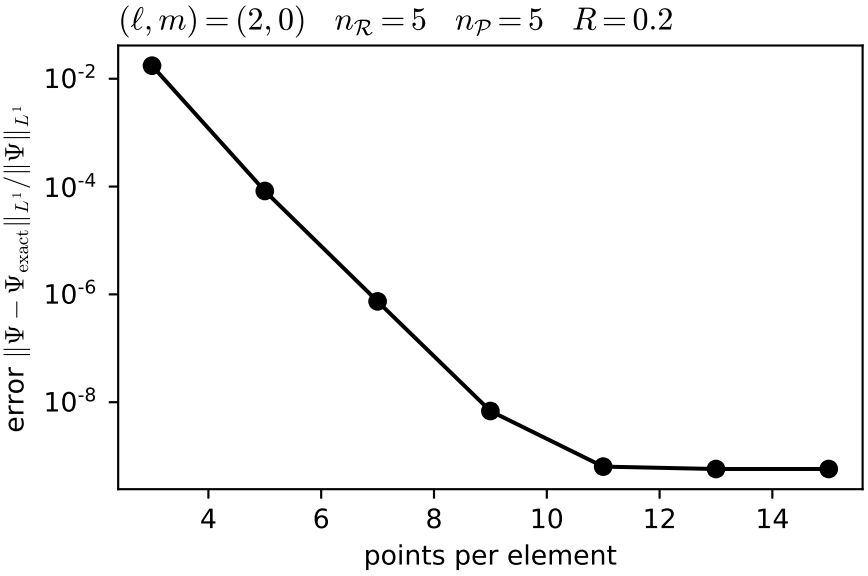

FIGURE 5.4: The error of the Ψ_{20} mode as a function of the number of grid points per spectral element. The grid consists of 128 elements and a has worldtube radius of $R = 0.2$. The puncture and regular parts of fields are expanded to fifth order.

Figure 5.4 shows the error as a function of the number of grid points per spectral element and again demonstrates the exponential convergence of our spectral discretisation scheme. The error levels off at high number of points, because error contributions in the matched analytical solution within the worldtube become the dominating source of error.

5.2.2.5 Convergence with Worldtube Size

We investigate the scheme with two different matching setups, which differ by the polynomial order of the matched regular field inside the worldtube, $n_{\mathcal{R}}$. We test one setup where the regular field is expanded to fifth-order. We compare this against a second setup where the regular field is expanded to third-order only, i.e. closing the system of auxiliary equations at Eqs. (5.12) instead of Eqs. (5.13).

The expansion of the puncture field varies from second to fifth-order and hence the second setup can probe a situation where the truncation error is dominated by the regular field, whereas the first setup always makes sure that the error in the puncture field converges slower or as fast as the regular field. Compared, these setups allow us to distinguish between the convergence behaviour stemming from the truncation of the puncture expansion and the one stemming from the expansion of the regular field; an analysis we did not perform in Scheme I.

In these Scheme II results, the achieved resolution is sufficiently high that its error does not saturate our external L^1 error results as it did in Scheme I. In general, the observed behaviour matches our overall findings from Scheme I. We find the error decreases with the worldtube size, for all models under investigation. We also find that increasing the order of the interior approximate analytical solution generally results in a smaller error norm.

Figure 5.5 demonstrates the convergence of the first setup, where the matched regular fields are all expanded up to order five. It shows the L^1 norm of the difference to the exact analytical solution, along with the corresponding convergence order $n_R^{(\mathrm{norm})}$ defined in Eq. (4.33). For even expansion orders $n_{\mathcal{P}}$ of the puncture field, the total scheme converges with $n_{\mathcal{P}}$, whereas for the odd orders the convergence is one order higher. It is not known to us what causes this irregular convergence pattern with respect to $n_{\mathcal{P}}$, but this finding suggests that the $\partial_n \Psi^N$ term in Eq. (4.30) is suppressed in this scheme for odd $n_{\mathcal{P}}$. As this is a *gain* in order compared to our original expectations, we leave further investigation of this to future work.

Figure 5.6 shows the convergence behaviour of the second setup. For the cases where the expansion order of the puncture is in the range from two to four, we find convergence consistent with the findings of the first setup. However, for a puncture expansion order of five, the convergence order is limited by the regular solution. Since the regular field is truncated at third order in this setup, the analysis of Subsec. 4.3.2.3 would predict a convergence order of only three, and disregarding the $\partial_n \Psi^N$ terms a convergence order of four, but it is observed that the convergence is actually of fifth order. Again, since this is a *gain* in order compared to our original expectations, we leave further investigation of this to future work.

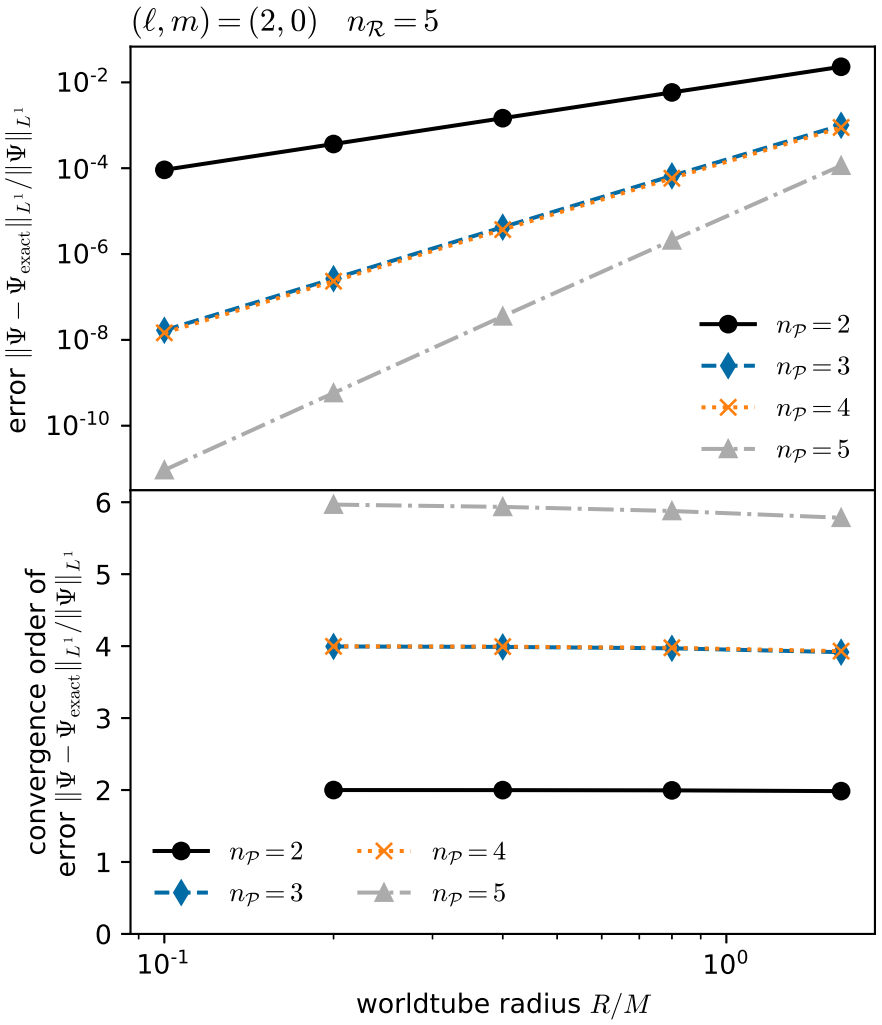

FIGURE 5.5: Top panel: L^1 norm of the difference to the analytical static solution with respect to the worldtube radius R for the Ψ_{20} mode. The indicated order $n_{\mathcal{P}}$ denotes the order of expansion of the puncture field $\Psi^{\mathcal{P}}$. The regular fields are all expanded to order five. Bottom panel: Convergence order for the L^1 norm.

The radiative modes exhibit an error convergence behaviour that is qualitatively identical to the static modes. For completeness we show the corresponding convergence behaviour in Figs. 5.7 and 5.8. As all models show results that are generally in-line with our expectations from theory and Scheme I, we now choose to move onto a 3+1D scalar model, whose architecture much more closely resembles that which will be used in the full BBH model.

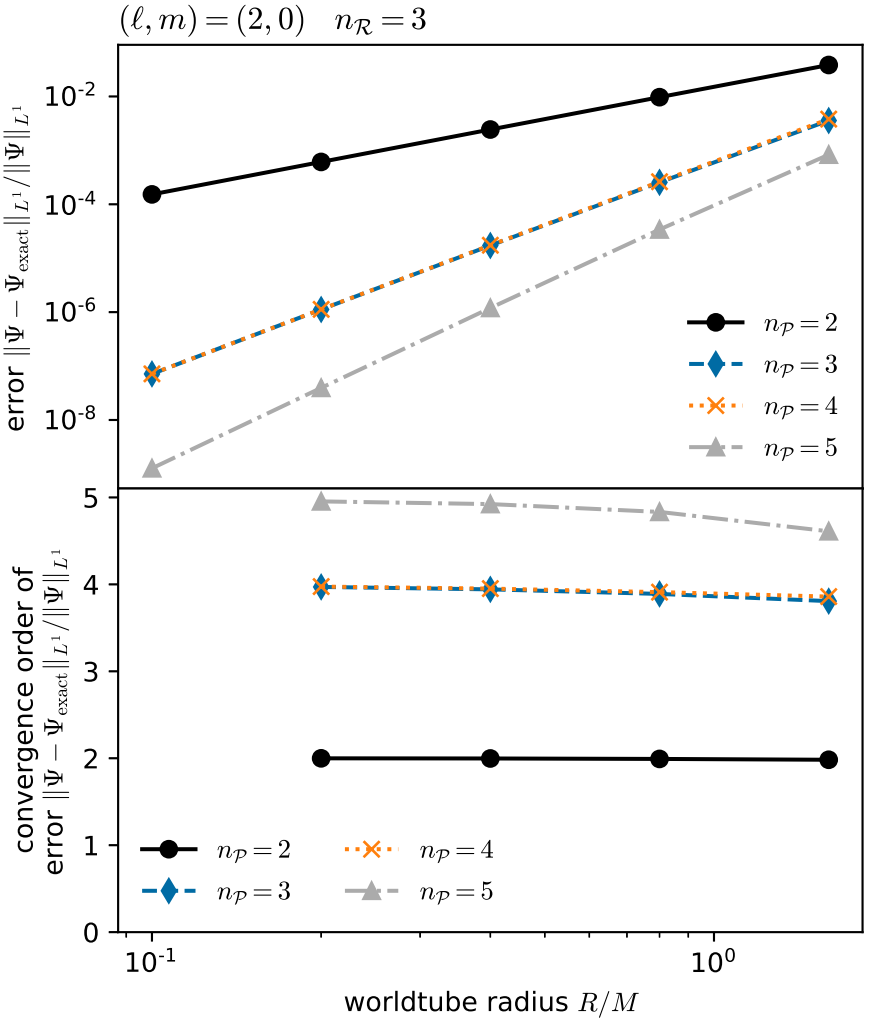

FIGURE 5.6: Top panel: L^1 norm of the difference to the analytical static solution with respect to the worldtube radius R for the Y_{20} mode. The indicated order $n_{\mathcal{P}}$ denotes the order of expansion of the puncture field $\Psi^{\mathcal{P}}$. The regular fields are all expanded to order three. Bottom panel: Convergence order for the L^1 norm.

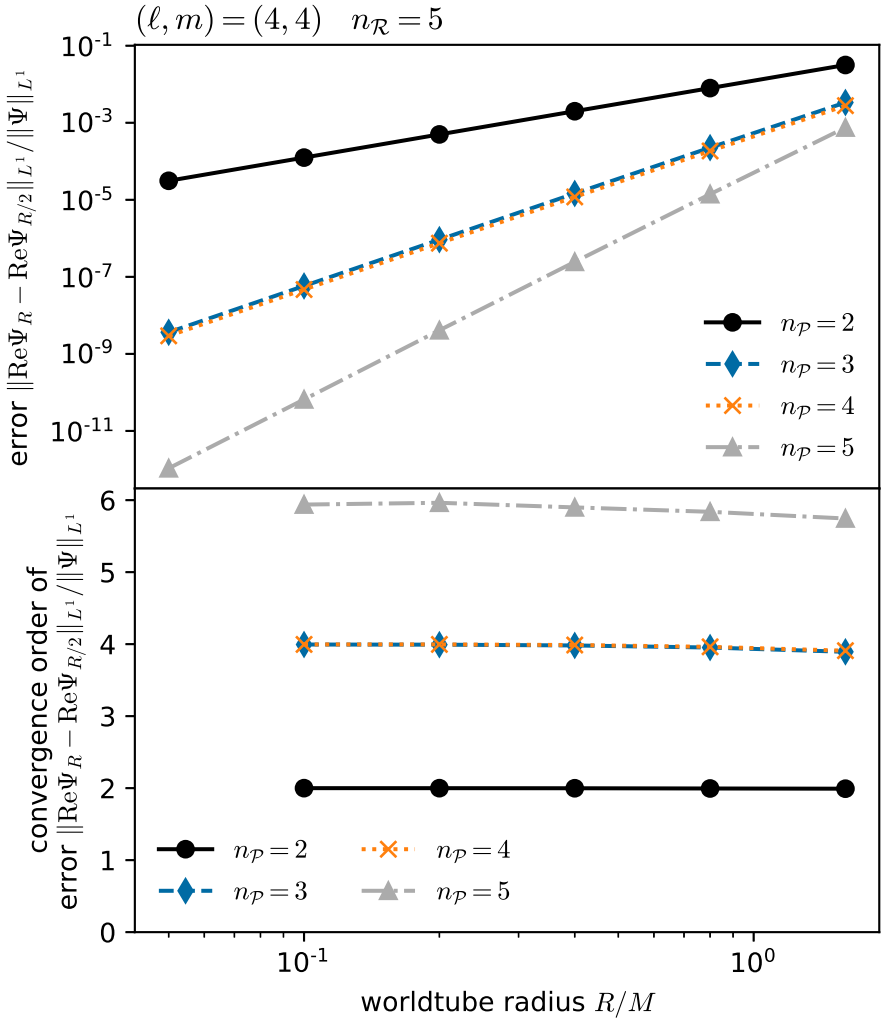

FIGURE 5.7: Top panel: L^1 norm of the difference between solutions with worldtube radius R and $R/2$ for the Y_{44} mode. The indicated order $n_{\mathcal{P}}$ denotes the order of expansion of the puncture field $\Psi^{\mathcal{P}}$. The regular fields are all expanded to order five. Bottom panel: Convergence order for the L^1 norm.

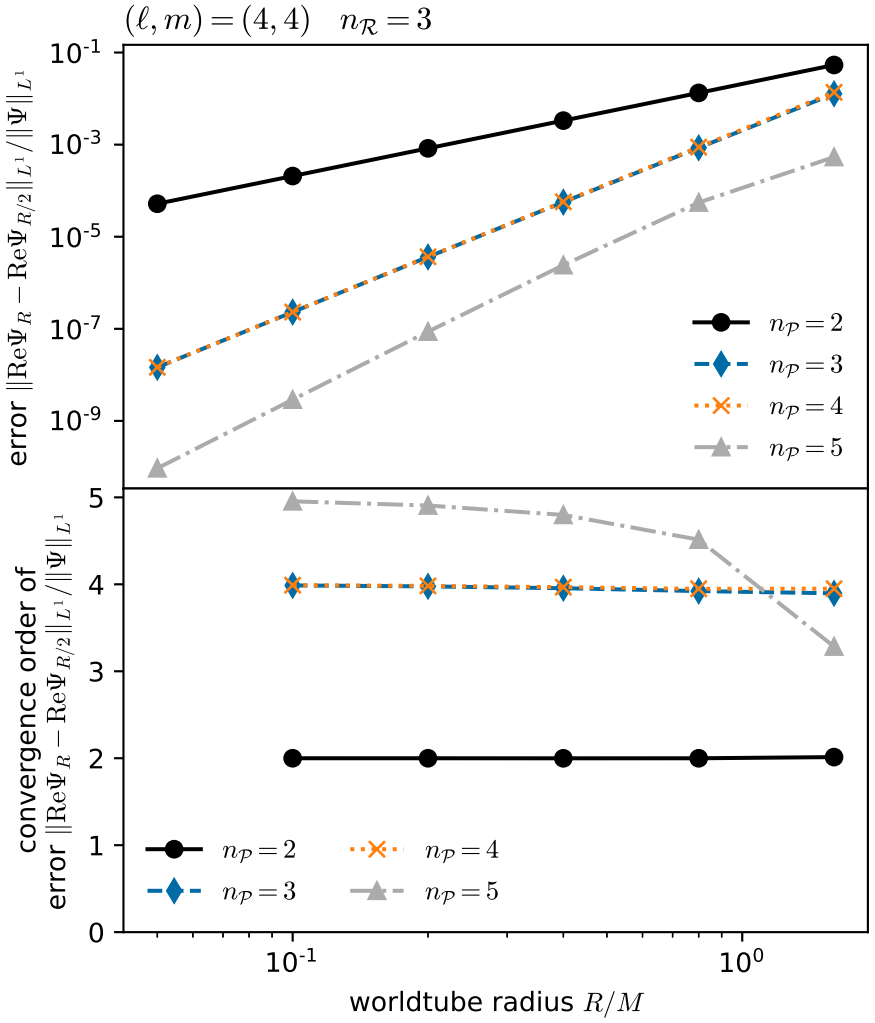

FIGURE 5.8: Top panel: L^1 norm of the difference between solutions with worldtube radius R and $R/2$ for the Y_{44} mode. The indicated order $n_{\mathcal{P}}$ denotes the order of expansion of the puncture field $\Psi^{\mathcal{P}}$. The regular fields are all expanded to order three. Bottom panel: Convergence order for the L^1 norm.

Chapter 6

3+1D Scalar-Field Model

In this chapter we present a 3+1D scalar-field toy model. The physical system that we are modelling is the same as in Chapters 4 and 5 but we now choose not to take advantage of the spherical symmetry with a spherical harmonic mode decomposition. This allows us to better simulate the BBH problem, where there will no longer be such spherical symmetry.

As a consequence, the spacetime topology of the worldtube is different compared to the 1+1D case. In the 1+1D models, the tube (at each given time) was a shell around the large black hole, with boundaries at $r_p \pm R$. However, in the 3+1D model to be discussed now, the tube is a sphere centred around the scalar charge.

6.1 Setup

We maintain the physical system of a scalar point charge e orbiting a Schwarzschild black hole M at a fixed radius r_p. However, we refrain from decomposing into spherical harmonics and now work in 3+1D. Consequently, here we develop a develop worldtube architecture, numerical evolution and matching method in a 3+1D environment. The numerical evolution will now be carried out by SpECTRE [56] and the numerical domain is illustrated in Fig. 6.1. This model infrastructure will largely carry over to the BBH case.

As described at the end of Sec. 2.2, SpECTRE uses the standard excision method to remove the spacetime within the larger black hole's horizon from the computational grid. This is shown as the white region on the left in Fig. 6.1. A worldtube region surrounding the charge e is then also excised from the domain, shown as a smaller white region on the right in Fig. 6.1.

The SpECTRE numerical evolution is much more complex compared to the numerical evolutions used in the Scheme I or II 1+1D toy models. We give fuller details on its

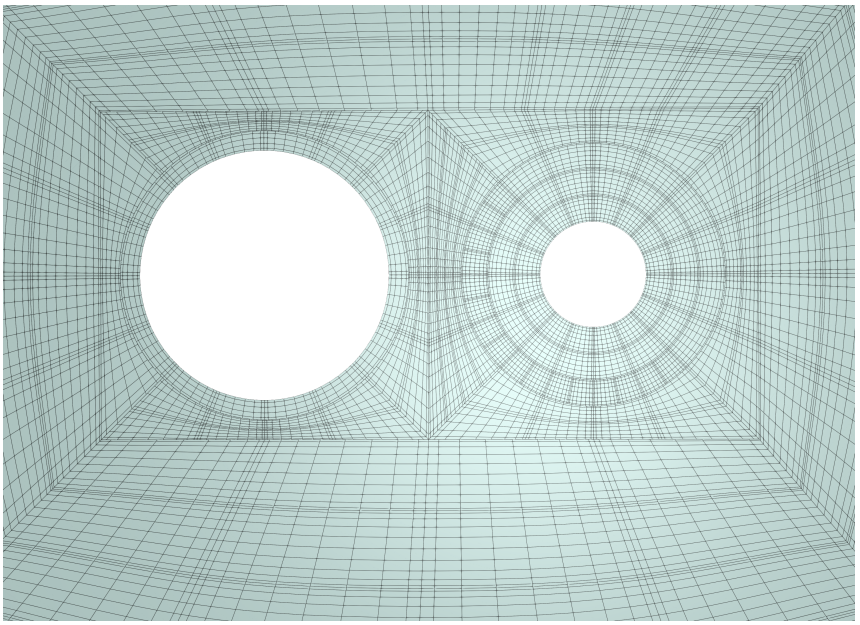

FIGURE 6.1: SpECTRE domain for a binary consisting of a black hole, whose horizon interior is excised from the computational grid (left white region), and a worldtube populated with a local approximate solution (right white region). The division into elements is visible with the grid line structure.

structure in Sec. 6.2. The local approximate analytical solution here is still the scalar singular field plus a regular field piece, which are now, however, formulated in 3+1D.

In this 3+1D model we employ a matching method that is conceptually similar to the one used in Scheme II, described in Subsec. 5.2.1. First we expand the field in a spherical harmonic basis centered on the charge rather than on the black hole. We then match the field and its derivatives on a mode-by-mode basis at the worldtube boundary. To facilitate this matching, the known singular part of the approximate analytical solution will be transformed into the same coordinates as the numerics. In this case, these are Kerr-Schild coordinates.

Sec. 6.2 gives more detail on SpECTRE itself, Kerr-Schild coordinates, and the 3+1 numerical evolution. Sec. 6.3 pedagogically presents the structure of the local approximate analytical solution and the matching method, followed by the derivation of the singular part of the scalar field in Kerr-Schild coordinates. Sec. 6.4 demonstrates the matching method in practice up to second-order in the approximate analytical solution. Sec. 6.5 then presents preliminary results from this model.

6.2 Numerical Evolution

6.2.1 SpECTRE

The numerical evolution in the 3+1D scalar field model will be carried out by SpECTRE, the successor to the Spectral Einstein Code (SpEC) [4], being developed by the Simulating eXtreme Spacetimes (SXS) collaboration. The aim of SpECTRE is to achieve accurate solutions for challenging relativistic astrophysics problems.

SpECTRE uses Cauchy slicing and Discontinuous Galerkin (DG) methods for the numerical evolution [83]. A key difference between DG methods and classic spectral methods is the independent nature of the spectral elements. Each element is evolved separately, only requiring boundary data from its neighbour. This makes DG methods well suited to code parallelization. A task-based parallelism model allows the efficient use supercomputers and minimizes the number of idle cores at any time, as tasks are assigned to cores dynamically during the computation. This is a distinct advantage of SpECTRE over more traditional synchronous, data parallelism models used in other grid-based astrophysics codes [83].

Furthermore, the local nature of DG schemes can better facilitate adaptive mesh refinement and local timestepping. SpECTRE uses adaptive strategies to either split the elements into smaller elements (h-refinement) or increase the order of the polynomial within each element (p-refinement) [83]. To evolve dynamical spacetimes, SpECTRE implements the Einstein equations using a generalised harmonic formulation [125, 71], written with first-order time and first-order space derivatives [89].

Although SpECTRE is under development, we choose to construct our 3+1D model using this code to provide us with experience prior to implementing a BBH model, by which time it should be a well-established software.

6.2.2 Kerr-Schild Coordinates

For the 3+1D scalar field model SpECTRE is set to work in Kerr-Schild coordinates. The choice of Kerr-Schild coordinates in SpECTRE is motivated by the NR excision method for handling black hole singularities, reviewed in Sec. 2.2. Kerr-Schild time slicing, in comparison with Schwarzschild time slicing, penetrates the event horizon, making it a good candidate for black hole singularity excision [40].

The Schwarzschild metric in Kerr-Schild coordinates (t, x, y, z) is,

$$ds^2 = -dt^2 + dx^2 + dy^2 + dz^2 + \frac{2M}{r}\left[dt + \frac{xdx + ydy + zdz}{r}\right]^2, \tag{6.1}$$

with $r = \sqrt{x^2 + y^2 + z^2}$. In this chapter (t, r) will always denote Kerr-Schild time and radius. We fix our particle e so that it is moving on a circular orbit in the $z = 0$ plane. In this case, the four-velocity of the particle is given by

$$u^t = \frac{1}{\sqrt{1 - \frac{3M}{r_p}}}, \quad u^x = -\frac{\sqrt{M}y}{\sqrt{r_p^2(-3M + r_p)}}, \quad u^y = -\frac{\sqrt{M}x}{\sqrt{r_p^2(-3M + r_p)}}, \quad u^z = 0. \tag{6.2}$$

and its trajectory is

$$x_p^\alpha(t) = (t, r_p \cos(\Omega t), r_p \sin(\Omega t), 0), \tag{6.3}$$

where $\Omega = \sqrt{\frac{M}{r_p^3}}$.

6.2.3 Numerical Details

SpECTRE is an NR code and is therefore built on the principles of the ADM (3+1) formalism. We now present the key principles of this formalism, following the explanation in Sec. 4.2.2 of [106].

The formalism foliates the spacetime $g_{\alpha\beta}$ into a family of spacelike hypersurfaces, which we call Σ_t. The spacelike three-surfaces Σ_t, are level sets of a scalar function $t(y^\alpha)$ which then defines a universal time. On each hypersurface spatial coordinates x^a are installed. A congruence of curves γ can be constructed that pass through the hypersurfaces. On these curves we can use t as a parameter and have a vector t^α that is tangent to the congruence. A particular curve γ_P passes through the point P on Σ_t, P' on $\Sigma_{t'}$ and so on. The coordinates on the hypersurfaces can then be fixed such that $x^a(P) = x^a(P')$ and so on. This defines a coordinate system (t, x^a). The transformation between these coordinates and any generic system, $y^\alpha = y^\alpha(t, x^a)$, is set by

$$t^\alpha = \left(\frac{\partial y^\alpha}{\partial t}\right)_{x^a}, \quad e_a^\alpha = \left(\frac{\partial y^\alpha}{\partial x^a}\right)_t, \tag{6.4}$$

where e_a^α are tangent vectors on Σ_t. We can now form a unit normal to the hypersurfaces, n_α, which we write as

$$n_\alpha = -N\partial_\alpha t, \quad n_\alpha e_a^\alpha = 0, \tag{6.5}$$

where N is known as the lapse function. The congruence of curves are not assumed to intersect the surfaces Σ_t orthogonally, and so t^α is not fixed to be parallel to n^α. It is therefore decomposed in the basis (n^α, e_a^α),

$$t^\alpha = Nn^\alpha + N^a e_a^\alpha, \tag{6.6}$$

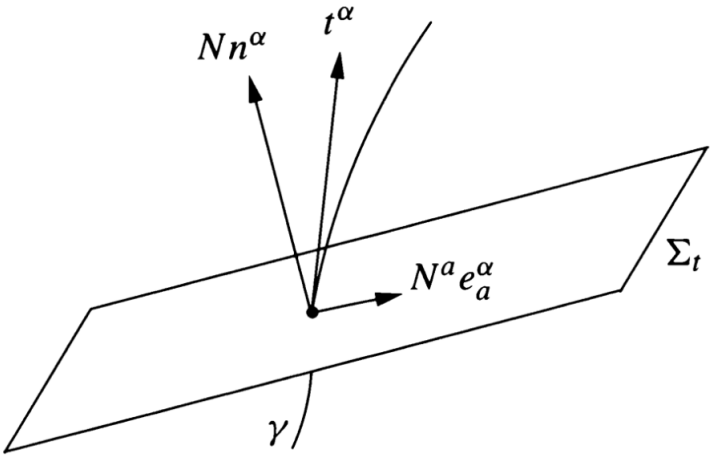

FIGURE 6.2: Sketch from [106] illustrating key elements in the 3+1 decomposition of spacetime. Σ_t are spatial hypersurfaces, through which a family of congruent curves γ pass. t^α are tangential to the curves and can be decomposed into the basis (n^α, e_a^α), where n^α are unit normals to the hypersurface and e_a^α are tangent vectors to the hypersurface.

where the final key ingredient N^a is introduced, known as the shift function. The metric can now be expressed in the coordinates (t, x^a). First we construct

$$\begin{aligned} dy^\alpha &= t^\alpha dt + e_a^\alpha dx^a \\ &= (Ndt)n^\alpha + (dx^a + N^a dt)e_a^\alpha, \end{aligned} \tag{6.7}$$

from which we can then form the line element

$$\begin{aligned} ds^2 &= g_{\alpha\beta} dy^\alpha dy^\beta \\ &= -N^2 dt^2 + g_{ab}(dx^a + N^a dt)(dx^b + N^b dt), \end{aligned} \tag{6.8}$$

where $g_{ab} = g_{\alpha\beta} e_a^\alpha e_b^\beta$ is the induced spatial metric on Σ_t.

In Kerr-Schild coordinates, the spatial metric, lapse and shift are given by

$$g_{ab} = \begin{bmatrix} 1 + \frac{2Mx^2}{r^3} & \frac{2Mxy}{r^3} & \frac{2Mxz}{r^3} \\ \frac{2Mxy}{r^3} & 1 + \frac{2My^2}{r^3} & \frac{2Myz}{r^3} \\ \frac{2Mxz}{r^3} & \frac{2Mxy}{r^3} & 1 + \frac{2Mz^2}{r^3} \end{bmatrix}, \tag{6.9}$$

$N = 1$, and $N_x = \frac{Mx}{r^2}, N_y = \frac{My}{r^2}, N_z = \frac{Mz}{r^2}$.

In our 3+1D scalar worldtube excision model, we are solving the standard scalar field equation on a fixed Schwarzschild spacetime,

$$\nabla^\mu \nabla_\mu \Phi = 0. \tag{6.10}$$

Just as in Scheme II of the 1+1D scalar model, we reduce this equation to a first-order evolution system. This is now done in the standard NR way (see for full details [133]):

$$\partial_t \Phi - N^k \partial_k \Phi, = -N\pi, \tag{6.11}$$
$$\partial_t \pi - N^k \partial_k \pi + N g^{ki} \partial_k \chi_i = N J^i \chi_i + NK\pi, \tag{6.12}$$
$$\partial_t \chi_i - N^k \partial_k \chi_i + N \partial_i \pi = -\pi \partial_i N + \chi_j \partial_i N^j. \tag{6.13}$$

where

$$\pi = -N^{-1}(\partial_t \Phi - N^i \partial_i \Phi),$$
$$\chi_i = \partial_i \Phi.$$

Φ, π, χ_i, are referred to as the set of fundamental fields. Here, K and J^i are defined by

$$J^i = -N^{-1} g^{-1/2} \partial_j (N g^{1/2} g^{ij}), \tag{6.14}$$
$$K = -N^{-1} g^{-1/2} [\partial_t g^{1/2} - \partial_j (g^{1/2} N^j)], \tag{6.15}$$

where g is the determinant of the spatial metric g_{ij}. K is known as the trace of the extrinsic curvature, providing information as to how the three-dimensional hypersurfaces are embedded into the four-dimensional spacetime. The extrinsic curvature is defined as $K_{ab} := n_{\alpha;\beta} e^\alpha_a e^\beta_b$.

The field is only a solution to Eq. (6.10) if the following constraints are satisfied [5, 81]:

$$\mathcal{C}_i = \partial_i \Phi - \chi_i = 0, \tag{6.16}$$
$$\mathcal{C}_{ij} = \partial_{[i} \chi_{j]} = 0. \tag{6.17}$$

The first of these ensures that the evolved variable χ_i is indeed acting as the spatial derivative of Φ, while the second ensures the field obeys the commutative rule for partial derivatives.

We run simulations on a domain out to a Kerr-Schild coordinate radius $r = 400M$. Although dependent on the desired resolution of our run, the number of spectral elements is usually set ≈ 4000. We adopt a Legendre polynomial basis and have a range in $n_{\mathcal{L}}$ (polynomial order) across the domain, with a maximum of $n_{\mathcal{L}} = 12$. The model sets the initial field data equal to zero across the domain. At $t = 0$ of the evolution we introduce a Gaussian error function at the worldtube boundary, whose argument smoothly takes the field from 0 to 1 at $t = 250M$. This is similar to the handling of initial data in the Scheme I 1+1D model. In doing this, we reduce the amplitude of the initial junk and numerical noise in our simulation and obtain smoother convergence.

Similarly to the Scheme II 1+1D model, this model requires boundary conditions in three locations: (i) on the outer boundaries of the computational domain, (ii) at the

interfaces between neighbouring elements, and (iii) on the excision boundary $\partial\Gamma$.

At the outer boundaries we implement what are known as constraint-preserving boundary conditions, plus a Bayliss-Turkel radiation boundary condition [5]. The constraint-preserving boundary conditions are similar to the Penalty method introduced in Scheme II, in that they modify the time derivatives of the fundamental fields, Φ, π, χ_i. Their inclusion is standard practice in NR evolutions and for our implementation we follow the method laid out in Sec. III of [81]. The Bayliss-Turkel boundary conditions, as presented in [41], are employed when spacetime is approximately Minkowski, as is the case at our outer boundary. The condition ensures that the solution has a form of an outgoing-wave with an appropriate fall-off.

At the element boundaries we implement the upwind flux boundary condition. The upwind flux condition is a standard numerical boundary condition, commonly employed in problems of hydrodynamics, electromagnetism and general relativity. We will not provide detail on it within this thesis but the underlying theory can be found in [77], while implementation details with respect to Discontinuous Galerkin methods can be found in [137] and [64].

Finally, at the worldtube boundary we implement Dirichlet boundary conditions, i.e. direct matching of the field values themselves. This is explained in detail in Sec. 6.4. In this 3+1D model, we implement the approximate analytical solution to zeroth, first, and then second order in accuracy i.e. order in distance from the worldline. Extending the boundary conditions to higher order implementations should be a straightforward extension of theory laid out in Sec. 6.4.

6.3 Local Approximate Solution and Matching Method

In this section, we examine the 4D structure of the local solution near the particle and develop a general method of matching it to a 3+1D numerical solution. For simplicity, we first carry out this analysis in locally inertial coordinates comoving with the particle; we then conclude the section by expressing the singular part of the local solution in Kerr-Schild coordinates.

6.3.1 First Principles Derivation

The worldtube must now be populated with a local approximate analytical solution that is valid in 3+1D. To characterize the field's local form near the particle, we can adopt locally Cartesian co-moving coordinates (τ, x^a) centered on the particle's worldline. This gives us an intuitive understanding of the field's structure, before we move to other coordinate systems that are more amenable to the numerics.

Fermi-Walker coordinates are an example in which $g_{\alpha\beta} = \eta_{\alpha\beta}$ on the worldline, τ is proper time along the worldline, surfaces Σ_τ of constant τ are generated by spatial geodesics emanating orthogonally from the point $z^\mu(\tau)$, x^a are coordinates on each Σ_τ, and $s := \sqrt{\delta_{ab}x^a x^b}$ is the proper geodesic distance from $z^\mu(\tau)$ to the point labelled by x^a in Σ_τ. For more detail see Chapter 1 of [106]. (Note, in Sec. 6.3.1 and Sec. 6.3.2, lowercase Latin indices denote the spatial Fermi-Walker coordinates, while in the rest of the chapter they denote the spatial Kerr-Schild coordinates.)

Constructing the local field in Fermi-Walker coordinates allows us to exemplify its structure and the ability to split it into a regular and singular contribution. To do this we follow the algorithm laid out in [113]. Ref. [113] obtains the general solution to the linear wave equation in the local neighbourhood outside a compact mass or charge distribution in any coordinates satisfying $g_{\alpha\beta} = \eta_{\alpha\beta}$ on the worldline, such as Fermi-Walker coordinates.

The focus in [113] is on metric perturbations at nonlinear orders in gravitational perturbation theory, but the algorithm applies straightforwardly to the linear scalar field outside a monopolar scalar particle. In this case we start with the ansatz

$$\Phi = \sum_{p\geq -1}\sum_{\ell\geq 0} s^p \Phi_L^{(p,\ell)}(\tau)\hat{n}^L. \tag{6.18}$$

$n^a = x^a/s$ is a radial unit vector, and $L := a_1 \cdots a_\ell$ is a multi-index. The quantity $\hat{n}^L := n^{\langle a_1} n^{a_2} \cdots n^{a_\ell\rangle}$ is the symmetric trace-free (STF) combination of ℓ unit vectors and the set $\{\hat{n}^L\}_\ell$ is equivalent to the set of spherical harmonics. It provides an orthogonal basis for functions on a sphere, and each $\hat{n}^L$ is an eigenfunction of the Laplacian $\nabla^2 := \delta^{ab}\partial_a\partial_b$, satisfying $\nabla^2\hat{n}^L = -\frac{\ell(\ell+1)}{s^2}\hat{n}^L$, the same eigenvalue equation satisfied by $Y_{\ell m}$. Recall these bases are defined on spheres of constant s, centered on the particle.

We substitute the ansatz Eq. (6.18) into the wave equation $g^{\mu\nu}\nabla_\mu\nabla_\nu\Phi = 0$ (outside the charge) and solve order by order in s. A spatial derivative lowers the power of s while a τ derivative does not. This implies that we can write the wave operator as ∇^2 plus a subdominant operator D:

$$\begin{aligned} g^{\mu\nu}\nabla_\mu\nabla_\nu\Phi &= \frac{1}{\sqrt{-g}}\partial_\mu\left(\sqrt{-g}g^{\mu\nu}\partial_\nu\Phi\right) \\ &= \nabla^2\Phi + \frac{\partial_\mu\left(\sqrt{-g}g^{\mu\nu}\right)}{\sqrt{-g}}\partial_\nu\Phi + \delta g^{\mu\nu}\partial_\mu\partial_\nu\Phi := \nabla^2\Phi + D\Phi, \end{aligned} \tag{6.19}$$

where $\delta g^{\mu\nu} := g^{\mu\nu} - \delta^\mu_a\delta^\nu_b\delta^{ab}$. More concretely,

$$D = D^{\tau\tau}\partial_\tau^2\Phi + D^{\tau a}\partial_\tau\partial_a + D^{ab}\partial_a\partial_b + D^\tau\partial_\tau + D^a\partial_a, \tag{6.20}$$

with $D^{\tau\tau} = -1 + O(s)$, $D^{\tau a} = O(s^2)$, $D^{ab} = O(s^2)$, $D^\tau = O(s)$, and $D^a = O(s)$. These powers of s hold for a generic coordinate system with $g_{\alpha\beta}(s=0) = \eta_{\alpha\beta}$, including

Fermi-Walker coordinates centred on an accelerated worldline. If the particle moves on a geodesic, then in Fermi-Walker coordinates they become $D^{\tau\tau} = -1 + O(s^2)$, $D^{\tau a} = O(s^2)$, $D^{ab} = O(s^2)$, $D^{\tau} = O(s)$, and $D^{a} = O(s^2)$. In either case, in Fermi-Walker coordinates, we have

$$D = -\partial_\tau^2 - \frac{s^2}{3} R^a{}_i{}^b{}_j n^i n^j \partial_a \partial_b + O(s), \tag{6.21}$$

where we count ∂_τ as $O(s^0)$ and ∂_a as $O(s^{-1})$. Here $R^a{}_i{}^b{}_j = \delta^{ac}\delta^{bd}R_{cidj}$ is the Riemann tensor evaluated on the worldline.

Given the split in Eq. (6.19), the wave equation reduces to a sequence of Poisson equations, one at each order s. These become algebraic equations for the coefficients $\Phi_L^{(p,\ell)}$:

$$s^{p-2}[p(p+1) - \ell(\ell+1)]\Phi_L^{(p,\ell)}(\tau)\hat{n}^L = s^{p-2} S_L^{(p,\ell)}(\tau)\hat{n}^L, \tag{6.22}$$

where the source terms are constructed from D acting on lower-order terms $s^{p'}\Phi_{L'}^{(p',\ell')}\hat{n}^{L'}$ with $p' < p$.

At each value of p, there is one ℓ for which the left-hand side of Eq. (6.22) automatically vanishes: $\ell = -p-1$ if $p < 0$ and $\ell = p$ if $p \geq 0$. These are the standard $\frac{1}{s^{\ell+1}}$ and s^ℓ solutions of the Laplace equation. For these special combinations of p and ℓ, one can prove that $S_L^{(p,\ell)} = 0$, meaning Eq. (6.22) is trivially satisfied for any $\Phi_L^{(p,\ell)}(\tau)$. For all other ℓ at each p, we can immediately solve Eq. (6.22) to obtain $\Phi_L^{(p,\ell)} = S_L^{(p,\ell)}/[p(p+1) - \ell(\ell+1)]$. It follows that to all orders, the solution is fully specified by the "seed coefficients" $\{\Phi^{(-1,0)}, \Phi^{(0,0)}, \Phi_i^{(1,1)}, \ldots, \Phi_P^{(p,p)}, \ldots\}$; these free functions of τ fully characterize the freedom in the solution [119].

$$\Phi = \frac{\Phi^{(-1,0)}(\tau)}{s} + \Phi^{(0,0)}(\tau) + \Phi_i^{(0,1)}(\tau)n^i + \ldots + s^p \left[\Phi_P^{(p,p)}(\tau)\hat{n}^P + \sum_{\ell\neq p,\, \ell=0}^{p+1} \Phi_L^{(p,\ell)}(\tau)\hat{n}^L \right] + \ldots, \tag{6.23}$$

where all coefficients $\Phi_L^{(p\geq 0, \ell\neq p)}$ are expressed in terms of the seed coefficients and their τ derivatives. We note that in this expansion, the only smooth terms are those with $\ell = p - 2k$ for integers k in the range $0 \leq k \leq \lfloor p/2 \rfloor$, where $\lfloor p/2 \rfloor$ denotes the largest integer smaller than $p/2$. To see why these are smooth, observe that $s^p \hat{n}^{P-2K} = s^{2k}\hat{x}^{P-2K} = (\delta_{ab}x^a x^b)^k \hat{x}^{P-2K}$, where here we use the notation $\hat{x}^P := x^{\langle P\rangle} := x^{\langle a_1} \cdots x^{a_p\rangle}$. All other terms in Eq. (6.23) have finite differentiability at $x^a = 0$.

We can use this local multipole structure to define a singular and regular field. Φ_S is the piece of Eq. (6.23) seeded by $\Phi^{(-1,0)}$, i.e. Eq. (6.23) with all other seed coefficients set to zero. Φ_R is the piece seeded by the coefficients $\Phi_P^{(p,p)}$ ($p \geq 0$). To all known orders in s this singular-regular split agrees with the Detweiler-Whiting decomposition.

For our particle with constant charge e, the only seed coefficient in the singular field is $\Phi^{(-1,0)} = e$. One can prove that in the algorithmic construction of Eq. (6.23), the

smooth terms $s^p \hat{n}^{P-2K}$ never involve $\Phi^{(-1,0)}$. We can therefore write the generic form

$$\Phi^S = \frac{e}{s} + \Phi_i^{(0,1)}(\tau) n^i + \ldots + s^p \sum_{\substack{\ell=0 \\ \ell \neq p-2k}}^{p+1} \Phi_L^{(p,\ell)}(\tau) \hat{n}^L + \ldots \tag{6.24}$$

Explicitly, for a nonaccelerating charge in Fermi-Walker coordinates, the first few orders in the singular field are

$$\Phi^S = \frac{e}{s} - \frac{es}{6} \mathcal{E}_{ij}(\tau) \hat{n}^{ij} - \frac{es^2}{24} \mathcal{E}_{ijk}(\tau) \hat{n}^{ijk} + O(s^3). \tag{6.25}$$

where $\mathcal{E}_{ij}(\tau) := R_{i\tau j\tau}(\tau, x^a = 0)$ and $\mathcal{E}_{ijk}(\tau) := \mathrm{STF}_{ijk} R_{i\tau j\tau;k}(\tau, x^a = 0)$.

The regular field then contains all the other terms in Eq. (6.23):

$$\Phi^R = \Phi^{(0,0)}(\tau) + s\Phi_i^{(1,1)}(\tau) n^i + \ldots + s^p \sum_{k=0}^{\lfloor p/2 \rfloor} \Phi_{P-2K}^{(p,p-2k)}(\tau) \hat{n}^{P-2K} + \ldots \tag{6.26}$$

Since this is a smooth field, we can write it as the Taylor series

$$\Phi^R = \Phi^R(\tau, 0) + \partial_i \Phi^R(\tau, 0) x^i + \ldots + \frac{1}{p!} \partial_P \Phi^R(\tau, 0) x^P + \ldots \tag{6.27}$$

where $\partial_P := \partial_{a_1} \cdots \partial_{a_p}$. We can relate the two forms (6.26) and (6.27) using the fact that

$$x^P = s^p n^P = s^p \left(\hat{n}^P + c_1 \delta^{(i_1 i_2} \hat{n}^{P-2)} + c_2 \delta^{(i_1 i_2} \delta^{i_3 i_4} \hat{n}^{P-4)} + \cdots + c_k \delta^{(i_1 i_2} \cdots \hat{n}^{P-2K)} \right) \tag{6.28}$$

where the c_n's are constants and $k = \lfloor p/2 \rfloor$. Each seed coefficient $\Phi_P^{(p,p)}$ is then identified with the STF piece of the pth derivative of Φ^R at $s = 0$:

$$\Phi^R(\tau, 0) = \Phi^{(0,0)}(\tau), \quad \partial_i \Phi^R(\tau, 0) = \Phi_i^{(1,1)}(\tau), \quad \ldots, \quad \frac{1}{p!} \hat{\partial}_P \Phi^R(\tau, 0) = \Phi_P^{(p,p)}(\tau), \tag{6.29}$$

with $\hat{\partial}_P := \partial_{\langle P \rangle}$. The non-STF pieces (i.e. the trace pieces) of the derivatives are related to the lower-order seed coefficients. Explicitly, the first few terms in (6.27) are

$$\Phi^R = \Phi^R(\tau, 0) + \partial_i \Phi^R(\tau, 0) x^i + \frac{s^2}{2} \left[\hat{\partial}_{ij} \Phi^R(\tau, 0) \hat{n}^{ij} + \frac{1}{3} \delta^{ij} \partial_{ij} \Phi^R(\tau, 0) \right] + O(s^3). \tag{6.30}$$

We observe that the Laplacian on the worldline, $\delta^{ij} \partial_{ij} \Phi^R(\tau, 0) = \nabla^2 \Phi^R(\tau, 0)$, is the coefficient $3\Phi^{(2,0)}(\tau)$ in Eq. (6.23). It is written in terms of the lower-order seed coefficients using Eqs. (6.22) and (6.21), which implies

$$\Phi^{(2,0)}(\tau) = \frac{1}{3} \partial_\tau^2 \Phi^{(0,0)}(\tau) \qquad \text{or} \qquad \nabla^2 \Phi_R(\tau, 0) = \partial_\tau^2 \Phi_R(\tau, 0). \tag{6.31}$$

The second version of the equality is a trivial statement of the wave equation evaluated

on the worldline. At higher orders in distance, the Riemann term in Eq. (6.21) will be involved in such relations.

In summary, we conclude that the local solution is fully specified by the set of STF derivatives $\hat{\partial}_P \Phi^R(\tau, 0)$. Through any given order s^n, the local solution is fully specified by $\Phi^R(\tau, 0)$, $\partial_i \Phi^R(\tau, 0)$, $\hat{\partial}_{ij} \Phi^R(\tau, 0)$, etc., up to $\hat{\partial}_N \Phi^R(\tau, 0)$. We can use equations such as Eq. (6.31) to replace one of these free functions with an alternative free function. For example, we can treat $\nabla^2 \Phi^R(\tau, 0)$ as the free function rather than $\Phi^R(\tau, 0)$. The wave equation does not impose any conditions on the generating set $\{\hat{\partial}_P \Phi^R(\tau, 0)\}_p$. We can use the wave equation to replace an element of this set, but we cannot use it to determine relationships between elements of the set. We make use of this in practice in our second order matching method, explained in Fermi coordinates in Sec. 6.3.2 and in generic coordinates in Sec. 6.4.3.

6.3.2 Matching Ethos

Through order s^p, our local solution contains $(p+1)^2$ unknown independent components. These can be determined by matching to the external field. In this section we lay out the core principles of our matching method.

Suppose we match on a worldtube $\Gamma = \{s = s_0\}$. In this model we choose to expand the external field in multipoles as $\Phi|_\Gamma = \sum_\ell \Phi_L^{(\ell)}(\tau, s_0)\hat{n}^L$, and match multipole by multipole. For the zeroth-order approximation

$$\Phi = \frac{e}{s} + \Phi^R(\tau, 0), \tag{6.32}$$

we have the single unknown $\Phi^R(\tau, 0)$, and our matching condition is

$$\Phi^{(0)}(\tau, s_0) = \frac{e}{s_0} + \Phi^R(\tau, 0). \tag{6.33}$$

For the first-order approximation

$$\Phi = \frac{e}{s} + \Phi^R(\tau, 0) + s\left[\partial_i \Phi^R(\tau, 0) n^i + \Phi_{ij}^{(1,2)}(\tau)\hat{n}^{ij}\right], \tag{6.34}$$

we have the unknowns $\Phi^R(\tau, 0)$ and $\partial_i \Phi^R(\tau, 0)$, and our matching conditions are

$$\Phi^{(0)}(\tau, s_0) = \frac{e}{s_0} + \Phi^R(\tau, 0), \tag{6.35}$$

$$\Phi_i^{(1)}(\tau, s_0) = s_0 \partial_i \Phi^R(\tau, 0). \tag{6.36}$$

For the second-order approximation

$$\Phi = \frac{e}{s} + \Phi^R(\tau,0) + s\left[\partial_i \Phi^R(\tau,0) n^i + \Phi^{(1,2)}_{ij}(\tau)\hat{n}^{ij}\right] + s^2\left[\frac{1}{2}\partial_{ij}\Phi^R(\tau,0)n^{ij} + \sum_{\ell=1,3}\Phi^{(2,\ell)}_L(\tau)\hat{n}^L\right], \tag{6.37}$$

we have the unknowns $\Phi^R(\tau,0)$, $\partial_i\Phi^R(\tau,0)$, and $\hat{\partial}_{ij}\Phi^R(\tau,0)$, and our matching conditions are

$$\Phi^{(0)}(\tau,s_0) = \frac{e}{s_0} + \Phi^R(\tau,0) + \frac{1}{6}s_0^2\partial_\tau^2\Phi^R(\tau,0), \tag{6.38}$$

$$\Phi^{(1)}_i(\tau,s_0) = s_0\partial_i\Phi^R(\tau,0) + s_0^2\Phi^{(2,1)}_i(\tau), \tag{6.39}$$

$$\Phi^{(2)}_{ij}(\tau,s_0) = s_0\Phi^{(1,2)}_{ij}(\tau) + \frac{1}{2}s_0^2\hat{\partial}_{ij}\Phi^R(\tau,0), \tag{6.40}$$

where $\partial_\tau^2\Phi^R(\tau,0)$ has appeared through Eqs. (6.30) and (6.31). In these equations, the quantities $\Phi^{(1,2)}_{ij}$, $\Phi^{(2,1)}_i$, and $\Phi^{(2,3)}_{ijk}$ are expressible in terms of the Riemann tensor: from Eq. (6.24), $\Phi^{(1,2)}_{ij} = -\frac{1}{6}e\mathcal{E}_{ij}$, $\Phi^{(2,1)}_i = 0$, and $\Phi^{(2,3)}_{ijk} = -\frac{1}{24}e\mathcal{E}_{ijk}$. For our 3+1D scalar model implementation, as presented in Sec. 6.4 we do not go beyond a second-order approximation for the local approximate analytical solution.

In summary, when we use a zeroth-order order approximation, the matching condition Eq. (6.33) determines the unknown in the internal approximation in terms of the $\ell = 0$ piece of the external field on the worldtube; when we use a first-order approximation, the matching condition of Eqs. (6.35)-(6.36) determine the 4 unknowns in terms of the $\ell = 0$ and 1 pieces of the external field; if we use a second-order approximation, the matching condition of Eqs. (6.38)-(6.40) determines 9 unknowns in terms of the $\ell = 0$, 1, and 2 pieces of the external field, but in this case some of the unknowns are determined through differential equations on the boundary rather than purely algebraic relations. For all higher-order approximations, the matching conditions will likewise yield differential equations governing the unknowns.

6.3.3 High-Order Covariant Expressions

In our worldtube excision model, our approach will be to subtract the singular field piece Φ^S from the full numerical field Φ^N at each time-step, and then match this residual field, mode by mode, to Φ^R at the worldtube boundary. For this we require Φ^S in the same coordinates as Φ^N, which in this model is Kerr-Schild coordinates.

In principle, we could obtain Φ^S in Kerr-Schild coordinates by transforming the solution from Fermi-Walker coordinates. However, in practice that is generally done by converting from Fermi-Walker coordinates to a covariant expansion [115], and such covariant expansions are already readily available to high order in the literature [75, 73, 159]. In

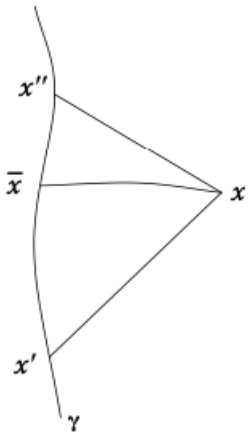

FIGURE 6.3: An illustration of field points used in the covariant calculation of the singular field. x is the point where the field is evaluated. x'' is the advanced point of x on the worldline and x' is the retarded point of x on the worldline. $\bar{x}$ is an arbitrary point on the worldline that lies after x' and before x''.

this section we review these covariant forms for the singular field. Ref. [75] derives the scalar singular field to the highest known order. The regular field will be written directly as a Taylor series in Kerr-Schild coordinates.

Refs. [75, 73, 159] use the following convention: the worldline of the charge is parametrised as $z^\mu(\tau)$, where τ is proper time, x refers to the point where the singular field is evaluated. $\bar{x}$ is an arbitrary point on the worldline, except for the fact that it is in spacelike separation with x. It is assumed that x belongs to a convex normal neighbourhood of $\bar{x}$, i.e. the set of points that are linked to $\bar{x}$ by unique geodesics. The indices we assign to the various spacetime points will mirror their notational form, e.g. at x we assign indices α, at $\bar{x}$, we assign indices $\bar{\alpha}$.

The covariant expressions contain several ingredients. $\sigma(x,\bar{x})$ is the Synge world function [141], equal to one half of the squared geodesic distance between x and $\bar{x}$ when x and $\bar{x}$ are spacelike separated. The gradient of the Synge's worldfunction is denoted by $\sigma_\alpha(x,\bar{x})$ if it is differentiated with respect to its first argument, or $\sigma_{\bar{\alpha}}(x,\bar{x})$ if it is differentiated with respect to its second argument. $\bar{r}$ and s are the tangential and normal projections of distance with respect to the worldline:

$$\bar{r} := \sigma_{\bar{\alpha}}(x,\bar{x})u^{\bar{\alpha}}, \tag{6.41}$$

and

$$s^2 := (g^{\bar{\alpha}\bar{\beta}} + u^{\bar{\alpha}}u^{\bar{\beta}})\sigma_{\bar{\alpha}}(x,\bar{x})\sigma_{\bar{\beta}}(x,\bar{x}). \tag{6.42}$$

The identity $s^2 = 2\sigma(x,\bar{x}) + \bar{r}^2$ shows that s^2 is positive when x and $\bar{x}$ are spacelike separated. This identity itself can be explained by noting $g^{\bar{\alpha}\bar{\beta}}\sigma_{\bar{\alpha}}\sigma_{\bar{\beta}} = 2\sigma$.

Finally, ϵ is a book-keeping quantity, measuring the fundamental scale of separation between x and $\bar{x}$. In terms of these quantities, the covariant expansion of Φ_S through order ϵ^4 is given by [75, 159]

$$\begin{aligned}\Phi^S =& e\Bigg\{\frac{1}{s}+\frac{\bar{r}^2+s^2}{6\bar{s}^3}C_{u\sigma u\sigma}+\frac{1}{24s^3}\Big((\bar{r}^2-3s^2)\bar{r}C_{u\sigma u\sigma|u}-(\bar{r}^2-s^2)C_{u\sigma u\sigma|\sigma}\Big)\\ &+\frac{1}{360s^5}\Big[\Phi_S\Big]_{(3)}+\mathcal{O}(\epsilon^4)\Bigg\},\end{aligned} \tag{6.43}$$

where

$$\begin{aligned}\Big[\Phi^S\Big]_{(3)} =& \,15\Big[\bar{r}^2-\bar{s}^2\Big]^2C_{u\sigma u\sigma}C_{u\sigma u\sigma}+\bar{s}^2\Big[(\bar{r}^2-\bar{s}^2)(3C_{u\sigma u\sigma|\sigma\sigma}+4C_{u\sigma\sigma\bar{\alpha}}C^{\bar{\alpha}}_{u\sigma\sigma})\\ &+(\bar{r}^4-6\bar{r}^2\bar{s}^2-3\bar{s}^4)(4C_{u\sigma u\bar{\alpha}}C^{\bar{\alpha}}_{u\sigma u}+3C_{u\sigma u\sigma|uu})+\bar{r}(\bar{r}^2-3\bar{s}^2)(16C^{\bar{\alpha}}_{u\sigma u}C_{u\sigma\sigma\bar{\alpha}}-3C_{u\sigma u\sigma|u\sigma})\Big]\\ &+\bar{s}^4\Big[2C^{\bar{\alpha}\bar{\beta}}_{uu}[(\bar{r}^2+\bar{s}^2)C_{\sigma\bar{\alpha}\sigma\bar{\beta}}+2\bar{r}(\bar{r}^2+3\bar{s}^2)C_{u\bar{\alpha}\sigma\bar{\beta}}]+2C^{\bar{\alpha}\bar{\beta}}_{u\sigma}[2\bar{r}C_{\sigma\bar{\alpha}\sigma\bar{\beta}}+(\bar{r}^2+\bar{s}^2)C_{u\bar{\beta}\sigma\bar{\alpha}}]\\ &+[\bar{r}^4+6\bar{r}^2\bar{s}^2+\bar{s}^4]C_{u\bar{\alpha}u\bar{\beta}}C^{\bar{\alpha}\bar{\beta}}_{uu}+[\bar{r}^2+\bar{s}^2]2C_{u\bar{\alpha}\sigma\bar{\beta}}C^{\bar{\alpha}\bar{\beta}}_{u\sigma}+C_{\sigma\bar{\alpha}\sigma\bar{\beta}}C^{\bar{\alpha}\bar{\beta}}_{\sigma\sigma}\Big].\end{aligned} \tag{6.44}$$

Here $C_{\alpha\beta\mu\nu}$ is the Weyl curvature tensor. The compact notation used represents the projection of the tensor along the vectors $\sigma^{\bar{\alpha}}$ and $u^{\bar{\alpha}}$:

$$C_{u\sigma u\sigma} := C_{\bar{\alpha}\bar{\beta}\bar{\mu}\bar{\nu}}u^{\bar{\alpha}}\sigma^{\bar{\beta}}u^{\bar{\mu}}\sigma^{\bar{\nu}}, \tag{6.45}$$

$$C_{u\sigma u\sigma|\sigma} := C_{\bar{\alpha}\bar{\beta}\bar{\mu}\bar{\nu};\bar{\gamma}}u^{\bar{\alpha}}\sigma^{\bar{\beta}}u^{\bar{\mu}}\sigma^{\bar{\nu}}\sigma^{\bar{\gamma}}. \tag{6.46}$$

The Weyl tensor, its derivatives and the velocity vector $u^{\bar{\alpha}}$ are all evaluated at the reference point $\bar{x}$ on the worldline of the particle.

6.3.4 Transformation to Kerr-Schild Coordinates

We now transform the above expressions for the scalar singular field into Kerr-Schild coordinates. To achieve this we follow the method in [159]. All terms in Eq. (6.43) can be written in terms of $\sigma_{\bar{\alpha}}$ and local quantities at $\bar{x}$. Forming a coordinate expression for $\Phi^S(x)$ involves re-expressing terms using an expansion in the coordinate separation between x and $\bar{x}$, which we define $\Delta x^\alpha := x^\alpha - \bar{x}^{\bar{\alpha}}$. In our implementation we choose $\bar{x}$ to be the point with the same Kerr-Schild time as x, such that $\Delta t = t - \bar{t} = 0$.

The expansion of $\sigma(x,\bar{x})$ about $\bar{x}$ in the powers of the coordinate separation Δx^α is given by [159]

$$\begin{aligned}\sigma = &\frac{1}{2}g_{\bar{\alpha}\bar{\beta}}\Delta x^\alpha \Delta x^\beta + A_{\bar{\alpha}\bar{\beta}\bar{\gamma}}\Delta x^\alpha \Delta x^\beta \Delta x^\gamma + B_{\bar{\alpha}\bar{\beta}\bar{\gamma}\bar{\delta}}\Delta x^\alpha \Delta x^\beta \Delta x^\gamma \Delta x^\delta \\ &+ C_{\bar{\alpha}\bar{\beta}\bar{\gamma}\bar{\delta}\bar{\rho}}\Delta x^\alpha \Delta x^\beta \Delta x^\gamma \Delta x^\delta \Delta x^\rho + \dots\end{aligned} \tag{6.47}$$

First we use the identity $2\sigma = \sigma_{\bar{\alpha}}\sigma^{\bar{\alpha}}$ to recursively determine the coefficients $A_{\bar{\alpha}\bar{\beta}\bar{\gamma}}, B_{\bar{\alpha}\bar{\beta}\bar{\gamma}\bar{\delta}}$ and $C_{\bar{\alpha}\bar{\beta}\bar{\gamma}\bar{\delta}\bar{\rho}}$ and so on, for example $A_{\bar{\alpha}\bar{\beta}\bar{\gamma}} = \frac{1}{4}g_{(\bar{\alpha}\bar{\beta},\bar{\gamma})}$. We can then differentiate this expression at $\bar{x}$ to give us

$$\begin{aligned}\sigma_{\bar{\alpha}} = &g_{\bar{\alpha}\bar{\beta}}\Delta x^\beta + (g_{\bar{\gamma}\bar{\gamma},\bar{\alpha}} + 3A_{\bar{\alpha}\bar{\beta}\bar{\gamma}})\Delta x^\beta \Delta x^\gamma + (A_{\bar{\alpha}\bar{\beta}\bar{\gamma},\bar{\alpha}} + 4B_{\bar{\alpha}\bar{\beta}\bar{\gamma}\bar{\delta}})\Delta x^\beta \Delta x^\gamma \Delta x^\delta \\ &+ (B_{\bar{\beta}\bar{\gamma}\bar{\delta}\bar{\rho},\bar{\alpha}} + 5C_{\bar{\alpha}\bar{\beta}\bar{\gamma}\bar{\delta}\bar{\rho}})\Delta x^\beta \Delta x^\gamma \Delta x^\delta \Delta x^\rho + \dots\end{aligned} \tag{6.48}$$

This expression is then substituted into Eq. (6.43). After this, $\sigma_{\bar{\alpha}}$ is contracted with the four-velocity, metric and Riemann tensor to get the coordinate expressions for $\bar{r}, s^2$ and the Weyl terms as per their formulae in Eqs. (6.41), (6.42) and Eqs. (6.45), (6.46).

All terms within Eq. (6.43) can now be expressed as a coordinate expansion in powers of Δx^α. By inserting these expansions the final result is an explicit expression for Φ_S in the adopted system of coordinates, expanded to the desired order of accuracy.

We choose to write the results for the field in the style of [34]; Φ^S expressed as an expansion in powers of $1/s_1$. Here s_1 is the leading-order piece of s. It is first easier to compute the coordinate expansion of s^2 in powers of ϵ,

$$s^2 = \epsilon^2 S_1 + \epsilon^3 S_2 + \epsilon^4 S_3 + \epsilon^5 S_4 + \mathcal{O}(\epsilon^6). \tag{6.49}$$

From this we can then obtain the expansion of $s = \epsilon\sqrt{S_1}\sqrt{1 + \frac{\epsilon S_2 + \epsilon^2 S_3 + \epsilon^3 S_4 + \mathcal{O}(\epsilon^5)}{S_1}}$, which takes the form

$$s = \epsilon s_1 + \frac{\epsilon^2 \mathrm{p}_3(\Delta x^\alpha)}{s_1} + \frac{\epsilon^3 \mathrm{p}_6(\Delta x^\alpha)}{s_1^3} + \frac{\epsilon^4 \mathrm{p}_9(\Delta x^\alpha)}{s_1^5} + \mathcal{O}(\epsilon^5), \tag{6.50}$$

and

$$\frac{1}{s} = \frac{1}{\epsilon s_1} + \frac{\mathrm{q}_3(\Delta x^\alpha)}{s_1^3} + \frac{\epsilon \mathrm{q}_6(\Delta x^\alpha)}{s_1^5} + \frac{\epsilon^2 \mathrm{q}_9(\Delta x^\alpha)}{s_1^7} + \mathcal{O}(\epsilon^3), \tag{6.51}$$

where $\mathrm{p}_n(\Delta x^\alpha)$ and $\mathrm{q}_n(\Delta x^\alpha)$ are polynomials in $\mathcal{O}(\Delta x^\alpha)$ of order n. These are related by $\mathrm{q}_3 = -\mathrm{p}_3, \mathrm{q}_6 = \mathrm{p}_3^2 - \mathrm{p}_6, \mathrm{q}_9 = -\mathrm{p}_3^3 + 2\mathrm{p}_3\mathrm{p}_6 - \mathrm{p}_9$. Here $s_1 = \sqrt{(g_{\bar{\alpha}\bar{\beta}} + u_{\bar{\alpha}}u_{\bar{\beta}})\Delta x^\alpha \Delta x^\beta}$.

At leading order $\Phi^S = 1/(s) + \mathcal{O}(\epsilon^0)$, but the structure seen in Eq. (6.51) carries over to the higher order terms in the covariant expression. This means

$$\Phi^S = e\left\{\frac{1}{\epsilon s} + \epsilon\frac{\bar{r}^2 + s^2}{6\bar{s}^3}C_{u\sigma u\sigma} + \epsilon^2\frac{1}{24 s^3}\left((\bar{r}^2 - 3s^2)\bar{r}C_{u\sigma u\sigma|u} - (\bar{r}^2 - s^2)C_{u\sigma u\sigma|\sigma}\right) + \mathcal{O}(\epsilon^3)\right\} \tag{6.52}$$

can be written as

$$\Phi^S = e\left\{\frac{1}{\epsilon s_1} + \frac{\mathrm{P}_3(\Delta x^\alpha)}{s_1^3} + \frac{\epsilon \mathrm{P}_6(\Delta x^\alpha)}{s_1^5} + \frac{\epsilon^2 \mathrm{P}_9(\Delta x^\alpha)}{s_1^7} + \mathcal{O}(\epsilon^3)\right\}. \tag{6.53}$$

The Kerr-Schild coordinate expressions are too long to be included here in print. Instead we give s_1 and the polynomials $\mathrm{P}_3(\Delta x^\alpha), \mathrm{P}_6(\Delta x^\alpha), \mathrm{P}_9(\Delta x^\alpha)$ in Appendix A.

6.4 Matching Method in Kerr-Schild Coordinates

We now want to generalize the Fermi-Walker matching procedure, presented in Sec. 6.3.2, to Kerr-Schild coordinates. (Though the presentation here is still valid in generic coordinates and a generic spacetime.) As motivated by the Fermi-Walker discussion, we want to match the numerical and analytical fields multipole by multipole, where multipoles are now defined on spheres of constant Kerr-Schild coordinate distance from the particle $\rho = \sqrt{\Delta x^2 + \Delta y^2 + \Delta z^2}$ where $(\Delta x^i) = x^i - \bar{x}^i(t)$, $\bar{x}^i(t)$ now denoting the coordinates of the particle.

We want to match the approximate analytical solution for the scalar field inside the worldtube ($\Phi^S + \Phi^R := \Phi^A$) to the numerical field (Φ^N) on the boundary of the worldtube. The matching method's function is to solve for the unknowns within Φ^R. Given we now have Φ^S in Kerr-Schild coordinates, it is simpler to subtract it from Φ^N as first step, defining $\tilde{\Phi}^N := \Phi^N - \Phi^S$. We will then match

$$\Phi^R_{\ell m}(t, x^i)|_\rho = \tilde{\Phi}^N_{\ell m}(t, x^i)|_\rho. \tag{6.54}$$

It should be noted that unlike in Fermi-Walker coordinates, the puncture does not have a simple multipole structure in Kerr-Schild coordinates, but we absorb that complexity into $\tilde{\Phi}_N$. In practice the multipole modes of $\tilde{\Phi}_N$ are found through numerical integration over the worldtube at each time step.

The regular field is taken to be a three-dimensional Taylor series in arbitrary (but in our case Kerr-Schild) spatial coordinate separation at each time slice,

$$\Phi^R(t, x^i) = \Phi^R_0(t) + \Phi^R_{1i}(t)\Delta x^i + \Phi^R_{2ij}(t)\Delta x^i \Delta x^j + \mathcal{O}(x^3), \tag{6.55}$$

with the notation $\Phi^R_0(t) \equiv \Phi^R(t, \Delta x^i = 0)$, $\Phi^R_{1i}(t) \equiv \partial_i \Phi^R(t, \Delta x^i = 0)$.... The multipole structure of the regular field here is the same as described in Fermi-Walker coordinates: a term with n powers of Δx^i is a linear combination of $\ell \leq n$ harmonics defined on spheres of constant $\rho = \sqrt{\delta_{ab}\Delta x^a \Delta x^b}$, and the STF pieces are precisely $\ell = n$ harmonics.

At the order of Eq. (6.55) the second-order derivative is broken up into the trace part and the STF part. The coefficients $\Phi^R_0(t), \delta^{ij}\Phi^R_{2ij}(t)$ will be determined from the $\ell = 0$

matching, Φ^R_{1i} will be determined from the $\ell = 1$ matching, and the STF part, $\Phi^R_{2\langle ij\rangle}$, will be determined from the $\ell = 2$ matching. Recall again ℓ refers to modes on a sphere around the particle rather than modes on spheres around the central black hole.

6.4.1 Zeroth-Order Implementation

We expand the regular field up to leading order in coordinates:

$$\Phi^R(t, x^i) = \Phi^R_0(t) + \mathcal{O}(\Delta x). \tag{6.56}$$

We now impose Dirichlet boundary conditions to match the fields

$$\Phi^R_{\ell m}(t, x^i)|_\rho = \tilde{\Phi}^N_{\ell m}(t, x^i)|_\rho \ \text{ for } \ \ell = 0. \tag{6.57}$$

This gives

$$\Phi^R_0(t) = \tilde{\Phi}^N_0(t), \tag{6.58}$$

where Eq. (6.58) is analogue of Eq. (6.35) in Sec. 6.3.2.

6.4.2 First-Order Implementation

We expand the regular field up to first order in coordinates:

$$\Phi^R(t, x^i) = \Phi^R_0(t) + \Phi^R_{1i}(t)\Delta x^i + \mathcal{O}(\Delta x^2). \tag{6.59}$$

We now impose Dirichlet boundary conditions to match the fields

$$\Phi^R_{\ell m}(t, x^i)|_\rho = \tilde{\Phi}^N_{\ell m}(t, x^i)|_\rho \ \text{ for } \ \ell = 0, 1. \tag{6.60}$$

This gives

$$\Phi^R_0(t) = \tilde{\Phi}^N_0(t), \tag{6.61}$$

$$\Phi^R_{1i}(t)\rho n^i = \tilde{\Phi}^N_{1i}(t) n^i, \tag{6.62}$$

where $n^i := \Delta x^i / r$. Here, Eqs. (6.61)-(6.62) are the analogues of Eqs. (6.35)-(6.36) in Sec. 6.3.2. Consequently, the field inside the worldtube is completely determined by the field on the boundary up to first order.

6.4.3 Second-Order Implementation

We now expand the scalar field to second order in x^i:

$$\Phi^R(t, x^i) = \Phi^R_0(t) + \Phi^R_{1i}(t)\Delta x^i + \Phi^R_{2ij}(t)\Delta x^i \Delta x^j + \mathcal{O}(x^3). \tag{6.63}$$

Just as seen in Sec. 6.3.2 in Fermi coordinates, the STF piece $\Phi^R_{2\langle ij\rangle}$ must be determined by matching the $\ell = 2$ multipole mode. Whereas, the trace piece of Φ^R_{2ij} can be expressed in terms of lower-order coefficients using the wave equation, using the fact that Φ^R must satisfy the homogeneous wave equation.

Just as in the lower-order implementations, we first impose Dirichlet boundary conditions to match the fields

$$\Phi^R_{\ell m}(t, x^i)|_\rho = \tilde{\Phi}^N_{\ell m}(t, x^i)|_\rho \text{ for } \ell = 0, 1, 2. \tag{6.64}$$

This gives

$$\Phi^R_0(t) + \frac{1}{3}\rho^2\delta^{ij}\Phi^R_{2ij} = \tilde{\Phi}^N_0(t), \tag{6.65}$$

$$\Phi^R_{1i}(t)\rho n^i = \tilde{\Phi}^N_{1i}(t)n^i, \tag{6.66}$$

$$\Phi^R_{2\langle ij\rangle}(t)\rho^2 n^i n^j = \Phi^N_{2\langle ij\rangle}(t)n^i n^j. \tag{6.67}$$

We see that for a second-order expansion, the boundary conditions will give us only 9 equations for 10 unknowns, i.e. we cannot solve for *both* $\Phi^R_0(t)$ and $\delta^{ij}\Phi^R_{2ij}$. Solving for the last unknown has to make use of the wave equation,

$$g^{\mu\nu}\nabla_\mu\nabla_\nu\Phi = g^{\mu\nu}\partial_\mu\partial_\nu\Phi - \Gamma^\rho\partial_\rho\Phi = 0. \tag{6.68}$$

where $\Gamma^\rho := g^{\mu\nu}\Gamma^\rho_{\mu\nu}$. To expand the wave equation near the particle, we require the expansions of the smooth fields $g^{\mu\nu}$ and Γ^μ, which we write as

$$g^{\mu\nu}(t, x^i) = g^{\mu\nu}_0(t) + g^{\mu\nu}_{1i}(t)\Delta x^i + g^{\mu\nu}_{2ij}(t)\Delta x^i\Delta x^j + \mathcal{O}(x^3), \tag{6.69}$$

$$\Gamma^\mu = \Gamma^\mu_0(t) + \Gamma^\mu_{1i}(t)\Delta x^i + \Gamma^\mu_{2ij}(t)\Delta x^i\Delta x^j + \mathcal{O}(x^3). \tag{6.70}$$

Inserting the expansions into the wave equation, Eq. (6.68), we obtain

$$\begin{aligned}&[g^{\mu\nu}_0(t) + g^{\mu\nu}_{1i}(t)\Delta x^i + g^{\mu\nu}_{2ij}(t)\Delta x^i\Delta x^j]\partial_\mu\partial_\nu[\Phi^R_0(t) + \Phi^R_{1i}(t)\Delta x^i + \Phi^R_{2ij}(t)\Delta x^i\Delta x^j]\\ &- [\Gamma^\mu_0(t) + \Gamma^\mu_{1i}(t)\Delta x^i + \Gamma^\mu_{2ij}(t)\Delta x^i\Delta x^j]\partial_\mu[\Phi^R_0(t) + \Phi^R_{1i}(t)\Delta x^i + \Phi^R_{2ij}(t)\Delta x^i\Delta x^j] = 0.\end{aligned} \tag{6.71}$$

Solving at order $(\Delta x^i)^0$, recalling $\Delta x^i = x^i - \bar{x}^i(t)$, we find

$$\begin{aligned}(\Delta x^i)^0 : \quad & g^{00}_0\ddot{\Phi}^R_0 - g^{00}_0\Phi^R_{1i}\ddot{\bar{x}}^i - 2g^{00}_0\dot{\Phi}^R_{1i}\dot{\bar{x}}^i + 2g^{00}_0\Phi^R_{2ij}\dot{\bar{x}}^i\dot{\bar{x}}^i + 2g^{0i}_0\dot{\Phi}^R_{1i}\\ & + 2g^{ij}_0\Phi^R_{2ij} - \Gamma^0_0\dot{\Phi}^R_0 + \Gamma^0_0\Phi^R_{1i}\dot{\bar{x}}^i - \Gamma^i_0\Phi^R_{1i} = 0.\end{aligned} \tag{6.72}$$

We then re-write Eq. (6.72) using $\Phi^R_{2ij} = \Phi^R_{2\langle ij\rangle} + \frac{1}{3}\delta_{ij}\delta^{kl}\Phi^R_{2kl}$, giving

$$\begin{aligned} &g_0^{00}\ddot{\Phi}^R_0 - g_0^{00}\Phi^R_{1i}\ddot{\bar{x}}^i - 2g_0^{00}\dot{\Phi}^R_{1i}\dot{\bar{x}}^i + 2g_0^{00}(\Phi^R_{2\langle ij\rangle} + \frac{1}{3}\delta_{ij}\delta^{kl}\Phi^R_{2kl})\dot{\bar{x}}^i\dot{\bar{x}}^i + 2g_0^{0i}\dot{\Phi}^R_{1i} \\ &+ 2g_0^{ij}(\Phi^R_{2\langle ij\rangle} + \frac{1}{3}\delta_{ij}\delta^{kl}\Phi^R_{2kl}) - \Gamma^0_0\dot{\Phi}^R_0 + \Gamma^0_0\Phi^R_{1i}\dot{\bar{x}}^i - \Gamma^i_0\Phi^R_{1i} = 0. \end{aligned} \tag{6.73}$$

We can rearrange the constant part of Eq. (6.65), which gives $g_0^{ij}\Phi^R_{2ij} = 3\frac{\tilde{\Phi}^N_0 - \Phi^R_0}{r^2}$. Inserting this into Eq. (6.73) yields a second-order ODE for Φ^R_0:

$$\begin{aligned} &g_0^{00}\ddot{\Phi}^R_0 - g_0^{00}\Phi^R_{1i}\ddot{\bar{x}}^i - 2g_0^{00}\dot{\Phi}^R_{1i}\dot{\bar{x}}^i + 2g_0^{00}\Phi^R_{2\langle ij\rangle} + 2g_0^{00}\delta_{ij}\frac{\tilde{\Phi}^N_0 - \Phi^R_0}{r^2}\dot{\bar{x}}^i\dot{\bar{x}}^i + 2g_0^{0i}\dot{\Phi}^R_{1i} \\ &+ 2g_0^{ij}\Phi^R_{2\langle ij\rangle} + 2g_0^{ij}\delta_{ij}\frac{\tilde{\Phi}^N_0 - \Phi^R_0}{r^2} - \Gamma^0_0\dot{\Phi}^R_0 + \Gamma^0_0\Phi^R_{1i}\dot{\bar{x}}^i - \Gamma^i_0\Phi^R_{1i} = 0. \end{aligned} \tag{6.74}$$

Solving this numerically will then fix the form of the final unknown at this order, Φ^R_0.

The full numerical algorithm can be laid out step by step, as follows:

1. We project the field $\tilde{\Phi}^N$ on the worldtube boundary onto spherical harmonics Y_{00}, Y_{1m} and Y_{2m}. The resulting coefficients can then be mapped to $\tilde{\Phi}^N_0$, $\tilde{\Phi}^N_{1i}$, $\tilde{\Phi}^N_{2\langle ij\rangle}$ using the relations between symmetric trace-free (STF) tensors and spherical harmonics, as detailed in Sec. II A of [145].

   Eqs. (6.65)-(6.67) then directly gives us the 8 coefficients Φ^R_{1i} and $\Phi^R_{2\langle ij\rangle}$ of the scalar field inside the worldtube.

2. We project the time derivative of the scalar field $\dot{\tilde{\Phi}}^N$ of the numerical domain on the worldtube boundary onto spherical harmonics Y_{00}, Y_{1m} and Y_{2m}. $\dot{\tilde{\Phi}}^N$ can be directly obtained from the numerical fields. This data can then be mapped directly to $\dot{\tilde{\Phi}}^N_0$, $\dot{\tilde{\Phi}}^N_{1i}$, $\dot{\tilde{\Phi}}^N_{2\langle ij\rangle}$ again using the relation between STF tensors and spherical harmonics. By taking a time derivative of Eqs. (6.65)-(6.67), we can immediately fix the time derivative of the 8 coefficients $\dot{\Phi}^R_{1i}$ and $\dot{\Phi}^R_{2\langle ij\rangle}$ of the scalar field inside the worldtube.

3. We now obtain Φ^R_0 and $\dot{\Phi}^R_0$ by solving the 2 coupled ODEs which come from the reduction of Eq. (6.74) to first order:

$$\frac{d}{dt}\Phi^R_0 = \hat{\Phi}^R_0, \tag{6.75}$$

$$\begin{aligned} g_0^{00}\frac{d}{dt}\hat{\Phi}^R_0 = {}& g_0^{00}\Phi^R_{1i}\ddot{\bar{x}}^i + 2g_0^{00}\dot{\Phi}^R_{1i}\dot{\bar{x}}^i - 2g_0^{00}\Phi^R_{2\langle ij\rangle} - 2g_0^{00}\delta_{ij}\frac{\tilde{\Phi}^N_0 + \Phi^R_0}{r^2}\dot{\bar{x}}^i\dot{\bar{x}}^i - 2g_0^{0i}\dot{\Phi}^R_{1i} \\ &- 2g_0^{ij}\Phi^R_{2\langle ij\rangle} - 2g_0^{ij}\delta_{ij}\frac{\tilde{\Phi}^N_0 + \Phi^R_0}{r^2} + \Gamma^0_0\hat{\Phi}^R_0 - \Gamma^0_0\Phi^R_{1i}\dot{\bar{x}}^i + \Gamma^i_0\Phi^R_{1i}. \end{aligned} \tag{6.76}$$

4. The last undetermined coefficients of the scalar field inside the worldtube, $\delta^{ij}\Phi^R_{2ij}$ and $\delta^{ij}\dot{\Phi}^R_{2ij}$, can be obtained from the constant part of Eq. (6.65) and its time derivative:

$$\delta^{ij}\Phi^R_{2ij} = \frac{3}{r^2}[\tilde{\Phi}^N_0 - \Phi^R_0(t)], \tag{6.77}$$

$$\delta^{ij}\dot{\Phi}^R_{2ij} = \frac{3}{r^2}[\dot{\tilde{\Phi}}^N_0 - \dot{\Phi}^R_0(t)]. \tag{6.78}$$

This completely specifies the scalar field Φ and its time derivative Φ inside the worldtube up to $\mathcal{O}(\Delta x^\alpha)^2$.

5. We need to provide boundary conditions to the numerical field on the worldtube boundary for all evolution variables which are linear combinations of Φ, $\dot{\Phi}$ and $\partial_i\Phi$. We can calculate the spatial derivative $\partial_i\Phi$ by differentiating Eq. (6.63):

$$\partial_i\Phi^R = \Phi^R_{1i} + \frac{2}{3}\delta^{lk}\Phi^R_{2lk}\delta_{ij}x^j + 2\Phi^R_{2\langle ij\rangle}x^j. \tag{6.79}$$

We then evaluate the evolved fields on the collocation points of the numerical domain on the worldtube boundary. This information is then passed into the domain as boundary conditions, which are applied via the upwind flux.

6.5 Results

The model is tested with the scalar charge e, on a circular orbit of radius of $5M$ around the Schwarzschild black hole, M. The outer boundary of the numerical domain is placed at $400M$. The radius of the worldtube is varied between $0.2M$ and $1.6M$ and we test the implementation of an approximate analytical solution to order $n = 0, 1$ and 2. The simulations are run until the field settles to a steady state solution over the entire domain, which takes between $t = 3000M$ and $t = 7000M$.

Figure 6.4 shows the equatorial plane of the domain, at a late time. The charge is at the location of the red dot, while the excised interior of the black hole is the white circle. The scalar charge is seen to emit scalar radiation as it orbits the black hole, creating an outward propagating spiral. The amplitude of the scalar radiation is illustrated by the color gradient scale.

6.5.1 Convergence with Resolution

We first examine the convergence of the model with respect to resolution, i.e. the Legendre polynomial basis order of the spectral elements. Figure 6.5 is taken from a $n = 2$, $R = 1.6M$ model. The model has 128 spectral elements, each of which has a polynomial basis of order 7. Each line in the figure represents an element and shows the magnitude

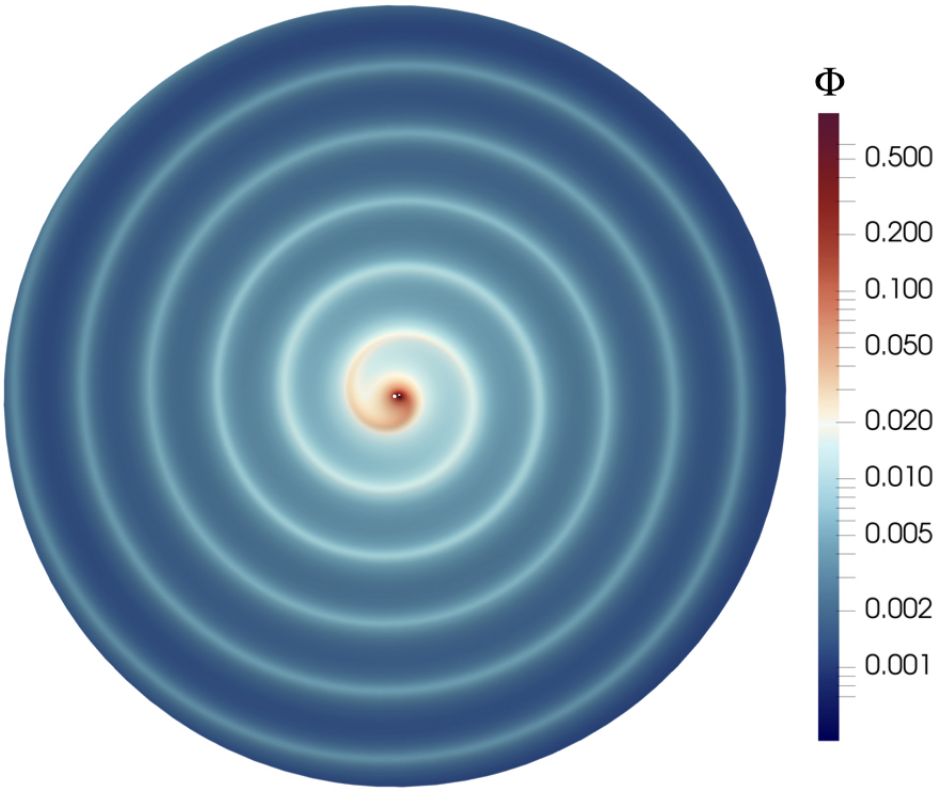

FIGURE 6.4: A late time slice showing the equatorial plane of the domain. The excised interior of the black hole is visible as the white circle in the center of the domain. Scalar waves are seen to emanate from the charge as it orbits the black hole, creating an outward propagating spiral. The amplitude of the scalar radiation is illustrated by the color gradient scale.

of the 0th to 7th basis coefficient within that element. When plotted on a semi-log plot, the straight line demonstrates the exponential convergence with respect to numerical resolution. Beyond polynomial order 7, the model employs a filter on higher-order coefficients for stability. This is seen in the steep gradient fall off from 7 onwards.

6.5.2 Convergence with Worldtube Size

We now turn to assessing the convergence of the 3+1D scalar-field model with worldtube size. The error's scaling with worldtube radius R can be estimated using the same type of argument as in Sec. 4.3.2.3. While Eq. (4.30) held for the 1D case, here we replace the integral over the line element ds' with the spatial element dS'

$$\Phi^N(\boldsymbol{x}) = \int_{\partial V} \left[\Phi^N(\boldsymbol{x}')\partial_{n'}G(\boldsymbol{x},\boldsymbol{x}') - G(\boldsymbol{x},\boldsymbol{x}')\partial_{n'}\Phi^N(\boldsymbol{x}')\right] R^2 d\Omega dt \tag{6.80}$$

where $d\Omega = \sin\theta d\theta d\phi$. In this case, due to the integration over the two-dimensional surface of radius R, assuming an R^{n+1} error in Φ^N and loss of one order of accuracy in the derivatives $\partial_{n'}\Phi^N$, the error would be expected to scale as $\mathcal{O}(R^{n+2})$.

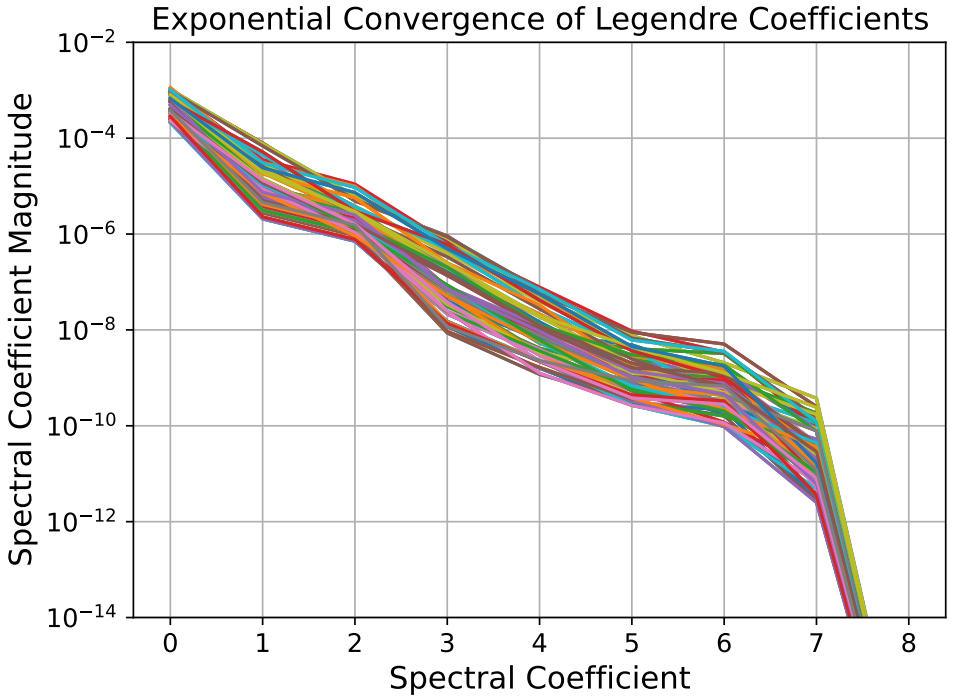

FIGURE 6.5: The magnitude of the spectral coefficient, plotted against the spectral coefficient on a semi-log scale, for 128 spectral elements. This shows exponential convergence of the model, with respect to resolution.

In these results, the numerical resolution is fixed at a sufficiently high value such that it does not affect the steady state solution. This ensures the measured errors are due to the worldtube size.

Solution along z-axis

Here we restrict our analysis to the value of the field on the z-axis. On the z-axis only axisymmetric ($m = 0$) modes contribute to the field. As long as we sum our exact analytical solution for an $\ell, m = 0$ mode from Eq. (3.13) over a sufficient number of ℓ modes, the solution can then act as an analytical baseline against which to compare our worldtube results. This is given by

$$\Phi^A(z) = e \sum_{\ell=0}^{\infty} \Psi_{\ell 0}(z) Y_{\ell 0}(\theta, \phi). \tag{6.81}$$

This mode-sum converges exponentially everywhere except for on and near the sphere $r = r_p$, where the convergence is very slow. As such, we do not have a method of reconstructing the analytical solution there, and so this region is omitted from any plots which use Φ^A as a baseline.

Figure 6.6 shows the relative error $|\Phi^N - \Phi^A|/|\Phi^A|$ for two worldtube radii $R = 0.4M$ and $R = 1.6M$, between $z = 0M$ and $z = 100M$. The error is fairly constant across the

axis after the solution has settled to its final value. We can see the error decreases with higher order n, or smaller worldtube radii R.

We now examine the relative L^1 error norm, as done in the analysis of the 1+1D model results. To calculate the relative L^1 error norm we integrate the relative error shown in Fig. 6.6 between $z = 10M$ and $z = 100M$ and then normalize by the analytical solution integrated over the same region. This is given by

$$\varepsilon = \frac{\|\Phi^N(z) - \Phi^A(z)\|_{L^1}}{\|\Phi^A(z)\|_{L^1}}. \tag{6.82}$$

The result is shown in the top panel of Fig. 6.7. Each cross represents the integrated, relative error of a simulation's final value. Also plotted is a best fit of the error convergence $\varepsilon \propto R^\alpha$, where R is the worldtube radius and α is the global convergence order. In the bottom panel, we have plotted the local convergence order between two simulations with adjacent worldtube radii,

$$\alpha_{loc,i} = \frac{\log(\varepsilon_i) - \log(\varepsilon_{i-1})}{\log(R_i) - \log(R_{i-1})}. \tag{6.83}$$

Generally we achieve the expected convergence order of $\alpha = n + 2$ in the volume outside the worldtube. The $n = 2$ model has a fitted global convergence order of 4.07 and the $n = 1$ model has a fitted global convergence order of 3.14. The $n = 0$ model has a fitted global convergence order of 2.36. The $n = 0$ model does show larger values for the local convergence order at larger worldtube radii, which suggests that here R is not sufficiently small to ensure the dominating error of the model is of $\mathcal{O}(R^{n+2})$. However, this value steadily decreases to the expected order of ≈ 2 as the worldtube radii decreases and the simulation enters the appropriately convergent regime.

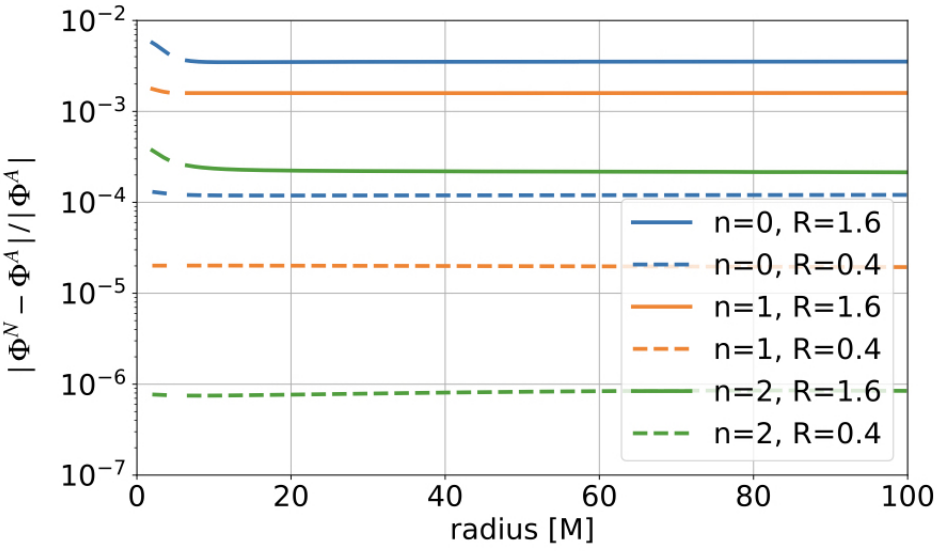

FIGURE 6.6: The relative error of the scalar field Φ^N along the z-axis compared to the analytical solution Φ^A given by Eq. (6.81). We show two simulations with worldtube radii $R = 1.6M$ and $R = 0.4M$ for $n = 0, 1$ and 2. The error decreases with higher order or smaller worldtube radii.

Solution along x-axis

Here we perform an internal comparison which demonstrates that the solution along the co-moving x-axis converges with the worldtube radius as expected. The x-axis connects the black hole's center with the scalar charge and here no analytical solution exists. Instead, we use the simulation with $n = 2$ and $R = 0.4$ as a baseline solution (denoted Φ^{ref}) as from the previous analysis, it is seen to have the lowest error.

Figure 6.8 shows the relative error $|\Phi^N - \Phi^{ref}|/|\Phi^{ref}|$ for two worldtube radii $R = 0.4M$ and $R = 1.6M$, between $x = 0M$ and $x = 100M$. The field along the x-axis has more sharp features as it lies in the orbital plane of the charge and therefore the relative error along the x-axis is not as smooth as along the z-axis.

We now calculate the relative L^1 error norm, by integrating the relative error shown in Fig. 6.8 between $x = 10M$ and $x = 100M$ and then normalizing by the reference solution Φ^{ref} integrated over the same region. This is given by

$$\varepsilon = \frac{\|\Phi^N(x) - \Phi^{ref}(x)\|_{L^1}}{\|\Phi^{ref}(x)\|_{L^1}}. \tag{6.84}$$

The result is shown in the top panel of Fig. 6.9. Again, each cross represents a simulation, the straight line shows a power law fit $\varepsilon \propto R^\alpha$ and in the bottom panel we show the local convergence order α_{loc}.

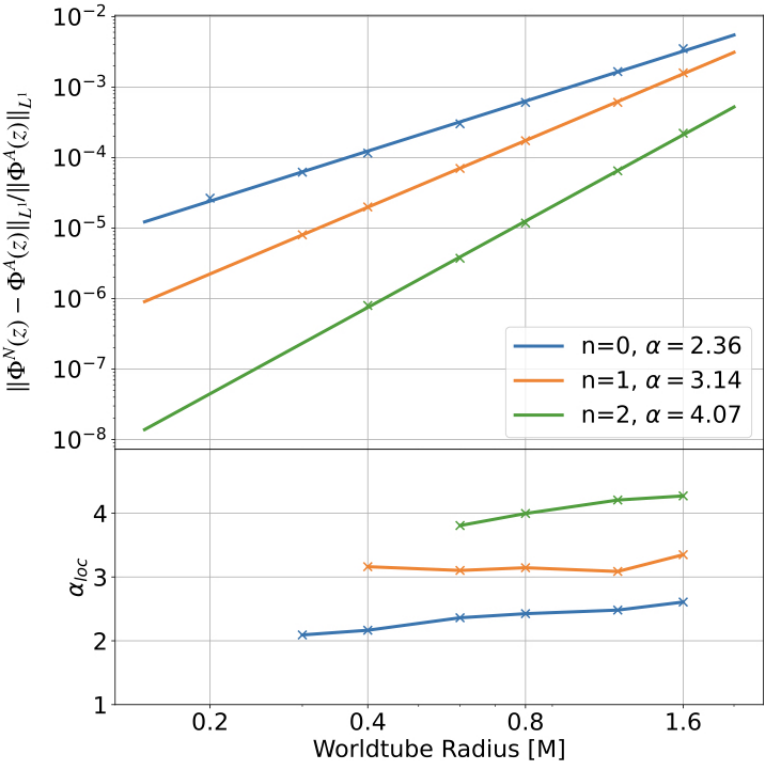

FIGURE 6.7: Top panel: the relative L^1 error norm along the z-axis with respect to the analytical solution Φ^A, defined in Eq. (6.81). Each cross represents the final value of a simulation and the straight lines are a best fit of the power law relation $\varepsilon \propto R^\alpha$. Bottom panel: the local convergence order between the simulations of adjacent worldtube radii as defined in Eq. (6.83). The results generally demonstrate the expected convergence order of $\alpha = n + 2$.

Once again, we generally achieve the expect the convergence order of $\alpha = n + 2$ in the volume outside the worldtube. The $n = 2$ model has a fitted global convergence order of 4.29. The local convergence order does appear to be increasing as the worldtube size decreases. This is unexpected, but as there are only 3 data points we do not deem it a significant result and future work will run simulations at smaller worldtube radii to investigate the trend further. The $n = 1$ model has a fitted global convergence order of 3.18. The $n = 0$ model has a fitted global convergence order of 2.29. At larger values of worldtube radii we see larger values for the local convergence order (as in the z-axis results) which again suggests that here R is not sufficiently small to ensure the dominating error of the model is of $\mathcal{O}(R^{n+2})$. However again this value steadily decreases to the expected order of ≈ 2 as the worldtube radii decreases and the simulation enters the appropriately convergent regime.

Overall the 3+1D scalar-field model shows convergent behaviour in line with our expectations when varying key parameters, and impressive relative error results. We are now ready to proceed to the BBH model.

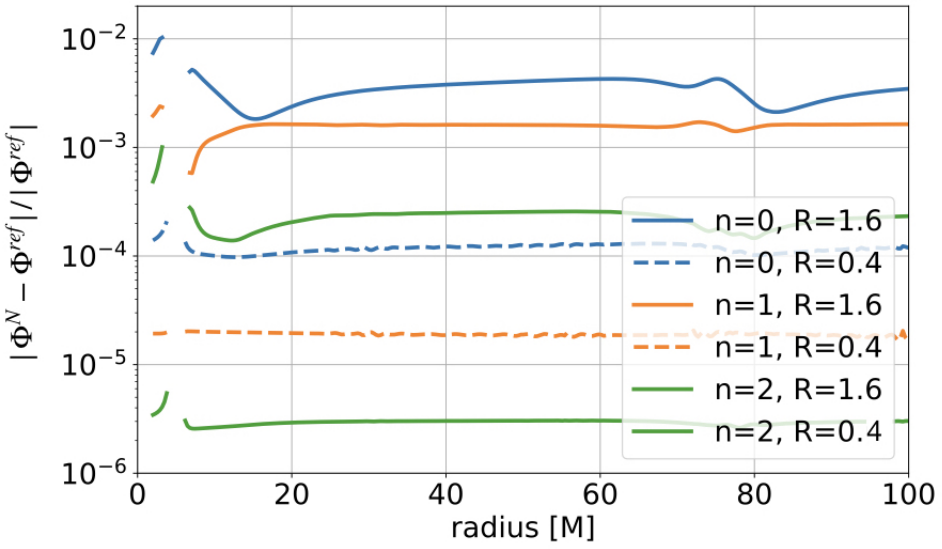

FIGURE 6.8: The relative error of the scalar field Φ^N along the x-axis compared to the reference solution Φ^{ref} which uses $n = 2$ and $R = 0.4M$. We show two simulations with worldtube radii $R = 1.6M$ and $R = 0.4M$ for $n = 0, 1$ and 2. The error decreases with higher order or smaller worldtube radii.

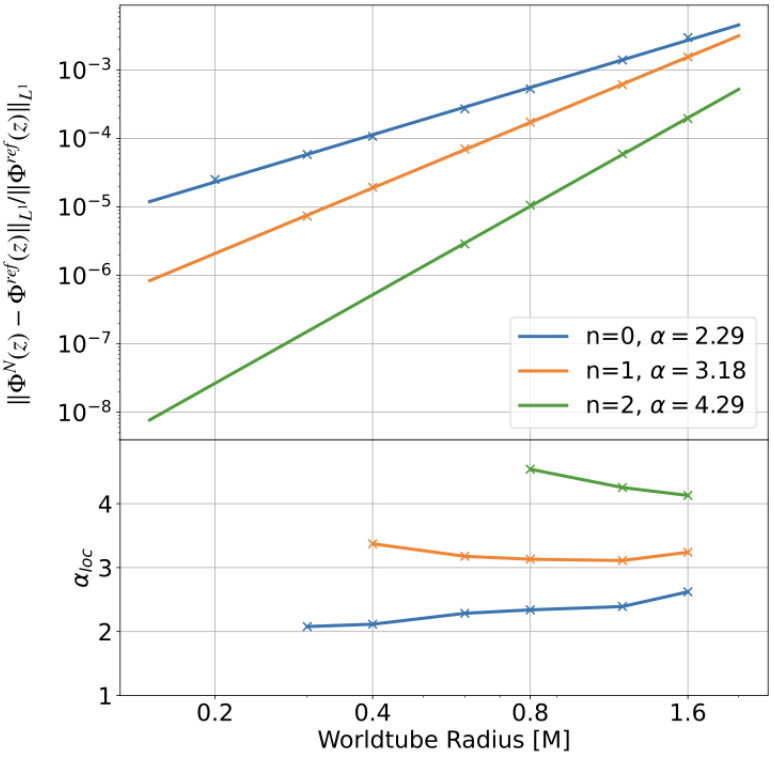

FIGURE 6.9: Top panel: The relative L^1 error norm along the x-axis with respect to the reference solution Φ^{ref} which uses $n = 2$ and $R = 0.4M$. Each cross represents a simulation and the straight lines are a best fit of the relation $\varepsilon \propto R^\alpha$. Bottom panel: The local convergence order as defined in Eq. (6.83). The results generally demonstrate the expected convergence order of $\alpha = n + 2$.

Chapter 7

Gravity Model

We now finally move on from the scalar-field toy model and begin to consider the physical BBH model. Specifically, we introduce a design for a worldtube scheme as applied to the astrophysically relevant problem of a BBH with an intermediate mass-ratio. We interchangeably refer to this as the "gravity model". We first describe the numerical evolution using SpECTRE. Here SpECTRE works with the generalised harmonic gauge formalism of NR and so we devote Sec. 7.2 to reviewing the key equations of this approach. Section 7.3 then presents the various coordinate systems that are necessary for the model's cohesion. Finally, Sec. 7.4 lays out the matching method.

7.1 Setup

The gravity model simulates the full BBH configuration, with two black holes of masses m_1 and m_2, so that $m_2/m_1 < 1$ is in the intermediate range. Our work in this thesis models two Schwarzschild black holes; a future step of the model's development will be to move to a model of Kerr black holes in order to represent realistic astrophysical IMRIs.

The NR evolution will be carried out by SpECTRE. As illustrated in Chapter 6, Fig. 6.1, standard excision will be used to remove the spacetime within the larger black hole's horizon from the computational grid. This is shown as the white region on the left in Fig. 6.1. A worldtube region now surrounding the smaller black hole will also be excised from the domain. For an idea of scale, we predict a worldtube size of order $\sqrt{m_1 m_2}$.

In this model the approximate analytical solution for the smaller black hole will be a tidally perturbed Schwarzschild metric, as first discussed in Sec. 1.3.3. The metric will now be expanded in terms of a perturbative parameter $\epsilon = \frac{m_2}{\mathcal{R}}$, where $\mathcal{R}$ is the local radius of curvature due to the larger black hole. As mentioned, the tidally perturbed

metric contains unknown tidal terms which can only be specified by matching to an external environment.

Just as in the 3+1D model, we will need this analytical solution to be in a coordinate system that is amenable to the numerical evolution. In a BBH model, SpECTRE uses the generalised harmonic gauge formulation for NR. This formulation is explained in further detail in Sec. 7.2 below. Our tidally perturbed Schwarzschild metric is given initially in light-cone coordinates to $\mathcal{O}(\epsilon^4)$ using [109] . Transforming this metric to generalised harmonic coordinates is too complex, instead we choose to transform to standard harmonic coordinates. However, this choices requires the evolution of extra numerical infrastructure to act as an intermediary system between the analytical solution and the numerics. This is explained in Sec. 7.3.

This chapter will, at a high level, cover the architecture of the BBH model: the numerical evolution, coordinates systems and matching method. For the purpose of this chapter we assume we have the tidally perturbed Schwarzschild metric readily available in harmonic coordinates. We devote Ch. 8 and Ch. 9 to the theory behind this solution; its derivation from first principles in the original coordinate system, the transformation into harmonic coordinates and the presentation of its final structure.

7.2 Generalised Harmonic Gauge

Harmonic coordinates have been valuable in studies of general relativity from the field's conception. These coordinates satisfy the covariant scalar-wave equation

$$\nabla^\gamma \nabla_\gamma z^\beta = 0. \tag{7.1}$$

In this chapter our notation is such that $\Psi_{\alpha\beta}$ is the NR spacetime metric, ∇_γ is the covariant derivative compatible with $\Psi_{\alpha\beta}$ and $z^\alpha = (t, z^a)$ is our harmonic coordinate system. The equation can instead be written in terms of partial derivatives and Christoffel symbols as

$$-\Gamma_\alpha = 0. \tag{7.2}$$

where Γ_α is the trace of the standard Christoffel symbol, $\Gamma_\alpha = \Psi^{\beta\gamma}\Gamma_{\alpha\beta\gamma}$, and

$$\Gamma_{\alpha\beta\gamma} = \frac{1}{2}(\partial_\beta \Psi_{\alpha\gamma} + \partial_\gamma \Psi_{\alpha\beta} - \partial_\alpha \Psi_{\beta\gamma}). \tag{7.3}$$

The Ricci curvature tensor can then be written as

$$R_{\alpha\beta} = -\frac{1}{2}\Psi^{\gamma\delta}\partial_\gamma\partial_\delta\Psi_{\alpha\beta} + \nabla_{(\alpha}\Gamma_{\beta)} + \Psi^{\gamma\delta}\Psi^{\rho\tau}(\partial_\rho\Psi_{\gamma\alpha}\partial_\tau\Psi_{\beta\delta} - \Gamma_{\alpha\gamma\rho}\Gamma_{\beta\delta\tau}), \tag{7.4}$$

where $\nabla_\alpha \Gamma_\beta = \partial_\alpha \Gamma_\beta - \Psi^{\gamma\delta}\Gamma_{\gamma\alpha\beta}\Gamma_\delta$. In the harmonic coordinates $\Gamma_\alpha = 0$ and so the vacuum Einstein equations, $R_{\alpha\beta} = 0$, form a hyperbolic system,

$$\Psi^{\gamma\delta}\partial_\gamma\partial_\delta\Psi_{\alpha\beta} = 2\Psi^{\gamma\delta}\Psi^{\rho\tau}(\partial_\rho\Psi_{\gamma\alpha}\partial_\tau\Psi_{\delta\beta} - \Gamma_{\alpha\gamma\rho}\Gamma_{\beta\delta\tau}). \tag{7.5}$$

BBH simulations using pure harmonic coordinates tend to be unstable. A reason for this is that Eq. (7.1) does not sufficiently constrain the behaviour of the coordinates and can admit dynamical wavelike solutions [153]. A choice must be made to reduce the dynamical range that the coordinates can take, thereby better controlling the behaviour of their evolution.

The idea of specifying arbitrary coordinates using a generalization of harmonic coordinates was first introduced by Friedrich in 1985 [65, 89]. This generalisation played a major role in the break-through first successful numerical simulation of the inspiral and merger of a binary black-hole system [124]. The generalization is implemented by assuming the coordinates instead satisfy the inhomogeneous wave equation

$$\Psi_{\alpha\beta}\nabla^\gamma\nabla_\gamma z^\beta = H_\alpha(z,\Psi) = -\Gamma_\alpha, \tag{7.6}$$

where $H_\alpha(z,\Psi)$ is some algebraic function of the coordinates z^α and the metric $\Psi_{\alpha\beta}$, but crucially not its derivatives. In these coordinates, $H_\alpha = -\Gamma_\alpha$ and the vacuum Einstein equations are given by

$$\Psi^{\gamma\delta}\partial_\gamma\partial_\delta\Psi_{\alpha\beta} = -2\nabla_{(\alpha}H_{\beta)} + 2\Psi^{\gamma\delta}\Psi^{\rho\tau}(\partial_\rho\Psi_{\gamma\alpha}\partial_\tau\Psi_{\delta\beta} - \Gamma_{\alpha\gamma\rho}\Gamma_{\beta\delta\tau}). \tag{7.7}$$

The H_β term operates here as a source term. It does not contain any derivatives of $\Psi_{\alpha\beta}$, thereby not altering the principal part of the equation and retaining hyperbolicity. The principal part of the system remains identical to the harmonic coordinate system, Eq. (7.5).

NR evolutions foliate the spacetime with spacelike hypersurfaces. In term of the lapse N and the shift N^k (as introduced in Sec. 6.2.3), the line element can be written as

$$\Psi_{\alpha\beta}dz^\alpha dz^\beta = -N^2dt^2 + \Psi_{ij}(dz^i + N^i dt)(dz^j + N^j dt). \tag{7.8}$$

The generalised harmonic coordinate condition from Eq. (7.7) can then be expressed in this 3+1 language as [89]

$$\partial_t N - N^k\partial_k N = -N(H_t - N^i H_i + NK), \tag{7.9}$$

$$\partial_t N^i - N^k\partial_k N^i = N\Psi^{ij}[N(H_j + \Psi^{kj}\Gamma_{jkl}) - \partial_j N], \tag{7.10}$$

where K is again the trace of the extrinsic curvature. Specifying the form of H_α determines the derivatives of the lapse and shift, and so fixes the gauge degrees of freedom in the system [89].

Our NR evolution using SpECTRE adopts a specific generalised harmonic gauge known as the damped harmonic gauge [5, 142]

$$\nabla^{\gamma}\nabla_{\gamma}z^{\alpha} = H^{\alpha}_{DH}(z,\Psi), \tag{7.11}$$

with

$$H^{\alpha}_{DH} = \mu_L \log\left(\frac{\sqrt{\Psi}}{N}\right)t^{\alpha} - \mu_S \Psi^{\alpha}_{i} N^{i}/N, \tag{7.12}$$

where μ_L and μ_S are damping factors set ≥ 0 and $\Psi = \det\Psi_{ij}$. The form of the gauge source function in Eq. (7.12) has been chosen carefully. Firstly, the spatial coordinates z^i satisfy a damped wave equation and are driven towards a solution of the spatial Laplace equation on a timescale of $\frac{1}{\mu_S}$. This reduces unwanted gauge dynamics so long as $\frac{1}{\mu_S}$ is smaller than the physical timescale. An analogous damped-wave condition for the time coordinate would be inappropriate as z^0 would then be driven towards a constant value, thereby no longer acting as a meaningful time coordinate. We instead choose to use the remaining gauge freedom to control the spatial volume element Ψ, which tends to experience explosive growth in the region near the black-hole horizons. This is imposed with the $\log\left(\frac{\sqrt{\Psi}}{N}\right)$ term, with damping factor μ_L. As H^{α}_{DH} depends on z^{α} and $\Psi_{\alpha\beta}$, but not its derivatives, the principal part of the Einstein equation continues to retain its hyperbolicity with this choice.

Finally, the damping factors are chosen such that

$$\mu_S = \mu_L = \mu_0\left[\log\left(\frac{\sqrt{\Psi}}{N}\right)\right]^2, \tag{7.13}$$

Again, this choice is found to effectively suppress the growth of singularities [142]. μ_0 is taken to be a function of time that reduces the damped harmonic gauge to the harmonic gauge far from the origin or at early times [142, 153]. Any choice such that $\mu_0 \approx 1$ near the black holes and $\mu_0 \approx 0$ near the outer boundary should achieve this and be sufficient.

It is expected that initial data will be prescribed for the SpECTRE evolution as is currently done in SpEC. Namely, using an extended conformal thin sandwich (XCTS) approach [105] which begins by choosing a conformal metric, the trace of the extrinsic curvature, and the first time-derivatives of these quantities. The conformal metric will be a superposition of Schwarzschild black holes in harmonic coordinates [154]. Further detail on the numerical implementation of the initial data is given in [103] and references therein.

7.3 Coordinate Systems in our Worldtube Scheme

The scheme involves three coordinate systems: (i) The NR generalised harmonic coordinate system in the bulk, (ii) the analytical harmonic coordinate system in the worldtube

and (iii) an auxiliary NR harmonic coordinate system that couples (i) and (ii) on the worldtube boundary. We denote the NR metric by $\Psi_{\alpha\beta}$ and the analytical metric by $g_{\alpha\beta}$, with the corresponding compatible derivatives ∇_Ψ and ∇_g.

We denote the NR generalised harmonic coordinate system by z^α. The coordinates satisfy the equation $\Box_\Psi z^\alpha = H^\alpha$, where H^α is the gauge-driver term given in Eq. (7.12). As the evolution proceeds, NR data is computed on successive hypersurfaces of constant generalised harmonic time, $z^0 = t = const$. Boundary conditions are required at three locations: (i) the edges of the numerical domain, (ii) at spectral element interfaces and (iii) at the worldtube boundary. These boundary conditions must of course also be specified on surfaces of constant generalised harmonic time. (i) and (ii) will be implemented as per standard spectral NR BBH evolutions [4, 5, 81], we provide further detail on (iii) in Sec. 7.4.

We denote the auxiliary NR harmonic coordinate system by y^α. The coordinates satisfy the equation $\Box_\Psi y^\alpha = 0$ and so their inclusion amounts to the co-evolution of 4 scalar fields. These y^α fields are harmonic coordinates in the NR domain with the property that they approach the generalised harmonic NR coordinates z^a at large distance. This is achieved by setting boundary conditions such that at early time or at large distances $y^\alpha = z^\alpha$.

The Jacobian between z^α and y^α can be readily computed numerically. This allows us to obtain the harmonic-coordinate metric from the generalised harmonic one:

$$\Psi^{y^\alpha y^\beta} = \frac{\partial y^\alpha}{\partial z^\alpha}\frac{\partial y^\beta}{\partial z^\beta}\Psi^{z^\alpha z^\beta}, \quad \Psi_{y^\alpha y^\beta} = (\Psi^{y^\alpha y^\beta})^{-1}. \tag{7.14}$$

The analytical metric is originally in light-cone coordinates, $x^\alpha = (v, r, \Theta^A)$, and the metric is denoted $g_{\alpha\beta}(x^\alpha; \lambda(v))$, where $\lambda(v)$ are the a priori unknown tidal moments. We define a new harmonic coordinate system $X^\alpha = (T, X, Y, Z)$ that satisfies the equation $\Box_g X^\alpha = 0$. We obtain the transformation $X^\alpha(x^\beta)$ and its inverse analytically, as detailed in Ch. 9.

The harmonic coordinates X^α are functions of the light-cone coordinates x^α, the original tidal moments $\lambda(v)$, and new unknown parameters $c(v)$, generated during the coordinate transform from x^α to X^α. The newly generated $c(v)$ functions encode the harmonic coordinate freedom within the transformation. The transformed analytical metric therefore also depends on these quantities, $g_{\alpha\beta} = g_{\alpha\beta}(X^\alpha; \lambda(T); c(T))$.

Due to the matching taking place on surfaces of constant generalised harmonic time t, as a final step we must transform the dependence of the unknown functions from T to t. This procedure is is detailed in Sec. 9.3. This then gives us $g_{\alpha\beta} = g_{\alpha\beta}(X^\alpha; \lambda(t); c(t))$, i.e. the harmonic components of the metric, in harmonic coordinates, as a function

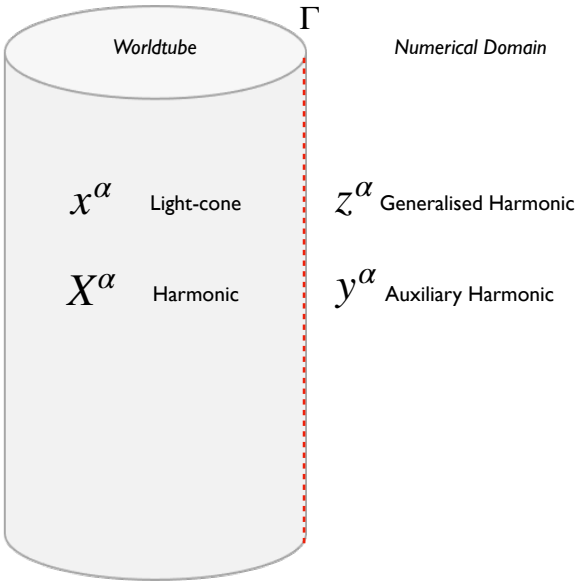

FIGURE 7.1: A sketch of the various coordinate systems in their respective domains, for the BBH worldtube excision model. Within the worldtube we have the approximate analytical solution originally in x^α light-cone coordinates, that we then transform into X^a harmonic coordinates. In the numerical bulk we have the z^α generalised harmonic coordinates and the y^a auxiliary harmonic coordinate system which couples the analytical solution and the numerical solution on the worldtube boundary, Γ.

of generalised harmonic time. The coordinate systems in their respective domains are illustrated in Fig. 7.1.

7.4 Matching Method

How the numerical algorithm will be implemented can be laid out step by set, as follows:

1. At each time step of the evolution we have the following NR data available on the $t = const$ hypersurface: the coordinates z^α, metric $\Psi^{\alpha\beta}$, and the values of the auxiliary harmonic coordinates as a function of the generalised harmonic coordinates, $y^\alpha(z^\beta)$.

2. Prepare the NR data for matching: from $\Psi^{z^\alpha z^\beta}$ we compute $\Psi^{y^\alpha y^\beta}$ using Eq. (7.14).

3. The worldtube Γ is represented by a 2D set of SpECTRE grid-points $z^i_\Gamma(\theta^A; t)$ at fixed generalised harmonic time t.

4. Project the equated metrics onto spherical harmonics, in order to match mode by mode for as many of the $\lambda(t), c(t)$ functions as possible.

5. Equate the value of the analytical metric with the auxiliary NR harmonic metric, along with their spatial derivatives, on Γ: $g^{X^\alpha X^\beta} = \Psi^{y^\alpha y^\beta}$, $\partial_i g^{X^\alpha X^\beta} = \partial_i \Psi^{y^\alpha y^\beta}$. Match for $\lambda(t), c(t)$ functions.

   Also equate the value of the fields themselves on Γ, to ensure the coordinates are smoothly matched: $X^\alpha = y^\beta$.

6. Match the time derivative of $\Psi^{\alpha\beta}$ to the time-derivative of $g^{\alpha\beta}$, $\dot{g}^{X^\alpha X^\beta} = \dot{\Psi}^{y^\alpha y^\beta}$ on Γ, and/or use the Einstein equations on Γ to yield ODEs for any remaining unknown $\lambda(t), c(t)$ functions.

7. Solve the ODEs numerically to match for any remaining $\lambda(t), c(t)$ functions. We now have a fully specified interior metric $g^{X^\alpha X^\beta}$ and the value of the interior harmonic coordinates X^α.

8. Time derivatives of the analytical solution will be required for boundary conditions for the NR evolution. $\dot{g}^{X^\alpha X^\beta}$ is now fully specified from the above. Calculate $\dot{X}^\alpha$.

9. Implement characteristic style boundary conditions on Γ, for both the generalised harmonic metric $\Psi_{\alpha\beta}$ and the auxiliary harmonic fields y^α.

10. The NR solution evolves to the next hypersurface of $t = const$ and the procedure repeats.

Chapter 8

Tidally Perturbed Black Hole Metric

The local approximate solution that will populate the excision region in the BBH world-tube mode will be a tidally perturbed Schwarzschild metric of the smaller black hole m_2. Tidally perturbed black hole metrics have been derived in the literature and we will make use of these works [107, 144, 109, 111]. Here the metric is expressed as an expansion in powers of $\epsilon := \frac{r}{\mathcal{R}} \ll 1$, where r is a measure of distance from the black hole and $\mathcal{R}$ is the local radius of curvature of the external spacetime. (In our model, in the next chapter, we will specialise r to be the mass of the small object m_2.) The metric contains unknowns that depend on the tidal gravitational fields that characterize the black hole's local environment, in our case those generated by the presence of m_1. As far as we are aware, such metric expansions have been derived up to $\mathcal{O}(\epsilon^4)$ [111].

The tidally perturbed black hole metric will need to be transformed into a coordinate system that is amenable to the NR evolution. As described in Chapter 7 this will be a harmonic coordinate system and this transformation is obtained in Chapter 9. However, our starting metric is the metric in (v, r) light-cone coordinates in the Regge-Wheeler gauge published in [109], and we devote this chapter to re-deriving its form. Although this is therefore a review of existing results, it is worth including as it is a fundamental building block of our model. Furthermore, our presentation includes a level of derivation of some of the results that in [109] were only postulated. We first derive the mode-decomposed perturbative Einstein field equations. The Regge-Wheeler gauge is then presented and the perturbative equations are then solved, yielding the solution for the metric to leading order in the tidal perturbation.

8.1 Manifolds, Coordinates, Metrics

Our first aim will be to obtain the metric perturbations of the Schwarzschild spacetime. For the work in this section we follow [98] and adopt their notational conventions. The manifold of the full spacetime is denoted $\mathcal{M}^4$. On this we have the full metric denoted ${}^4g_{\alpha\beta}$; this is comprised of the background Schwarzschild metric $g_{\alpha\beta}$, plus a perturbation $p_{\alpha\beta}$,

$$ {}^4g_{\alpha\beta} = g_{\alpha\beta} + p_{\alpha\beta}. \tag{8.1}$$

We then split the spacetime manifold $\mathcal{M}^4$ into the product of two submanifolds, $\mathcal{M}^4 = \mathcal{M}^2 \mathrm{x} S^2$. We treat $\mathcal{M}^2$ as the (t, r) plane with coordinates x^a, where the lower-case Latin indices run over the values 0 and 1. S^2 is the two-sphere with coordinates θ^A, where the upper-case Latin indices run over the values 2 and 3. The Schwarzschild metric $g_{\alpha\beta}$ is expressed as

$$ ds^2 = g_{ab}dx^a dx^b + r^2\Omega_{AB}d\theta^A d\theta^B, \tag{8.2}$$

which is covariant under two-dimensional coordinate transformations $x^a \to x'^a$ and $\theta^A \to \theta'^A$. Any desired coordinate system $x^a = (x^0, x^1)$ that can be obtained from the usual Schwarzschild coordinates (t, r) can be used, while we chose the angular coordinates remain to be fixed as $\theta^A = (\theta, \phi)$. The tensor g_{ab} and scalar r are functions of x^a, while Ω_{AB} is the metric on the unit two-sphere.

Some further structure on $\mathcal{M}^2$ and S^2 must now be introduced. A dual vector is specified by $r_a := \frac{\partial r}{\partial x^a}$, which is normal to surfaces of constant $r(x^a)$ and ϵ_{ab} is the Levi-Civita tensor on $\mathcal{M}^2$. From these quantities, the timelike Killing vector of the Schwarzwchild spacetime that is tangent to $\mathcal{M}^2$ can be constructed as $t^a = -\epsilon^{ab}r_b$. With this, r^a and t^a form a basis on $\mathcal{M}^2$. The covariant derivative on $\mathcal{M}^2$ is denoted ∇_a, such that $\nabla_a g_{bc} = 0$ and the Riemann tensor on $\mathcal{M}^2$ is $R_{abcd} = (\frac{2M}{r^3})(g_{ac}g_{bd} - g_{ad}g_{bc})$. The covariant derivative on S^2 is denoted D_A, such that $D_A\Omega_{BC} = 0$. The Levi-Civita tensor on S^2 is ϵ_{AB} with $\epsilon_{\theta\phi} = \sin\theta$, and the Riemann tensor on S^2 is $R_{ABCD} = \Omega_{AC}\Omega_{BD} - \Omega_{AD}\Omega_{BD}$. Finally, if Γ^a_{bc} is the connection associated with ∇_a and Γ^A_{BC} is the connected associated with D_A, then it can be shown that the nonvanishing components of the full spacetime connection ${}^4\Gamma$ are given by ${}^4\Gamma^a_{bc} = \Gamma^a_{bc}$, ${}^4\Gamma^a_{BC} = -rr^a\Omega_{BC}$, ${}^4\Gamma^A_{Bc} = r^{-1}r_c\delta^A_B$ and ${}^4\Gamma^A_{BC} = \Gamma^A_{BC}$.

8.2 Spherical-Harmonic Decomposition

The metric perturbations will be decomposed into scalar, vector and tensor spherical harmonics. Here we drop the (θ^A) dependence of these harmonics for brevity. The scalar harmonics Y^{lm} satisfy the eigenvalue equation

$$ [\Omega^{AB}D_A D_B + \ell(\ell+1)]Y^{\ell m} = 0. \tag{8.3}$$

The vectorial spherical harmonics are related to the standard scalar harmonics by

$$Y_A^{\ell m} := D_A Y^{\ell m}, \tag{8.4a}$$

$$Z_A^{\ell m} := -\epsilon_A^{\ B} D_B Y^{\ell m}, \tag{8.4b}$$

where $Y_A^{\ell m}$ are even-parity harmonics and $Z_A^{\ell m}$ are odd-parity harmonics. The tensorial spherical harmonics are related to the standard scalar harmonics by

$$Y_{AB}^{\ell m} := [D_A D_B + \frac{1}{2}\ell(\ell+1)\Omega_{AB}]Y^{\ell m}, \tag{8.5}$$

$$Z_{AB}^{\ell m} := -\frac{1}{2}\big(\epsilon_A^{\ C} D_B + \epsilon_B^{\ C} D_A\big) D_C Y^{\ell m}, \tag{8.6}$$

where again $Y_{AB}^{\ell m}$ are even-parity harmonics and $Z_{AB}^{\ell m}$ are odd-parity harmonics.

The vector and tensor spherical harmonics satisfy the following orthonormality relations:

$$\int \bar{Y}^A_{\ell m} Y_A^{\ell' m'} d\Omega = \ell(\ell+1)\delta_{\ell\ell'}\delta_{mm'}, \tag{8.7}$$

$$\int \bar{Z}^A_{\ell m} Z_A^{\ell' m'} d\Omega = \ell(\ell+1)\delta_{\ell\ell'}\delta_{mm'}, \tag{8.8}$$

$$\int \bar{Y}^A_{\ell m} Z_A^{\ell' m'} d\Omega = 0, \tag{8.9}$$

$$\int \bar{Y}^{AB}_{\ell m} Y_{AB}^{\ell' m'} d\Omega = \frac{1}{2}(\ell-1)\ell(\ell+1)(\ell+2)\delta_{\ell\ell'}\delta_{mm'}, \tag{8.10}$$

$$\int \bar{Z}^{AB}_{\ell m} Z_{AB}^{\ell' m'} d\Omega = \frac{1}{2}(\ell-1)\ell(\ell+1)(\ell+2)\delta_{\ell\ell'}\delta_{mm'}, \tag{8.11}$$

$$\int \bar{Y}^{AB}_{\ell m} Z_{AB}^{\ell' m'} d\Omega = 0, \tag{8.12}$$

where $d\Omega := \sin\theta d\theta d\phi$. Finally, $\Omega^{AB} Y_{AB}^{\ell m} = 0 = \Omega^{AB} Z_{AB}^{\ell m}$.

The metric perturbation $p_{\alpha\beta}$ is decomposed into spherical harmonics as follows:

$$p_{ab} = \sum_{\ell m} h_{ab}^{\ell m} Y^{\ell m}, \tag{8.13}$$

$$p_{aB} = \sum_{\ell m} \big(j_a^{\ell m} Y_B^{\ell m} + h_a^{\ell m} Z_B^{\ell m}\big), \tag{8.14}$$

$$p_{AB} = \sum_{\ell m} \big(r^2 K^{\ell m}\Omega_{AB} Y^{\ell m} + r^2 G^{\ell m} Y_{AB}^{\ell m} + h_2^{\ell m} Z_{AB}^{\ell m}\big). \tag{8.15}$$

The fields $h_{ab}^{\ell m}, j_a^{\ell m}, h_a^{\ell m}, K^{\ell m}, G^{\ell m}$, and $h_2^{\ell m}$ are all defined on $\mathcal{M}^2$ and so depend on the x^a coordinates only.

8.3 Regge-Wheeler Gauge

We now wish to analyse the effect of a gauge transformation. Even-parity gauge transformations are generated by a dual vector field $\Xi_\alpha = (\Xi_a, \Xi_A)$, which is expanded as

$$\Xi_a = \sum_{\ell m} \xi^{\ell m}_\alpha Y^{\ell m}, \tag{8.16}$$

$$\Xi_A = \sum_{\ell m} \xi^{\ell m} Y^{\ell m}_A. \tag{8.17}$$

Under such a transformation tensors on $\mathcal{M}^2$ will change according to

$$\chi' = \chi + \mathcal{L}_\xi \chi \tag{8.18}$$

where $\mathcal{L}_\xi$ is the Lie derivative with respect to the vector ξ. The perturbation fields become

$$h^{\ell m\prime}_{ab} = h^{\ell m}_{ab} - \nabla_a \xi^{\ell m}_b - \nabla_b \xi^{\ell m}_a, \tag{8.19}$$

$$j^{\ell m\prime}_a = j^{\ell m}_a - \xi^{\ell m}_a - \nabla_a \xi^{\ell m} + \frac{2}{r} r_a \xi^{\ell m}, \tag{8.20}$$

$$K^{\ell m\prime} = K^{\ell m} + \frac{\ell(\ell+1)}{r^2}\xi^{\ell m} - \frac{2}{r} r^a \xi^{\ell m}_a, \tag{8.21}$$

$$G^{\ell m\prime} = G^{\ell m} - \frac{2}{r^2}\xi^{\ell m}, \tag{8.22}$$

where we have dropped the ℓ, m labels for brevity. The combinations

$$\tilde{h}^{\ell m}_{ab} := h^{\ell m}_{ab} - \nabla_a \epsilon^{\ell m}_b - \nabla_b \epsilon^{\ell m}_a \tag{8.23}$$

and

$$\tilde{K}^{\ell m} := K^{\ell m} + \frac{1}{2}\ell(\ell+1) G^{\ell m} - \frac{2}{r} r^a \epsilon^{\ell m}_a \tag{8.24}$$

can be shown to be gauge-invariant, where

$$\epsilon^{\ell m}_a := j^{\ell m}_a - \frac{1}{2} r^2 \nabla_a G^{\ell m}. \tag{8.25}$$

Eqs. (8.20) and (8.22) show that a gauge can always be chosen such that $j^{\ell m}_a = 0 = G^{\ell m}$. This choices gives what is known as the Regge-Wheeler gauge. This Regge-Wheeler gauge is particularly useful, as in it the quantities in Eqs. (8.23) and (8.24) reduce to their untilde counterparts: $\tilde{h}^{\ell m}_{ab} = h^{\ell m}_{ab}$, $\tilde{K}^{\ell m} = K^{\ell m}$. This will allow us to write the covariant perturbation equations in the form of gauge-invariant quantities.

The odd-parity sector proceeds similarly. Odd-parity gauge transformations are generated by a dual vector field $\Xi_\alpha = (0, \Xi_A)$, which is expanded as

$$\Xi_A = \sum_{\ell m} \xi^{\ell m} Z_A^{\ell m}. \tag{8.26}$$

Under such a transformation the perturbation quantities on $\mathcal{M}^2$ change according to

$$h_a^{\ell m} \to h_a^{\ell m'} = h_a^{\ell m} - \nabla \xi^{\ell m} + \frac{2}{r} r_a \xi^{\ell m}, \tag{8.27}$$

$$h_2^{\ell m} \to h_2^{\ell m'} = h_2^{\ell m} - 2\xi^{\ell m}. \tag{8.28}$$

In this sector, the combination

$$\tilde{h}_a^{\ell m} = h_a^{\ell m} - \frac{1}{2} \nabla_a h_2^{\ell m} + \frac{1}{r} r_a h_2^{\ell m} \tag{8.29}$$

is gauge-invariant. Eq. (8.28) shows that a gauge can always be chosen such that $h_2^{\ell m} = 0$, and this is the odd-parity condition of the Regge-Wheeler gauge. Again, in this gauge, the quantity in Eq. (8.29) reduces to its untilde counterpart: $\tilde{h}_a^{\ell m} = h_a^{\ell m}$.

The collective Regge-Wheeler gauge conditions are numbered here for later reference

$$j_a^{\ell m} = 0, \tag{8.30a}$$

$$G^{\ell m} = 0, \tag{8.30b}$$

$$h_2^{\ell m} = 0. \tag{8.30c}$$

8.4 The Field Equations in the Regge-Wheeler Gauge

As our aim is to obtain the metric perturbations of the Schwarzschild spacetime, we must compute the linearised Einstein field equation

$$\delta G_{\alpha\beta} = 8\pi T_{\alpha\beta}, \tag{8.31}$$

where $G_{\alpha\beta}$ is the Einstein tensor, $T_{\alpha\beta}$ is the linear approximation to the full energy-momentum tensor, and the universal constants G and c have been set to 1. The linearised Einstein tensor is given by

$$\begin{aligned} \delta G_{\alpha\beta} = \frac{1}{2}(&-\nabla_\alpha \nabla_\beta p_\gamma^\gamma + \nabla_\mu \nabla_\alpha p_\beta^\mu + \nabla_\mu \nabla_\beta p_\alpha^\mu \\ &- g^{\mu\nu} \nabla_\mu \nabla_\nu p_{\alpha\beta} + g_{\alpha\beta} g^{\mu\nu} \nabla_\mu \nabla_\nu p_\gamma^\gamma - g_{\alpha\beta} \nabla_\mu \nabla_\nu p^{\mu\nu}). \end{aligned} \tag{8.32}$$

We substitute Eqs. (8.13), (8.14) and (8.15) to respectively create three separate equations for $\delta G_{ab}, \delta G_{aB}$, and δG_{AB}.

δG_{ab} is expanded in terms of $Y^{\ell m}$, δG_{aB} is expanded in terms of $Y^{\ell m}_B$ and $Z^{\ell m}_B$, and δG_{AB} is expanded in terms of $\Omega_{AB}Y^{\ell m}, Y^{\ell m}_{AB}$ and $Z^{\ell m}_{AB}$. The field equation now contains many terms involving the derivatives of the scalar, vector and tensorial harmonics. Using the relations given between Eqs. (8.3) and (8.6), we derived expressions relating all derivative quantities to the scalar, vector and tensorial harmonics themselves. These are given in Appendix B. We apply these relations as a necessary step in order to match the final form of the perturbation equations presented in [98]. Each separate spherical harmonic component can then be extracted to form an independent equation using the orthonormality relations given in Sec. 8.2.

As in [98] we remain in the Regge-Wheeler gauge and can then take advantage of the fact that in this gauge $h_{ab} \to \tilde{h}_{ab}, K \to \tilde{K}, h_a \to \tilde{h}_a$. This allows us to write the field equations in terms of gauge-invariant quantities. We now discard spherical harmonic ℓm indices for brevity. In covariant form our final results are

$$\begin{aligned} Q_{ab} =& \nabla_c \nabla_{(a}\tilde{h}^c_{b)} - \frac{1}{2}g_{ab}\nabla_c\nabla_d\tilde{h}^{cd} - \frac{1}{2}\Box(\tilde{h}^{ab} - g_{ab}\tilde{h}) - \frac{1}{2}\nabla_a\nabla_b\tilde{h} + \frac{2}{r}r_c(\nabla_{(a}\tilde{h}^c_{b)} - g_{ab}\nabla_d\tilde{h}^{cd}) \\ & - \frac{1}{r}r^c\nabla_c(\tilde{h}_{ab} - g_{ab}\tilde{h}) + \frac{\ell(\ell+1)}{2r^2}\tilde{h}_{ab} - \frac{1}{r^2}g_{ab}r_c r_d\tilde{h}^{cd} - \frac{1}{2}\left(\frac{\ell(\ell+1)}{r^2} + \frac{2M}{r^3}\right)g_{ab}\tilde{h} \\ & - \nabla_a\nabla_b\tilde{K} + g_{ab}\Box\tilde{K} - \frac{2}{r}r_{(a}\nabla_{b)}\tilde{K} + \frac{3}{r}g_{ab}r^c\nabla_c\tilde{K} - \frac{\ell(\ell-1)(\ell+2)}{2r^2}g_{ab}\tilde{K}, \end{aligned} \tag{8.33}$$

$$Q_a = \nabla_c\tilde{h}^c_a - \nabla_a\tilde{h} + \frac{1}{r}r_a\tilde{h} - \nabla_a\tilde{K}, \tag{8.34}$$

$$Q^\flat = \Box\tilde{h} - \nabla_a\nabla_b\tilde{h}^{ab} - \frac{2}{r}r_a\nabla_b\tilde{h}^{ab} - \frac{\ell(\ell+1)}{2r^2}\tilde{h} + \Box\tilde{K} + \frac{2}{r}r^a\nabla_a\tilde{K}, \tag{8.35}$$

$$Q^\sharp = -\tilde{h}, \tag{8.36}$$

$$P_a = -\Box\tilde{h}_a + \nabla_a\nabla_b\tilde{h}^b + \frac{2}{r}(r_b\nabla_a\tilde{h}^b - r_a\nabla_b\tilde{h}^b) - \frac{2}{r^2}r_a r_b\tilde{h}^b + \frac{\ell(\ell+1)}{r^2}\tilde{h}^a, \tag{8.37}$$

$$P = \nabla_a\tilde{h}^a, \tag{8.38}$$

where $\tilde{h} := g^{ab}\tilde{h}_{ab}$ and $\Box := g^{ab}\nabla_a\nabla_b$. The source terms are themselves given by

$$Q^{ab} = 8\pi\int T^{ab}\bar{Y}^{\ell m}d\Omega, \tag{8.39}$$

$$Q^a = \frac{16\pi r^2}{\ell(\ell+1)}\int T^{aB}\bar{Y}^{\ell m}_B d\Omega, \tag{8.40}$$

$$Q^\flat = 8\pi r^2\int T^{AB}\Omega_{AB}\bar{Y}^{\ell m}d\Omega, \tag{8.41}$$

$$Q^\sharp = \frac{32\pi r^4}{(\ell-1)\ell(\ell+1)(\ell+2)}\int T^{AB}\bar{Y}^{\ell m}_{AB}d\Omega, \tag{8.42}$$

$$P^a = \frac{16\pi r^2}{\ell(\ell+1)}\int T^{aB}\bar{Z}^{\ell m}_B d\Omega, \tag{8.43}$$

$$P = \frac{16\pi r^4}{(\ell-1)\ell(\ell+1)(\ell+2)} \int T^{AB} \bar{Z}^{\ell m}_{AB} d\Omega. \tag{8.44}$$

Finally we re-express these equations in terms of (v, r) coordinates. We firmly adopt the Regge-Wheeler gauge specified by Eqs. 8.30 and so can remove all the over-tildes, giving

$$Q^{vv} = -\partial^2_{rr}K - \frac{2}{r}\partial_r K - \frac{1}{r}\partial_v h_{rr} + \frac{f}{r}\partial_r h_{rr} + \frac{2}{r}\partial_r h_{vr} + \frac{\ell(\ell+1)r + 4M}{2r^3} h_{rr}, \tag{8.45}$$

$$\begin{aligned} Q^{vr} =& \partial^2_{vr}K + \frac{2}{r}\partial_v K - \frac{f}{r}\partial_v h_{rr} + \frac{r-M}{r^2}\partial_r K - \frac{1}{r}\partial_r h_{vv} \\ & - \frac{1}{r^2}h_{vv} - \frac{\ell(\ell+1)+4}{2r^2}h_{vr} - \frac{f}{r^2}h_{rr} - \frac{\mu}{2r^2}K, \end{aligned} \tag{8.46}$$

$$\begin{aligned} Q^{rr} =& -\partial^2_{vv}K + \frac{r-M}{r^2}\partial_v K + \frac{1}{r}\partial_v h_{vv} + \frac{2f}{r}\partial_v h_{vr} + \frac{(r-M)f}{r^2}\partial_r K \\ & - \frac{f}{r}\partial_r h_{vv} + \frac{\mu r + 4M}{2r^3}h_{vv} - \frac{2f}{r^2}h_{vr} - \frac{f^2}{r^2}h_{rr} - \frac{\mu f}{2r^2}K, \end{aligned} \tag{8.47}$$

$$Q^v = \partial_v h_{rr} - \partial_r h_{vr} - \partial_r K + \frac{2}{r}h_{vr} + \frac{r-M}{r^2}h_{rr}, \tag{8.48}$$

$$Q^r = -\partial_v h_{vr} - \partial_v K + \partial_r h_{uu} - f\partial_r K + \frac{2(r-M)}{r^2}h_{ur} + \frac{(r-M)f}{r^2}h_{rr}, \tag{8.49}$$

$$\begin{aligned} Q^\flat =& -\partial^2_{vv}h_{rr} + 2\partial^2_{vr}h_{vr} + 2\partial^2_{vr}K - \frac{r-M}{r^2}\partial_v h_{rr} + \frac{2}{r}\partial_v K - \partial^2_{rr}h_{vv} + f\partial^2_r K - \frac{2}{r}\partial_r h_{vv} \\ & - \frac{2(r-M)}{r^2}\partial_r h_{vr} - \frac{(r-M)f}{r^2}\partial_r h_{rr} + \frac{2(r-M)}{r^2}\partial_r K \\ & - \frac{\ell(\ell+1)}{r^2}h_{vr} - \frac{\ell(\ell+1)r^2 - 2\mu M\tilde{r} - 4M^2}{2r^4}h_{rr}, \end{aligned} \tag{8.50}$$

$$Q^\sharp = -2h_{vr} - f h_{rr}, \tag{8.51}$$

$$P^v = -\partial^2_{vr}h_r + \partial^2_{rr}h_v - \frac{2}{r}\partial_v h_r - \frac{2}{r^2}h_v + \frac{\mu}{r^2}h_r, \tag{8.52}$$

$$P^r = \partial^2_{vv}h_r - \partial^2_{vr}h_v + \frac{2}{r}\partial_v h_h + \frac{\mu}{r^2}h_v + \frac{\mu f}{r^2}h_r, \tag{8.53}$$

$$P = \partial_v h_r + \partial_r h_v + f\partial_r h_r + \frac{2M}{r^2}h_r. \tag{8.54}$$

where $\mu := \ell(\ell+1) - 2$.

8.5 Solution for a Tidally Perturbed Black Hole

A core assumption in our calculation is that the time dependence of the tidal perturbations is slow. Therefore we assume the perturbation depends on time only through $\tilde{v} := \epsilon v$. As a result any v derivatives at a particular order in ϵ of the calculation will

be demoted to the next order. Though we do not lay out the calculation fully explicitly here, the key features of the derivation are as follows.

For clarity, let us now make explicit the dependence of the metric on the coordinates x and the parameter ϵ:

$$^4g_{\alpha\beta}(x,\epsilon) = g_{\alpha\beta}(x) + p_{\alpha\beta}(x,\epsilon), \tag{8.55}$$

where $x^\alpha = (v, r, \theta^A)$. As we are in Schwarzschild spacetime, the full metric $^4g_{\alpha\beta}(x,\epsilon)$ must satisfy the vacuum Einstein field equation. This is expanded as

$$0 = G^{\alpha\beta}[g] + \delta G^{\alpha\beta}[p] + \delta^2 G^{\alpha\beta}[p] + \dots, \tag{8.56}$$

where we have dropped the spacetime indices on g and p. Each term is further expanded in a slow-time expansion as

$$G^{\alpha\beta}[g] = G^{(0)\alpha\beta}[g] + \epsilon G^{(1)\alpha\beta}[g] + \epsilon^2 G^{(2)\alpha\beta}[g], \tag{8.57}$$

$$\delta^k G^{\alpha\beta}[p] = \delta^k G^{(0)\alpha\beta}[p] + \epsilon \delta^k G^{(1)\alpha\beta}[p] + \epsilon^2 \delta^k G^{(2)\alpha\beta}[p]. \tag{8.58}$$

where $G^{(n)\alpha\beta}$ and $\delta^k G^{(n)\alpha\beta}$ consist of the terms in $G^{\alpha\beta}$ and $\delta^k G^{\alpha\beta}$ that contain n derivatives with respect to v. Finally, the perturbation itself is given as an expansion in powers of the parameter ϵ,

$$p_{\alpha\beta}(x,\epsilon) = \epsilon p^{(1)}_{\alpha\beta}(x) + \epsilon^2 p^{(2)}_{\alpha\beta}(x) + ... \tag{8.59}$$

Substituting into the Einstein field equation and solving order-by-order in powers of ϵ we obtain a series of equations,

$$G^{(0)\alpha\beta}[g] = 0, \tag{8.60}$$

$$\delta G^{(0)\alpha\beta}[p^{(1)}] = -G^{(1)\alpha\beta}[g], \tag{8.61}$$

$$\begin{aligned} \delta G^{(0)\alpha\beta}[p^{(2)}] &= -\delta^2 G^{(0)\alpha\beta}[p^{(1)}] - \delta G^{(1)\alpha\beta}[p^{(1)}] - G^{(2)\alpha\beta}[g]. \\ &\vdots \end{aligned} \tag{8.62}$$

Equation (8.60) is the ordinary Einstein equation for $g_{\alpha\beta}$, with all derivatives with respect to v removed. For the solution to Eq. (8.60), we take the Schwarzschild metric in advanced Eddington-Finkelstein coordinates,

$$g_{\alpha\beta} = -f(r)dv^2 + 2dvdr + r^2 d\Omega^2, \tag{8.63}$$

where $f = 1 - \frac{2M}{\tilde{r}}$.

We now seek to solve Eq. (8.61). The only non-zero source term in Eq. (8.61) is $G^{(1)rr}[g] = \frac{2}{r^2}\frac{dM}{dv}$ [106]. We note $G^{(1)\alpha\beta}$ is just the Einstein tensor of the Vaidya metric, the time-varying Schwarzschild metric. For $\ell \geq 2$, the equation can be solved for arbitrary ℓ. However, it should be noted that low multipoles ($\ell = 0, 1$) must be solved for separately as various quantities are only defined for $\ell \geq 2$. We solve

Eqs. (8.45)-(8.51) and Eqs. (8.52)-(8.54) in a hierarchical manner, to find the coefficients $K^{\ell m}, h^{\ell m}_{vv}, h^{\ell m}_{rr}, h^{\ell m}_{vr}, h^{\ell m}_{v}, h^{\ell m}_{r}$. The equations are solved in terms of undetermined functions of slow advanced time $\tilde{v}$, formally denoted $A^{k}_{(n)\ell m}(\tilde{v})$ where n denotes the power of ϵ.

We schematically explain the procedure for $\ell = 2$ and the even sector as an example. We start with Eq. (8.46). This equation allows us to solve for h^{2m}_{vr} in terms of h^{2m}_{rr}. This result is then substituted into the remaining set of equations. Eq. (8.47) then allows us to solve for h^{2m}_{rr} in terms of K^{2m}. Substituting this into the remaining set of equations, Eq. (8.48) then produces a second order ODE in r for K^{2m}. We then solve this differential equation, which produces two integration constants denoted $A^{1}_{(1)2m}(\tilde{v})$, $A^{2}_{(1)2m}(\tilde{v})$. The procedure repeats analogously for the odd-sector, hierarchically solving Eqs. (8.52)-(8.54).

Along the way certain physical conditions are then imposed on each solution, e.g. that it is regular at the horizon and does not contain any singularities. This forces certain $A^{k}_{(n)\ell m}(\tilde{v})$ to be set to zero. When the results are substituted into the remaining set of perturbation equations, this sets further restrictions on the various $A^{k}_{(n)\ell m}(\tilde{v})$ terms. As a last step we use any remaining gauge freedom to simplify the final results as best possible. It turns out that at $n = 1$ all $A^{k}_{(1)\ell m}(\tilde{v})$ terms can be set to zero. The $n = 1$ equations also demand that $\frac{dM}{dv} = 0$.

We now seek to solve Eq. (8.62), which, with the above findings, reduces to

$$\delta G^{(0)\alpha\beta}[p^{(2)}] = 0. \tag{8.64}$$

We repeat the procedure of systematically solving the equations for each ℓ, imposing physical conditions on our solutions and exploiting remaining gauge freedom to simply results. At this order even after the imposition of boundary and regularity conditions, we are left with a single non-vanishing term in each of the even and odd sectors, which we denote $A_{(2)2m}(\tilde{v})$ and $B_{(2)2m}(\tilde{v})$. These appear in the $\ell = 2$ perturbation only. Specifically,

$$h^{2m}_{vv} = \frac{1}{2} r^2 f^2 A_{(2)2m}(\tilde{v}), \tag{8.65}$$

$$h^{2m}_{vr} = -\frac{1}{2} r^2 f A_{(2)2m}(\tilde{v}), \tag{8.66}$$

$$h^{2m}_{rr} = r^2 A_{(2)2m}(\tilde{v}), \tag{8.67}$$

$$K^{2m} = \frac{1}{2} r^2 (-2M^2 + r^2) A_{(2)2m}(\tilde{v}), \tag{8.68}$$

$$h^{2m}_{v} = -r^3 f B_{(2)2m}(\tilde{v}), \tag{8.69}$$

$$h^{2m}_{r} = r^3 B_{(2)2m}(\tilde{v}). \tag{8.70}$$

We find these results match exactly the leading order form of the metric presented in [109]. We can now write the form of the full tidally perturbed metric up to $\mathcal{O}(\epsilon^2)$:

$$g_{vv=} - f + \epsilon^2 \frac{1}{2} r^2 f^2 \sum_m A_{2m}(\tilde{v}) Y^{2m}(\theta^A) + \mathcal{O}(\epsilon^3), \tag{8.71}$$

$$g_{vr} = 1 - \epsilon^2 \frac{1}{2} r^2 f \sum_m A_{2m}(\tilde{v}) Y^{2m}(\theta^A) + \mathcal{O}(\epsilon^3), \tag{8.72}$$

$$g_{rr} = \epsilon^2 r^2 \sum_m A_{2m}(\tilde{v}) Y^{2m}(\theta^A) + \mathcal{O}(\epsilon^3), \tag{8.73}$$

$$g_{vA} = -\epsilon^2 r^3 f \sum_m B_{2m}(\tilde{v}) Z_A^{2m}(\theta^A) + \mathcal{O}(\epsilon^3), \tag{8.74}$$

$$g_{rA} = \epsilon^2 r^3 \sum_m B_{2m}(\tilde{v}) Z_A^{2m}(\theta^A) + \mathcal{O}(\epsilon^3), \tag{8.75}$$

$$g_{AB} = r^2 \Omega_{AB} + \epsilon^2 \frac{1}{2} r^2 (-2M^2 + r^2) \Omega_{AB} \sum_m A_{2m}(\tilde{v}) Y^{2m}(\theta^A) + \mathcal{O}(\epsilon^3), \tag{8.76}$$

where we have dropped the (n) label from $A_{(2)2m}(\tilde{v})$ and $B_{(2)2m}(\tilde{v})$ as they are the only remaining terms. $A_{2m}(\tilde{v})$, $B_{2m}(\tilde{v})$ can now be thought of as quadrupole tidal potentials that must be determined by matching to the exterior spacetime.

Chapter 9

Transformation to Harmonic Coordinates

In this chapter we obtain the transformation of the tidally perturbed Schwarzschild metric, from light-cone coordinates to harmonic coordinates. We first perturbatively obtain the forward transform ($X^\mu \to x^\mu$), followed by the inverse transformation ($x^\mu \to X^\mu$). We then compute the contravariant components of the metric, expressed in harmonic coordinates. Our metric components are presented grouped by their multipolar structure. When implemented, our IMRI worldtube excision model will match these components, mode-by-mode, on the worldtube boundary to the NR solution.

9.1 Forward Transformation

9.1.1 Set Up

We start with the tidally perturbed Schwarzschild metric as given in [109] to order ϵ^2 and now use the notation $g_{\alpha\beta} = g^{(0)}_{\alpha\beta} + \epsilon p^{(1)}_{\alpha\beta} + \epsilon^2 p^{(2)}_{\alpha\beta}$, where recall $\epsilon = m_2/\mathcal{R}$.

We wish to transform this metric into harmonic coordinates $X^\mu := (T, X, Y, Z)$. The harmonic coordinate condition is that X^μ must satisfy the scalar wave equation,

$$\Box X^\mu = g^{\alpha\beta} \nabla_\alpha \nabla_\beta X^\mu = 0 \tag{9.1}$$

where $g^{\alpha\beta}$ is the full, perturbed spacetime metric, given in Eqs. (8.71) to (8.76).

We begin with an ansatz for X^μ which takes the form of a power series in ϵ at fixed $(\tilde{v}, r, \theta^A)$ coordinates

$$X^\mu = \bar{X}^\mu + X^\mu_0(\tilde{v}, r, \theta^A) + \epsilon X^\mu_1(\tilde{v}, r, \theta^A) + \epsilon^2 X^\mu_2(\tilde{v}, r, \theta^A) + \mathcal{O}(\epsilon^3), \tag{9.2}$$

where $\bar{X}^\mu$ is a chosen leading-order contribution. The time dependence is again slow ($\tilde{v} := \epsilon v$) and so whenever we encounter derivatives of X^n_μ with respect to v during our calculation, these terms will be demoted to the next order in ϵ.

We make two demands of X^μ, (i) that it be smooth at the horizon $r = 2M$ and (ii) that the metric does not blow up as $M \to 0$, at fixed r values. These conditions should allow the solution to be extended arbitrary far into the interior of the worldtube and thus facilitate a smooth matching to the NR solution.

We now examine the structure of the wave operator and its expansion in powers of ϵ. The wave operator can be written in terms of covariant derivatives ∇_α or partial derivatives ∂_α

$$\begin{aligned} \Box X^\mu &= \nabla_\alpha(g^{\alpha\beta}\partial_\beta X^\mu) \\ &= \frac{1}{\sqrt{-g}}\partial_\alpha(\sqrt{-g}g^{\alpha\beta}\partial_\beta X^\mu), \end{aligned} \tag{9.3}$$

where g is the determinant of the metric. It can be seen clearly from the balancing of indices that the wave operator is a scalar quantity.

The expansion of the inverse metric is given by

$$g^{\alpha\beta} = g^{\alpha\beta}_{(0)} - \epsilon^2 g^{\alpha\mu}_{(0)} g^{\beta\nu}_{(0)} p^{(2)}_{\mu\nu} + \mathcal{O}(\epsilon^3), \tag{9.4}$$

while the square root of the determinant is expanded as

$$\sqrt{-g} = \sqrt{-g^{(0)}}\left[1 + \frac{\epsilon^2}{2} g^{\gamma\delta}_{(0)} p^{(2)}_{\gamma\delta} + \mathcal{O}(\epsilon^3)\right]. \tag{9.5}$$

Combining these expansions we obtain an overall expansion for $\Box X^\mu$ as

$$\begin{aligned} \Box X^\mu =& \frac{1}{\sqrt{-g^{(0)}}}\partial_\alpha(\sqrt{-g^{(0)}} g^{\alpha\beta}_{(0)}\partial_\beta X^\mu) \\ &+ \frac{\epsilon^2}{\sqrt{-g^{(0)}}}\Bigg[-\frac{1}{2} g^{\gamma\delta}_{(0)} p^{(2)}_{\gamma\delta}\partial_\alpha\left(\sqrt{-g^{(0)}} g^{\alpha\beta}_{(0)}\partial_\beta X^\mu\right) \\ &+ \partial_\alpha\left(\sqrt{-g^{(0)}}\frac{1}{2} g^{\gamma\delta}_{(0)} p^{(2)}_{\gamma\delta} g^{\alpha\beta}_{(0)}\partial_\beta X^\mu - \sqrt{-g^{(0)}} g^{\alpha\nu}_{(0)} g^{\beta\rho}_{(0)} p^{(2)}_{\nu\rho}\partial_\beta X^\mu\right)\Bigg] + \mathcal{O}(\epsilon^3). \end{aligned} \tag{9.6}$$

We compactify this expression with the notation

$$\Box X^\mu = DX^\mu - \epsilon^2\left[\frac{1}{2} p^{(2)\gamma}_{\gamma} DX^\mu + \frac{1}{\sqrt{-g^{(0)}}}\left(\partial_\alpha[\sqrt{-g^{(0)}}\overline{p}^{(2)\alpha\beta}\partial_\beta X^\mu]\right)\right] + \mathcal{O}(\epsilon^3), \tag{9.7}$$

where

$$\overline{p}^{(2)\alpha\beta} := g^{\alpha\nu}_{(0)} g^{\beta\rho}_{(0)} p^{(2)}_{\nu\rho} - \frac{1}{2} g^{\gamma\delta}_{(0)} p^{(2)}_{\gamma\delta} g^{\alpha\beta}_{(0)} \tag{9.8}$$

is the trace-reverse of the metric perturbation and

$$D := \frac{1}{r^2}\partial_a(r^2 g^{ab}_{(0)}\partial_b) + \frac{1}{r^2}D_A D^A. \tag{9.9}$$

As stated above, derivatives of X^μ_n with respect to v are of order ϵ and therefore Eq. (9.9) can be broken into two pieces, $D = D_0 + \epsilon D_1$, with

$$D_0 = \frac{1}{r^2}\partial_r(r^2 f\partial_r) + \frac{1}{r^2}D_A D^A, \tag{9.10}$$

$$D_1 = \frac{2}{r}\partial_{\tilde{v}} + 2\partial_r\partial_{\tilde{v}}. \tag{9.11}$$

We now take Eq. (9.7) and expand X^μ as in Eq. (9.2), grouping terms in powers of ϵ. This gives us

$$\begin{aligned}\Box X^\mu =& D_0\bar{X}^\mu + D_0 X_0^\mu + \epsilon\big(D_0 X_1^\mu + D_1(\bar{X}^\mu + X_0^\mu)\big) + \epsilon^2\Bigg[D_0 X_2^\mu - \frac{1}{2}p^{(2)\gamma}_\gamma D_0(\bar{X}^\mu + X_0^\mu) \\ &+ D_1 X_1^\mu - \frac{1}{r^2\sqrt{\Omega}}\big(\partial_\alpha[r^2\sqrt{\Omega}\overline{p}^{(2)\alpha\beta}\partial_\beta(\bar{X}^\mu + X_0^\mu)]\big)\Bigg] + \mathcal{O}(\epsilon^3),\end{aligned} \tag{9.12}$$

where $\sqrt{-g^{(0)}} = r^2\sqrt{\Omega}$ and Ω is the determinant of the Ω_{AB} metric.

We next make a choice for the leading order barred components of the expansion. Demanding the coordinates are harmonic and regular at the horizon, we choose

$$\bar{T} = v - \rho^*, \tag{9.13}$$

$$\bar{X}^i = \rho n^i, \tag{9.14}$$

where we define

$$\rho := r - M \tag{9.15}$$

and

$$\rho^* := r + 2M\ln\Big(\frac{r}{2M}\Big). \tag{9.16}$$

Latin indices represents the spatial coordinates, and $n^i := \frac{x^i}{r}$ is the radial unit vector.

We now have a series of equations to solve order by order in ϵ. As $D\bar{X}_\mu = 0$ by construction, we are left with

$$\epsilon^0 : D_0(X_0^\mu) = 0, \tag{9.17}$$

$$\epsilon^1 : D_0 X_1^\mu = -D_1(X_0^\mu), \tag{9.18}$$

$$\epsilon^2 : D_0 X_2^\mu = \frac{1}{2}p^{(2)\gamma}_\gamma D_0(X_0^\mu) + \frac{1}{r^2\sqrt{\Omega}}\partial_\alpha[r^2\sqrt{\Omega}\overline{p}^{(2)\alpha\beta}\partial_\beta(\bar{X}^\mu + X_0^\mu)] - D_1 X_1^\mu. \tag{9.19}$$

It should be reminded that, in Eq. (9.19), to retain $\mathcal{O}(\epsilon^2)$, ∂_v on X_0^μ is ignored.

In solving Eqs. (9.17)-(9.19), we will find the forms of X_0^μ, X_1^μ and X_2^μ in terms of the light-cone coordinates. As we are only working with the expressions for $g_{\alpha\beta}$ to order ϵ^2, we truncate the expansion of X^μ at order $\epsilon^2 X_2^\mu$ for consistency.

9.1.2 Solution at $\mathcal{O}(\epsilon^0)$

The leading order equation, Eq. (9.17), can be readily solved by hand, mode by mode in a multipole expansion. We perform a decomposition of the scalar functions X_n^μ into spherical harmonic modes,

$$X_n^\mu = \sum_{\ell m} X_{n\ell m}^\mu Y^{\ell m}. \tag{9.20}$$

Using the relation $D_A D^A Y^{\ell m} = -\ell(\ell+1)Y^{\ell m}$, Eq. (9.17) separates into the model equations

$$f X_{0\ell m,rr}^\mu + \frac{2\rho}{r^2} X_{0\ell m,r}^\mu - \frac{\ell(\ell+1)}{r^2} X_{0\ell m}^\mu = 0. \tag{9.21}$$

Upon inspection we can see this is of the form of Legendre's differential equation. Therefore, the solution is a combination of Legendre functions of the first and second kind

$$X_{0\ell m}^\mu = c_{0\ell m}^\mu(\tilde{v}) P_\ell\big(\check{\rho}\big) + d_{0\ell m}^\mu(\tilde{v}) Q_\ell\big(\check{\rho}\big), \tag{9.22}$$

where $c_{0\ell m}^\mu(\tilde{v})$ and $d_{0\ell m}^\mu(\tilde{v})$ are unknown functions of slow time $\tilde{v}$ and we have introduced $\check{\rho} = \frac{\rho}{M}$. For reference, the forms of the Legendre functions are

$$P_\ell(z) = \frac{1}{2^\ell \ell!} \frac{d^\ell}{dz^\ell}(z^2-1)^\ell, \tag{9.23}$$

$$Q_\ell(z) = \begin{cases} \frac{1}{2}\log\left(\frac{1+z}{1-z}\right) & \ell = 0, \\ P_1(z)Q_0(z) - 1 & \ell = 1, \\ \frac{2\ell-1}{\ell} z Q_{\ell-1}(z) - \frac{\ell-1}{\ell} Q_{\ell-2}(z) & \ell \geq 2. \end{cases} \tag{9.24}$$

We now recall the demands we are making on the form of X^μ. The first is that it must be smooth on the horizon, $r = 2M$. $P_\ell(\check{\rho})$ is a polynomial of order ℓ in ρ (and in r) and therefore regular on the horizon. However, $Q_\ell(\check{\rho})$ blows up on the event horizon for all ℓ modes. We therefore use the freedom we have in the solution to set $d_{0\ell m}^\mu(\tilde{v}) = 0$, removing the divergent Q_ℓ term. Our second demand is that there are no negative powers of M in the overall transformation, such that the metric does not blow up as $M \to 0$. This is only achieved here for the $\ell = 0$ case of the P_ℓ Legendre function, $P_0(\check{\rho}) = 1$, and so we set $c_{0\ell m}^\mu(\tilde{v}) = 0$ for all $\ell \geq 1$. The final solution is then,

$$X_{000}^\mu = c_{000}^\mu(\tilde{v}). \tag{9.25}$$

This form of X_0^μ represents a simple spacetime translation which re-aligns the coordinate origins. We now have the transformation to leading order in ϵ,

$$T = v - \rho^* + c^0_{000}(\tilde{v})Y^{00} + \mathcal{O}(\epsilon), \tag{9.26}$$

$$X^i = \rho n^i + c^i_{000}(\tilde{v})Y^{00} + \mathcal{O}(\epsilon). \tag{9.27}$$

9.1.3 Solution at $\mathcal{O}(\epsilon^1)$

Now that we have the form of X_0^μ, the ϵ^1 order equation can also clearly be examined by hand. Starting with

$$D_0 X_1^\mu = -D_1 X_0^\mu, \tag{9.28}$$

and again employing a spherical harmonic decomposition of X_1^μ, the overall equation becomes an inhomogeneous Legendre equation with $X^\mu_{1\ell m}$ as the subject and with a source term formed from $X^\mu_{0\ell m}$. Explicitly, this reads

$$fX^{\mu,rr}_{1\ell m,rr} + \frac{2\rho}{r^2}X^\mu_{1\ell m,r} - \frac{\ell(\ell+1)}{r^2}X^\mu_{1\ell m} = -\frac{2}{r}\dot{X}^\mu_{0\ell m} - 2\partial_r \dot{X}^\mu_{0\ell m}, \tag{9.29}$$

where an overdot represents a derivative with respect to $\tilde{v}$.

For $\ell = 0$ we obtain

$$fX^\mu_{100,rr} + \frac{2\rho}{r^2}X^\mu_{100,r} = -\frac{2}{r}\dot{c}^\mu_{000}(\tilde{v}). \tag{9.30}$$

This equation can be solved for X^μ_{100} using the variation of parameters method. The general solution is

$$\begin{aligned} X^\mu_{100} = &\int_{2M}^{r} \left(-\frac{2\dot{c}^\mu_{000}(\tilde{v})}{f(r')r'W(r')} \right) \Big[P_0\big(\check{\rho}\big)Q_0\big(\check{\rho}'\big) - Q_0\big(\check{\rho}\big)P_0\big(\check{\rho}'\big) \Big] dr' \\ &+ c^\mu_{100}(\tilde{v})P_0\big(\check{\rho}\big) + d^\mu_{100}(\tilde{v})Q_0\big(\check{\rho}\big) \end{aligned} \tag{9.31}$$

where

$$W(r) := \frac{dP_\ell(\check{\rho})}{dr}Q_\ell(\check{\rho}) - P_\ell(\check{\rho})\frac{dQ_\ell(\check{\rho})}{dr} = \frac{M}{r^2 f} \tag{9.32}$$

is the Wronskian. Evaluating the right hand side of Eq. (9.31) we obtain

$$X^\mu_{100} = \dot{c}^\mu_{000}(\tilde{v})\big(2M - \rho^*\big) + c^\mu_{100}(\tilde{v})P_0\big(\check{\rho}\big) + d^\mu_{100}(\tilde{v})Q_0\big(\check{\rho}\big). \tag{9.33}$$

Regularity on the horizon demands $d^\mu_{100}(\tilde{v}) = 0$. The most general horizon-regular solution is therefore

$$X^\mu_{100} = \dot{c}^\mu_{000}(\tilde{v})\big(2M - \rho^*\big) + c^\mu_{100}(\tilde{v}). \tag{9.34}$$

We absorb the $2M\dot{c}^\mu_{000}(\tilde{v})$ into a redefinition of $c^\mu_{100}(\tilde{v})$, leaving

$$X^\mu_{100} = -\dot{c}^\mu_{000}(\tilde{v})\rho^* + c^\mu_{100}(\tilde{v}). \tag{9.35}$$

For $\ell \geq 1$ the right hand side of Eq. (9.29) is zero and we are left with the homogeneous Legendre equation for X_1^μ. The solution then reads

$$X^\mu_{1\ell m} = c^\mu_{1\ell m}(\tilde{v})P_\ell(\check{\rho}) + d^\mu_{1\ell m}(\tilde{v})Q_\ell(\check{\rho}). \tag{9.36}$$

Once again due to our demand for a smooth solution at the horizon, we set $d^\mu_{1\ell m}[v] = 0$. For $\ell = 1$ we have the solution

$$X^\mu_{11m} = c^\mu_{11m}(\tilde{v})\check{\rho}, \tag{9.37}$$

as X^1_μ appears with a pre-factor of ϵ in Eq. (9.2), this solution is permissible as it does not lead to any overall negative powers of M in the transformation. However, for all $\ell > 1$ we set $c^{1\mu}_{1\ell m}[v] \to 0$. We then have the transformation up to order ϵ,

$$T = v - \rho^* + c^0_{000}(\tilde{v})Y^{00} + \epsilon\left(c^0_{100}(\tilde{v}) - \dot{c}^0_{000}(\tilde{v})\rho^*\right)Y^{00} + \epsilon\sum_{m=-1}^{1} c^0_{11m}(\tilde{v})\check{\rho}Y^{1m} + \mathcal{O}(\epsilon^2), \tag{9.38}$$

$$X^i = \rho n^i + c^i_{000}(\tilde{v})Y^{00} + \epsilon\left(c^i_{100}(\tilde{v}) - \dot{c}^i_{000}(\tilde{v})\rho^*\right)Y^{00} + \epsilon\sum_{m=-1}^{1} c^i_{11m}(\tilde{v})\check{\rho}Y^{1m} + \mathcal{O}(\epsilon^2). \tag{9.39}$$

As the monopolar c^μ_{100} piece has no radial dependence, it can be absorbed into a redefinition of the monopolar piece from ϵ^0, c^μ_{000}. Our final form for the inverse solution up to ϵ^1 is therefore

$$T = v - \rho^* + c^0_{000}(\tilde{v})Y^{00} - \epsilon\dot{c}^0_{000}(\tilde{v})\rho^*Y^{00} + \epsilon\sum_{m=-1}^{1} c^0_{11m}(\tilde{v})\check{\rho}Y^{1m} + \mathcal{O}(\epsilon^2), \tag{9.40}$$

$$X^i = \rho n^i + c^i_{000}(\tilde{v})Y^{00} - \epsilon\dot{c}^i_{000}(\tilde{v})\rho^*Y^{00} + \epsilon\sum_{m=-1}^{1} c^i_{11m}(\tilde{v})\check{\rho}Y^{1m} + \mathcal{O}(\epsilon^2). \tag{9.41}$$

9.1.4 Solution at $\mathcal{O}(\epsilon^2)$

We now move to the ϵ^2 equation. The calculation at this order is more involved as it is the first to contain the metric perturbation $p^{(2)}_{\alpha\beta}$. Returning to Eq. (9.19), we see the first term is zero due to Eq. (9.17), and so we have

$$\begin{aligned}
D_0X^\mu_2 &= \frac{1}{r^2\sqrt{\Omega}}\partial_\alpha[r^2\sqrt{\Omega}\overline{p}^{(2)\alpha\beta}\partial_\beta(\bar{X}^\mu_0 + X^\mu_0)] - D_1X^\mu_1, \\
&= \frac{1}{r^2\sqrt{\Omega}}\partial_\alpha(r^2\sqrt{\Omega}\overline{p}^{(2)\alpha\beta}\partial_\beta\bar{X}^\mu_0) - D_1X^\mu_1, \\
&= \frac{1}{r^2}\partial_a(r^2\overline{p}^{(2)a\beta}\partial_\beta\bar{X}^\mu_0) + D_A(\overline{p}^{(2)A\beta}\partial_\beta\bar{X}^\mu_0) - D_1X^\mu_1, \\
&= \frac{1}{r^2}\partial_r(r^2\overline{p}^{(2)r\beta}\partial_\beta\bar{X}^\mu_0) + D_A(\overline{p}^{(2)A\beta}\partial_\beta\bar{X}^\mu_0) - D_1X^\mu_1.
\end{aligned} \tag{9.42}$$

In moving to the second line we note that $\partial_\beta X_0^\mu = 0$ since the only non-zero derivative of $X_0^\mu = c_{000}^\mu(\tilde{v})$ is with respect to v and such terms are demoted to order ϵ^3. In moving to the last line we note that $\partial_v(r^2\overline{p}^{(2)v\beta}\partial_\beta \bar{X}_\mu^0)$ terms will also be demoted to the next order of ϵ.

Before examining the T_2 and X_2^i components we state the values of $\overline{p}^{(2)\alpha\beta}$ in the Regge-Wheeler gauge which will greatly help us simplify the computation at this order. Computing the components of $\overline{p}^{(2)\alpha\beta} = g_{(0)}^{\alpha\nu} g_{(0)}^{\beta\rho} p_{\nu\rho}^{(2)} - \frac{1}{2} g_{(0)}^{\gamma\delta} p_{\gamma\delta}^{(2)} g_{(0)}^{\alpha\beta}$ in (v, r, θ, ϕ) coordinates we obtain

$$\overline{p}^{\alpha\beta} = \begin{bmatrix} r^2 A_{2m} Y^{2m} & -M\rho A_{2m} Y^{2m} & r B_{2m} Z_\theta^{2m} & \frac{r}{\sin(\theta)} B_{2m} Z_\phi^{2m} \\ -M\rho A_{2m} Y^{2m} & -Mf\rho A_{2m} Y^{2m} & 0 & 0 \\ r B_{2m} Z_\theta^{2m} & 0 & 0 & 0 \\ \frac{r}{\sin(\theta)} B_{2m} Z_\phi^{2m} & 0 & 0 & 0 \end{bmatrix}. \tag{9.43}$$

For the T coordinate Eq. (9.42) thus reads

$$D_0 T_2 = \frac{1}{r^2}\partial_r \left[r^2 \overline{p}^{(2)rv} - r^2 \overline{p}^{(2)rr}(1 + \frac{2M}{r}) \right] Y^{00} - \frac{2}{r}\partial_{\tilde{v}} T_1 - 2\partial_r \partial_{\tilde{v}} T_1, \tag{9.44}$$

where the D_A term drops away due to the fact that the only contributing term would be $D_A\big(\overline{p}^{(2)Ar}(1 + \frac{2M}{r})\big)$, which vanished by virtue of $\overline{p}^{(2)Ar} = 0$.

For the X^i coordinates we obtain

$$D_0 X_2^i = \frac{1}{r^2}\partial_r (r^2 \overline{p}^{(2)rr}) n^i - \frac{2}{r}\partial_{\tilde{v}} X_1^i - 2\partial_r \partial_{\tilde{v}} X_1^i. \tag{9.45}$$

We expand Eqs. (9.44) and (9.45) in terms of spherical harmonics, noting that

$$n^i = \sum_{m=-1}^{1} \alpha_m^i Y_{1m}, \tag{9.46}$$

where the only non-vanishing components are

$$\alpha_{\pm 1}^X = \mp\sqrt{\frac{2\pi}{3}}, \qquad \alpha_{\pm 1}^Y = i\sqrt{\frac{2\pi}{3}}, \qquad \alpha_0^Z = 2\sqrt{\frac{2\pi}{3}}. \tag{9.47}$$

Once expanded in spherical harmonics, the relations in Appendix B are used to re-write any derivatives of scalar, vector, or tensor harmonics in terms of scalar, vector, or tensor harmonics themselves.

Once evaluated, the right-hand sides of Eqs. (9.44) and (9.45) contain products of three spherical harmonic terms. For these, we use the identity

$$\int \overline{Y}^{\ell m} Y^{\ell' m'} Y^{\ell'' m''} d\Omega = C^{\ell m}_{\ell' m' \ell'' m''}, \tag{9.48}$$

where the coupling constant is given by

$$C^{\ell m}_{\ell' m' \ell'' m''} = (-1)^m \sqrt{\frac{(2\ell+1)(2\ell'+1)(2\ell''+1)}{4\pi}} \begin{pmatrix} \ell & \ell' & \ell'' \\ 0 & 0 & 0 \end{pmatrix} \begin{pmatrix} \ell & \ell' & \ell'' \\ -m & m' & m'' \end{pmatrix}, \quad (9.49)$$

in which the arrays are the Wigner $3j$ symbols. The Wigner $3j$ symbols have a value of 0 except in the case where $m' + m'' = m$ and $|\ell - \ell'| \leq \ell'' \leq \ell + \ell'$.

The final ODEs for the $X^{\mu}_{2\ell m}$ coefficients are found to be

$$D_0 X^{\mu}_{2\ell m} = S^{\mu}_{2\ell m} \quad (9.50)$$

where

$$S^0_{200} = \frac{2\ddot{c}^0_{000}(\tilde{v})(\rho^* + r + 2M)}{r}, \quad (9.51a)$$

$$S^0_{21m} = \frac{-2(\rho + r)\dot{c}^0_{11m}(\tilde{v})}{Mr}, \quad (9.51b)$$

$$S^0_{22m} = -\frac{4M^3 A_{2m}(\tilde{v})}{r^2}, \quad (9.51c)$$

$$S^0_{2\ell m} = 0 \ \text{ for } \ell \geq 3, \quad (9.51d)$$

$$S^i_{200} = \frac{2\ddot{c}^i_{000}(\tilde{v})(\rho^* + r + 2M)}{r}, \quad (9.51e)$$

$$S^i_{21m} = -\frac{2A^i_{1m}(\tilde{v})M^4 P_2(\check{\rho}) + 2r(\rho + r)\dot{c}^i_{11m}(\tilde{v})}{Mr^2}, \quad (9.51f)$$

$$S^i_{22m} = 0, \quad (9.51g)$$

$$S^i_{23m} = -\frac{2A^i_{3m}(\tilde{v})M^3 P_2(\check{\rho})}{r^2}, \quad (9.51h)$$

$$S^i_{2\ell m} = 0 \ \text{ for } \ell > 3. \quad (9.51i)$$

$$(9.51j)$$

Here we have introduced

$$A^i_{1m}(\tilde{v}) := \sum_{m'=-1}^{1} C^{1m}_{1m'2m''} \alpha^i_{m'} A_{2m''}(\tilde{v}), \quad A^i_{3m}(\tilde{v}) := \sum_{m'=-3}^{3} C^{3m}_{1m'2m''} \alpha^i_{m'} A_{2m''}(\tilde{v}), \quad (9.52)$$

with m'' fixed such that $m' + m'' = m$.

We use the method of variation parameters, with a lower integration bound of $r = 2M$, to solve for $X^{\mu}_{2\ell m}$ just as we solved for $X^{\mu}_{1\ell m}$ in Sec. 9.1.3:

$$X^{\mu}_{2\ell m} = \int_{2M}^{r} \left(\frac{S^{\mu}_{2\ell m}(r')}{f(r')W(r')} \right) \Big[P_\ell(\check{\rho}) Q_\ell(\check{\rho}') - Q_\ell(\check{\rho}) P_\ell(\check{\rho}') \Big] dr' + c^{\mu}_{2\ell m}(\tilde{v}) P_\ell(\check{\rho}) + d^{\mu}_{2\ell m}(\tilde{v}) Q_\ell(\check{\rho}).$$

We find that the first two terms always give a horizon-regular contribution, so horizon regularity implies $d^{\mu}_{2\ell m} = 0$ in all cases. We then ensure to restrict the $P_\ell\big(\frac{r}{M} - 1\big)$ terms that appear such that the overall solution does not blow up for $M \to 0$ at fixed r. The most general solutions satisfying these conditions are found to be

$$\begin{aligned}
T_{200} =& c^0_{200}(\tilde{v}) - 4\ddot{c}^0_{000}(\tilde{v})M^2 Li_2(1 - \frac{r}{2M}) && \text{(9.53a)}\\
&+ \frac{\ddot{c}^0_{000}(\tilde{v})}{3}\bigg((3\rho + 14M)\rho^* - (\rho^2 + 8M\rho + 25M^2)\bigg),\\
T_{21m} =& c^0_{21m}(\tilde{v})\check{\rho} - \dot{c}^0_{11m}(\tilde{v})\bigg(\check{\rho}\rho^* + 2(\rho - 2M)\bigg), && \text{(9.53b)}\\
T_{22m} =& c^0_{22m}(\tilde{v})P_2\big(\check{\rho}\big) - A_{2m}(\tilde{v})M(\rho^2 - M^2), && \text{(9.53c)}\\
T_{2\ell m} =& 0 \text{ for } \ell \geq 3, && \text{(9.53d)}\\
X^i_{200} =& c^i_{200}(\tilde{v}) - 4\ddot{c}^i_{000}(\tilde{v})M^2 Li_2(1 - \frac{r}{2M}) && \text{(9.53e)}\\
&+ \frac{\ddot{c}^i_{000}(\tilde{v})}{3}\bigg((3\rho + 14M)\rho^* - (\rho^2 + 8M\rho + 25M^2)\bigg),\\
X^i_{21m} =& c^i_{21m}(\tilde{v})\check{\rho} - \dot{c}^i_{11m}(\tilde{v})\bigg(\check{\rho}\rho^* + 2(\rho - 2M)\bigg) && \text{(9.53f)}\\
&+ \frac{1}{4}A^i_{1m}(\tilde{v})M(\rho^2 - M^2)(3\rho + M),\\
X^i_{22m} =& c^i_{22m}(\tilde{v})P_2\big(\check{\rho}\big), && \text{(9.53g)}\\
X^i_{23m} =& \frac{1}{6}A^i_{3m}(\tilde{v})(\rho^2 - M^2)(5\rho^2 + 2M\rho - M^2), && \text{(9.53h)}\\
X^i_{2\ell m} =& 0 \text{ for } \ell > 3, && \text{(9.53i)}
\end{aligned}$$

where $Li_2(1 - \frac{r}{2M})$ is a polylogarithm defined by $Li_n(z) = \sum_{k=1}^{\infty} \frac{z^k}{k^n}$. With the argument $1 - \frac{r}{2M}$ the polylogarithm is smooth all the way down to $r = 2M$. At $r = 2M$ all $X^{\mu}_{2\ell m}$ coefficients reduce to being equal to the newly generated $c^{\mu}_{2\ell m}(\tilde{v})$ term or 0.

On examination of the solutions, we see the monopole piece $c^{\mu}_{200}(\tilde{v})$ can be absorbed into a further redefinition of $c^{\mu}_{000}(\tilde{v})$, and the dipole piece $c^{\mu}_{21m}(\tilde{v})\check{\rho}$ can be absorbed into

$c^{\mu}_{11m}(\tilde{v})\check{\rho}$. Our final solutions are therefore

$$T_{200} = -4\ddot{c}^{0}_{000}(\tilde{v})M^2 Li_2(1-\frac{r}{2M}) + \frac{\ddot{c}^{0}_{000}(\tilde{v})}{3}\Big((3\rho+14M)\rho^* - (\rho^2+8M\rho+25M^2)\Big), \tag{9.54a}$$

$$T_{21m} = -\dot{c}^{0}_{11m}(\tilde{v})\Big(\check{\rho}\rho^* + 2(\rho-2M)\Big), \tag{9.54b}$$

$$T_{22m} = c^{0}_{22m}(\tilde{v})P_2\big(\check{\rho}\big) - A_{2m}(\tilde{v})M(\rho^2-M^2), \tag{9.54c}$$

$$T_{2\ell m} = 0 \text{ for } \ell \geq 3, \tag{9.54d}$$

$$X^{i}_{200} = -4\ddot{c}^{i}_{000}(\tilde{v})M^2 Li_2(1-\frac{r}{2M}) + \frac{\ddot{c}^{i}_{000}(\tilde{v})}{3}\Big((3\rho+14M)\rho^* - (\rho^2+8M\rho+25M^2)\Big), \tag{9.54e}$$

$$X^{i}_{21m} = -\dot{c}^{i}_{11m}(\tilde{v})\Big(\check{\rho}\rho^* + 2(\rho-2M)\Big) + \frac{1}{4}A^{i}_{1m}(\tilde{v})M(\rho^2-M^2)(3\rho+M), \tag{9.54f}$$

$$X^{i}_{22m} = c^{i}_{22m}(\tilde{v})P_2\big(\check{\rho}\big), \tag{9.54g}$$

$$X^{i}_{23m} = \frac{1}{6}A^{i}_{3m}(\tilde{v})(\rho^2-M^2)(5\rho^2+2M\rho-M^2), \tag{9.54h}$$

$$X^{i}_{2\ell m} = 0 \text{ for } \ell > 3, \tag{9.54i}$$

The coefficients X^{μ}_{2lm} are then multiplied by their respective spherical harmonics to form the overall X^{μ}_{2} solution,

$$X^{\mu}_{2} = \sum_{\ell=0}^{3}\sum_{m=-\ell}^{\ell} X^{\mu}_{2\ell m}Y^{\ell m}. \tag{9.55}$$

9.1.5 Final Results

The overall transformation can be written in the following form:

$$T = v - \rho^* + [f^0_{00} + \epsilon f^0_{10} + \epsilon^2 f^0_{20}]Y^{00} + [\epsilon f^0_{11} + \epsilon^2 f^0_{21}]Y^{1m} + \epsilon^2 f^0_{22}Y^{2m} + \mathcal{O}(\epsilon^3), \tag{9.56}$$

$$X^i = [f^i_{00} + \epsilon f^i_{10} + \epsilon^2 f^i_{20}]Y^{00} + [f^i_{01} + \epsilon f^i_{11} + \epsilon^2 f^i_{21}]Y^{1m} + \epsilon^2 f^i_{22}Y^{2m} + \epsilon^2 f^i_{23}Y^{3m} + \mathcal{O}(\epsilon^3). \tag{9.57}$$

We have chosen to group our transformation results by their spherical harmonic structure. The $f^{\mu}_{\epsilon\ell}$-type coefficients are functions of v and ρ, where $\rho = r - M$.

The $f^{\mu}_{\epsilon\ell}$-type coefficients are given in Tables 9.1 and 9.2.

TABLE 9.1: $f^0_{\epsilon\ell}$-type functions featuring in Eqs. (9.56)-(9.57)

$$f^0_{00} = c^0_{000}(\tilde{v}) \;\; f^0_{10} = -\dot{c}^0_{000}(\tilde{v})\rho^* \;\; f^0_{20} = -4\dot{c}^0_{000}(\tilde{v})M^2 Li_2(1-\frac{r}{2M}) + \frac{\ddot{c}^0_{000}(\tilde{v})}{3}\Big((3\rho+14M)\rho^* - (\rho^2+8M\rho+25M^2)\Big),$$

$$f^0_{11} = c^0_{11m}(\tilde{v})\hat{\rho} \quad f^0_{21} = -\dot{c}^0_{11m}(\tilde{v})\Big(\check{\rho}\rho^* + 2(\rho-2M)\Big),$$

$$f^0_{22} = c^0_{22m}(\tilde{v})P_2(\check{\rho}) - A_{2m}(\tilde{v})M(\rho^2-M^2)$$

TABLE 9.2: $f^i_{\epsilon\ell}$-type functions featuring in Eqs. (9.56)-(9.57)

$$f^i_{00} = c^i_{000}(\tilde{v}) \;\; f^i_{10} = -\dot{c}^i_{000}(\tilde{v})\rho^* \;\; f^i_{20} = -4\dot{c}^i_{000}(\tilde{v})M^2 Li_2(1-\frac{r}{2M}) + \frac{\ddot{c}^i_{000}(\tilde{v})}{3}\Big((3\rho+14M)\rho^* - (\rho^2+8M\rho+25M^2)\Big)$$

$$f^i_{01} = \alpha^i_m\rho \;\; f^i_{11} = c^i_{11m}(\tilde{v})\hat{\rho} \;\; f^0_{21} = -\dot{c}^i_{11m}(\tilde{v})\Big(\check{\rho}\rho^* + 2(\rho-2M)\Big) + \frac{1}{4}A^i_{1m}(\tilde{v})M(\rho^2-M^2)(3\rho+M)$$

$$f^i_{22} = c^i_{22m}(\tilde{v})P_2(\check{\rho})$$

$$f^i_{23} = \frac{1}{6}A^i_{3m}(\tilde{v})(\rho^2-M^2)(5\rho^2+2M\rho-M^2)$$

We now have the transformation from X^μ to x^μ up to order ϵ^2. This would allow us to obtain the harmonic components of the tidally perturbed metric up to ϵ^2. However, in order to express these components in the harmonic coordinates themselves, we also require the inverse relation i.e. from x^μ to X^μ. We now solve for this inverse transformation in a perturbative manner.

9.2 Inverse Transformation

9.2.1 Setup

For the rest of this chapter we will temporarily refer to the (v, r, θ^A) coordinates as w^μ instead of x^μ. This is to avoid confusion with standard Cartesian coordinates, naturally denoted $x^\mu = (t, x, y, z)$, which will also feature as an intermediary coordinate system within this calculation.

The calculation of the inverse transformation first involves writing an expansion for the w^μ coordinates in terms of the $X^\mu = (T, X, Y, Z)$ harmonic coordinates,

$$w^\beta(X^\mu, \epsilon) = w_0^\beta(X^\mu) + \epsilon w_1^\beta(X^\mu) + \epsilon^2 w_2^\beta(X^\mu) + \mathcal{O}(\epsilon^3). \tag{9.58}$$

Eq. (9.58) is then substituted back into Eq. (9.2) and solved for, order by order in ϵ. This gives

$$\begin{aligned} X^\mu =& X_0^\mu(w_0) + \epsilon w_1^\beta \partial_\beta X_0^\mu(w_0) + \epsilon X_1^\mu(w_0) \\ &+ \epsilon^2 w_2^\beta \partial_\beta X_0^\mu(w_0) + \epsilon^2 w_1^\beta \partial_\beta X_1^\mu(w_0) + \epsilon^2 \frac{1}{2} w_1^\beta w_1^\gamma \partial_\beta \partial_\gamma X_0^\mu(w_0) + \epsilon^2 X_2^\mu(w_0) + \mathcal{O}(\epsilon^3), \end{aligned} \tag{9.59}$$

where X_0^μ now combines both ϵ^0 contributions in Sec. 9.1, $\bar{X}^\mu + X_0^\mu$.

A scalar function F can be expanded on the unit-sphere as

$$F = \sum_{\ell m} f_{\ell m} Y^{\ell m}(\theta^A). \tag{9.60}$$

This can be alternatively written as

$$F = \sum_{\ell=0}^{\infty} \hat{f}_L n^L \tag{9.61}$$

where L is a multi-index $L := i_1 i_2 ... i_\ell$. The tensor coefficients $\hat{F}_L$ are then defined by

$$\hat{F}_L = \frac{(2\ell+1)!!}{4\pi \ell!} \int F \hat{n}^L d\Omega. \tag{9.62}$$

Going forwards we shall adopt the notation that upon the transformation from spherical harmonics to symmetric trace-free tensors the $c^\mu_{n\ell m}(\tilde{v})$ functions are re-scaled as

$$\sum_{m=-\ell}^{\ell} c^\mu_{n\ell m}(\tilde{v}) Y^{\ell m}(\theta^A) =: \hat{c}^\mu_{n\ell L}(\tilde{v}) \hat{n}^L. \tag{9.63}$$

To deal with the unknown $\hat{c}^\mu_{n\ell L}(\tilde{v})$ functions that appear in X^μ, we follow an iterative procedure to re-write them as functions of $\tilde{T} := \epsilon T$.

$$\hat{c}^\mu_{n\ell L}(\tilde{v}) = \hat{c}^{0\mu}_{n\ell L}(\tilde{T}) + \epsilon \hat{c}^{1\mu}_{n\ell L}(\tilde{T}) + \epsilon^2 \hat{c}^{2\mu}_{n\ell L}(\tilde{T}) + \mathcal{O}(\epsilon^3), \tag{9.64}$$

and using Eq. (9.40) we obtain

$$\hat{c}^\mu_{n\ell L}(\tilde{v}) = \hat{c}^\mu_{n\ell L}(\tilde{T} + \epsilon\rho^* - \epsilon \hat{c}^0_{000}(\tilde{v}) - \epsilon^2(-\rho^* \dot{\hat{c}}^0_{000}(\tilde{v}) + \hat{c}^0_{11i}(\tilde{v}) n^i \check{\rho}) + \mathcal{O}(\epsilon^3)). \tag{9.65}$$

Identifying the $\mathcal{O}(\epsilon^0)$ and $\mathcal{O}(\epsilon)$ pieces, we find

$$\hat{c}^{0\mu}_{n\ell L}(\tilde{T}) = \hat{c}^{\mu}_{n\ell L}(\tilde{T}), \tag{9.66}$$

and

$$\hat{c}^{1\mu}_{n\ell L}(\tilde{T}) = \dot{\hat{c}}^{\mu}_{n\ell L}(\tilde{T})(\rho^* - \hat{c}^0_{000}(\tilde{T})). \tag{9.67}$$

Using this we express the $\epsilon\hat{c}^0_{000}(\tilde{v})$ term in Eq. (9.65) as

$$\epsilon\hat{c}^0_{000}(\tilde{v}) = \epsilon\hat{c}^0_{000}(\tilde{T}) + \epsilon^2\dot{\hat{c}}^0_{000}(\tilde{T})(\rho^* - \hat{c}^0_{000}(\tilde{T})) + \mathcal{O}(\epsilon^3). \tag{9.68}$$

The overall ϵ^2 piece is then given by

$$\begin{aligned}\hat{c}^{2\mu}_{n\ell L}(\tilde{T}) &= \frac{1}{2}\ddot{\hat{c}}^{\mu}_{n\ell L}(\tilde{T})(\rho^* - \hat{c}^0_{000}(\tilde{T}))^2 - \dot{\hat{c}}^{\mu}_{n\ell L}(\tilde{T})\dot{\hat{c}}^0_{000}(\tilde{T})(\rho^* - \hat{c}^0_{000}(\tilde{T})) \\ &\quad - \dot{\hat{c}}^{\mu}_{n\ell L}(\tilde{T})(-\rho^*\dot{\hat{c}}^0_{000}(\tilde{T}) + \hat{c}^0_{11i}(\tilde{T})n^i\check{\rho}) \\ &= \frac{1}{2}\ddot{\hat{c}}^{\mu}_{n\ell L}(\tilde{T})(\rho^* - \hat{c}^0_{000}(\tilde{T}))^2 + \dot{\hat{c}}^{\mu}_{n\ell L}(\tilde{T})\dot{\hat{c}}^0_{000}(\tilde{T})\hat{c}^0_{000}(\tilde{T}) \\ &\quad - \dot{\hat{c}}^{\mu}_{n\ell L}(\tilde{T})\hat{c}^0_{11i}(\tilde{T})n^i\check{\rho},\end{aligned} \tag{9.69}$$

where recall $\check{\rho} := \rho/M$.

9.2.2 Inversion at $\mathcal{O}(\epsilon^0)$

The order $\mathcal{O}(\epsilon^0)$ piece of the transformation is given by

$$X^\mu = X^\mu_0(w_0). \tag{9.70}$$

Explicitly:

$$T = v_0 - \rho^*_0 + c^0_{000}(\tilde{T})Y^{00}, \tag{9.71}$$

$$X^i = \rho_0 n^i_0 + c^i_{000}(\tilde{T})Y^{00}, \tag{9.72}$$

where $n^i_0 := \frac{x^i_0}{r_0}$, within which x^i_0 are cartesian coordinates x, y, z and $r_0 = \sqrt{\delta_{ij}x^i_0x^j_0}$. Recall $\rho_0 := r_0 - M$ and $\rho^*_0 = r_0 + 2M\log\left(\frac{r_0}{2M}\right)$.

We now need to invert Eqs. (9.71) and (9.72) to obtain x^μ_0 in terms of X^μ. We begin by solving Eq. (9.72) for ρ_0:

$$\begin{aligned}&\delta_{ij}(X^i - \hat{c}^i_{000}(\tilde{T}))(X^j - \hat{c}^j_{000}(\tilde{T})) = \delta_{ij}\rho_0 n^i_0\rho_0 n^j_0, \\ &\rightarrow \rho_0 = \sqrt{\delta_{ij}(X^i - \hat{c}^i_{000}(\tilde{T}))(X^j - \hat{c}^j_{000}(\tilde{T}))}.\end{aligned} \tag{9.73}$$

Rearranging Eq. (9.72) then gives

$$x^i_0 = r_0 n^i_0 = \frac{M + \rho_0(X)}{\rho_0(X)}\left(X^i - \hat{c}^i_{000}(\tilde{T})\right). \tag{9.74}$$

Substituting r_0 into Eq. (9.71) finally gives us

$$v_0 = T + \rho_0^*(X) - \hat{c}^0_{000}(\tilde{T}). \tag{9.75}$$

9.2.3 Inversion at $\mathcal{O}(\epsilon^1)$

At $\mathcal{O}(\epsilon)$ we need to solve

$$0 = w_1^\beta \partial_\beta X_0^\mu(w_0) + X_1^\mu(w_0) + X_0^\mu(w_0)|_\epsilon \tag{9.76}$$

for w_1^β in terms of X^μ. The last term in Eq. (9.76) comes from the expansion of $c^\mu_{n\ell m}(\tilde{v})$ terms within X_0^μ in terms of $\tilde{T}$. Recalling Eq. (9.65) and

$$X_0^\mu = \bar{X}^\mu + \hat{c}^\mu_{000}(\tilde{v}), \tag{9.77}$$

we have:

$$X_0^\mu|_\epsilon(w_0) = \dot{\hat{c}}^\mu_{000}(\tilde{T})(\rho_0^* - \hat{c}^0_{000}(\tilde{T})). \tag{9.78}$$

Recalling also Eqs. (9.40) and (9.41) we have

$$X_1^\mu = -\dot{c}^\mu_{000}(\tilde{T})\rho_0^* Y^{00} + \sum_{m=-1}^{1} c^\mu_{11m}(\tilde{T})\check{\rho}_0 Y^{1m}. \tag{9.79}$$

Here we transform from spherical harmonics to symmetric trace-free tensors which gives

$$X_1^\mu = -\dot{\hat{c}}^\mu_{000}(\tilde{T})\rho_0^* + \hat{c}^\mu_{11j}(\tilde{T})n^j\check{\rho}_0. \tag{9.80}$$

Substituting into Eq. (9.76), we obtain

$$0 = w_1^\beta \partial_\beta X_0^\mu(w_0) - \dot{\hat{c}}^\mu_{000}(\tilde{T})\hat{c}^0_{000}(\tilde{T}) + \hat{c}^\mu_{11j}(\tilde{T})n^j\check{\rho}_0. \tag{9.81}$$

Recall our goal is to solve this for w_1^β. We hereafter omit the argument $(\tilde{T})$ of the $\hat{c}^\mu_{n\ell L}$ functions for brevity. Using

$$\partial_v T_0 = 1, \quad \partial_k T_0 = -(1 + \frac{2M}{r_0})n_{0k}, \tag{9.82}$$

$$\partial_v X_0^i = 0, \quad \partial_k X_0^i = \delta^i_k - \frac{M}{r_0}(\delta^i_k - n_0^i n_{0k}), \tag{9.83}$$

where we have used $\partial_k r = n_k$, Eq. (9.81) becomes

$$0 = v_1 - w_1^k n_{0k}(1 + \frac{2M}{r_0}) - \dot{\hat{c}}^0_{000}\hat{c}^0_{000} + \hat{c}^0_{11i}n_0^i\check{\rho}_0, \tag{9.84}$$

and

$$0 = w_1^k\left(\delta_k^i - M\frac{p_k^i}{r_0}\right) - \dot{\hat{c}}_{000}^i\hat{c}_{000}^0 + \hat{c}_{11j}^i n_0^j\check{\rho}_0, \tag{9.85}$$

where $p_k^i = \delta_k^i - n_0^i n_{0k}$ is a projection operator. We now introduce the notation $C^r := C^i n_{0i}$ for any vector C. With this, the equations take the form

$$0 = v_1 - w_1^r(1 + \frac{2M}{r_0}) - \dot{\hat{c}}_{000}^0\hat{c}_{000}^0 + \hat{c}_{11r}^0\check{\rho}_0, \tag{9.86}$$

$$0 = w_1^k\left(\delta_k^i - M\frac{p_k^i}{r_0}\right) - \dot{\hat{c}}_{000}^i\hat{c}_{000}^0 + \hat{c}_{11r}^i\check{\rho}_0. \tag{9.87}$$

We start by solving Eq. (9.87) for w_1^k. Here we notice that we can solve for the projected spatial components of w_1^k with the basis (n_0^i, Ω_A^i), where $\Omega_A^i = \frac{\partial n_0^i}{\partial\theta^A}$. Contracting with n_{0i} we obtain the radial component

$$r_1 := w_1^i n_{0i} = \dot{\hat{c}}_{000}^r\hat{c}_{000}^0 - \hat{c}_{11r}^r\check{\rho}_0. \tag{9.88}$$

Contracting with Ω_i^A we obtain the angular components

$$\theta_1^A := w_1^i\Omega_i^A = \frac{r_0}{\rho_0}\left[\dot{\hat{c}}_{000}^A\hat{c}_{000}^0 - \hat{c}_{11r}^A\check{\rho}_0\right], \tag{9.89}$$

where we have introduced the notation $C^A := C^i\Omega_i^A$ for any vector C. From this we can form the Cartesian x_1^k coordinate

$$x_1^k = r_1 n_0^k + \theta_1^A\Omega_A^k. \tag{9.90}$$

Finally, solving Eq. (9.86) for v_1, we obtain

$$v_1 = r_1\left(1 + \frac{2M}{r_0}\right) + \dot{\hat{c}}_{000}^0\hat{c}_{000}^0 - \hat{c}_{11r}^0\check{\rho}_0, \tag{9.91}$$

where r_1 is given by Eq. (9.88).

9.2.4 Inversion at $\mathcal{O}(\epsilon^2)$

Recalling Eq. (9.59), at $\mathcal{O}(\epsilon^2)$ we need to solve

$$\begin{aligned} 0 = {} & w_2^\beta\partial_\beta X_0^\mu(w_0) + w_1^\beta\partial_\beta X_1^\mu(w_0) + \frac{1}{2}w_1^\beta w_1^\gamma\partial_\beta\partial_\gamma X_0^\mu(w_0) \\ & + X_2^\mu(w_0) + X_1^\mu(w_0)|_\epsilon + X_0^\mu(w_0)|_{\epsilon^2} + w_1^\beta\partial_\beta X_0^\mu(w_0)|_\epsilon \end{aligned} \tag{9.92}$$

for w_2^β in terms of X^μ.

The last three terms in Eq. (9.92) come from the expansion of $c^{\mu}_{n\ell m}(\tilde{v})$ within X^{μ}_0 and X^{μ}_1, in terms of $\tilde{T}$. Recalling Eq. (9.65) and

$$X^{\mu}_0 = \bar{X}^{\mu} + \hat{c}^{\mu}_{000}, \tag{9.93}$$

$$X^{\mu}_1 = -\dot{\hat{c}}^{\mu}_{000}\rho^*_0 + \hat{c}^{\mu}_{11r}\check{\rho}_0, \tag{9.94}$$

we have

$$w^{\beta}_1 \partial_{\beta} X^{\mu}_0(w_0)|_{\epsilon} = v_1 \dot{\hat{c}}^{\mu}_{000}, \tag{9.95}$$

$$X^{\mu}_0|_{\epsilon^2} = \frac{1}{2}\ddot{c}^{\mu}_{000}(\rho^*_0 - c^0_{000})^2 + \dot{c}^{\mu}_{000}\dot{c}^0_{000}c^0_{000} - \dot{c}^{\mu}_{000}c^0_{11i}n^i\check{\rho}_0, \tag{9.96}$$

$$X^{\mu}_1|_{\epsilon} = -\ddot{\hat{c}}^{\mu}_{000}\rho^*_0\Big(\rho^*_0 - \hat{c}^0_{000}\Big) + \dot{\hat{c}}^{\mu}_{11i}n^i\check{\rho}_0\Big(\rho^*_0 - \hat{c}^0_{000}\Big). \tag{9.97}$$

From Sec. 9.1.4 we have

$$\begin{aligned} T_2 =& \Big[-4\ddot{c}^0_{000}M^2 Li_2(1 - \frac{r_0}{2M}) + \frac{\ddot{c}^0_{000}}{3}\Big((3\rho_0 + 14M)\rho^*_0 - (\rho^2_0 + 8M\rho_0 + 25M^2)\Big)\Big]Y_{00} \\ &+ \sum_{m=-1}^{1}\Big[-\dot{c}^0_{11m}\Big(\check{\rho}_0\rho^*_0 + 2(\rho_0 - 2M)\Big)\Big]Y_{1m} + \sum_{m=-2}^{2}\Big[c^0_{22m}P_2\big(\check{\rho}_0\big) - A_{2m}M(\rho^2 - M^2)\Big]Y_{2m}, \end{aligned} \tag{9.98}$$

$$\begin{aligned} X^i_2 =& \Big[-4\ddot{c}^i_{000}M^2 Li_2(1 - \frac{r_0}{2M}) + \frac{\ddot{c}^i_{000}}{3}\Big((3\rho_0 + 14M)\rho^*_0 - (\rho^2_0 + 8M\rho_0 + 25M^2)\Big)\Big]Y_{00} \\ &+ \sum_{m=-1}^{1}\Big[-\dot{c}^i_{11m}\Big(\hat{\rho}_0\rho^*_0 + 2(\rho_0 - 2M)\Big) + \frac{1}{4}A^i_{1m}M(\rho^2_0 - M^2)(3\rho_0 + M)\Big]Y_{1m} \\ &+ \sum_{m=-2}^{2}\Big[c^i_{22m}P_2\big(\check{\rho}_0\big)\Big]Y_{2m} + \sum_{m=-3}^{3}\Big[\frac{1}{6}A^i_{3m}(\rho^2_0 - M^2)(5\rho^2 + 2M\rho - M^2)\Big]Y_{3m}. \end{aligned} \tag{9.99}$$

Performing the transformation to symmetric trace-free tensors we obtain

$$\begin{aligned} T_2 =& -4\ddot{\hat{c}}^0_{000}M^2 Li_2(1 - \frac{r_0}{2M}) + \frac{\ddot{\hat{c}}^0_{000}}{3}\Big((3\rho_0 + 14M)\rho^*_0 - (\rho^2_0 + 8M\rho_0 + 25M^2)\Big) \\ &- \dot{\hat{c}}^0_{11i}n^i_0\Big(\check{\rho}_0\rho^*_0 + 2(\rho_0 - 2M)\Big) + \hat{c}^0_{22ij}n^{ij}_0 P_2\big(\check{\rho}_0\big) - \hat{A}_{2ij}n^{ij}_0 M(\rho^2 - M^2), \end{aligned} \tag{9.100}$$

$$\begin{aligned} X^i_2 =& -4\ddot{\hat{c}}^i_{000}M^2 Li_2(1 - \frac{r_0}{2M}) + \frac{\ddot{\hat{c}}^i_{000}}{3}\Big((3\rho_0 + 14M)\rho^*_0 - (\rho^2_0 + 8M\rho_0 + 25M^2)\Big) \\ &- \dot{\hat{c}}^i_{11j}n^j_0\Big(\check{\rho}_0\rho^*_0 + 2(\rho_0 - 2M)\Big) + \frac{1}{4}\hat{A}^i_{1j}n^j_0 M(\rho^2_0 - M^2)(3\rho_0 + M) + \hat{c}^i_{22jk}n^{jk}_0 P_2\big(\check{\rho}_0\big) \\ &+ \frac{1}{6}\hat{A}^i_{3jkl}n^{jkl}_0(\rho^2_0 - M^2)(5\rho^2_0 + 2M\rho_0 - M^2), \end{aligned} \tag{9.101}$$

where an n_0^i with multiple indices denotes multiplication of terms, $n_0^{ij} := n_0^i n_0^j$ and where $\hat{A}^i_{1j}, \hat{A}^i_{3jkl}$ are by definition symmetric trace-free tensors. They are given by $\hat{A}^i_{1j} = \frac{3}{4\pi}\int \sum A^i_{1m} Y^{1m} n_j d\Omega$ and $\hat{A}^i_{3jkl} = \frac{35}{8\pi}\int \sum A^i_{3m} Y^{3m} \hat{n}_{jkl} d\Omega$. Again we are now dropping the $(\tilde{T})$ arguments of the $\hat{c}, \hat{A}$ functions everywhere for brevity.

To evaluate Eq. (9.92) we require the derivatives

$$\partial_v \partial_v T_0 = 0, \quad \partial_v \partial_v X^i_0 = 0, \tag{9.102}$$

$$\partial_v \partial_k T_0 = 0, \quad \partial_v \partial_k X^i_0 = 0, \tag{9.103}$$

$$\partial_j \partial_k T_0 = \partial_j \big[(-1 - \frac{2M}{r_0}) n^i_0 \delta_{ik}\big] = -\frac{\delta_{kj}}{r_0} + \frac{n_{0kj}}{r_0} + \frac{4M}{r_0^2} n_{0jk} - \frac{2M}{r_0^2}\delta_{kj}, \tag{9.104}$$

$$\partial_j \partial_k X^i_0 = \partial_j \big[\delta^i_k - M\frac{p^i_k}{r_0}\big] = \frac{M}{r_0^2} n_{0j}\delta^i_k - \frac{3M}{r_0^2} n^i_{0jk} + \frac{M}{r_0^2} n_{0k}\delta^i_j + \frac{M}{r_0^2} n^i_0 \delta_{kj}, \tag{9.105}$$

$$\partial_v T_1 = 0, \quad \partial_v X^i_1 = 0, \tag{9.106}$$

$$\partial_k T_1 = \partial_k \big[\hat{c}^0_{11i} n^i_0 (\frac{r_0}{M} - 1)\big] = \hat{c}^0_{11i} (\frac{\delta^i_k}{M} - \frac{\delta^i_k}{r_0} + \frac{n^i_{0k}}{r_0}), \tag{9.107}$$

$$\partial_k X^i_1 = \partial_k \big[\hat{c}^i_{11j} n^j_0 (\frac{r_0}{M} - 1)\big] = \hat{c}^i_{11j} (\frac{\delta^j_k}{M} - \frac{\delta^j_k}{r_0} + \frac{n^j_{0k}}{r_0}). \tag{9.108}$$

We now substitute everything into Eq. (9.92) and perform any possible cancellations. Due to the appearance of $w^k_2\Big(\delta^i_k - \frac{M}{r_0}(\delta^i_k - n^i_0 n_{0k})\Big)$ in the equations, we are again able to solve for the radial and angular projections of w^k_2 by contracting with n_{0k} and Ω^A_k. We then substitute in the values for $w^k_1 n_{0k}, w^k_1 \Omega^A_k$ given by Eqs. (9.88) and (9.89) respectively.

Finally, we collects over n_0^i, and in turn group their coefficients into powers of ρ_0 and ρ_0^*. The results are:

$$
\begin{aligned}
r_2 =& -\frac{M\dot{\hat{c}}^i_{000}\dot{\hat{c}}^i_{000}(\hat{c}^0_{000})^2}{2\rho_0^2} + n_{i0}\Bigg[\frac{\dot{\hat{c}}^j_{000}\hat{c}^0_{000}\hat{c}^i_{11j}}{M} - 2\dot{\hat{c}}^i_{000}\hat{c}^0_{000}\dot{\hat{c}}^0_{000} + \frac{1}{6}\ddot{\hat{c}}^i_{000}\Bigg(50M^2 - 3(\hat{c}^0_{000})^2 \\
&+ 24M^2 Li_2(\frac{M-\rho}{2M})\Bigg) - \frac{\dot{\hat{c}}^j_{000}\hat{c}^i_{11j}\hat{c}^0_{000}}{\rho_0} + \rho_0\frac{8M\ddot{\hat{c}}^i_{000}}{3} + \rho_0^2\frac{\dddot{\hat{c}}^i_{000}}{3} - \rho_0^*\frac{14}{3}M\ddot{\hat{c}}^i_{000} + \rho_0^{*2}\frac{1}{2}\dddot{\hat{c}}^i_{000} - \rho_0\rho_0^*\dddot{\hat{c}}^i_{000}\Bigg] \\
&+ n_{0ij}\Bigg[-\frac{M^3}{4}\hat{A}_1^{ij} - \frac{1}{2M}\hat{c}^j_{11k}\hat{c}^{ki}_{11} - 4M\dot{\hat{c}}^{ij}_{11} + \frac{M^2\dot{\hat{c}}^i_{000}\dot{\hat{c}}^j_{000}(\hat{c}^0_{000})^2}{2\rho_0^2(M+\rho_0)} + \frac{M\dot{\hat{c}}^i_{000}\dot{\hat{c}}^j_{000}(\hat{c}^0_{000})^2}{2\rho_0(M+\rho_0)} \\
&- \frac{3M\dot{\hat{c}}^i_{000}\dot{\hat{c}}^j_{000}\hat{c}^0_{000}}{M+\rho_0} - \frac{\dot{\hat{c}}^i_{000}\dot{\hat{c}}^j_{000}\hat{c}^0_{000}\rho_0}{M+\rho_0} + \rho_0\Bigg(-\frac{1}{2}M^2\hat{A}_1^{ij} + \frac{1}{M^2}\hat{c}^j_{11k}\hat{c}^{ik}_{11} + 2\dot{\hat{c}}^{ij}_{11} + \frac{\dot{\hat{c}}^{ij}_{11}\hat{c}^0_{000}}{M} + \frac{2\dot{\hat{c}}^i_{000}\hat{c}^{0j}_{11}}{M}\Bigg) \\
&+ \rho_0^2\frac{3}{4}M\hat{A}_1^{ij}\Bigg] + n_{0ijk}\Bigg[\frac{M\hat{c}^{ijk}_{22}}{2(M+\rho_0)} - \frac{\dot{\hat{c}}^i_{000}\hat{c}^{jk}_{11}\hat{c}^0_{000}}{M+\rho_0} - \frac{M\dot{\hat{c}}^i_{000}\hat{c}^{jk}_{11}\hat{c}^0_{000}}{\rho_0(M+\rho_0)} + \frac{3\dot{\hat{c}}^i_{000}\hat{c}^{jk}_{11}\rho_0}{M+\rho_0} \\
&+ \frac{\hat{c}^{ijk}_{22}\rho_0}{2(M+\rho_0)} + \frac{\dot{\hat{c}}^i_{000}\hat{c}^{jk}_{11}\rho_0^2}{M(M+\rho_0)} - \frac{3\hat{c}^{ijk}_{22}\rho_0^2}{2M(M+\rho_0)} - \frac{3\hat{c}^{ijk}_{22}\rho_0^3}{2M^2(M+\rho_0)}\Bigg] \\
&n_{0ijkp}\Bigg[\frac{M^4\hat{A}_3^{ijkp} + 3\hat{c}^{ij}_{11}\hat{c}^{kp}_{11}}{6M} - \frac{1}{2}M^2\hat{A}_3^{ijkp}\rho_0 - \frac{1}{2}M\hat{A}_3^{ijkp}\rho_0^2 + \frac{5}{6}\hat{A}_3^{ijkp}\rho_0^3\Bigg],
\end{aligned}
\tag{9.109}
$$

$$
\begin{aligned}
\theta_2^A =& \Bigg[\Bigg(-\frac{1}{2}\ddot{\hat{c}}^i_{000}(\hat{c}^0_{000})^2 - \ddot{\hat{c}}^i_{000}\dot{\hat{c}}^0_{000}\hat{c}^0_{000} + M^2\ddot{\hat{c}}^i_{000}\big(11 + 4Li_2(2, \frac{M-\rho_0}{2M})\big)\Bigg)\Omega_i^A - \frac{\dot{\hat{c}}^i_{000}\hat{c}^j_{11i}\hat{c}^0_{000}\Omega_j^A}{M} \\
&+ \frac{1}{\rho_0}\Bigg(\frac{1}{6}M\ddot{\hat{c}}^i_{000}(50M^2 - 3(\hat{c}^0_{000})^2 + 24M^2 Li_2(\frac{M-\rho_0}{2M}) - 28M\rho_0^* + 3\rho_0^{*2}\Bigg)\Omega_i^A - \dot{\hat{c}}^i_{000}\hat{c}^0_{000}(2M\dot{\hat{c}}^0_{000}\Omega_i^A \\
&+ \hat{c}^j_{11i}\Omega_j^A)\Bigg) + \rho_0(3M\ddot{\hat{c}}^i_{000}\Omega_i^A - \ddot{\hat{c}}^i_{000}\rho_0^*\Omega_i^A) + \rho_0^2\frac{1}{3}\ddot{\hat{c}}^i_{000}\Omega_i^A - \rho_0^*\frac{17M}{3}\ddot{c}^i_{000}\Omega_i^A + \rho_0^{*2}\frac{1}{2}\ddot{\hat{c}}^i_{000}\Omega_i^A\Bigg] \\
&+ n_{0j}\Bigg[\frac{1}{4}\Bigg(-3M^2\hat{A}_1^{aj} + 4\dot{\hat{c}}^{aj}_{11}(-2M + \dot{\hat{c}}^0_{000}) + 4\dot{\hat{c}}^a_{000}(-\dot{\hat{c}}^j_{000}\hat{c}^0_{000} + \hat{c}^{0j}_{11} + \dot{\hat{c}}^{0j}_{11})\Bigg)\Omega_a^A \\
&+ \frac{\hat{c}^{aj}_{11}\hat{c}^b_{11a}\Omega_b^A}{M} + \frac{1}{\rho_0^2}M\dot{\hat{c}}^a_{000}\dot{\hat{c}}^j_{000}(\hat{c}^0_{000})^2\Omega_a^A - \frac{1}{\rho_0}\frac{1}{4}M(M^3\hat{A}_1^{aj} + 12\dot{\hat{c}}^j_{000}\hat{c}^0_{000}\dot{\hat{c}}^a_{000} + 16M\dot{\hat{c}}^{aj}_{11})\Omega_a^A \\
&+ \rho_0\frac{1}{4M^2}\Bigg(M\big(M^3\hat{A}_1^{aj} + 4\dot{\hat{c}}^{aj}_{11}(2M + \dot{\hat{c}}^0_{000}) + 8\dot{\hat{c}}^a_{000}\hat{c}^{0j}_{11}\big)\Omega_a^A + 4\hat{c}^{aj}_{11}\hat{c}^b_{11a}\Omega_b^A\Bigg) + \frac{3}{4}M\hat{A}_1^{aj}\rho_0^2\Omega_a^A\Bigg] \\
&+ n_{0jk}\Bigg[\frac{1}{2}(6\ddot{\hat{c}}^i_{000}\hat{c}^{jk}_{11} + \hat{c}^{ijk}_{22})\Omega_i^A + \frac{1}{\rho_0}\frac{1}{2}(2\dot{\hat{c}}^j_{000}\hat{c}^{ik}_{11} + 2\dot{\hat{c}}^i_{000}\hat{c}^0_{000}\hat{c}^{jk}_{11} + M\hat{c}^{ijk}_{22})\Omega_i^A \\
&+ \rho_0\frac{1}{2M}(2\dot{\hat{c}}^a_{000}\hat{c}^{jk}_{11} - 3\hat{c}^{ajk}_{22})\Omega_a^A - \rho_0^2\frac{3}{2M^2}\hat{c}^{ijk}_{22}\Omega_i^A\Bigg] + n_{0jkp}\Bigg[-\frac{(M^4\hat{A}_3^{ijkp} + 3\hat{c}^{ij}_{11}\hat{c}^{kp}_{11})\Omega_i^A}{3M} \\
&+ \frac{1}{\rho_0}\frac{M^4}{6}\hat{A}_3^{ijkp}\Omega_i^A - \rho_0 M^2\hat{A}_3^{ijkp}\Omega_i^A + \rho_0^2\frac{M}{3}\hat{A}_3^{ijkp}\Omega_i^A + \rho_0^3\frac{5}{6}\hat{A}_3^{ijkp}\Omega_i^A\Bigg],
\end{aligned}
\tag{9.110}
$$

$$
\begin{aligned}
v_2 =& \Bigg[\frac{1}{6}\Bigg(50M^2\ddot{\hat{c}}^0_{000} - 3\hat{c}^0_{000}(4(\dot{\hat{c}}^0_{000})^2 + \hat{c}^0_{000}\ddot{\hat{c}}^0_{000}) - \frac{6\dot{\hat{c}}^i_{000}\hat{c}^0_{11i}\hat{c}^0_{000}}{M} + 24M^2 Li_2(\frac{M-\rho_0}{2M}) \\
&+ \frac{3\dot{\hat{c}}^i_{000}\dot{\hat{c}}_{i000}(\hat{c}^0_{000})^2(3M+\rho_0)}{\rho_0^2} + \rho_0 16M\ddot{\hat{c}}^0_{000} + \rho_0^2 2\ddot{\hat{c}}^0_{000}\Bigg) - \rho_0^*\frac{1}{3}\ddot{\hat{c}}^0_{000}(14M+3\rho_0) + \rho_0^{*2}\frac{1}{2}\ddot{\hat{c}}^0_{000}\Bigg] \\
&+ n_{0i}\Bigg[\frac{3M+\rho_0}{M+\rho_0}y_2^i - \frac{\dot{\hat{c}}^j_{000}\hat{c}^i_{11j}}{M} - 4M\dot{\hat{c}}^{0i}_{11} - \frac{1}{\rho_0}3\dot{\hat{c}}^j_{000}\hat{c}^i_{11j} - \frac{3M+\rho_0}{M+\rho_0}\dot{\hat{c}}^i_{000}\hat{c}^0_{000}\dot{\hat{c}}^0_{000} \\
&+ \rho_0\frac{1}{M^2}(2M\dot{\hat{c}}^0_{000}\hat{c}^{0i}_{11} + \hat{c}^{ij}_{11}\hat{c}^0_{11j} + 2M^2\dot{\hat{c}}^{0i}_{11} + 2M\dot{\hat{c}}^0_{000}\dot{\hat{c}}^{0i}_{11})\Bigg] + n_{0ij}\Bigg[-M^3\hat{A}^{ij}_2 + \frac{3\hat{c}^j_{11k}\hat{c}^{ki}_{11}}{2M} \\
&- \frac{\hat{c}^{ij}_{11}\dot{\hat{c}}^0_{000}\rho_0}{M} + \frac{(\hat{c}^j_{11k}\hat{c}^{ki}_{11} + 2M\hat{c}^{ij}_{11}\dot{\hat{c}}^0_{000})\rho_0}{2M^2} + M^2\hat{A}^{ij}_2\rho_0^2 - \frac{7M\dot{\hat{c}}^i_{000}\dot{\hat{c}}^j_{000}(\hat{c}^0_{000})^2}{2(M+\rho_0)^2} \\
&+ \frac{M^2\hat{c}^{0ij}_{22}}{2(M+\rho_0)^2} - \frac{3M^2\dot{\hat{c}}^i_{000}\dot{\hat{c}}^j_{000}(\hat{c}^0_{000})^2}{2\rho_0^2(M+\rho_0)^2} - \frac{7M^2\dot{\hat{c}}^i_{000}\dot{\hat{c}}^j_{000}(\hat{c}^0_{000})^2}{2\rho_0(M+\rho_0)^2} - \frac{\rho_0\dot{\hat{c}}^i_{000}\dot{\hat{c}}^j_{000}(\hat{c}^0_{000})^2}{2(M+\rho_0)^2} + \frac{3M\hat{c}^{ij}_{11}\dot{\hat{c}}^0_{000}\rho_0}{(M+\rho_0)^2} \\
&+ \frac{M\hat{c}^{0ij}_{22}\rho_0}{(M+\rho_0)^2} + \frac{4\hat{c}^{ij}_{11}\dot{\hat{c}}^0_{000}\rho_0^2}{(M+\rho_0)^2} - \frac{\hat{c}^{0ij}_{22}\rho_0^2}{(M+\rho_0)^2} + \frac{\hat{c}^{ij}_{11}\dot{\hat{c}}^0_{000}\rho_0^3}{M(M+\rho_0)^2} - \frac{3\hat{c}^{0ij}_{22}\rho_0^2}{M(M+\rho_0)^2} - \frac{3\hat{c}^{0ij}_{22}\rho_0^4}{2M^2(M+\rho_0)^2}\Bigg] \\
&+ n_{0ijk}\Bigg[\frac{7M\dot{\hat{c}}^i_{000}\hat{c}^0_{000}\hat{c}^{jk}_{11}}{(M+\rho_0)^2} + \frac{3M^2\dot{\hat{c}}^i_{000}\hat{c}^0_{000}\hat{c}^{jk}_{11}}{\rho_0(M+\rho_0)^2} + \rho_0\frac{7\dot{\hat{c}}^i_{000}\hat{c}^0_{000}\hat{c}^{jk}_{11}}{(M+\rho_0)^2} + \rho_0^2\frac{\dot{\hat{c}}^i_{000}\hat{c}^0_{000}\hat{c}^{jk}_{11}}{M(M+\rho_0)^2}\Bigg] \\
&+ n_{0ijkp}\Bigg[-\frac{3M\hat{c}^{ij}_{11}\hat{c}^{kp}_{11}}{2(M+\rho_0)^2} - \rho_0\frac{7\hat{c}^{ij}_{11}\hat{c}^{kp}_{11}}{2(M+\rho_0)^2} - \rho_0^2\frac{7M\hat{c}^{ij}_{11}\hat{c}^{kp}_{11}}{2M(M+\rho_0)^2} - \rho_0^3\frac{\hat{c}^{ij}_{11}\hat{c}^{kp}_{11}}{2M^2(M+\rho_0)^2}\Bigg].
\end{aligned}
\tag{9.111}
$$

9.2.5 Final Results

The overall inverse transformation can be written in the following form:

$$
v = e_{v0} + \epsilon e_{v1} + \epsilon^2 e_{v2} + \left[\epsilon e^i_{v1} + \epsilon^2 e^i_{v2}\right] n_{0i} + \left[\epsilon e^{ij}_{v1} + \epsilon^2 e^{ij}_{v2}\right] n_{0ij} + \epsilon^2 e^{ijk}_{v2} n_{0ijk} + \epsilon^2 e^{ijkp}_{v2} n_{0ijkp} + \mathcal{O}(\epsilon^3), \tag{9.112}
$$

$$
r = \epsilon^2 e_{r2} + \left[e^i_{r0} + \epsilon e^i_{r1} + \epsilon^2 e^i_{r2}\right] n_{0i} + \left[\epsilon e^{ij}_{r1} + \epsilon^2 e^{ij}_{r2}\right] n_{0ij} + \epsilon^2 e^{ijk}_{r2} n_{0ijk} + \epsilon^2 e^{ijkp}_{r2} n_{0ijkp} + \mathcal{O}(\epsilon^3), \tag{9.113}
$$

$$
\theta^A = e^A_0 + \epsilon e^A_1 + \epsilon^2 e^A_2 + \left[\epsilon e^{Aj}_1 + \epsilon^2 e^{Aj}_2\right] n_{0j} + \epsilon^2 e^{Ajk}_2 n_{0jk} + \epsilon^2 e^{Ajkp}_2 n_{0jkp} + \epsilon^2 e^{Aijkp}_2 n_{0ijkp} + \mathcal{O}(\epsilon^3). \tag{9.114}
$$

We have chosen to group our inverse transformation results by their multipolar structure as (as described in Sec. 7.4) we will eventually be matching the analytical metric mode-by-mode to the NR metric. The e-type coefficients are functions of T, ρ_0 and ρ_0^*; they are given in explicit form in Tables 9.3 - 9.5.

TABLE 9.3: e_0, e_1-type functions featuring in Eqs. (9.112)-(9.114)

$$e_{v0} = T + \rho_0^* - \hat{c}^0_{000}, \;\; e_{v1} = \dot{\hat{c}}^0_{000}\hat{c}^0_{000}, \;\; e^i_{v1} = \dot{\hat{c}}^i_{000}\hat{c}^0_{000}\left(1 + \frac{2M}{r_0}\right) - \hat{c}^{0i}_{11}\check{\rho}_0, \;\; e^{ij}_{v1} = -\hat{c}^{ij}_{11}\check{\rho}_0\left(1 + \frac{2M}{r_0}\right)$$

$$e^i_{r0} = \frac{M + \rho_0}{\rho_0}\left(X^i - \hat{c}^i_{000}\right), \;\; e^i_{r1} = \dot{\hat{c}}^i_{000}\hat{c}^0_{000}, \;\; e^{ij}_{r1} = -\hat{c}^{ij}_{11}\check{\rho}_0$$

$$e^A_0 = \frac{M + \rho_0}{\rho_0}\left(X^i - \hat{c}^i_{000}\right)\Omega^A_i, \;\; e^A_1 = \frac{M + \rho_0}{\rho_0}\dot{\hat{c}}^i_{000}\hat{c}^0_{000}\Omega^A_i, \;\; e^{Aj}_1 = \frac{M + \rho_0}{\rho_0}\hat{c}^{ij}_{11}\check{\rho}_0\Omega^A_i$$

TABLE 9.4: e_2-type functions featuring in Eqs. (9.112)-(9.114)

$$e_{v2} = \frac{1}{6}\Big(50M^2\ddot{\hat{c}}^0_{000} - 3\hat{c}^0_{000}(4(\dot{\hat{c}}^0_{000})^2 + \hat{c}^0_{000}\ddot{\hat{c}}^0_{000}) - \frac{6\dot{\hat{c}}^i_{000}\hat{c}^0_{11i}\hat{c}^0_{000}}{M} + 24M^2 Li_2(\frac{M-\rho_0}{2M}) + \frac{3\dot{\hat{c}}^i_{000}\dot{\hat{c}}_{i000}(\hat{c}^0_{000})^2(3M+\rho_0)}{\rho_0^2} + \rho_0 16M\ddot{\hat{c}}^0_{000} + \rho_0^2 2\ddot{\hat{c}}^0_{000}\Big) - \rho_0^*\frac{1}{3}\ddot{\hat{c}}^0_{000}(14M+3\rho_0) + \rho_0^{*2}\frac{1}{2}\ddot{\hat{c}}^0_{000}$$

$$e^i_{v2} = \frac{3M+\rho_0}{M+\rho_0}x^i_2 - \frac{\dot{\hat{c}}^j_{000}\hat{c}^i_{11j}}{M} - 4M\dot{\hat{c}}^{0i}_{11} - \frac{1}{\rho_0}3\dot{\hat{c}}^j_{000}\hat{c}^i_{11j} - \frac{3M+\rho_0}{M+\rho_0}\dot{\hat{c}}^i_{000}\hat{c}^0_{000}\dot{\hat{c}}^0_{000} + \rho_0\frac{1}{M^2}(2M\dot{\hat{c}}^0_{000}\hat{c}^{0i}_{11} + \hat{c}^{ij}_{11}\hat{c}^0_{11j} + 2M^2\dot{\hat{c}}^{0i}_{11} + 2M\dot{\hat{c}}^0_{000}\dot{\hat{c}}^{0i}_{11})$$

$$e^{ij}_{v2} = -M^3\hat{A}^{ij}_2 + \frac{3\hat{c}^j_{11k}\hat{c}^{ki}_{11}}{2M} - \frac{\hat{c}^{ij}_{11}\dot{\hat{c}}^0_{000}\rho_0}{M} + \frac{(\hat{c}^j_{11k}\hat{c}^{ki}_{11} + 2M\hat{c}^{ij}_{11}\dot{\hat{c}}^0_{000})\rho_0}{2M^2} + M^2\hat{A}^{ij}_2\rho_0^2 - \frac{7M\dot{\hat{c}}^i_{000}\dot{\hat{c}}^j_{000}(\hat{c}^0_{000})^2}{2(M+\rho_0)^2} + \frac{M^2\hat{c}^{0ij}_{22}}{2(M+\rho_0)^2} - \frac{3M^2\dot{\hat{c}}^i_{000}\dot{\hat{c}}^j_{000}(\hat{c}^0_{000})^2}{2\rho_0^2(M+\rho_0)^2} - \frac{7M^2\dot{\hat{c}}^i_{000}\dot{\hat{c}}^j_{000}(\hat{c}^0_{000})^2}{2\rho_0(M+\rho_0)^2} - \frac{\rho_0\dot{\hat{c}}^i_{000}\dot{\hat{c}}^j_{000}(\hat{c}^0_{000})^2}{2(M+\rho_0)^2} + \frac{3M\hat{c}^{ij}_{11}\dot{\hat{c}}^0_{000}\rho_0}{(M+\rho_0)^2} + \frac{M\hat{c}^{0ij}_{22}\rho_0}{(M+\rho_0)^2} + \frac{4\hat{c}^{ij}_{11}\dot{\hat{c}}^0_{000}\rho_0^2}{(M+\rho_0)^2} - \frac{\hat{c}^{0ij}_{22}\rho_0^2}{(M+\rho_0)^2} + \frac{\hat{c}^{ij}_{11}\dot{\hat{c}}^0_{000}\rho_0^3}{M(M+\rho_0)^2} - \frac{3\hat{c}^{0ij}_{22}\rho_0^2}{M(M+\rho_0)^2} - \frac{3\hat{c}^{0ij}_{22}\rho_0^4}{2M^2(M+\rho_0)^2}$$

$$e^{ijk}_{v2} = \frac{7M\dot{\hat{c}}^i_{000}\hat{c}^0_{000}\hat{c}^{jk}_{11}}{(M+\rho_0)^2} + \frac{3M^2\dot{\hat{c}}^i_{000}\hat{c}^0_{000}\hat{c}^{jk}_{11}}{\rho_0(M+\rho_0)^2} + \rho_0\frac{7\dot{\hat{c}}^i_{000}\hat{c}^0_{000}\hat{c}^{jk}_{11}}{(M+\rho_0)^2} + \rho_0^2\frac{\dot{\hat{c}}^i_{000}\hat{c}^0_{000}\hat{c}^{jk}_{11}}{M(M+\rho_0)^2}$$

$$e^{ijkp}_{v2} = -\frac{3M\hat{c}^{ij}_{11}\hat{c}^{kp}_{11}}{2(M+\rho_0)^2} - \rho_0\frac{7\hat{c}^{ij}_{11}\hat{c}^{kp}_{11}}{2(M+\rho_0)^2} - \rho_0^2\frac{7M\hat{c}^{ij}_{11}\hat{c}^{kp}_{11}}{2M(M+\rho_0)^2} - \rho_0^3\frac{\hat{c}^{ij}_{11}\hat{c}^{kp}_{11}}{2M^2(M+\rho_0)^2}$$

$$e_{r2} = -\frac{M\dot{\hat{c}}^i_{000}\dot{\hat{c}}^i_{000}(\hat{c}^0_{000})^2}{2\rho_0^2}$$

$$e^i_{r2} = \frac{\dot{\hat{c}}^j_{000}\hat{c}^0_{000}\hat{c}^i_{11j}}{M} - 2\dot{\hat{c}}^i_{000}\hat{c}^0_{000}\dot{\hat{c}}^0_{000} + \frac{1}{6}\ddot{\hat{c}}^i_{000}\Big(50M^2 - 3(\hat{c}^0_{000})^2 + 24M^2 Li_2(\frac{M-\rho}{2M})\Big) - \frac{\dot{\hat{c}}^j_{000}\hat{c}^i_{11j}\hat{c}^0_{000}}{\rho_0} + \rho_0\frac{8M\ddot{\hat{c}}^i_{000}}{3} + \rho_0^2\frac{\ddot{\hat{c}}^i_{000}}{3} - \rho_0^*\frac{14}{3}M\ddot{\hat{c}}^i_{000} + \rho_0^{*2}\frac{1}{2}\ddot{\hat{c}}^i_{000} - \rho_0\rho_0^*\ddot{\hat{c}}^i_{000}$$

$$e^{ij}_{r2} = -\frac{M^3}{4}\hat{A}^{ij}_1 - \frac{1}{2M}\hat{c}^j_{11k}\hat{c}^{ki}_{11} - 4M\dot{\hat{c}}^{ij}_{11} + \frac{M^2\dot{\hat{c}}^i_{000}\dot{\hat{c}}^j_{000}(\hat{c}^0_{000})^2}{2\rho_0^2(M+\rho_0)} + \frac{M\dot{\hat{c}}^i_{000}\dot{\hat{c}}^j_{000}(\hat{c}^0_{000})^2}{2\rho_0(M+\rho_0)} - \frac{3M\dot{\hat{c}}^i_{000}\dot{\hat{c}}^j_{000}\hat{c}^0_{000}}{M+\rho_0} - \frac{\dot{\hat{c}}^i_{000}\dot{\hat{c}}^j_{000}\hat{c}^0_{000}\rho_0}{M+\rho_0} + \rho_0\Big(-\frac{1}{2}M^2\hat{A}^{ij}_1 + \frac{1}{M^2}\hat{c}^j_{11a}\hat{c}^{ia}_{11} + 2\dot{\hat{c}}^{ij}_{11} + \frac{\dot{\hat{c}}^{ij}_{11}\hat{c}^0_{000}}{M} + \frac{2\dot{\hat{c}}^i_{000}\hat{c}^{0j}_{11}}{M}\Big) + \rho_0^2\frac{3}{4}M\hat{A}^{1ij}$$

$$e^{ijk}_{r2} = \frac{M\hat{c}^{ijk}_{22}}{2(M+\rho_0)} - \frac{\dot{\hat{c}}^i_{000}\hat{c}^{jk}_{11}\hat{c}^0_{000}}{M+\rho_0} - \frac{M\dot{\hat{c}}^i_{000}\hat{c}^{jk}_{11}\hat{c}^0_{000}}{\rho_0(M+\rho_0)} + \frac{3\dot{\hat{c}}^i_{000}\hat{c}^{jk}_{11}\rho_0}{M+\rho_0} + \frac{\hat{c}^{ijk}_{22}\rho_0}{2(M+\rho_0)} + \frac{\dot{\hat{c}}^i_{000}\hat{c}^{jk}_{11}\rho_0^2}{M(M+\rho_0)} - \frac{3\hat{c}^{ijk}_{22}\rho_0^2}{2M(M+\rho_0)} - \frac{3\hat{c}^{ijk}_{22}\rho_0^3}{2M^2(M+\rho_0)}$$

$$e^{ijkp}_{r2} = \frac{M^4\hat{A}^{ijkp}_3 + 3\hat{c}^{ij}_{11}\hat{c}^{kp}_{11}}{6M} - \frac{1}{2}M^2\hat{A}^{ijkp}_3\rho_0 - \frac{1}{2}M\hat{A}^{ijkp}_3\rho_0^2 + \frac{5}{6}\hat{A}^{ijkp}_3\rho_0^3$$

TABLE 9.5: e_2^A-type functions featuring in Eqs. (9.112)-(9.114)

$$
\begin{aligned}
e_2^A =& \Big(-\frac{1}{2}\ddot{\hat{c}}^i_{000}(\hat{c}^0_{000})^2 - \ddot{\hat{c}}^i_{000}\dot{\hat{c}}^0_{000}\hat{c}^0_{000} + M^2\ddot{\hat{c}}^i_{000}\big(11 + 4Li_2(2, \frac{M-\rho_0}{2M})\big)\Big)\Omega^A_i - \frac{\dot{\hat{c}}^i_{000}\hat{c}^j_{11i}\hat{c}^0_{000}\Omega^A_j}{M} \\
&+ \frac{1}{\rho_0}\Big(\frac{1}{6}M\ddot{\hat{c}}^i_{000}(50M^2 - 3(\hat{c}^0_{000})^2 + 24M^2 Li_2(\frac{M-\rho_0}{2M}) - 28M\rho^*_0 + 3\rho^{*2}_0\Big)\Omega^A_i - \dot{\hat{c}}^i_{000}\hat{c}^0_{000}(2M\dot{\hat{c}}^0_{000}\Omega^A_i \\
&+ \hat{c}^j_{11i}\Omega^A_j)\Big) + \rho_0(3M\ddot{\hat{c}}^i_{000}\Omega^A_i - \ddot{\hat{c}}^i_{000}\rho^*_0\Omega^A_i) + \rho^2_0\frac{1}{3}\ddot{\hat{c}}^i_{000}\Omega^A_i - \rho^*_0\frac{17M}{3}\ddot{c}^i_{000}\Omega^A_i + \rho^{*2}_0\frac{1}{2}\ddot{\hat{c}}^i_{000}\Omega^A_i
\end{aligned}
$$

$$
\begin{aligned}
e_2^{Aj} =& \frac{1}{4}\Big(-3M^2\hat{A}^{aj}_1 + 4\dot{\hat{c}}^{aj}_{11}(-2M + \dot{\hat{c}}^0_{000}) + 4\dot{\hat{c}}^a_{000}(-\dot{\hat{c}}^j_{000}\hat{c}^0_{000} + \hat{c}^{0j}_{11} + \dot{\hat{c}}^{0j}_{11})\Big)\Omega^A_a \\
&+ \frac{\hat{c}^{aj}_{11}\hat{c}^b_{11a}\Omega^A_b}{M} + \frac{1}{\rho^2_0}M\dot{\hat{c}}^a_{000}\dot{\hat{c}}^j_{000}(\hat{c}^0_{000})^2\Omega^A_a - \frac{1}{\rho_0}\frac{1}{4}M(M^3\hat{A}^{1aj} + 12\dot{\hat{c}}^j_{000}\hat{c}^0_{000}\dot{\hat{c}}^a_{000} + 16M\dot{\hat{c}}^{aj}_{11})\Omega^A_a \\
&+ \rho_0\frac{1}{4M^2}\Big(M\big(M^3\hat{A}^{aj}_1 + 4\dot{\hat{c}}^{aj}_{11}(2M + \dot{\hat{c}}^0_{000}) + 8\dot{\hat{c}}^a_{000}\hat{c}^{0j}_{11}\big)\Omega^A_a + 4\hat{c}^{aj}_{11}\hat{c}^b_{11a}\Omega^A_b\Big) + \frac{3}{4}M\hat{A}^{aj}_1\rho^2_0\Omega^A_a
\end{aligned}
$$

$$
\begin{aligned}
e_2^{Ajk} =& \frac{1}{2}(6\ddot{\hat{c}}^i_{000}\hat{c}^{jk}_{11} + \hat{c}^{ijk}_{22})\Omega^A_i + \frac{1}{\rho_0}\frac{1}{2}(2\dot{\hat{c}}^j_{000}\hat{c}^{ik}_{11} + 2\dot{\hat{c}}^i_{000}\hat{c}^0_{000}\hat{c}^{jk}_{11} + M\hat{c}^{ijk}_{22})\Omega^A_i \\
&+ \rho_0\frac{1}{2M}(2\dot{\hat{c}}^a_{000}\hat{c}^{jk}_{11} - 3\hat{c}^{ajk}_{22})\Omega^A_a - \rho^2_0\frac{3}{2M^2}\hat{c}^{ijk}_{22}\Omega^A_i
\end{aligned}
$$

$$
e_2^{Ajkp} = -\frac{(M^4\hat{A}^{ijkp}_3 + 3\hat{c}^{ij}_{11}\hat{c}^{kp}_{11})\Omega^A_i}{3M} + \frac{1}{\rho_0}\frac{M^4}{6}\hat{A}^{ijkp}_3\Omega^A_i - \rho_0 M^2\hat{A}^{ijkp}_3\Omega^A_i + \rho^2_0\frac{M}{3}\hat{A}^{ijkp}_3\Omega^A_i + \rho^3_0\frac{5}{6}\hat{A}^{ijkp}_3\Omega^A_i
$$

9.3 Transformed Metric

Now that we have the coordinate transformation to harmonic coordinates, our final task is to express the metric itself in these coordinates.

9.3.1 Preliminaries

We will perform an intermediary transformation to Cartesian coordinates as this will allow us to move from the arbitrary angles θ^A that appear in the metric to a fully specified spatial coordinate basis (x, y, z). Such a transformation is effected by $x^a = rn^a(\theta^A)$, where $\theta^A = (\theta, \phi)$ [109]. The Jacobian matrix is given by

$$
\frac{\partial x^a}{\partial r} = n^a, \quad \frac{\partial x^a}{\partial \theta^A} = r\Omega^a_A, \tag{9.115}
$$

where $\Omega^a_A := \partial n^a/\partial\theta^A$. The inverse of the Jacobian matrix is

$$
\frac{\partial r}{\partial x^a} = n_a, \quad \frac{\partial \theta^A}{\partial x^a} = \frac{1}{r}\Omega^A_a, \tag{9.116}
$$

where $\Omega^A_a := \Omega^{AB}\delta_{ab}\Omega^b_B = diag[1, \sin^2\theta]$.

We now return to the original Regge-Wheeler gauge metric as presented in Eqs. (8.71)-(8.76). First we re-write the two terms that involve spherical harmonics in terms of symmetric trace-free tensors. Straightforwardly,

$$\sum_m A_m(\tilde{v})Y^{2m} = \hat{A}_{2ij}(\tilde{v})n^{ij}. \tag{9.117}$$

The Z^{2m}_A term is a little more involved:

$$\begin{aligned}\sum_m B_m(\tilde{v})Z^{2m}_A &= \sum_m B_m(\tilde{v})D_B Y^{2m}\varepsilon^B_A \\ &= D_B \sum_m Y^{2m}B_m(\tilde{v})\varepsilon^B_A \\ &= D_B\hat{B}_{2ij}(\tilde{v})n^{ij}\varepsilon^B_A \\ &= 2\hat{B}_{2ij}(\tilde{v})n^i\Omega^j_B\varepsilon^B_A,\end{aligned} \tag{9.118}$$

where in the last line we have used $\frac{\partial x^a}{\partial\theta^A} = r\Omega^a_A$.

The covariant components of the tidally perturbed metric are then

$$g_{vv=} - f + \epsilon^2\frac{1}{2}r^2f^2\hat{A}_{2ij}(\tilde{v})n^{ij} + \mathcal{O}(\epsilon^3), \tag{9.119}$$

$$g_{vr} = 1 - \epsilon^2\frac{1}{2}r^2f\hat{A}_{2ij}(\tilde{v})n^{ij} + \mathcal{O}(\epsilon^3), \tag{9.120}$$

$$g_{rr} = \epsilon^2 r^2\hat{A}_{2ij}(\tilde{v})n^{ij} + \mathcal{O}(\epsilon^3), \tag{9.121}$$

$$g_{vA} = -\epsilon^2 2r^3 f\hat{B}_{2ij}(\tilde{v})n^i\Omega^j_B\varepsilon^B_A + \mathcal{O}(\epsilon^3), \tag{9.122}$$

$$g_{rA} = \epsilon^2 2r^3\hat{B}_{2ij}(\tilde{v})n^i\Omega^j_B\varepsilon^B_A + \mathcal{O}(\epsilon^3), \tag{9.123}$$

$$g_{AB} = r^2\delta_{ij}\Omega^i_A\Omega^j_B + \epsilon^2\frac{1}{2}r^2(-2M^2 + r^2)\delta_{ij}\Omega^i_A\Omega^j_B\hat{A}_{2kp}(\tilde{v})n^{kp} + \mathcal{O}(\epsilon^3), \tag{9.124}$$

where $r = \sqrt{\delta_{ij}x^ix^j}$.

We chose to compute the *contravariant* components of the metric in harmonic coordinates. This is preferable theoretically, as it avoids derivative of the inverse transformation. The contravariant metric is also the preferable form of the metric in NR, as the information readily available in the numerical domain is that of the auxiliary harmonic coordinates, y^μ, as functions of the generalised harmonic coordinates, z^μ.

From the calculation in Sec. 9.1.5, we have

$$\begin{aligned}T =& v - r - 2M\ln\Big(\frac{r}{2M}\Big) + \hat{c}^0_{000} + \epsilon\Big(- \dot{\hat{c}}^0_{000}\big(2M\ln\Big(\frac{r}{2M}\Big) + r\big) + \hat{c}^0_{11i}n_i(-1+\frac{r}{2M})\Big)\\ &\epsilon^2\Big(\frac{1}{3}\ddot{\hat{c}}^0_{000}(-18M^2 - 12M^2 Li_2(1-\frac{r}{2M}) + 5Mr + 2r^2 + 2M\ln\Big(\frac{r}{2M}\Big)(11M+3r))\\ &+ Mn^{ij}(2M-r)r\hat{A}_{2ij} + \frac{1}{M}\dot{\hat{c}}^0_{11i}n^i(6M^2 + 2M\ln\Big(\frac{r}{2M}\Big)(M-r) - Mr - r^2)\\ &+ \frac{1}{2M^2}\hat{c}^0_{22ij}n^{ij}(2M^2 - 6Mr + 3r^2)\Big) + \mathcal{O}(\epsilon^3),\end{aligned} \tag{9.125}$$

$$\begin{aligned}X^i =& (r-M)n^i + \hat{c}^i_{000} + \epsilon\Big(- \dot{\hat{c}}^i_{000}\big(2M\ln\Big(\frac{r}{2M}\Big) + r\big) + \hat{c}^i_{11j}n^j(-1+\frac{r}{2M})\Big)\\ &\frac{1}{6}\epsilon^2\Big(- 24M^2\ddot{\hat{c}}^i_{000}Li_2(1-\frac{r}{2M}) + 2\ddot{\hat{c}}^i_{000}(-18M^2 + 5Mr + 2r^2 + 2M\ln\Big(\frac{r}{2M}\Big)(11M+3r))\\ &+ \frac{6}{M}n^j\big(\dot{\hat{c}}^i_{11j}(6M^2 + 2M\ln\Big(\frac{r}{2M}\Big)(M-r) - Mr - r^2) + M^2 r(4M^2 - 8Mr + 3r^2)\hat{A}^i_{1j}\big)\\ &+ \frac{3}{M^2}\hat{c}^i_{22jk}n^{jk}(2M^2 - 6Mr + 3r^2) - \hat{A}^i_{3jkp}n^{jkp}(2M-r)r(2M^2 - 8Mr + 5r^2)\Big) + \mathcal{O}(\epsilon^3).\end{aligned} \tag{9.126}$$

Here we have chosen to write the forward transformation in terms of r instead of ρ, as we will be taking derivatives with respect to $w^\alpha = (v, r, \theta^A)$. For brevity of expression we have dropped the $\tilde{v}$ time dependence of the unknown $\hat{c}$ functions and the $\hat{A}, \hat{B}$ tidal moments.

From the outset of this calculation we now assume we can set $\hat{c}^\mu_{000}$ along with its derivatives to zero. For $\mu = i$, the spatial pieces, this is entirely acceptable as it simply represents a shift of the harmonic coordinate origin to be in-line with the center of mass of the binary system. For $\mu = 0$, the temporal piece, this is less clear. At the initial time, this alignment of coordinate times is perfectly acceptable. However, whether we can consistently impose $\hat{c}^0_{000} = 0$ throughout the evolution needs to be checked in later analysis. For now we assume it is a consistent simplification and proceed with our calculation of the metric.

We first compute and store the derivatives of X^μ with respect to w^α. From the metric in components $g_{w^\alpha w^\beta}$ we compute the inverse metric $g^{w^\alpha w^\beta}$. We can then form

$$g^{X^\mu X^\nu} = \frac{\partial X^\mu}{\partial w^\alpha}\frac{\partial X^\nu}{\partial w^\beta}g^{w^\alpha w^\beta}. \tag{9.127}$$

At this stage we have obtained the harmonic components of the metric. These have not yet been expressed in *harmonic coordinates* themselves; for this we will require the inverse transformation.

Next we make use of the useful identities

$$\Omega^{Ai}\Omega_i^B = \Omega^{AB}, \tag{9.128}$$

$$\Omega^{Ai}\Omega_A^j = \delta^{ij} - n^i n^j, \tag{9.129}$$

$$\Omega^{Ai}\varepsilon_{AB}\Omega^{Bj} = n^k \varepsilon_k^{ij}, \tag{9.130}$$

to remove any Ω dependence from the metric components. The results at this stage are now in terms of n^i, $\frac{\partial n^i}{\partial v}$, r, $\hat{c}^\mu_{n\ell m}(\tilde{v})$, $\hat{A}_{2ij}(\tilde{v})$ and $\hat{B}_{2ij}(\tilde{v})$. As a last step of this stage, we expand all functions of $\tilde{v}$ in terms of ϵ and $\tilde{T}$ using the relations in Eq. (9.66), (9.67) and (9.69). We then perform a series re-expansion in ϵ, with truncation at ϵ^2 to remove higher-order terms generated from multiplicative expansions. The results at this stage are now in terms of n^i, $\frac{\partial n^i}{\partial v}$, r, $\hat{c}^\mu_{n\ell L}(\tilde{T})$, $\hat{A}_{2ij}(\tilde{T})$, $\hat{B}_{2ij}(\tilde{T})$.

Next, n^i, $\frac{\partial n^i}{\partial v}$, and r must be written in terms of harmonic coordinates. To do this appropriate to $\mathcal{O}(\epsilon^2)$ we write $n^i = n_0^i + \epsilon n_1^i + \epsilon^2 n_2^i$, where $n^i = \frac{x_0^i + \epsilon x_1^i + \epsilon^2 x_2^i}{r_0 + \epsilon r_1 + \epsilon^2 r_2}$. This gives us

$$\begin{aligned} n_0^i &= \frac{x_0^i}{r_0}, \quad n_1^i = \frac{-r_1 x_0^i + r_0 x_1^i}{r_0^2} = \frac{\theta_1^A \Omega_A^i}{r_0}, \\ n_2^i &= \frac{r_1^2 x_0^i - r_0 r_2 x_0^i - r_0 r_1 x_1^i + r_0^2 x_2^i}{r_0^3} = \frac{-r1\theta_1^A \Omega_A^i + r_0 \theta_2^A \Omega_A^i}{r_0^2}, \end{aligned} \tag{9.131}$$

where we have used $x_n^i = r_n n_0^i + \theta_n^A \Omega_A^i$ to simplify the expressions. We again make use of $\Omega^{Ai}\Omega_A^j = \delta^{ij} - n^i n^j$ to remove $\Omega_{\alpha\beta}$ dependence. Equivalently, we write $r = r_0 + \epsilon r_1 + \epsilon^2 r_2$. We now use the results for the inverse transformation in Sec. 9.2 for $r_0, r_1, r_2, \theta_1^A, \theta_2^A$, with $\hat{c}^\mu_{000}(\tilde{T}) = 0$. Though n_0^i can be expressed as $\frac{X^i}{\rho_0}$, where $\rho_0 = \sqrt{\delta_{ij} X^i X^j}$, we choose to leave it unevaluated in our expressions. This is due to our desire to group our final results into powers of n_0^i to assess the multipolar structure of the transformed metric. Again we perform a series re-expansion in ϵ, with truncation at ϵ^2 to remove higher-order terms generated from multiplicative expansions.

The results are now in terms of $n_0^i, \rho_0, \hat{c}^\mu_{n\ell L}(\tilde{T}), A_{2ij}(\tilde{T})$ and $B_{2ij}(\tilde{T})$. A final step is for us to re-expand all functions of $\tilde{T}$ in terms of ϵ and t, where t is generalised harmonic time. This is necessary (as explained in Sec. 7.4), since the matching to the NR solution will take place on slices of constant generalised harmonic t. To do this we perform a Taylor series expansion in X^i:

$$\begin{aligned} \hat{c}^\mu_{n\ell L}(\tilde{T}(t, X^i)) &= \hat{c}^\mu_{n\ell L}(t, 0) + \epsilon X^j \partial_j \tilde{T}(t, 0) \dot{\hat{c}}^\mu_{n\ell L}(t, 0) + \mathcal{O}(\epsilon^2), \\ &= \hat{c}^\mu_{n\ell L}(t, 0) + \epsilon \rho_0 n_0^j \partial_j \tilde{T}(t, 0) \dot{\hat{c}}^\mu_{n\ell L}(t, 0) + \mathcal{O}(\epsilon^2). \end{aligned} \tag{9.132}$$

Within our working order, the only term that requires a post-leading-order expansion in t is $\hat{c}^\mu_{11i}(\tilde{T})$. All other terms appear with a factor of ϵ^2, and terms would therefore be higher order than required. $\hat{c}^\mu_{11i}(\tilde{T})$ always appears with a factor of n_0^i and so we can

re-write it in the following way:

$$\begin{aligned}
&\epsilon\hat{c}^{\mu}_{11i}(\tilde{T}(t,X^i))n^i_0 = \epsilon\hat{c}^{\mu}_{11i}(t,0)n^i_0 + \epsilon^2\rho_0 n^i_0 n^j_0\partial_j\tilde{T}(t,0)\dot{\hat{c}}^{\mu}_{11i}(t,0) + \mathcal{O}(\epsilon^3),\\
&= \epsilon\hat{c}^{\mu}_{11i}(t,0)n^i_0 + \epsilon^2\rho_0\left(\frac{1}{3}n^i_0 n^j_0\delta_{ij}\partial_k\tilde{T}(t,0)\dot{\hat{c}}^{\mu}_{11l}(t,0)\delta^{kl} + n^i_0 n^j_0\partial_{\langle j}\tilde{T}(t,0)\dot{\hat{c}}^{\mu}_{11i\rangle}(t,0)\right) + \mathcal{O}(\epsilon^3),\\
&= \epsilon\hat{c}^{\mu}_{11i}(t,0)n^i_0 + \epsilon^2\rho_0\hat{c}^{\mu}_{N00}(t,0) + \epsilon^2\rho_0 n^i_0 n^j_0\hat{c}^{\mu}_{Nij}(t,0) + \mathcal{O}(\epsilon^3),
\end{aligned} \tag{9.133}$$

where in the second line have used $\chi_{ij} = \chi_{\langle ij\rangle} + \frac{1}{3}\delta_{ij}\delta^{kl}\chi_{kl}$, with angular brackets denoting a trace-free piece. In going to the final line we redefine $\frac{1}{3}n^i_0 n^j_0\delta_{ij}\partial_k\tilde{T}(t,0)\dot{\hat{c}}^{\mu}_{11l}(t,0)\delta^{kl} \to \hat{c}^{\mu}_{N00}$, i.e. a newly generated monopole moment, and $\partial_{\langle j}\tilde{T}(t,0)\dot{\hat{c}}^{\mu}_{11i\rangle}(t,0) \to \hat{c}^{\mu}_{Nij}$, i.e. a newly generated quadrupole moment. Therefore, transforming to functions of generalised harmonic time at $\mathcal{O}(\epsilon^2)$ creates two more unknowns. We now have the harmonic components of the metric, in harmonic coordinates, as a function of generalised harmonic time.

Finally, we group our results in powers of n^i_0 to assess multipolar structure. We re-write $n^i_0 n^j_0 = n^{ij}_0, n^i_0 n^j_0 n^k_0 = n^{ijk}_0$ and so on. During this step X^i is written as $n^i_0\rho_0$. This creates $\ell = 5$ terms in g^{tX^i}, and $\ell = 6$ terms in $g^{X^iX^j}$. The final results are now in terms of $n^i_0, \rho_0, \hat{c}^{\mu}_{n\ell L}(t), \hat{A}_{2ij}(t)$ and $\hat{B}_{2ij}(t)$. $\hat{A}_{1ij}(t)$ and $\hat{A}_{3ijkp}(t)$ appear, but these are related to $\hat{A}_{2ij}(t)$ as given by Eq. (9.52). As a final step, for each multipolar component we set $\epsilon \to 1$ and further simplify the results. This can be done as we are at the stage where we will match the analytical expression for the metric to the NR metric, which does not carry a reference to ϵ.

9.3.2 Tidally Perturbed Black Hole Metric in Harmonic Coordinates

We now present the contravariant components of the tidally perturbed metric in our harmonic coordinate system, X^μ. We have perturbatively derived $g^{\alpha\beta} = g^{(0)\alpha\beta} + \epsilon p^{(1)\alpha\beta} + \epsilon^2 p^{(2)\alpha\beta} + \mathcal{O}(\epsilon^3)$. As described in Sec. 7.4, we will match this analytical metric to the NR metric mode-by-mode on the worldtube boundary, at each time-step. We therefore present the metric components as grouped by their multipolar structure.

Our results are given as:

$$g^{TT} = e^{TT} + e^{TTi}n_{0i} + e^{TTij}n_{0ij} + e^{TTijk}n_{0ijk} + e^{TTijkp}n_{0ijkp}, \tag{9.134}$$

$$g^{Ta} = e^{Ta} + e^{Tai}n_{0i} + e^{Taij}n_{0ij} + e^{Taijk}n_{0ijk} + e^{Taijkp}n_{0ijkp} + e^{Taijkpg}n_{0ijkpg}, \tag{9.135}$$

$$g^{ab} = e^{ab} + e^{abi}n_{0i} + e^{abij}n_{0ij} + e^{abijk}n_{0ijk} + e^{abijkp}n_{0ijkp} + e^{abijkpg}n_{0ijkpg}, + e^{abijkpgh}n_{0ijkpgh} \tag{9.136}$$

where Latin letters are spatial indices that are left covariant, $n_0^i = \frac{X^i}{\rho}$ and $n_0^{ij} = n_0^i n_0^j$ and so on. The e-type coefficients are functions of t, $\rho_0 = \sqrt{X^i X^j \delta_{ij}}$ and M, the mass of the small black hole.

The e-type coefficients are given in Tables 9.6 - 9.8 below wherein we have used symmetric tensor bracket notation,

$$\chi_{(i_1 i_2 \ldots i_k)} = \frac{1}{k!} \sum_{permutations} \chi_{i_1 i_2 \ldots i_k}. \tag{9.137}$$

In these results we have dropped the explicit time dependence of the $\hat{A}, \hat{B}, \hat{c}$ functions everywhere for brevity. Matching to the NR metric will allow us to fit for all these a priori unknown functions, both the tidal moments and those generated during the coordinate transformation. The matched analytical solution will then provide boundary conditions for the NR evolution at the next time step, as described in Sec. 7.4.

TABLE 9.6: g^{TT} metric components in harmonic coordinates

$$e^{TT} = \frac{\hat{c}^0{}_{11a}\hat{c}^0{}_{11}{}^a\rho^2}{M^2(M+\rho)^2} - \frac{15M^3 + M^2(11 - 8\hat{c}^0{}_{N0})\rho + M(5 - 8\hat{c}^0{}_{N0})\rho^2 + \rho^3}{(M+\rho)^3}$$

$$\begin{aligned} e^{TTi} = &- \frac{2}{M(M+\rho)^4}\big(4M\hat{c}_{11}{}^{ai}\hat{c}^0{}_{11a}(M+\rho)^2 - 4M^2\hat{c}^0{}_{11}{}^i(M+\rho)^2 + M\hat{c}_{N0}{}^i\rho^2(17M^2+6M\rho+\rho^2) \\ &+ \dot{\hat{c}}^0{}_{11}{}^i(8M^5+31M^4\rho+34M^3\rho^2+16M^2\rho^3+6M\rho^4+\rho^5)\big) \end{aligned}$$

$$\begin{aligned} e^{TTij} = &- \frac{1}{2M(M+\rho)^4}\Big(34M^3\hat{c}_{11a}{}^i\hat{c}_{11}{}^{aj} + 17M^7\hat{A}_2{}^{ij} + 17M^7\hat{A}_1{}^{ij} + 68M^3\hat{c}^0{}_{11}{}^{ij}\rho - 48M^3\hat{c}^0{}_{22}{}^{ij}\rho - 16M^4\hat{c}^0{}_{N2}{}^{ij}\rho \\ &- 68M^2\hat{c}_{11}{}^{ik}\hat{c}_{11k}{}^j\rho + 12M^2\hat{c}_{11a}{}^i\hat{c}_{11}{}^{aj}\rho + 70M^6\hat{A}_2{}^{ij}\rho + 40M^6\hat{A}_1{}^{ij}\rho + 24M^2\hat{c}^0{}_{11}{}^{ij}\rho^2 - 96M^2\hat{c}^0{}_{22}{}^{ij}\rho^2 - 32M^3\hat{c}^0{}_{N2}{}^{ij}\rho^2 \\ &- 24M\hat{c}_{11}{}^{ik}\hat{c}_{11k}{}^j\rho^2 + 2M\hat{c}_{11a}{}^j\hat{c}_{11}{}^{ai}\rho^2 + 95M^5\hat{A}_2{}^{ij}\rho^2 - 38M^5\hat{A}_1{}^{ij}\rho^2 + 4M\hat{c}^0{}_{11}{}^{ij}\rho^3 - 48M\hat{c}^0{}_{22}{}^{ij}\rho^3 - 16M^2\hat{c}^0{}_{N2}{}^{ij}\rho^3 \\ &- 4\hat{c}_{11}{}^{ik}\hat{c}_{11k}{}^j\rho^3 + 52M^4\hat{A}_2{}^{ij}\rho^3 - 16M^4\hat{A}_1{}^{ij}\rho^3 + 15M^3\hat{A}_2{}^{ij}\rho^4 - 3M^3\hat{A}_1{}^{ij}\rho^4 + 6M^2\hat{A}_2{}^{ij}\rho^5 + M\hat{A}_2{}^{ij}\rho^6 \\ &+ 2M\hat{c}^0{}_{11}{}^i\hat{c}^0{}_{11}{}^j(M+\rho)^2 - 8M^2\dot{\hat{c}}_{11}{}^{ij}(-34M^3+5M^2\rho+4M\rho^2+\rho^3)\Big) \end{aligned}$$

$$\begin{aligned} e^{TTijk} = &\frac{1}{M(M+\rho)^4}\big(\hat{c}_{22}{}^{ijk}(17M^4+6M^3\rho-50M^2\rho^2-18M\rho^3-3\rho^4) - 2M\hat{c}_{N2}{}^{ijk}\rho^2(17M^2+6M\rho+\rho^2) \\ &+ 8M\hat{c}_{11}^{ij}\hat{c}^{0k}_{11}(M^2+4M\rho+3\rho^2)\big) \end{aligned}$$

$$\begin{aligned} e^{TTijkp} = &\frac{1}{3M(M+\rho)^5}\big(3\hat{c}_{11}{}^{ij}\hat{c}_{11}{}^{kp}(17M^4+23M^3\rho-55M^2\rho^2-15M\rho^3-2\rho^4) \\ &+ M^2\hat{A}_3{}^{ijkp}(17M^6-28M^5\rho-113M^4\rho^2-4M^3\rho^3+91M^2\rho^4+32M\rho^5+5\rho^6)\big) \end{aligned}$$

TABLE 9.7: g^{Ta} metric components in harmonic coordinates

$$e^{Ta} = \frac{\rho\big(2M^2\dot{\hat{c}}^0{}_{11}{}^a(2M-\rho) + (M\hat{c}^0{}_{11}{}^a + \hat{c}_{11}{}^{ab}\hat{c}^0{}_{11b})\rho\big)}{M^2(M+\rho)^2}$$

$$\begin{aligned}e^{Tai} =& -\frac{1}{2M^2\rho(M+\rho)^3}\Big(8M^3\dot{\hat{c}}_{11}{}^{ai}(4M^3+4M^2\rho+3M\rho^2+\rho^3) + (M+\rho)\Big(\rho\big(2M^3\delta^{ai}(-4M+\hat{c}^0{}_{N0}\rho) + 2\hat{c}^0{}_{22}{}^{ai}\rho(M^2-3\rho^2)\big)\\ &+ 2\Big(4M^5\hat{A}_1{}^{ai}\rho^2(3M^2-2M\rho-9\rho^2) + M^3(M-\rho)(-2\hat{A}_2^{ai}\rho^2(M+\rho) + M^2\hat{A}_1^{ai}(M+3\rho))\Big)\Big)\Big)\end{aligned}$$

$$\begin{aligned}e^{Taij} =& \frac{1}{M\rho(M+\rho)^3}\Big(2M\hat{c}_{22k}{}^{ij}\delta^{ak}(M^3+M^2\rho-3M\rho^2-3\rho^3) + \rho\big(M^2\hat{c}_{11}{}^{kj}\hat{c}^0{}_{11k}\delta^{ai} + 4M^3\hat{c}_{N0}{}^j\delta^{ai}\rho + M\hat{c}_{11}{}^{kj}\hat{c}^0{}_{11k}\delta^{ai}\rho\\ &+ 12M^2\hat{c}_{22}{}^{aij}\rho - 2M^5\hat{B}_{2k}^j\varepsilon^{kai}\rho + 12M^2\hat{c}_{N0}{}^j\delta^{ai}\rho^2 - 2\hat{c}_{11}{}^{ij}\hat{c}^0{}_{11}{}^a\rho^2 + 12M\hat{c}_{22}{}^{aij}\rho^2 - 8M^4\hat{B}_{2k}^j\varepsilon^{kai}\rho^2\\ &- 12M^3\hat{B}_{2k}^j\varepsilon^{kai}\rho^3 - 8M^2\hat{B}_{2k}^j\varepsilon^{kai}\rho^4 - 2M\hat{B}_{2k}^j\varepsilon^{kai}\rho^5 - M^2\hat{c}^0{}_{11}{}^j\delta^{ai}(M+\rho) + 2M^3\dot{\hat{c}}^0{}_{11}{}^j\delta^{ai}(M+\rho)\big)\Big)\end{aligned}$$

$$\begin{aligned}e^{Taijk} =& \frac{1}{3M\rho(M+\rho)^3}\Big(2M^3\delta^{ab}\hat{A}_{3b}{}^{ijk}(M^4-2M^3\rho-6M^2\rho^2+2M\rho^3+5\rho^4) + 3\dot{\hat{c}}_{11}{}^{jk}\delta^{ai}(16M^5+40M^4\rho-27M^3\rho^2-7M^2\rho^3\\ &- 5M\rho^4-\rho^5) - 4M\rho\Big(M^2\hat{A}_3{}^{aijk}(M^4+7M^3\rho+3M^2\rho^2-13M\rho^3-10\rho^4) + 3\hat{c}_{11}{}^{gj}\big(-M\hat{c}_{11g}{}^k\delta^{ai} + \hat{c}_{11g}{}^k\delta^{ai}(M+3\rho)\big)\Big)\\ &+ 3M\delta^{ai}\Big(4M\hat{c}_{11}{}^{jk}\rho(M+3\rho) + M^3\hat{A}_1{}^{jk}(M-\rho)(M+3\rho)^2 + \rho(M+\rho)\big(-(2\hat{c}^0{}_{22}{}^{jk} + M\hat{c}^0{}_{N2}{}^{jk})\rho + 2\hat{A}_2{}^{jk}(M^4-M^2\rho^2)\big)\Big)\Big)\end{aligned}$$

$$e^{Taijkp} = -\frac{2\delta^{ai}\Big(\hat{c}_{22}{}^{jkp}(M^3+3M^2\rho-3M\rho^2-9\rho^3) + \rho\big(\hat{c}_{11}{}^{jk}\hat{c}^0{}_{11}{}^p(M+2\rho) - 2M\hat{c}_{N2}{}^{jkp}\rho(M+3\rho)\big)\Big)}{\rho(M+\rho)^3}$$

$$e^{Taijkpg} = -\frac{1}{3\rho(M+\rho)^4}\Big(2\delta^{ai}\big(-18\hat{c}_{11}{}^{jk}\hat{c}_{11}{}^{pg}\rho^2(M+2\rho) + M^2\hat{A}_3{}^{jkpg}(M^5+M^4\rho-12M^3\rho^2-16M^2\rho^3+11M\rho^4+15\rho^5)\big)\Big)$$

TABLE 9.8: g^{ab} metric components in harmonic coordinates

$$
\begin{aligned}
e^{ab} =& \frac{1}{M^2(M+\rho)^2}\Big(\rho\big(-2M^6\hat{A}_1{}^{ab} + 4M^2\dot{\hat{c}}_{11}{}^{(ab)}(2M-\rho) + 2M\hat{c}_{11}{}^{(ab)}\rho + \hat{c}_{11}{}^{ai}\hat{c}_{11}{}^{b}{}_{i}\rho \\
&+ M^2\delta^{ab}\rho - 6M^5\hat{A}_1{}^{ab}\rho + 2M^4\hat{A}_1{}^{ab}\rho^2 + 6M^3\hat{A}_1{}^{ab}\rho^3\big)\Big)
\end{aligned}
$$

$$
e^{abi} = -\frac{1}{M^2(M+\rho)^3}\Big(2\hat{c}_{22}{}^{abi}\rho(M^3+M^2\rho-3M\rho^2-3\rho^3) - M\rho^3\big(-2M\hat{c}_{N0}{}^{i}\delta^{ab} + 2\hat{c}_{N0}{}^{(a}\delta^{b)i}(M+\rho)\big)\Big)
$$

$$
\begin{aligned}
e^{abij} =& \frac{1}{4M\rho(M+\rho)^3}\Big(2M^7\delta^{i(a}\hat{A}_1{}^{b)j} - 4M^4\delta^{ai}\delta^{bj}\rho + 6M^6\delta^{i(a}\hat{A}_1{}^{b)j}\rho + 24M^7\delta^{j(b}\hat{A}_1{}^{a)i}\rho - 4M^3\delta^{ai}\delta^{bj}\rho^2 \\
&- 32M^3\dot{\hat{c}}_{11}^{ij}\delta^{ab}\rho^2 - 4M\hat{c}_{11k}{}^{i}\hat{c}_{11}{}^{kj}\delta^{ab}\rho^2 - 2M^5\delta^{i(b}\hat{A}_1^{a)j}\rho^2 + 16M^6\delta^{i(b}\hat{A}_1^{a)j}\rho^2 - 2M^5\delta^{ab}\hat{A}_1{}^{ij}\rho^2 \\
&+ 4M^6\hat{A}_3{}^{abij}\rho^2 - 16\hat{c}_{11}{}^{(ab)}\hat{c}_{11}{}^{ij}\rho^3 - 8M\hat{c}_{11}{}^{ij}\delta^{ab}\rho^3 + 16M^2\dot{\hat{c}}_{11}{}^{ij}\delta^{ab}\rho^3 + 8\hat{c}_{11}{}^{ik}\hat{c}_{11k}^{j}\delta^{ab}\rho^3 \\
&+ 2M^4\delta^{ab}\hat{A}_2{}^{ij}\rho^3 - 6M^4\delta^{i(b}\hat{A}_1{}^{a)j}\rho^3 - 80M^5\delta^{i(b}\hat{A}_1{}^{a)j}\rho^3 - 4M^4\delta^{ab}\hat{A}_1{}^{ij}\rho^3 - 4M^5\hat{A}_3{}^{abij}\rho^3 \\
&- 2M^3\delta^{ab}\hat{A}_2{}^{ij}\rho^4 - 64M^4\delta^{i(b}\hat{A}_1{}^{a)j}\rho^4 + 6M^3\delta^{ab}\hat{A}_1{}^{ij}\rho^4 - 32M^4\hat{A}_3{}^{abij}\rho^4 - 6M^2\delta^{ab}\hat{A}_2{}^{ij}\rho^5 \\
&+ 56M^3\delta^{i(b}\hat{A}_1{}^{a)j}\rho^5 - 16M^3\hat{A}_3{}^{abij}\rho^5 - 2M\delta^{ab}\hat{A}_2{}^{ij}\rho^6 + 48M^2\delta^{i(b}\hat{A}_1{}^{a)j}\rho^6 + 28M^2\hat{A}_3^{abij}\rho^6 + 20M\hat{A}_3{}^{abij}\rho^7 \\
&+ 8\dot{\hat{c}}_{11}{}^{j(b}\delta^{a)i}(4M^5+4M^4\rho-M^3\rho^2-3M^2\rho^3-3M\rho^4-\rho^5)\Big).
\end{aligned}
$$

$$
\begin{aligned}
e^{abijk} =& -\frac{1}{2M\rho(M+\rho)^3}\Big(2M\delta^{i(a}\hat{c}_{22}^{b)jk}(M^3+M^2\rho+M\rho^2+\rho^3) - 2\rho^2\Big(-2M^2\hat{c}_{N0}^{k}\delta^{ai}\delta^{bj}(M+2\rho) + \hat{c}_{22}^{ijk}\delta^{ab}(M^2-3\rho^2) \\
&+ \rho^2\big(-2M\hat{c}_{N2}^{ijk}\delta^{ab} + 2\delta^{i(a}\hat{c}_{N2}^{b)jk}(M+\rho)\big)\Big)\Big)
\end{aligned}
$$

$$
\begin{aligned}
e^{abijkp} =& -\frac{1}{6M\rho(M+\rho)^4}\Big(2M^8\delta^{i(b}\hat{A}_3^{a)jkp} - 12M^3\hat{c}_{11}^{kg}\hat{c}_{11g}^{p}\delta^{ai}\delta^{bj}\rho + 6M^3\hat{c}_{11g}^{k}\hat{c}_{11}^{gp}\delta^{ai}\delta^{bj}\rho - 2M^7\delta^{i(b}\hat{A}_3{}^{a)jkp}\rho \\
&- 4M^8\delta^{i(b}\hat{A}_3^{a)jkp}\rho - 36M^2\hat{c}_{11}{}^{kg}\hat{c}_{11g}^{p}\delta^{ai}\delta^{bj}\rho^2 + 6M^2\delta^{ai}\delta^{bj}\hat{c}_{11g}^{k}\hat{c}_{11}{}^{gp}\rho^2 - 6M^2\hat{c}_{11}{}^{ij}\hat{c}_{11}{}^{kp}\delta^{ab}\rho^2 \\
&- 16M^6\delta^{i(b}\hat{A}_3^{a)jkp}\rho^2 - 26M^7\delta^{i(b}\hat{A}_3{}^{a)jkp}\rho^2 - 2M^6\delta^{ab}\hat{A}_3^{ijkp}\rho^2 - 24M\hat{c}_{11}{}^{kg}\hat{c}_{11g}{}^{p}\delta^{ai}\delta^{bj}\rho^3 - 12M\hat{c}_{11}{}^{ij}\hat{c}_{11}{}^{kp}\delta^{ab}\rho^3 \\
&- 8M^5\delta^{i(b}\hat{A}_3^{a)jkp}\rho^3 - 36M^6\delta^{i(b}\hat{A}_3{}^{a)jkp}\rho^3 + 4M^5\delta^{ab}\hat{A}_3^{ijkp}\rho^3 + 12\hat{c}_{11}{}^{ij}\hat{c}_{11}{}^{kp}\delta^{ab}\rho^4 + 14M^4\delta^{i(b}\hat{A}_3{}^{a)jkp}\rho^4 \\
&+ 18M^5\delta^{i(a}\hat{A}_3{}^{b)jkp}\rho^4 + 12M^4\delta^{ab}\hat{A}_3^{ijkp}\rho^4 + 10M^3\delta^{i(b}\hat{A}_3{}^{a)jkp}\rho^5 + 60M^4\delta^{i(b}\hat{A}_3{}^{a)jkp}\rho^5 \\
&- 4M^3\delta^{ab}\hat{A}_3^{ijkp}\rho^5 + 18M^3\delta^{i(b}\hat{A}_3^{a)jkp}\rho^6 - 10M^2\delta^{ab}\hat{A}_3^{ijkp}\rho^6 - 20M^2\delta^{i(b}\hat{A}_3{}^{a)jkp}\rho^7 - 10M\delta^{i(b}\hat{A}_3{}^{a)jkp}\rho^8 \\
&+ 12\dot{\hat{c}}_{11}{}^{kp}\delta^{ai}\delta^{bj}(4M^6+10M^5\rho+M^4\rho^2-8M^3\rho^3-6M^2\rho^4-4M\rho^5-\rho^6) \\
&+ 3M^2\delta^{ai}\delta^{bj}(M+\rho)\big(4\hat{c}_{11}{}^{kp}\rho(M+2\rho) + M^2\hat{A}_1{}^{kp}(M^3+4M^2\rho+M\rho^2-6\rho^3) \\
&+ \hat{A}_2{}^{kp}\rho(M^4+M^3\rho-M^2\rho^2-3M\rho^3-2\rho^4)\big)\Big)
\end{aligned}
$$

$$
e^{abijkpg} = \frac{\delta^{ai}\delta^{bj}(M+2\rho)\big(-2M\hat{c}_{N2}{}^{kpg}\rho^2 + \hat{c}_{22}{}^{kpg}(M^2-3\rho^2)\big)}{\rho(M+\rho)^3}
$$

$$
e^{abijkpgh} = \frac{1}{3\rho(M+\rho)^4}\delta^{ai}\delta^{bj}(M+2\rho)\big(-3\hat{c}_{11}^{kp}\hat{c}_{11}^{gh}\rho(2M+5\rho) + M^2\hat{A}_3^{kpgh}(M^4-2M^3\rho-6M^2\rho^2+2M\rho^3+5\rho^4)\big)
$$

Chapter 10

Summary and Concluding Remarks

Numerical simulations of binary black holes are increasingly costly with more extreme mass ratios q. This is partially due to the CFL condition forcing a reduction of the evolution time step $\Delta t \lesssim m_2 \propto q$. This thesis presented a novel technique to circumvent the time step limitations that arise from solving the field equations fully numerically in the region of spacetime near the small mass m_2. We place a worldtube of radius $R \gg m_2$ around m_2. Inside this worldtube we replace the fully numerical solution by a perturbative solution, while retaining a fully numerical solution outside the worldtube. Thus, the smallest length scales remaining on the numerical grid are of order R, and the CFL limit is relaxed to $\Delta t \sim R$.

The work in this thesis provides a strong foundation for the implementation of the worldtube excision method for modelling IMRIs. The implementation and trial of two testbed cases:—a scalar charge on a fixed circular orbit around a Schwarzschild black hole evolving in 1+1D (Chapters 4 and 5), followed by an advancement to 3+1D (Chapter 6) provided understanding of the core behaviours of the worldtube model. The framework for the BBH case was then laid out (Chapter 7) and the derivation of the appropriate form of the perturbative solution presented (Chapters 8 and 9).

The 1+1D scalar model allowed the exploration of two different algorithms to match the perturbed solution inside the worldtube with the fully numerical solution outside: (i) A matching scheme that fits over an extended region, and (ii) a boundary scheme that imposes conditions precisely at one radius. We explored two different numerical implementations for the numerical exterior solution, one based on finite differences on a characteristic grid, the other on spectral methods on spatial hypersurfaces. The most accurate solutions are obtained with the spectral scheme, which allows significantly smaller discretisation errors than the finite-difference scheme.

We achieved stable evolutions in both schemes. We also established convergence of the results with respect to various key quantities: the numerical resolution, the radius R of the worldtube, and the order of the approximate perturbative solution n inside the worldtube. Of primary concern is convergence with worldtube radius R. For the finite-difference scheme, Fig. 4.20 demonstrates convergence $\propto R^n$ for a perturbative solution of order n. For the spectral scheme, Figs. 5.5 and 5.7 demonstrate cases of convergence $\propto R^{n+1}$.

For a worldtube radius of $R = 0.8M$ (where here $M = m_1$) we achieve relative errors $\approx 10^{-4}$ for a third-order internal solution and $\lesssim 10^{-6}$ for a fifth-order perturbative solution. This level of accuracy at such a large worldtube radius is encouraging for our ultimate goal, the application of the worldtube method for IMRIs.

The 3+1D scalar model and the usage of SpECTRE progressed the worldtube implementation far closer to resembling the BBH case. Here we were able to trial a matching procedure that foreseeably can be transferred to the BBH model's implementation: matching the perturbative solution and the NR solution mode-by-mode on the worldtube boundary. The model also evidenced the practicality of transforming the perturbative solution to the coordinates of the numerics, prior to performing the matching.

Fig. 6.7 and 6.9 presented convergence results with respect to R for zeroth, first and second-order internal models models. The results demonstrate that model achives the expected convergence $\propto R^{n+2}$. For worldtube radius of $R = 0.8M$, the second-order internal solution achieves a relative error of $\approx 10^{-5}$. This is again an extremely encouraging level of accuracy, at such a large worldtube radius.

This thesis then laid the foundations for the BBH model, whose actual numerical implementation is left to future work. The main ingredient of the BBH model namely is an approximate analytical model of a tidally perturbed black hole in a gauge compatible with that of the NR solution. Our derivation of such an analytical model should allow the practical implementation of the scheme. The evolution procedure is laid out schematically, to be followed in the future.

10.1 Future Work

We now discuss possible follow-ups to the work presented in this thesis. Firstly, there remain a couple of tests to be run on the 3+1D scalar model. Further investigation is ongoing into the $n = 2$ model in the hope of obtaining the expected $\mathcal{O}(R^{n+2})$ convergence rate. Up until this point the work has focused on the implementation of the worldtube architecture and exploration of matching approaches. With the 3+1D scalar model we also wish to probe the runtime saving of the worldtube excision method. This

will provide a first quantification of the predictions in Sec. 2.3. It can be done either implicitly, by comparing the runtime for successively smaller worldtube sizes, or explicitly, comparing the runtime of a worldtube model to that of an exposed charge distribution.

Future work will numerically implement the BBH model in the IMRI case. Here the perturbed solution will initially be the $\mathcal{O}(\epsilon^2)$ tidally perturbed Schwarzschild metric in suitable coordinates, derived in Chapter 9. At this stage, work will test the matching method in the BBH case and hopefully achieve a stable evolution.

The model can then continue to advance to progressively higher level:

(i) The perturbed Schwarzschild solution can be extended to higher order in ϵ, hence increasing its accuracy and so the overall accuracy of the worldtube model. This will require the matching of a larger number of unknowns. However, this should be a fairly straightforward extension of the mode-by-mode matching method developed here, taken to higher ℓ.

(ii) The model can advance to include spin of the black holes. For the larger black hole, this can be done by adding spin into the SpECTRE evolution; for the smaller black hole this would mean working with a tidally perturbed Kerr metric. Building on preliminary work for tidally perturbed Kerr metrics [108, 87], we would first have to derive the metric to a suitable order in the most natural set of coordinates. We would then have to transform it to harmonic coordinates as functions of generalised harmonic time, as done in this thesis for the Schwarzschild case.

(iii) The model can advance to include matter. For an IMRI model this would, for example, mean replacing the smaller black hole with a neutron star, hence working with a tidally perturbed neutron-star metric [55, 164, 128, 80]. Again, such metrics would have to be transformed into suitable coordinates. Achieving this would allow us to model black hole-neutron star binaries.

iv) The model can advance to include eccentricity, which may be astrophysically relevant at the high mass-ratio end of the IMRI range.

10.2 Perspective

With the advancement of our GW detectors, it is of high priority to have a bank of waveform templates that cover the entire parameter range of detectable sources. The push towards lower-frequency observational ranges means the prospect of detecting ever-more disparate mass binaries in the years to come. Third-generation ground detectors and LISA promise this extended frequency window, and so the potential for a wealth of new discoveries during their years of operation is high.

The worldtube excision method seeks to complement existing efforts from NR and BHPT (as reviewed in Sec. 1.3) to bridge the mass-ratio modelling gap. Despite the strong recent advancements from both NR and BHPT, there is a still a compelling case for a novel technique to generate IMRI waveforms in a shorter timeframe, working towards the aim of ensuring we can obtain the maximum scientific return from all active GW detectors.

From a broader perspective, the scientific body of knowledge from the GW community is extending at an impressive rate. The community is enjoying advancements in all areas of the field, from instrumentation design to data processing and analysis and to waveform template creation. The size of the community is also growing at an accelerated pace, with more human power being applied to unlocking the truths that can come from GW analysis. This thesis hopes to have tackled a challenge in a subspace of this cutting-edge field, and helped push the goal of better understanding the universe using GWs a little further along.

Appendix A

Singular Part of the Scalar Field in Kerr-Schild Coordinates

In this appendix we give the singular part of the scalar field in Kerr-Schild coordinates. This is used in our 3+1D scalar-field model as presented in Chapter 6. The singular piece of the scalar field can be expressed as [34]

$$\Phi^S = e\left\{\frac{1}{\epsilon s_1} + \frac{\mathrm{P}_3(\Delta x^\alpha)}{s_1^3} + \frac{\epsilon \mathrm{P}_6(\Delta x^\alpha)}{s_1^5} + \frac{\epsilon^2 \mathrm{P}_9(\Delta x^\alpha)}{s_1^7} + \mathcal{O}(\epsilon^3)\right\}. \tag{A.1}$$

Here ϵ is a book-keeping quantity, measuring the fundamental scale of separation $\Delta x^\alpha = x^\alpha - \bar{x}^\alpha$, where x^α is the field point and $\bar{x}^\alpha$ is the position of the scalar charge. In this expression, $P_n(\Delta x^\alpha)$ are polynomials in (Δx^α) of homogeneous order n, and s_1 is the leading-order piece of the orthogonal distance from x^α to the worldline. The forms of s_1 and $P_n(\Delta x^\alpha)$ in Kerr-Schild coordinates are obtained by following the procedure laid out in Sec. 6.3.4 .

In the following expressions M is the mass of the black hole, $r_p = \sqrt{\bar{x}^2 + \bar{y}^2 + \bar{z}^2}$ is the radius of the scalar charge, and

$$\xi = r_p - 3M \tag{A.2}$$

s_1 is given by

$$\begin{aligned} s_1 =& \sqrt{\left\{\Delta x^2\left(1 + \frac{2M\bar{x}^2}{r_p^3}\right) + \Delta y^2 + \Delta z^2 + \frac{4M\Delta x\Delta y\bar{x}\bar{y}}{r_p^3}\right.} \\ &\left. + \frac{2M\Delta y^2\bar{y}^2}{r_p^3} + \left((-\Delta y\bar{x} + \Delta x\bar{y})\sqrt{\frac{M}{\xi r_p^2}} - \frac{2M(\Delta x\bar{x} + \Delta y\bar{y})}{\sqrt{\xi r_p^3}}\right)^2\right\}. \end{aligned} \tag{A.3}$$

We now give the expressions for the polynomials $P_n(\Delta x^\alpha)$ in Kerr-Schild coordinates, up to $\mathcal{O}(\epsilon^2)$ as this is the highest order currently used within the 3+1D scalar-field model. These are given as a Mathematica file exportation.

$P_3(\Delta x^\alpha)$

Out[25]=

$$\frac{1}{2\,r_p^6}\left(M\,(\Delta x\,\bar{x}+\Delta y\,\bar{y})\,\left(\left(\Delta x^2-2\left(\Delta y^2+\Delta z^2\right)\right)\bar{x}^2+6\,\Delta x\,\Delta y\,\bar{x}\,\bar{y}+\left(-2\,\Delta x^2+\Delta y^2-2\,\Delta z^2\right)\bar{y}^2\right)\,r_p+\right.$$
$$2\left(\frac{M}{\xi}\right)^{3/2}\left(\left(\Delta x^2-\Delta y^2-\Delta z^2\right)\bar{x}^2+4\,\Delta x\,\Delta y\,\bar{x}\,\bar{y}-\left(\Delta x^2-\Delta y^2+\Delta z^2\right)\bar{y}^2\right)$$
$$\left.\left(2\,\sqrt{M\,\xi}\,\left(\Delta x\,\bar{x}+\Delta y\,\bar{y}\right)\,r_p+\left(\Delta y\,\bar{x}-\Delta x\,\bar{y}\right)\,\sqrt{\xi\,r_p^3}\right)\right)$$

$P_6\,(\Delta x^\alpha)$

Out[28]=

$$\frac{1}{24\,r_p^{12}}\left(-M\,r_p^2\left(\Delta y^2+\Delta z^2+\Delta x^2\left(1+\frac{2\,M\,\bar{x}^2}{r_p^3}\right)+\right.\right.$$
$$\left.\frac{4\,M\,\Delta x\,\Delta y\,\bar{x}\,\bar{y}}{r_p^3}+\frac{2\,M\,\Delta y^2\,\bar{y}^2}{r_p^3}+\frac{\left(2\,M\,(\Delta x\,\bar{x}+\Delta y\,\bar{y})\,r_p+(\Delta y\,\bar{x}-\Delta x\,\bar{y})\,\sqrt{M\,r_p^3}\right)^2}{\xi\,r_p^5}\right)$$
$$\left(\frac{12\,M\left(\left(\Delta x^2-\Delta y^2-\Delta z^2\right)\bar{x}^2+4\,\Delta x\,\Delta y\,\bar{x}\,\bar{y}-\left(\Delta x^2-\Delta y^2+\Delta z^2\right)\bar{y}^2\right)^2\,r_p^3}{\xi}+\right.$$
$$r_p\left(2\,M^2\,(\Delta x\,\bar{x}+\Delta y\,\bar{y})^4+M\,(\Delta x\,\bar{x}+\Delta y\,\bar{y})^2\right.$$
$$\left(\left(3\,\Delta x^2-4\left(\Delta y^2+\Delta z^2\right)\right)\bar{x}^2+14\,\Delta x\,\Delta y\,\bar{x}\,\bar{y}+\left(-4\,\Delta x^2+3\,\Delta y^2-4\,\Delta z^2\right)\bar{y}^2\right)\,r_p+$$
$$4\left(\left(2\,\Delta x^4-11\,\Delta x^2\left(\Delta y^2+\Delta z^2\right)+2\left(\Delta y^2+\Delta z^2\right)^2\right)\bar{x}^4+30\,\Delta x\,\Delta y\left(\Delta x^2-\Delta y^2-\Delta z^2\right)\bar{x}^3\,\bar{y}-\right.$$
$$\left(11\,\Delta x^4+11\,\Delta y^4+7\,\Delta y^2\,\Delta z^2-4\,\Delta z^4+\Delta x^2\left(-68\,\Delta y^2+7\,\Delta z^2\right)\right)\bar{x}^2\,\bar{y}^2-$$
$$30\,\Delta x\,\Delta y\left(\Delta x^2-\Delta y^2+\Delta z^2\right)\bar{x}\,\bar{y}^3+$$
$$\left.\left.\left(2\,\Delta x^4+2\,\Delta y^4-11\,\Delta y^2\,\Delta z^2+2\,\Delta z^4+\Delta x^2\left(-11\,\Delta y^2+4\,\Delta z^2\right)\right)\bar{y}^4\right)\,r_p^2\right)+$$
$$\frac{1}{\xi^{3/2}}\,4\times\left(-2\,M^2\,\sqrt{\xi}\,(\Delta x\,\bar{x}+\Delta y\,\bar{y})^3-2\,M\,\sqrt{\xi}\,(\Delta x\,\bar{x}+\Delta y\,\bar{y})\right.$$
$$\left(\left(\Delta x^2-\Delta y^2-\Delta z^2\right)\bar{x}^2+4\,\Delta x\,\Delta y\,\bar{x}\,\bar{y}-\left(\Delta x^2-\Delta y^2+\Delta z^2\right)\bar{y}^2\right)\,r_p+\sqrt{M\,\xi}\,(\Delta y\,\bar{x}-\Delta x\,\bar{y})$$
$$\left(\left(\Delta x^2-2\left(\Delta y^2+\Delta z^2\right)\right)\bar{x}^2+6\,\Delta x\,\Delta y\,\bar{x}\,\bar{y}+\left(-2\,\Delta x^2+\Delta y^2-2\,\Delta z^2\right)\bar{y}^2\right)\,r_p^{3/2}-4\,\sqrt{\xi}$$
$$(\Delta x\,\bar{x}+\Delta y\,\bar{y})\,\left(\left(\Delta x^2-3\left(\Delta y^2+\Delta z^2\right)\right)\bar{x}^2+8\,\Delta x\,\Delta y\,\bar{x}\,\bar{y}+\left(-3\,\Delta x^2+\Delta y^2-3\,\Delta z^2\right)\bar{y}^2\right)$$
$$r_p^2+2\,M^{3/2}\,(\Delta y\,\bar{x}-\Delta x\,\bar{y})\,(\Delta x\,\bar{x}+\Delta y\,\bar{y})^2\,\sqrt{\xi\,r_p}\,)\times$$
$$\left.\left(-2\,M\,(\Delta x\,\bar{x}+\Delta y\,\bar{y})\,r_p+(-\Delta y\,\bar{x}+\Delta x\,\bar{y})\,\sqrt{M\,r_p^3}\right)\right)+$$
$$9\left(M\,(\Delta x\,\bar{x}+\Delta y\,\bar{y})\,\left(\left(\Delta x^2-2\left(\Delta y^2+\Delta z^2\right)\right)\bar{x}^2+6\,\Delta x\,\Delta y\,\bar{x}\,\bar{y}+\left(-2\,\Delta x^2+\Delta y^2-2\,\Delta z^2\right)\bar{y}^2\right)\,r_p+\right.$$
$$2\left(\frac{M}{\xi}\right)^{3/2}\left(\left(\Delta x^2-\Delta y^2-\Delta z^2\right)\bar{x}^2+4\,\Delta x\,\Delta y\,\bar{x}\,\bar{y}-\left(\Delta x^2-\Delta y^2+\Delta z^2\right)\bar{y}^2\right)$$
$$\left.\left.\left(2\,\sqrt{M\,\xi}\,\left(\Delta x\,\bar{x}+\Delta y\,\bar{y}\right)\,r_p+\left(\Delta y\,\bar{x}-\Delta x\,\bar{y}\right)\,\sqrt{\xi\,r_p^3}\right)\right)^2\right)$$

$P_9\,(\Delta x^{\alpha})$

Out[•]=

$$\frac{1}{48\,\xi^{7/2}\,r_p^{17}}\,M\Big(9\,M^2\,\sqrt{\xi}\,r_p^2\,\Big(\xi\,(\Delta x\,\bar{x}+\Delta y\,\bar{y})\,\Big(\big(\Delta x^2-2\,\big(\Delta y^2+\Delta z^2\big)\big)\,\bar{x}^2+6\,\Delta x\,\Delta y\,\bar{x}\,\bar{y}+\big(-2\,\Delta x^2+\Delta y^2-2\,\Delta z^2\big)\,\bar{y}^2\Big)+2\,\Big(\big(\Delta x^2-\Delta y^2-\Delta z^2\big)\,\bar{x}^2+4\,\Delta x\,\Delta y\,\bar{x}\,\bar{y}-\big(\Delta x^2-\Delta y^2+\Delta z^2\big)\,\bar{y}^2\Big)\,\Big(2\,M\,(\Delta x\,\bar{x}+\Delta y\,\bar{y})+(\Delta y\,\bar{x}-\Delta x\,\bar{y})\,\sqrt{M\,r_p}\Big)\Big)^3+2\,\Big(4\,M\,\Delta x\,\Delta y\,\xi\,\bar{x}\,\bar{y}+2\,M\,\Delta y^2\,\xi\,\bar{y}^2+\Delta y^2\,\xi\,r_p^3+\Delta z^2\,\xi\,r_p^3+\Delta x^2\,\xi\,\big(2\,M\,\bar{x}^2+r_p^3\big)+\Big(2\,M\,(\Delta x\,\bar{x}+\Delta y\,\bar{y})+(\Delta y\,\bar{x}-\Delta x\,\bar{y})\,\sqrt{M\,r_p}\Big)^2\Big)^2\,\Big(\xi^{3/2}\,(\Delta x\,\bar{x}+\Delta y\,\bar{y})\,\Big(M^2\,(\Delta x\,\bar{x}+\Delta y\,\bar{y})^2\,\Big(\big(5\,\Delta x^2-4\,\big(\Delta y^2+\Delta z^2\big)\big)\,\bar{x}^2+18\,\Delta x\,\Delta y\,\bar{x}\,\bar{y}+\big(-4\,\Delta x^2+5\,\Delta y^2-4\,\Delta z^2\big)\,\bar{y}^2\Big)+2\,M\,\Big(\Big(3\,\Delta x^4-9\,\Delta x^2\,\big(\Delta y^2+\Delta z^2\big)+2\,\big(\Delta y^2+\Delta z^2\big)^2\Big)\,\bar{x}^4+2\,\Delta x\,\Delta y\,\big(15\,\Delta x^2-13\,\big(\Delta y^2+\Delta z^2\big)\big)\,\bar{x}^3\,\bar{y}-\big(9\,\Delta x^4+9\,\Delta y^4+5\,\Delta y^2\,\Delta z^2-4\,\Delta z^4+\Delta x^2\,\big(-66\,\Delta y^2+5\,\Delta z^2\big)\big)\,\bar{x}^2\,\bar{y}^2-2\,\Delta x\,\Delta y\,\big(13\,\Delta x^2-15\,\Delta y^2+13\,\Delta z^2\big)\,\bar{x}\,\bar{y}^3+\big(2\,\Delta x^4+3\,\Delta y^4-9\,\Delta y^2\,\Delta z^2+2\,\Delta z^4+\Delta x^2\,\big(-9\,\Delta y^2+4\,\Delta z^2\big)\big)\,\bar{y}^4\Big)\,r_p+3\,\Big(\Big(2\,\Delta x^4-21\,\Delta x^2\,\big(\Delta y^2+\Delta z^2\big)+12\,\big(\Delta y^2+\Delta z^2\big)^2\Big)\,\bar{x}^4+10\,\Delta x\,\Delta y\,\big(5\,\Delta x^2-9\,\big(\Delta y^2+\Delta z^2\big)\big)\,\bar{x}^3\,\bar{y}-3\times\big(7\,\Delta x^4+7\,\Delta y^4-\Delta y^2\,\Delta z^2-8\,\Delta z^4-\Delta x^2\,\big(56\,\Delta y^2+\Delta z^2\big)\big)\,\bar{x}^2\,\bar{y}^2-10\,\Delta x\,\Delta y\,\big(9\,\Delta x^2-5\,\Delta y^2+9\,\Delta z^2\big)\,\bar{x}\,\bar{y}^3+\big(12\,\Delta x^4+2\,\Delta y^4-21\,\Delta y^2\,\Delta z^2+12\,\Delta z^4-3\,\Delta x^2\,\big(7\,\Delta y^2-8\,\Delta z^2\big)\big)\,\bar{y}^4\Big)\,r_p^2\Big)+2\times\Big(2\,M\,(\Delta x\,\bar{x}+\Delta y\,\bar{y})+(\Delta y\,\bar{x}-\Delta x\,\bar{y})\,\sqrt{M\,r_p}\Big)\times\Big(2\,M^2\,\sqrt{\xi}\,(\Delta x\,\bar{x}+\Delta y\,\bar{y})^2\,\Big(\big(5\,\Delta x^2-3\,\big(\Delta y^2+\Delta z^2\big)\big)\,\bar{x}^2+16\,\Delta x\,\Delta y\,\bar{x}\,\bar{y}+\big(-3\,\Delta x^2+5\,\Delta y^2-3\,\Delta z^2\big)\,\bar{y}^2\Big)+2\,M\,\sqrt{\xi}\,\Big(\Big(4\,\Delta x^4-9\,\Delta x^2\,\big(\Delta y^2+\Delta z^2\big)+\big(\Delta y^2+\Delta z^2\big)^2\Big)\,\bar{x}^4+2\,\Delta x\,\Delta y\,\big(17\,\Delta x^2-11\,\big(\Delta y^2+\Delta z^2\big)\big)\,\bar{x}^3\,\bar{y}-\big(9\,\Delta x^4+9\,\Delta y^4+7\,\Delta y^2\,\Delta z^2-2\,\Delta z^4+\Delta x^2\,\big(-66\,\Delta y^2+7\,\Delta z^2\big)\big)\,\bar{x}^2\,\bar{y}^2-2\,\Delta x\,\Delta y\,\big(11\,\Delta x^2-17\,\Delta y^2+11\,\Delta z^2\big)\,\bar{x}\,\bar{y}^3+\big(\Delta x^4+4\,\Delta y^4-9\,\Delta y^2\,\Delta z^2+\Delta z^4+\Delta x^2\,\big(-9\,\Delta y^2+2\,\Delta z^2\big)\big)\,\bar{y}^4\Big)\,r_p+6\,\sqrt{\xi}\,\Big(\Big(\Delta x^4-6\,\Delta x^2\,\big(\Delta y^2+\Delta z^2\big)+\big(\Delta y^2+\Delta z^2\big)^2\Big)\,\bar{x}^4+16\,\Delta x\,\Delta y\,\big(\Delta x^2-\Delta y^2-\Delta z^2\big)\,\bar{x}^3\,\bar{y}-2\times\big(3\,\Delta x^4+3\,\Delta y^4+2\,\Delta y^2\,\Delta z^2-\Delta z^4+2\,\Delta x^2\,\big(-9\,\Delta y^2+\Delta z^2\big)\big)\,\bar{x}^2\,\bar{y}^2-16\,\Delta x\,\Delta y\,\big(\Delta x^2-\Delta y^2+\Delta z^2\big)\,\bar{x}\,\bar{y}^3+\big(\Delta x^4+\Delta y^4-6\,\Delta y^2\,\Delta z^2+\Delta z^4+\Delta x^2\,\big(-6\,\Delta y^2+2\,\Delta z^2\big)\big)\,\bar{y}^4\Big)\,r_p^2-4\,M^{3/2}\,\big(\Delta x\,\Delta y\,\bar{x}^2+\big(-\Delta x^2+\Delta y^2\big)\,\bar{x}\,\bar{y}-\Delta x\,\Delta y\,\bar{y}^2\big)\,\Big(\big(2\,\Delta x^2-\Delta y^2-\Delta z^2\big)\,\bar{x}^2+6\,\Delta x\,\Delta y\,\bar{x}\,\bar{y}-\big(\Delta x^2-2\,\Delta y^2+\Delta z^2\big)\,\bar{y}^2\Big)\,\sqrt{\xi\,r_p}-3\,\big(\Delta x\,\Delta y\,\bar{x}^2+\big(-\Delta x^2+\Delta y^2\big)\,\bar{x}\,\bar{y}-\Delta x\,\Delta y\,\bar{y}^2\big)\,\Big(\big(\Delta x^2-4\,\big(\Delta y^2+\Delta z^2\big)\big)\,\bar{x}^2+10\,\Delta x\,\Delta y\,\bar{x}\,\bar{y}+\big(-4\,\Delta x^2+\Delta y^2-4\,\Delta z^2\big)\,\bar{y}^2\Big)\,r_p\,\sqrt{M\,\xi\,r_p}\Big)+4\,M\,\Big(\big(\Delta x^2-\Delta y^2-\Delta z^2\big)\,\bar{x}^2+4\,\Delta x\,\Delta y\,\bar{x}\,\bar{y}-\big(\Delta x^2-\Delta y^2+\Delta z^2\big)\,\bar{y}^2\Big)\,\Big(2\,M^2\,\sqrt{\xi}\,(\Delta x\,\bar{x}+\Delta y\,\bar{y})^3+2\,M\,\sqrt{\xi}\,(\Delta x\,\bar{x}+\Delta y\,\bar{y})\,\Big(\big(\Delta x^2-\Delta y^2-\Delta z^2\big)\,\bar{x}^2+4\,\Delta x\,\Delta y\,\bar{x}\,\bar{y}-\big(\Delta x^2-\Delta y^2+\Delta z^2\big)\,\bar{y}^2\Big)\,r_p+4\,\sqrt{\xi}\,(\Delta x\,\bar{x}+\Delta y\,\bar{y})\,\Big(\big(\Delta x^2-3\,\big(\Delta y^2+\Delta z^2\big)\big)\,\bar{x}^2+8\,\Delta x\,\Delta y\,\bar{x}\,\bar{y}+\big(-3\,\Delta x^2+\Delta y^2-3\,\Delta z^2\big)\,\bar{y}^2\Big)\,r_p^2-2\,M^{3/2}\,(\Delta y\,\bar{x}-\Delta x\,\bar{y})\,(\Delta x\,\bar{x}+\Delta y\,\bar{y})^2\,\sqrt{\xi\,r_p}-(\Delta y\,\bar{x}-\Delta x\,\bar{y})\,\Big(\big(\Delta x^2-2\,\big(\Delta y^2+\Delta z^2\big)\big)\,\bar{x}^2+6\,\Delta x\,\Delta y\,\bar{x}\,\bar{y}+\big(-2\,\Delta x^2+\Delta y^2-2\,\Delta z^2\big)\,\bar{y}^2\Big)\,r_p\,\sqrt{M\,\xi\,r_p}\Big)\Big)-M\,\Big(\xi\,(\Delta x\,\bar{x}+\Delta y\,\bar{y})\,\Big(\big(\Delta x^2-2\,\big(\Delta y^2+\Delta z^2\big)\big)\,\bar{x}^2+6\,\Delta x\,\Delta y\,\bar{x}\,\bar{y}+\big(-2\,\Delta x^2+\Delta y^2-2\,\Delta z^2\big)\,\bar{y}^2\Big)+$$

$$
\begin{aligned}
&2\left(\left(\Delta x^2-\Delta y^2-\Delta z^2\right)\bar{x}^2+4\,\Delta x\,\Delta y\,\bar{x}\,\bar{y}-\left(\Delta x^2-\Delta y^2+\Delta z^2\right)\bar{y}^2\right)\\
&\quad\left(2\,M\,(\Delta x\,\bar{x}+\Delta y\,\bar{y})+(\Delta y\,\bar{x}-\Delta x\,\bar{y})\,\sqrt{M\,r_p}\right)\Big)\\
&\left(4\,M\,\Delta x\,\Delta y\,\xi\,\bar{x}\,\bar{y}+2\,M\,\Delta y^2\,\xi\,\bar{y}^2+\Delta y^2\,\xi\,r_p^3+\Delta z^2\,\xi\,r_p^3+\Delta x^2\,\xi\left(2\,M\,\bar{x}^2+r_p^3\right)+\right.\\
&\quad\left.\left(2\,M\,(\Delta x\,\bar{x}+\Delta y\,\bar{y})+(\Delta y\,\bar{x}-\Delta x\,\bar{y})\,\sqrt{M\,r_p}\right)^2\right)\times\\
&\left(12\,M\,\sqrt{\xi}\,\left(\left(\Delta x^2-\Delta y^2-\Delta z^2\right)\bar{x}^2+4\,\Delta x\,\Delta y\,\bar{x}\,\bar{y}-\left(\Delta x^2-\Delta y^2+\Delta z^2\right)\bar{y}^2\right)^2 r_p^2+\right.\\
&\quad\xi^{3/2}\left(2\,M^2\,(\Delta x\,\bar{x}+\Delta y\,\bar{y})^4+M\,(\Delta x\,\bar{x}+\Delta y\,\bar{y})^2\right.\\
&\qquad\left(\left(3\,\Delta x^2-4\left(\Delta y^2+\Delta z^2\right)\right)\bar{x}^2+14\,\Delta x\,\Delta y\,\bar{x}\,\bar{y}+\left(-4\,\Delta x^2+3\,\Delta y^2-4\,\Delta z^2\right)\bar{y}^2\right)\,r_p+\\
&\qquad4\left(\left(2\,\Delta x^4-11\,\Delta x^2\left(\Delta y^2+\Delta z^2\right)+2\left(\Delta y^2+\Delta z^2\right)^2\right)\bar{x}^4+\right.\\
&\qquad\quad30\,\Delta x\,\Delta y\left(\Delta x^2-\Delta y^2-\Delta z^2\right)\bar{x}^3\,\bar{y}-\left(11\,\Delta x^4+11\,\Delta y^4+7\,\Delta y^2\,\Delta z^2-4\,\Delta z^4+\right.\\
&\qquad\qquad\left.\Delta x^2\left(-68\,\Delta y^2+7\,\Delta z^2\right)\right)\bar{x}^2\,\bar{y}^2-30\,\Delta x\,\Delta y\left(\Delta x^2-\Delta y^2+\Delta z^2\right)\bar{x}\,\bar{y}^3+\\
&\qquad\quad\left.\left.\left(2\,\Delta x^4+2\,\Delta y^4-11\,\Delta y^2\,\Delta z^2+2\,\Delta z^4+\Delta x^2\left(-11\,\Delta y^2+4\,\Delta z^2\right)\right)\bar{y}^4\right)\,r_p^2\right)+\\
&\quad4\times\left(2\,M\,(\Delta x\,\bar{x}+\Delta y\,\bar{y})+(\Delta y\,\bar{x}-\Delta x\,\bar{y})\,\sqrt{M\,r_p}\right)\times\left(2\,M^2\,\sqrt{\xi}\,(\Delta x\,\bar{x}+\Delta y\,\bar{y})^3+2\,M\,\sqrt{\xi}\right.\\
&\qquad(\Delta x\,\bar{x}+\Delta y\,\bar{y})\left(\left(\Delta x^2-\Delta y^2-\Delta z^2\right)\bar{x}^2+4\,\Delta x\,\Delta y\,\bar{x}\,\bar{y}-\left(\Delta x^2-\Delta y^2+\Delta z^2\right)\bar{y}^2\right)\,r_p+4\,\sqrt{\xi}\\
&\qquad(\Delta x\,\bar{x}+\Delta y\,\bar{y})\left(\left(\Delta x^2-3\left(\Delta y^2+\Delta z^2\right)\right)\bar{x}^2+8\,\Delta x\,\Delta y\,\bar{x}\,\bar{y}+\left(-3\,\Delta x^2+\Delta y^2-3\,\Delta z^2\right)\bar{y}^2\right)\\
&\qquad r_p^2-2\,M^{3/2}\,(\Delta y\,\bar{x}-\Delta x\,\bar{y})\,(\Delta x\,\bar{x}+\Delta y\,\bar{y})^2\,\sqrt{\xi\,r_p}-(\Delta y\,\bar{x}-\Delta x\,\bar{y})\\
&\qquad\left.\left(\left(\Delta x^2-2\left(\Delta y^2+\Delta z^2\right)\right)\bar{x}^2+6\,\Delta x\,\Delta y\,\bar{x}\,\bar{y}+\left(-2\,\Delta x^2+\Delta y^2-2\,\Delta z^2\right)\bar{y}^2\right)\,r_p\,\sqrt{M\,\xi\,r_p}\right)\Big)+\\
&2\,M\left(\xi\,(\Delta x\,\bar{x}+\Delta y\,\bar{y})\left(\left(\Delta x^2-2\left(\Delta y^2+\Delta z^2\right)\right)\bar{x}^2+6\,\Delta x\,\Delta y\,\bar{x}\,\bar{y}+\left(-2\,\Delta x^2+\Delta y^2-2\,\Delta z^2\right)\bar{y}^2\right)+\right.\\
&\quad2\left(\left(\Delta x^2-\Delta y^2-\Delta z^2\right)\bar{x}^2+4\,\Delta x\,\Delta y\,\bar{x}\,\bar{y}-\left(\Delta x^2-\Delta y^2+\Delta z^2\right)\bar{y}^2\right)\\
&\quad\left(2\,M\,(\Delta x\,\bar{x}+\Delta y\,\bar{y})+(\Delta y\,\bar{x}-\Delta x\,\bar{y})\,\sqrt{M\,r_p}\right)\Big)\\
&\left(3\,M\,\sqrt{\xi}\,r_p^2\left(\xi\,(\Delta x\,\bar{x}+\Delta y\,\bar{y})\left(\left(\Delta x^2-2\left(\Delta y^2+\Delta z^2\right)\right)\bar{x}^2+6\,\Delta x\,\Delta y\,\bar{x}\,\bar{y}+\left(-2\,\Delta x^2+\Delta y^2-2\,\Delta z^2\right)\right.\right.\right.\\
&\qquad\left.\left.\left.\bar{y}^2\right)+2\left(\left(\Delta x^2-\Delta y^2-\Delta z^2\right)\bar{x}^2+4\,\Delta x\,\Delta y\,\bar{x}\,\bar{y}-\left(\Delta x^2-\Delta y^2+\Delta z^2\right)\bar{y}^2\right)\right.\\
&\qquad\left.\left(2\,M\,(\Delta x\,\bar{x}+\Delta y\,\bar{y})+(\Delta y\,\bar{x}-\Delta x\,\bar{y})\,\sqrt{M\,r_p}\right)\right)^2-\\
&\left(4\,M\,\Delta x\,\Delta y\,\xi\,\bar{x}\,\bar{y}+2\,M\,\Delta y^2\,\xi\,\bar{y}^2+\Delta y^2\,\xi\,r_p^3+\Delta z^2\,\xi\,r_p^3+\Delta x^2\,\xi\left(2\,M\,\bar{x}^2+r_p^3\right)+\right.\\
&\quad\left.\left(2\,M\,(\Delta x\,\bar{x}+\Delta y\,\bar{y})+(\Delta y\,\bar{x}-\Delta x\,\bar{y})\,\sqrt{M\,r_p}\right)^2\right)\times\\
&\left(12\,M\,\sqrt{\xi}\,\left(\left(\Delta x^2-\Delta y^2-\Delta z^2\right)\bar{x}^2+4\,\Delta x\,\Delta y\,\bar{x}\,\bar{y}-\left(\Delta x^2-\Delta y^2+\Delta z^2\right)\bar{y}^2\right)^2 r_p^2+\right.\\
&\quad\xi^{3/2}\left(2\,M^2\,(\Delta x\,\bar{x}+\Delta y\,\bar{y})^4+M\,(\Delta x\,\bar{x}+\Delta y\,\bar{y})^2\right.\\
&\qquad\left(\left(3\,\Delta x^2-4\left(\Delta y^2+\Delta z^2\right)\right)\bar{x}^2+14\,\Delta x\,\Delta y\,\bar{x}\,\bar{y}+\left(-4\,\Delta x^2+3\,\Delta y^2-4\,\Delta z^2\right)\bar{y}^2\right)\,r_p+\\
&\qquad4\left(\left(2\,\Delta x^4-11\,\Delta x^2\left(\Delta y^2+\Delta z^2\right)+2\left(\Delta y^2+\Delta z^2\right)^2\right)\bar{x}^4+30\,\Delta x\,\Delta y\left(\Delta x^2-\Delta y^2-\Delta z^2\right)\right.\\
&\qquad\quad\bar{x}^3\,\bar{y}-\left(11\,\Delta x^4+11\,\Delta y^4+7\,\Delta y^2\,\Delta z^2-4\,\Delta z^4+\Delta x^2\left(-68\,\Delta y^2+7\,\Delta z^2\right)\right)\\
&\qquad\quad\bar{x}^2\,\bar{y}^2-30\,\Delta x\,\Delta y\left(\Delta x^2-\Delta y^2+\Delta z^2\right)\bar{x}\,\bar{y}^3+\\
&\qquad\quad\left.\left.\left(2\,\Delta x^4+2\,\Delta y^4-11\,\Delta y^2\,\Delta z^2+2\,\Delta z^4+\Delta x^2\left(-11\,\Delta y^2+4\,\Delta z^2\right)\right)\bar{y}^4\right)\,r_p^2\right)+\\
&\quad4\times\left(2\,M\,(\Delta x\,\bar{x}+\Delta y\,\bar{y})+(\Delta y\,\bar{x}-\Delta x\,\bar{y})\,\sqrt{M\,r_p}\right)\times\left(2\,M^2\,\sqrt{\xi}\,(\Delta x\,\bar{x}+\Delta y\,\bar{y})^3+\right.\\
&\qquad2\,M\,\sqrt{\xi}\,(\Delta x\,\bar{x}+\Delta y\,\bar{y})\left(\left(\Delta x^2-\Delta y^2-\Delta z^2\right)\bar{x}^2+4\,\Delta x\,\Delta y\,\bar{x}\,\bar{y}-\left(\Delta x^2-\Delta y^2+\Delta z^2\right)\bar{y}^2\right)\\
&\qquad r_p+4\,\sqrt{\xi}\,(\Delta x\,\bar{x}+\Delta y\,\bar{y})\left(\left(\Delta x^2-3\left(\Delta y^2+\Delta z^2\right)\right)\bar{x}^2+8\,\Delta x\,\Delta y\,\bar{x}\,\bar{y}+\right.\\
&\qquad\left.\left(-3\,\Delta x^2+\Delta y^2-3\,\Delta z^2\right)\bar{y}^2\right)\,r_p^2-2\,M^{3/2}\,(\Delta y\,\bar{x}-\Delta x\,\bar{y})\,(\Delta x\,\bar{x}+\Delta y\,\bar{y})^2\,\sqrt{\xi\,r_p}-\\
&\qquad(\Delta y\,\bar{x}-\Delta x\,\bar{y})\left(\left(\Delta x^2-2\left(\Delta y^2+\Delta z^2\right)\right)\bar{x}^2+6\,\Delta x\,\Delta y\,\bar{x}\,\bar{y}+\right.\\
&\qquad\left.\left.\left.\left(-2\,\Delta x^2+\Delta y^2-2\,\Delta z^2\right)\bar{y}^2\right)\,r_p\,\sqrt{M\,\xi\,r_p}\right)\right)\Big)\Big)
\end{aligned}
$$

Appendix B

Derivatives of Spherical Harmonics

Here we give the relations to express the derivatives of scalar, vector and tensor spherical harmonics in terms of the scalar, vector, tensor spherical harmonics themselves. These are used in the derivation of the tidally perturbed Schwarzschild metric in Chapter 8, specifically Sec. 8.4, with the aim of matching the metric as presented in [109].

These relations were derived using the identities:

$$Y_A^{\ell m} := D_A Y^{\ell m} = Y_A^{\ell m}, \tag{B.1}$$

$$X_A^{\ell m} := \epsilon_A^B D_B Y^{\ell m}, \tag{B.2}$$

$$Y_{AB}^{\ell m} := \left[D_A D_B + \frac{1}{2}\ell(\ell+1)\Omega_{AB} \right] Y^{\ell m}, \tag{B.3}$$

$$X_{AB}^{\ell m} := -\frac{1}{2}\left(\epsilon_A^C D_B + \epsilon_B^C D_A \right) D_C Y^{\ell m}, \tag{B.4}$$

along with the relations

$$\left[\Omega^{AB} D_A D_B + \ell(\ell+1) \right] Y^{\ell m} = 0, \tag{B.5}$$

$$\epsilon_A^F Y_F^{\ell m} = -X_A^{\ell m}, \tag{B.6}$$

$$\epsilon_B^F Y_{AF}^{\ell m} + \epsilon_A^F Y_{BF}^{\ell m} = -2X_{AB}^{\ell m}. \tag{B.7}$$

We split the results into the even and odd sector.

Even vector harmonics:

$$D_A Y^{A\ell m} = -\ell(\ell+1)Y^{\ell m}, \tag{B.8}$$

$$D_A Y_B^{\ell m} = \frac{1}{2}\ell(\ell+1)\Omega_{AB}Y^{\ell m} + Y_{AB}^{\ell m}, \tag{B.9}$$

$$D^B D_B Y_A^{\ell m} = -\ell(\ell+1)Y_A^{\ell m}, \tag{B.10}$$

$$D^A D_B Y_A^{\ell m} = -\ell(\ell+1)Y_B^{\ell m} + Y_B^{\ell m}. \tag{B.11}$$

Even tensor harmonics:

$$D_B Y_A^{B\ell m} = -\ell(\ell+1)Y_A^{\ell m} + \frac{1}{2}\ell(\ell+1)\Omega_{AB}Y^{B\ell m}, \tag{B.12}$$

$$D^F D_F Y_{AB}^{\ell m} = -\ell(\ell+1)Y_{AB}^{\ell m}, \tag{B.13}$$

$$D_B D_A Y^{AB\ell m} = \frac{1}{2}\ell^2(\ell+1)^2 Y^{\ell m}, \tag{B.14}$$

$$D_F D_B Y_A^{F\ell m} = \frac{1}{4}\ell^2(\ell+1)^2\Omega_{AB}Y^{\ell m} - \frac{1}{2}\ell(\ell+1)Y_{AB}^{\ell m}. \tag{B.15}$$

Odd vector harmonics:

$$D_A X^{A\ell m} = 0, \tag{B.16}$$

$$D_A X_B^{\ell m} = 2X_{AB}^{\ell m} - \frac{1}{2}\ell(\ell+1)\epsilon_A^F\Omega_{BF}Y^{\ell m} + \epsilon_A^F Y_{BF}^{\ell m}, \tag{B.17}$$

$$D_A D_B X^{B\ell m} = X_A^{\ell m}, \tag{B.18}$$

$$D^B D_B X_A^{\ell m} = [\ell(\ell+1)+1]X_A^{\ell m}. \tag{B.19}$$

Odd tensor harmonics:

$$D_B X_A^{B\ell m} = \frac{1}{2}\ell(\ell+1)\epsilon_A^B Y_B^{\ell m}, \tag{B.20}$$

$$D_B D_A X^{AB\ell m} = 0, \tag{B.21}$$

$$D_F D_B X_A^{F\ell m} = -\frac{1}{4}\ell^2(\ell+1)^2\epsilon_A^G\Omega_{BG}Y^{\ell m} + \frac{1}{2}\ell(\ell+1)\epsilon_A^G Y_{BG}^{\ell m}, \tag{B.22}$$

$$D_F D^F X_{AB}^{\ell m} = \frac{1}{2}\ell(\ell+1)[\epsilon_A^G Y_{BG}^{\ell m} + \epsilon_B^G Y_{AG}^{\ell m}]. \tag{B.23}$$

References

[1] GEO600 website. https://www.geo600.org.

[2] LIGO website. https://www.ligo.caltech.edu.

[3] LISA website. https://www.elisascience.org.

[4] SPeC website. https://www.black-holes.org/code/SpEC.html.

[5] SPeCTRE website. https://spectre-code.org.

[6] VIRGO website. https://www.virgo-gw.eu.

[7] B. P. Abbott et al. GW151226: Observation of Gravitational Waves from a 22-Solar-Mass Binary Black Hole Coalescence. *Phys. Rev. Lett.*, 116(24):241103, 2016.

[8] B. P. Abbott et al. Observation of Gravitational Waves from a Binary Black Hole Merger. *Phys. Rev. Lett.*, 116(6):061102, 2016.

[9] B. P. Abbott et al. Tests of general relativity with GW150914. *Phys. Rev. Lett.*, 116(22):221101, 2016. [Erratum: Phys.Rev.Lett. 121, 129902 (2018)].

[10] B. P. Abbott et al. GW170817: Observation of Gravitational Waves from a Binary Neutron Star Inspiral. *Phys. Rev. Lett.*, 119(16):161101, 2017.

[11] B. P. Abbott et al. Prospects for observing and localizing gravitational-wave transients with Advanced LIGO, Advanced Virgo and KAGRA. *Living Rev. Rel.*, 21(1):3, 2018.

[12] R. Abbott et al. GW190521: A Binary Black Hole Merger with a Total Mass of $150M_{\odot}$. *Phys. Rev. Lett.*, 125(10):101102, 2020.

[13] R. Abbott et al. GW190814: Gravitational Waves from the Coalescence of a 23 Solar Mass Black Hole with a 2.6 Solar Mass Compact Object. *Astrophys. J. Lett.*, 896(2):L44, 2020.

[14] R. Abbott et al. Tests of General Relativity with Binary Black Holes from the second LIGO-Virgo Gravitational-Wave Transient Catalog. 10 2020.

[15] R. Abbott et al. GWTC-3: Compact Binary Coalescences Observed by LIGO and Virgo During the Second Part of the Third Observing Run. 11 2021.

[16] R. Abbott et al. The population of merging compact binaries inferred using gravitational waves through GWTC-3. 11 2021.

[17] Andrew M. Abrahams, Stuart L. Shapiro, and Saul A. Teukolsky. Calculation of gravitational wave forms from black hole collisions and disk collapse: Applying perturbation theory to numerical space-times. *Phys. Rev. D*, 51:4295–4301, 1995.

[18] Pau Amaro-Seoane. Detecting Intermediate-Mass Ratio Inspirals From The Ground And Space. *Phys. Rev. D*, 98(6):063018, 2018.

[19] Pau Amaro-Seoane et al. Laser Interferometer Space Antenna. 2 2017.

[20] Pau Amaro-Seoane, Jonathan R. Gair, Marc Freitag, M. Coleman Miller, Ilya Mandel, Curt J. Cutler, and Stanislav Babak. Astrophysics, detection and science applications of intermediate- and extreme mass-ratio inspirals. *Class. Quant. Grav.*, 24:R113–R169, 2007.

[21] Peter Anninos and Steven Brandt. Headon collision of two unequal mass black holes. *Phys. Rev. Lett.*, 81:508–511, 1998.

[22] Peter Anninos, David Hobill, Edward Seidel, Larry Smarr, and Wai-Mo Suen. The Collision of two black holes. *Phys. Rev. Lett.*, 71:2851–2854, 1993.

[23] Peter Anninos, David Hobill, Edward Seidel, Larry Smarr, and Wai-Mo Suen. The headon collision of two equal mass black holes. *Phys. Rev. D*, 52:2044–2058, 1995.

[24] M. E. Araujo, P. S. Letelier, and S. R. Oliveira. Two Kerr black holes with axisymmetric spins: An Improved Newtonian model for the head - on collision and gravitational radiation. *Class. Quant. Grav.*, 15:3051–3060, 1998.

[25] Richard L. Arnowitt, Stanley Deser, and Charles W. Misner. The Dynamics of general relativity. *Gen. Rel. Grav.*, 40:1997–2027, 2008.

[26] Vishal Baibhav and Emanuele Berti. Multimode black hole spectroscopy. *Phys. Rev. D*, 99(2):024005, 2019.

[27] John G. Baker, Andrew Abrahams, Peter Anninos, Steve Brandt, Richard Price, Jorge Pullin, and Edward Seidel. The Collision of boosted black holes. *Phys. Rev. D*, 55:829–834, 1997.

[28] John G. Baker, Joan Centrella, Dae-Il Choi, Michael Koppitz, and James van Meter. Gravitational wave extraction from an inspiraling configuration of merging black holes. *Phys. Rev. Lett.*, 96:111102, 2006.

[29] John G. Baker, James R. van Meter, Sean T. McWilliams, Joan Centrella, and Bernard J. Kelly. Consistency of post-Newtonian waveforms with numerical relativity. *Phys. Rev. Lett.*, 99:181101, 2007.

[30] Leor Barack. Late time dynamics of scalar perturbations outside black holes. 2. Schwarzschild geometry. *Phys. Rev. D*, 59:044017, 1999.

[31] Leor Barack et al. Black holes, gravitational waves and fundamental physics: a roadmap. *Class. Quant. Grav.*, 36(14):143001, 2019.

[32] Leor Barack and Darren A. Golbourn. Scalar-field perturbations from a particle orbiting a black hole using numerical evolution in 2+1 dimensions. *Phys. Rev. D*, 76:044020, 2007.

[33] Leor Barack and Carlos O. Lousto. Perturbations of Schwarzschild black holes in the Lorenz gauge: Formulation and numerical implementation. *Phys. Rev. D*, 72:104026, 2005.

[34] Leor Barack and Amos Ori. Regularization parameters for the self-force in Schwarzschild space-time. 1. Scalar case. *Phys. Rev. D*, 66:084022, 2002.

[35] Leor Barack and Adam Pound. Self-force and radiation reaction in general relativity. *Rept. Prog. Phys.*, 82(1):016904, 2019.

[36] Leor Barack and Norichika Sago. Gravitational self-force on a particle in circular orbit around a Schwarzschild black hole. *Phys. Rev. D*, 75:064021, 2007.

[37] Leor Barack and Norichika Sago. Gravitational self-force on a particle in eccentric orbit around a Schwarzschild black hole. *Phys. Rev. D*, 81:084021, 2010.

[38] Barry C. Barish. An overview of LIGO. *AIP Conf. Proc.*, 342:479–486, 1995.

[39] Thomas W. Baumgarte and Stuart L. Shapiro. On the numerical integration of Einstein's field equations. *Phys. Rev. D*, 59:024007, 1998.

[40] Thomas W. Baumgarte and Stuart L. Shapiro. *Numerical Relativity: Solving Einstein's Equations on the Computer*. Cambridge University Press, 2010.

[41] Alvin Bayliss and Eli Turkel. Radiation boundary condition for wave-like equations. *Communications on Pure and Applied Mathematics*, 33:707 – 725, 11 1980.

[42] Jillian Bellovary, Alyson Brooks, Monica Colpi, Michael Eracleous, Kelly Holley-Bockelmann, Ann Hornschemeier, Lucio Mayer, Priya Natarajan, Jacob Slutsky, and Michael Tremmel. Where are the Intermediate Mass Black Holes? 3 2019.

[43] Taylor Binnington and Eric Poisson. Relativistic theory of tidal Love numbers. *Phys. Rev. D*, 80:084018, 2009.

[44] M. Bjørhus. The ODE Formulation of Hyperbolic PDEs Discretized by the Spectral Collocation Method. *SIAM J. Sci. Comput.*, 16(3):542–557, 1995.

[45] Luc Blanchet, Alessandro D.A.M. Spallicci di Filottrano, and Bernard Whiting. *Mass and Motion in General Relativity.* 01 2011.

[46] Michael Boyle et al. The SXS Collaboration catalog of binary black hole simulations. *Class. Quant. Grav.*, 36(19):195006, 2019.

[47] Dieter R. Brill and Richard W. Lindquist. Interaction energy in geometrostatics. *Phys. Rev.*, 131:471–476, 1963.

[48] Duncan A. Brown, Hua Fang, Jonathan R. Gair, Chao Li, Geoffrey Lovelace, Ilya Mandel, and Kip S. Thorne. Prospects for detection of gravitational waves from intermediate-mass-ratio inspirals. *Phys. Rev. Lett.*, 99:201102, 2007.

[49] Lior M. Burko. Self-force on static charges in Schwarzschild space-time. *Class. Quant. Grav.*, 17:227–250, 2000.

[50] Manuela Campanelli, C. O. Lousto, P. Marronetti, and Y. Zlochower. Accurate evolutions of orbiting black-hole binaries without excision. *Phys. Rev. Lett.*, 96:111101, 2006.

[51] Joan Centrella, John G. Baker, Bernard J. Kelly, and James R. van Meter. Black-hole binaries, gravitational waves, and numerical relativity. *Rev. Mod. Phys.*, 82:3069, 2010.

[52] Monica Colpi and Alberto Sesana. *Gravitational Wave Sources in the Era of Multi-Band Gravitational Wave Astronomy.* 2017.

[53] R. Courant, K. Friedrichs, and H. Lewy. *On the partial difference equations of mathematical physics.* 1956.

[54] T. Damour. Gravitational radiation reaction in the binary pulsar and the quadrupole fomula controvery. *Phys. Rev. Lett.*, 51:1019–1021, 1983.

[55] Thibault Damour and Alessandro Nagar. Relativistic tidal properties of neutron stars. *Phys. Rev. D*, 80:084035, 2009.

[56] Nils Deppe, William Throwe, Lawrence E. Kidder, Nils L. Vu, François Hébert, Jordan Moxon, Cristóbal Armaza, Gabriel S. Bonilla, Yoonsoo Kim, Prayush Kumar, Geoffrey Lovelace, Alexandra Macedo, Kyle C. Nelli, Eamonn O'Shea, Harald P. Pfeiffer, Mark A. Scheel, Saul A. Teukolsky, Nikolas A. Wittek, et al. `SpECTRE v2022.07.18`. 10.5281/zenodo.6856873, 7 2022.

[57] Steven Detweiler. Gravitational radiation reaction and second order perturbation theory. *Phys. Rev. D*, 85:044048, 2012.

[58] Mekhi Dhesi, Hannes R. Rüter, Adam Pound, Leor Barack, and Harald P. Pfeiffer. Worldtube excision method for intermediate-mass-ratio inspirals: Scalar-field toy model. *Phys. Rev. D*, 104(12):124002, 2021.

[59] Sam R. Dolan and Leor Barack. Self-force via m-mode regularization and 2+1D evolution: III. Gravitational field on Schwarzschild spacetime. *Phys. Rev. D*, 87:084066, 2013.

[60] Matthew D. Duez and Yosef Zlochower. Numerical Relativity of Compact Binaries in the 21st Century. *Rept. Prog. Phys.*, 82(1):016902, 2019.

[61] Albert Einstein. The Foundation of the General Theory of Relativity. *Annalen Phys.*, 49(7):769–822, 1916.

[62] Albert Einstein and N. Rosen. The Particle Problem in the General Theory of Relativity. *Phys. Rev.*, 48:73–77, 1935.

[63] Milinda Fernando, David Neilsen, Hyun Lim, Eric Hirschmann, and Hari Sundar. Massively Parallel Simulations of Binary Black Hole Intermediate-Mass-Ratio Inspirals. 7 2018.

[64] Nils L. Fischer and Harald P. Pfeiffer. Unified discontinuous Galerkin scheme for a large class of elliptic equations. *Phys. Rev. D*, 105(2):024034, 2022.

[65] Helmut Friedrich. On the hyperbolicity of Einstein's and other gauge field equations. *Communications in Mathematical Physics*, 100(4):525 – 543, 1985.

[66] Jonathan R. Gair, Ilya Mandel, M. Coleman Miller, and Marta Volonteri. Exploring intermediate and massive black-hole binaries with the Einstein Telescope. *Gen. Rel. Grav.*, 43:485–518, 2011.

[67] Jonathan R Gair, Ilya Mandel, Alberto Sesana, and Alberto Vecchio. Probing seed black holes using future gravitational-wave detectors. *Class. Quant. Grav.*, 26:204009, 2009.

[68] Samuel E. Gralla. Second Order Gravitational Self-Force. *Phys. Rev. D*, 85:124011, 2012.

[69] Philippe Grandclement. Introduction to spectral methods. *EAS Publ. Ser.*, 21:153–180, 2006.

[70] Philippe Grandclement and Jerome Novak. Spectral methods for numerical relativity. *Living Rev. Rel.*, 12:1, 2009.

[71] Carsten Gundlach, Jose M. Martin-Garcia, Gioel Calabrese, and Ian Hinder. Constraint damping in the Z4 formulation and harmonic gauge. *Class. Quant. Grav.*, 22:3767–3774, 2005.

[72] Roland Haas. Scalar self-force on eccentric geodesics in Schwarzschild spacetime: A Time-domain computation. *Phys. Rev. D*, 75:124011, 2007.

[73] Roland Haas and Eric Poisson. Mode-sum regularization of the scalar self-force: Formulation in terms of a tetrad decomposition of the singular field. *Phys. Rev. D*, 74:044009, 2006.

[74] Evan D. Hall and Matthew Evans. Metrics for next-generation gravitational-wave detectors. *Class. Quant. Grav.*, 36(22):225002, 2019.

[75] Anna Heffernan, Adrian Ottewill, and Barry Wardell. High-order expansions of the Detweiler-Whiting singular field in Schwarzschild spacetime. *Phys. Rev. D*, 86:104023, 2012.

[76] Daniel A. Hemberger, Mark A. Scheel, Lawrence E. Kidder, Béla Szilágyi, Geoffrey Lovelace, Nicholas W. Taylor, and Saul A. Teukolsky. Dynamical Excision Boundaries in Spectral Evolutions of Binary Black Hole Spacetimes. *Class. Quant. Grav.*, 30:115001, 2013.

[77] Jan S. Hesthaven and Tim Warburton. *Nodal Discontinuous Galerkin Methods: Algorithms, Analysis, and Applications*. Springer Publishing Company, Incorporated, 1st edition, 2007.

[78] David Hilditch, Andreas Weyhausen, and Bernd Brügmann. Pseudospectral method for gravitational wave collapse. *Phys. Rev. D*, 93(6):063006, 2016.

[79] Ian Hinder et al. Error-analysis and comparison to analytical models of numerical waveforms produced by the NRAR Collaboration. *Class. Quant. Grav.*, 31:025012, 2014.

[80] Tanja Hinderer, Benjamin D. Lackey, Ryan N. Lang, and Jocelyn S. Read. Tidal deformability of neutron stars with realistic equations of state and their gravitational wave signatures in binary inspiral. *Phys. Rev. D*, 81:123016, 2010.

[81] Michael Holst, Lee Lindblom, Robert Owen, Harald P. Pfeiffer, Mark A. Scheel, and Lawrence E. Kidder. Optimal constraint projection for hyperbolic evolution systems. *Phys. Rev. D*, 70:084017, 2004.

[82] Karan Jani, Deirdre Shoemaker, and Curt Cutler. Detectability of Intermediate-Mass Black Holes in Multiband Gravitational Wave Astronomy. *Nature Astron.*, 4(3):260–265, 2019.

[83] Lawrence E. Kidder et al. SpECTRE: A Task-based Discontinuous Galerkin Code for Relativistic Astrophysics. *J. Comput. Phys.*, 335:84–114, 2017.

[84] Lawrence E. Kidder, Mark A. Scheel, Saul A. Teukolsky, Eric D. Carlson, and Gregory B. Cook. Black hole evolution by spectral methods. *Phys. Rev. D*, 62:084032, 2000.

[85] David A. Kopriva. *Implementing Spectral Methods for Partial Differential Equations*. Springer, New York, 2009.

[86] Philippe Landry and Eric Poisson. Dynamical response to a stationary tidal field. *Phys. Rev. D*, 92(12):124041, 2015.

[87] Alexandre Le Tiec, Marc Casals, and Edgardo Franzin. Tidal Love Numbers of Kerr Black Holes. *Phys. Rev. D*, 103(8):084021, 2021.

[88] Luis Lehner. Numerical relativity: A Review. *Class. Quant. Grav.*, 18:R25–R86, 2001.

[89] Lee Lindblom, Mark A. Scheel, Lawrence E. Kidder, Robert Owen, and Oliver Rinne. A new generalized harmonic evolution system. *Class. Quant. Grav.*, 23:S447–S462, 2006.

[90] Carlos O. Lousto. A time-domain fourth-order-convergent numerical algorithm to integrate black hole perturbations in the extreme-mass-ratio limit. *Class. Quant. Grav.*, 22:S543–S568, 2005.

[91] Carlos O. Lousto and James Healy. Exploring the Small Mass Ratio Binary Black Hole Merger via Zeno's Dichotomy Approach. *Phys. Rev. Lett.*, 125(19):191102, 2020.

[92] Carlos O. Lousto and James Healy. Study of the Intermediate Mass Ratio Black Hole Binary Merger up to 1000:1 with Numerical Relativity. 3 2022.

[93] Carlos O. Lousto and Richard H. Price. Understanding initial data for black hole collisions. *Phys. Rev. D*, 56:6439–6457, 1997.

[94] Jun Luo et al. TianQin: a space-borne gravitational wave detector. *Class. Quant. Grav.*, 33(3):035010, 2016.

[95] Ilya Mandel, Duncan A. Brown, Jonathan R. Gair, and M. Coleman Miller. Rates and Characteristics of Intermediate-Mass-Ratio Inspirals Detectable by Advanced LIGO. *Astrophys. J.*, 681:1431–1447, 2008.

[96] Ilya Mandel and Jonathan R. Gair. Can we Detect Intermediate Mass Ratio Inspirals? *Class. Quant. Grav.*, 26:094036, 2009.

[97] Ilya Mandel and Jonathan R Gair. Can we detect intermediate mass ratio inspirals? *Classical and Quantum Gravity*, 26(9):094036, apr 2009.

[98] Karl Martel and Eric Poisson. Gravitational perturbations of the Schwarzschild spacetime: A Practical covariant and gauge-invariant formalism. *Phys. Rev. D*, 71:104003, 2005.

[99] R. A. Matzner, H. E. Seidel, Stuart L. Shapiro, L. Smarr, W. M. Suen, Saul A. Teukolsky, and J. Winicour. Geometry of a black hole collision. *Science*, 270:941–947, 1995.

[100] J. Miller, B. Wardell, and A. Pound. Second-order perturbation theory: the problem of infinite mode coupling. *Phys. Rev.*, D94(10):104018, 2016.

[101] Jeremy Miller. *The second-order gravitational self-force.* PhD thesis, University of Southampton, 2017.

[102] David Neilsen, Milinda Fernando, Hari Sundar, and Eric Hirschmann. Dendro-gr: A scalable framework for adaptive computational general relativity on heterogeneous clusters. *APS*, 2019:G11–003, 2019.

[103] Serguei Ossokine, Francois Foucart, Harald P. Pfeiffer, Michael Boyle, and Béla Szilágyi. Improvements to the construction of binary black hole initial data. *Class. Quant. Grav.*, 32:245010, 2015.

[104] Harald Pfeiffer. Numerical relativity: Mathematical formulation, 2020. talk given at Gravitational Wave Astrophysics, International Centre for Theoretical Sciences. Available at https://www.icts.res.in/program/gws2020/talks.

[105] Harald P. Pfeiffer and James W. York, Jr. Extrinsic curvature and the Einstein constraints. *Phys. Rev. D*, 67:044022, 2003.

[106] Eric Poisson. *A Relativist's Toolkit: The Mathematics of Black-Hole Mechanics.* Cambridge University Press, 2004.

[107] Eric Poisson. Metric of a tidally distorted, nonrotating black hole. *Phys. Rev. Lett.*, 94:161103, 2005.

[108] Eric Poisson. Tidal deformation of a slowly rotating black hole. *Phys. Rev. D*, 91(4):044004, 2015.

[109] Eric Poisson and Eamonn Corrigan. Nonrotating black hole in a post-Newtonian tidal environment II. *Phys. Rev. D*, 97(12):124048, 2018.

[110] Eric Poisson, Adam Pound, and Ian Vega. The Motion of point particles in curved spacetime. *Living Rev. Rel.*, 14:7, 2011.

[111] Eric Poisson and Igor Vlasov. Geometry and dynamics of a tidally deformed black hole. *Phys. Rev. D*, 81:024029, 2010.

[112] Simon F. Portegies Zwart, Holger Baumgardt, Piet Hut, Junichiro Makino, and Stephen L. W. McMillan. The Formation of massive black holes through collision runaway in dense young star clusters. *Nature*, 428:724, 2004.

[113] A. Pound. Nonlinear gravitational self-force. I. Field outside a small body. *Phys. Rev.*, D86(8):084019, 2012.

[114] A. Pound. Second-order perturbation theory: problems on large scales. *Phys. Rev.*, D92(10):104047, 2015.

[115] A. Pound and J. Miller. Practical, covariant puncture for second-order self-force calculations. *Phys. Rev.*, D89(10):104020, 2014.

[116] Adam Pound. Self-consistent gravitational self-force. *Phys. Rev. D*, 81:024023, 2010.

[117] Adam Pound. Second-order gravitational self-force. *Phys. Rev. Lett.*, 109:051101, 2012.

[118] Adam Pound. Gauge and motion in perturbation theory. *Phys. Rev. D*, 92(4):044021, 2015.

[119] Adam Pound. Motion of small objects in curved spacetimes: An introduction to gravitational self-force. *Fund. Theor. Phys.*, 179:399–486, 2015.

[120] Adam Pound. Nonlinear gravitational self-force: second-order equation of motion. *Phys. Rev. D*, 95(10):104056, 2017.

[121] Adam Pound, Cesar Merlin, and Leor Barack. Gravitational self-force from radiation-gauge metric perturbations. *Phys. Rev. D*, 89(2):024009, 2014.

[122] Adam Pound and Barry Wardell. Black hole perturbation theory and gravitational self-force. 1 2021.

[123] Adam Pound, Barry Wardell, Niels Warburton, and Jeremy Miller. Second-Order Self-Force Calculation of Gravitational Binding Energy in Compact Binaries. *Phys. Rev. Lett.*, 124(2):021101, 2020.

[124] Frans Pretorius. Evolution of binary black hole spacetimes. *Phys. Rev. Lett.*, 95:121101, 2005.

[125] Frans Pretorius. Numerical relativity using a generalized harmonic decomposition. *Class. Quant. Grav.*, 22:425–452, 2005.

[126] Richard H. Price. Nonspherical perturbations of relativistic gravitational collapse. 1. Scalar and gravitational perturbations. *Phys. Rev. D*, 5:2419–2438, 1972.

[127] Hulse R.A. and Taylor J.H. Discovery of a pulsar in a binary system. *Astrophys. J*, 195:L51–L53, January 1975.

[128] Guilherme Raposo and Paolo Pani. Axisymmetric deformations of neutron stars and gravitational-wave astronomy. *Phys. Rev. D*, 102(4):044045, 2020.

[129] Carl L. Rodriguez, Ilya Mandel, and Jonathan R. Gair. Verifying the no-hair property of massive compact objects with intermediate-mass-ratio inspirals in advanced gravitational-wave detectors. *Phys. Rev. D*, 85:062002, 2012.

[130] Nicole Rosato, James Healy, and Carlos O. Lousto. Adapted gauge to small mass ratio binary black hole evolutions. 3 2021.

[131] Eran Rosenthal. Second-order gravitational self-force. *Phys. Rev. D*, 74:084018, 2006.

[132] Jaime Salcido, Richard G. Bower, Tom Theuns, Stuart McAlpine, Matthieu Schaller, Robert A. Crain, Joop Schaye, and John Regan. Music from the heavens – gravitational waves from supermassive black hole mergers in the EAGLE simulations. *Mon. Not. Roy. Astron. Soc.*, 463(1):870–885, 2016.

[133] Mark A. Scheel, Adrienne L. Erickcek, Lior M. Burko, Lawrence E. Kidder, Harald P. Pfeiffer, and Saul A. Teukolsky. 3-D simulations of linearized scalar fields in Kerr space-time. *Phys. Rev. D*, 69:104006, 2004.

[134] Bernard Schutz. Discussion on emri/imri using numerical relativity. 20th Capra Meeting, 2017.

[135] Alberto Sesana, Jonathan Gair, Ilya Mandel, and Alberto Vecchio. Observing gravitational waves from the first generation of black holes. *Astrophys. J. Lett.*, 698:L129–L132, 2009.

[136] Masaru Shibata and Takashi Nakamura. Evolution of three-dimensional gravitational waves: Harmonic slicing case. *Phys. Rev. D*, 52:5428–5444, 1995.

[137] Chi-Wang Shu. Discontinuous galerkin methods: General approach and stability. *Numerical Solutions of Partial Differential Equations*, 01 2009.

[138] L. Smarr, A. Cadez, Bryce S. DeWitt, and K. Eppley. Collision of Two Black Holes: Theoretical Framework. *Phys. Rev. D*, 14:2443–2452, 1976.

[139] R. J. E. Smith, I. Mandel, and A. Vechhio. Studies of waveform requirements for intermediate mass-ratio coalescence searches with advanced gravitational-wave detectors. *Phys. Rev. D*, 88(4):044010, 2013.

[140] Ulrich Sperhake, Bernard J. Kelly, Pablo Laguna, Kenneth L. Smith, and Erik Schnetter. Black hole head-on collisions and gravitational waves with fixed mesh-refinement and dynamic singularity excision. *Phys. Rev. D*, 71:124042, 2005.

[141] J. L. Synge. *Relativity: The General theory.* 1960.

[142] Bela Szilagyi, Lee Lindblom, and Mark A. Scheel. Simulations of Binary Black Hole Mergers Using Spectral Methods. *Phys. Rev. D*, 80:124010, 2009.

[143] J. H. Taylor, L. A. Fowler, and P. M. McCulloch. Measurements of general relativistic effects in the binary pulsar PSR 1913+16. *Nature*, 277:437–440, 1979.

[144] Stephanne Taylor and Eric Poisson. Nonrotating black hole in a post-Newtonian tidal environment. *Phys. Rev. D*, 78:084016, 2008.

[145] K. S. Thorne. Multipole Expansions of Gravitational Radiation. *Rev. Mod. Phys.*, 52:299–339, 1980.

[146] Samuel D. Upton and Adam Pound. Second-order gravitational self-force in a highly regular gauge. 1 2021.

[147] Maarten van de Meent. Gravitational self-force on eccentric equatorial orbits around a Kerr black hole. *Phys. Rev. D*, 94(4):044034, 2016.

[148] Maarten van De Meent. The mass and angular momentum of reconstructed metric perturbations. *Class. Quant. Grav.*, 34(12):124003, 2017.

[149] Maarten van de Meent. Gravitational self-force on generic bound geodesics in Kerr spacetime. *Phys. Rev. D*, 97(10):104033, 2018.

[150] Maarten van de Meent and Harald P. Pfeiffer. Intermediate mass-ratio black hole binaries: Applicability of small mass-ratio perturbation theory. *Phys. Rev. Lett.*, 125(18):181101, 2020.

[151] Maarten van de Meent and Abhay G. Shah. Metric perturbations produced by eccentric equatorial orbits around a Kerr black hole. *Phys. Rev. D*, 92(6):064025, 2015.

[152] Vijay Varma, Parameswaran Ajith, Sascha Husa, Juan Calderon Bustillo, Mark Hannam, and Michael Pürrer. Gravitational-wave observations of binary black holes: Effect of nonquadrupole modes. *Phys. Rev. D*, 90(12):124004, 2014.

[153] Vijay Varma and Mark A. Scheel. Constructing a boosted, spinning black hole in the damped harmonic gauge. *Phys. Rev. D*, 98(8):084032, 2018.

[154] Vijay Varma, Mark A. Scheel, and Harald P. Pfeiffer. Comparison of binary black hole initial data sets. *Phys. Rev. D*, 98(10):104011, 2018.

[155] Ian Vega, Barry Wardell, Peter Diener, Samuel Cupp, and Roland Haas. Scalar self-force for eccentric orbits around a Schwarzschild black hole. *Phys. Rev. D*, 88:084021, 2013.

[156] Niels Warburton. New results from second-order black hole perturbation theory, 2020. Talk given at Advances and Challenges in Computational Relativity, Brown University. Slides available at https://icerm.brown.edu/programs/sp-f20/w1/.

[157] Niels Warburton and Barry Wardell. Applying the effective-source approach to frequency-domain self-force calculations. *Phys. Rev. D*, 89(4):044046, 2014.

[158] Barry Wardell, Adam Pound, Niels Warburton, Jeremy Miller, Leanne Durkan, and Alexandre Le Tiec. Gravitational waveforms for compact binaries from second-order self-force theory. 12 2021.

[159] Barry Wardell, Ian Vega, Jonathan Thornburg, and Peter Diener. A Generic effective source for scalar self-force calculations. *Phys. Rev. D*, 85:104044, 2012.

[160] Barry Wardell and Niels Warburton. Applying the effective-source approach to frequency-domain self-force calculations: Lorenz-gauge gravitational perturbations. *Phys. Rev. D*, 92(8):084019, 2015.

[161] Eric W. Weisstein. Runge-Kutta method. *MathWorld–A Wolfram Web Resource*, 2020.

[162] Alan G. Wiseman. The self-force on a static scalar test charge outside a Schwarzschild black hole. *Phys. Rev. D*, 61:084014, 2000.

[163] Helvi Witek, Miguel Zilhao, Leonardo Gualtieri, Vitor Cardoso, Carlos Herdeiro, Andrea Nerozzi, and Ulrich Sperhake. Numerical relativity for D dimensional space-times: head-on collisions of black holes and gravitational wave extraction. *Phys. Rev. D*, 82:104014, 2010.

[164] Kent Yagi and Nicolas Yunes. I-Love-Q Relations: From Compact Stars to Black Holes. *Class. Quant. Grav.*, 33(9):095005, 2016.

[165] Y. Zlochower, J. G. Baker, Manuela Campanelli, and C. O. Lousto. Accurate black hole evolutions by fourth-order numerical relativity. *Phys. Rev. D*, 72:024021, 2005.